

Design of a High Speed High Power Switched Reluctance Motor



Maede Besharati

School of Electrical and Electronic Engineering

Newcastle University

A thesis submitted for the degree of

Doctor of Philosophy

November 2016

Abstract

An increase in the price of rare earth materials in 2009 prompted research into alternative motor technologies without permanent magnets. The SRMs have become more of an attractive solution as they are relatively simpler to construct than other machines technologies hence cost effective. Furthermore, the rugged structure of the rotor makes it suitable for high speed operation, if appropriately designed.

This thesis investigates the design, analysis and prototype manufacture of an SRM, that from electromagnetic point of view, meets the power output of the PM machine used in the Toyota Prius, although operating at a higher speed of 50,000 rpm. As a result, the required torque is considerably less than an equivalent motor with the same output power running at lower speed, hence this approach allows for much smaller frame sizes. To achieve the required torque, careful choice of stator/rotor tooth combination, coil number of turns and number of phases is needed. Running at high speed, increases the AC copper loss (consisting of skin effect and proximity effects) and iron loss. These shortcomings are extensively discussed and investigated.

The mechanical design of this motor requires careful consideration in order to minimise the high mechanical stresses acting upon the rotor, which are due to the high radial forces caused by the centripetal force at high speed. In order to address the mechanical constraints caused by the hoop stress, a structure common to flywheels is applied to the rotor. In this approach, the shaft bore is removed and the laminations are sandwiched together using cheek plates, which are secured using tie rods. The cheek plates have their extending shafts, which consequently will transfer the torque to the rest of the system. The proposed model is analysed for both the electromagnetic and mechanical aspects, successfully demonstrating a promising rotor topology for the design speed. A high speed motor design needs to take into account shaft design, rotor design and bearing design. The high speed operation of the salient rotor gives dramatic rise to the windage loss. These factors are carefully considered in this work and the results are presented.

Contents

List of Figures	vi
List of Tables	x
Nomenclature	xi
1 Introduction	1
1.1 Overview	2
1.2 Publications	4
1.3 Contribution to Knowledge	5
2 A Review of Switched Reluctance Motor Technology	6
2.1 Why SRM?	8
2.2 SRM Design Methods	9
2.3 SRM Operation	11
2.4 Torque Production	11
2.5 Control of the SRM for High Speed Operations	15
2.5.1 Advancing The Inverter Commuting Angle	15
2.6 SRM Topologies	18
2.6.1 Radial SRMs	18
2.6.2 C-Core Stator SRMs	19
2.6.3 Disk Type (Pancake Shaped) SRMs	19
2.6.4 Hybrid SRMs	20
2.7 SRM in Automotive applications	21
2.8 Designing an SRM for Toyota Prius, University of Tokyo Experiment	22
2.8.1 Tapered Angles	23
2.9 High Speed Motors	26
2.10 High Speed Switched Reluctance Motors	31
2.10.1 Benchmark SRM	35
2.11 Summary	36

3	Mechanical Design Methodology	38
3.1	Mechanical Stresses	38
3.1.1	Notch Effect	39
3.1.2	Tangential (Hoop) Stress	39
3.1.3	Lame Equation for Defining Stresses on a Disk	40
3.1.4	Simulation Assumptions	41
3.2	Rotor Vibrations	42
3.2.1	Rotor Slenderness (Aspect Ratio)	42
3.2.2	Vibration Modes	43
3.2.3	Predicting the Critical Speeds using Rayleigh's Method	45
3.2.4	Predicting Critical Speed Using the FEA Method	46
3.3	Bearings	46
3.3.1	Bearing Types	46
3.3.2	Bearing Selection	47
3.3.3	Bearing Mounting Types	48
3.3.4	Pre-load	49
3.3.5	Bearing Specification	50
3.4	Shaft	50
3.4.1	Tip Speed	52
3.5	Balancing	52
3.6	Acoustic Noise	52
3.7	Windage Loss	53
3.8	Conclusion	53
4	Electromagnetic Design Methodology	55
4.1	Introduction to SRMs and their Operation	56
4.1.1	The Aligned Position	56
4.1.2	The Unaligned Position	56
4.1.3	SRM Operation Principle	56
4.1.4	Equivalent Circuit	58
4.2	Design Investigation	59
4.2.1	Number of Phases	60
4.2.2	Stator/Rotor Teeth Combination	60
4.2.3	Analytical Design	61
4.2.4	Coil Design and Number of Turns	62
4.2.5	Air Gap	63
4.3	Motor Specification Investigation	63
4.4	DC Voltage	64
4.5	Conclusion	64

5	Mechanical Design Investigation	65
5.1	FEA model for Mechanical Analysis	66
5.1.1	Simulation Assumptions	66
5.2	Design Process	67
5.3	Mechanical Analysis	68
5.3.1	Conventional SRM Rotor Topology	68
5.3.2	Addressing The Notch Effect	68
5.3.3	Addressing The Tangential Stress	69
5.3.4	Flywheel Structure	70
5.3.5	Physical Features of the Proposed Model	72
5.4	Vibration Frequencies	78
5.4.1	Bearing Stiffness	78
5.4.2	Vibration Modes	79
5.4.3	Spring Pre-Load	80
5.5	Conclusion	80
6	Further Electromagnetic Design Investigation	82
6.1	Rotor Structure Development	83
6.1.1	Rotor Tooth Width (t_r)	83
6.1.2	Tie Rod Cutting Location (Tr_r)	83
6.1.3	Diameter of the Fillet at the Bottom of Rotor Tooth (h_r)	85
6.2	Static Simulation	85
6.2.1	Two Dimensional FEA Simulation Results	86
6.2.2	Three Dimensional FEA Simulation Results	88
6.3	Dynamic Simulation	90
6.3.1	Dynamic Simulations at Base Speed	90
6.3.2	Dynamic Simulations at Full Speed	93
6.4	Losses	93
6.4.1	DC Winding Loss	94
6.4.2	AC Winding Loss	95
6.4.3	Iron Loss	100
6.4.4	Eddy Current at Tie Rods	101
6.4.5	Windage Loss	101
6.5	Efficiency Map	104
6.6	Conclusion	107
7	Prototype Construction	108
7.1	Static Test Prototype	108
7.1.1	Stator Laminations	108
7.1.2	Slot Insulation	111
7.1.3	Coils	111

7.1.4	Rotor Laminations	115
7.1.5	Cheek Plates	116
7.1.6	Tie Rods	117
7.1.7	Rotor Assembly	119
7.2	Modified Construction for Spin Testing	121
7.2.1	Soft Mounting Bearing	121
7.2.2	Probes	122
7.2.3	Balancing	123
7.2.4	Spin Test Drive Technique	123
7.3	Case and End Caps for Static Test	125
7.4	Final Assembly	125
7.5	Conclusion	126
8	Testing and Analysis	128
8.1	Electromagnetic Tests	128
8.1.1	DC Resistance	130
8.1.2	Flux Linkage	131
8.1.3	Static Torque	134
8.1.4	Thermal Behaviour	137
8.2	Mechanical Tests	138
8.2.1	Test Set Up	139
8.2.2	Spin Test Results	139
8.3	Conclusion	144
9	Conclusion	146
9.1	Introduction	146
9.1.1	Electromagnetic Design Process	146
9.1.2	Static Simulation	147
9.1.3	Dynamic Simulation	147
9.2	Mechanical Design Process	148
9.2.1	Mechanical Stresses	148
9.2.2	Rotor Vibration	150
9.3	Prototype Construction	150
9.4	Motor Testing	152
9.4.1	Electromagnetic Tests	152
9.4.2	Mechanical Tests	153
9.5	Comparison to Motors with Similar Specification	153
9.6	Recommendations for Future Research	154
A	Photographs and Mechanical Drawings	156
	References	177

List of Figures

2.1	Rare Earth Metal Prices compared with Gold	7
2.2	Rare Earth Metal Prices	7
2.3	World Motor Vehicle Annual Production	8
2.4	SRM Operation	12
2.5	A Sample Magnetization curve SRM.	13
2.6	Induction and Torque profile	14
2.7	Asymmetric Bridge Converter	15
2.8	Conventional Drive Circuit Modes for an SRM	16
2.9	Single Pulse Mode to Continuous Current Operation	17
2.10	Simple SRM	18
2.11	Schematic of a Multi Layer C-Core SRM	19
2.12	Pancake Shaped C-Core SRM	20
2.13	Hybrid SRM	21
2.14	Torque Improvement Techniques	24
2.15	Speed vs Power Plot for different machine topologies	28
2.16	Speed vs Power Plot for Different Machine Topology	30
2.17	Plot of Speed vs High Speed Index by for Various Machine Topologies	31
2.18	Rotor Designed for 750,000rpm Rotational Speed with Carbon Fibre Sleeves	33
2.19	Rotor Designed for 50,000rpm Rotational Speed Using Flux Bridges .	33
2.20	Non-uniform Air Gap in a High Speed SRM	35
3.1	The Rotor Coordinate System for Stress Analysis	39
3.2	Hoop Stress Definition	40
3.3	Radial and Tangential Stress Behaviour for a Generic Disk (Left) and a Generic Disk with a Central Hole (Right).	41
3.4	The Bounce, Rock, First and Second Bending Resonant Modes. . . .	43
3.5	Main Parameter for Evaluating Critical Speed	45
3.6	Single Angular Contact Bearing.	48
3.7	Angular Contact Bearing Connections, Back to Back (Left) and Tandem (Right)	49
4.1	Coenergy and Stored Field Energy	57

4.2	Equivalent Circuit of a Single Phase	59
5.1	Stress Analysis of a Conventional SRM	69
5.2	Stress Analysis of a Conventional SRM with Added Fillets	70
5.3	Flywheel Simple Schematic	71
5.4	Pullen Patent	71
5.5	Rotor Simple Schematic with a Flywheel Structure	72
5.6	Detailed Drawing Dimensions of The Proposed Rotor	73
5.7	Tie Rod Cutting Diameter Vs. Equivalent stress	74
5.8	Tie Rod Location From Centre Vs. Equivalent stress	74
5.9	Rotor Tooth Width Vs Torque	75
5.10	Stress Analysis of the proposed Rotor	77
5.11	Stress Analysis of the proposed Rotor with a Shaft Hole	77
5.12	Deflection of a Pre-load spring	80
6.1	Rotor Tooth Width	84
6.2	Tie Rod Location	84
6.3	Rotor Bottom OD	85
6.4	Model Used for 2D Static Simulation	86
6.5	Winding Current Direction	87
6.6	Flux Density	87
6.7	Expanded Magnetisation Curve.	88
6.8	Model Used for 3D Static Simulation	89
6.9	Comparison of Magnetization Curves for a 2D and 3D FE Model	89
6.10	Torque Vs. Rotor Position Using the 3D FEA Model	90
6.11	Square Wave Phase Current Used for Control at Base Speed	91
6.12	Advancing the Stator Excitation Angle	92
6.13	Transient Torque Vs. Rotor Position at the Base Speed	92
6.14	Square Wave Phase Current Used for Control at Full Speed	93
6.15	Transient Torque Vs. Rotor Position at 50,000 rpm	94
6.16	Skin Effect	95
6.17	An Example of Proximity Effect	96
6.18	Proximity Effect in an Electrical Machine Coil	97
6.19	Current Density in the Conductors of a Coil Inside the Slot	98
6.20	Comparison of Current Density in A Solid vs Finely Stranded Conductor	99
6.21	Ohmic Loss in the Solid Conductors Inside the Slot	99
6.22	Ohmic Loss in the Finely Stranded Conductor	100
6.23	Magnetic Field Solution at Full Speed	101
6.24	Tie Rod Current Density	102
6.25	Windage Loss Comparison	104
6.26	Efficiency Map Considering a Salient Pole Rotor	106

6.27	Efficiency Map Considering a Cylindrical Rotor	106
7.1	One Stator Laminate	109
7.2	Stack of Stator Lamination in the Case	110
7.3	Stator Lamination Lock Ring	110
7.4	Coil Forming Bobbin	112
7.5	Pressed Coil with 5 Turns	113
7.6	Coils, Nomex and Tufnol Insulations	114
7.7	Tying Cords, Heat Shrinks and Thermal Coupling	114
7.8	Phase Winding Series Connection	115
7.9	One Rotor Laminate of Each Rotor Topology	116
7.10	Fully Manufactured Cheek Plate	117
7.11	Bearing Locating Ring	118
7.12	Rotor Tie Rods	118
7.13	Roughly Made Cheek Plate	119
7.14	Static Rotor	120
7.15	Bearing Assembled On the Rotor	120
7.16	Soft Mounted Bearing System	121
7.17	Fitted Magnet on the Rotor Shaft, Potted Thermocouple and Accelerometer Stud	122
7.18	Fitted O’rings on the Bearing Cups	123
7.19	Volute of The Compressor Wheel, The Side Tube is Exhaust and the Middle One is the Inlet.	124
7.20	Air Redirection Sleeve	125
7.21	Static Test Rig	126
8.1	Static Test Set Up	129
8.2	Rotor Mounted on The Test Rig and The Rotary Table	130
8.3	DC Resistance Test Circuit	130
8.4	The Voltage and Current Pulses Used to Calculate the $\psi - I$ Curves	132
8.5	The Start and End Points of The Rise and Fall Transients	133
8.6	Generic Flux Linkage vs Current	133
8.7	Flux Linkage vs Current	135
8.8	Effect of Reduced Permeability on the Aligned Curve	135
8.9	Static Torque Result	136
8.10	Static Torque Comparison Between Test and Simulation Results	137
8.11	Thermal Test Result	138
8.12	Mechanical Test Set Up	140
8.13	Mechanical Test Rig and Set Up	140
8.14	Speed Test Result of Rotor1	141
8.15	Temperature rise of the bearing of Rotor1	142

8.16 Evidence of Damage on the Compressor Wheel	142
8.17 Speed Test Result of Rotor2	143
8.18 Temperature rise of the bearing of Rotor2	144
A.1 Wire Erosion Machine	157
A.2 Stator and Case	157
A.3 End Windings	158

List of Tables

2.1	Phase and Pole combination	10
2.2	Comparison of the IPMSM in the Second Generation of Toyota Prius and a Competitive SRM	25
2.3	Comparison of the IPMSM in the Third Generation of Toyota Prius and a Competitive SRM	26
2.4	Comparison of SRM1 and the Designed SRM	36
3.1	Bearing Specification	50
3.2	Torsion in Shaft Parameters	52
4.1	Detailed Specifications of SRM1	55
4.2	Detailed Specifications of SRM	63
5.1	Detailed Specifications of SRM1	66
5.2	Materials Used in The Motor Construction	76
5.3	The Optimised Rotor Physical Specifications	78
5.4	The Vibration Modes and Their Frequencies	79
6.1	Loss Type Contribution at Base Speed and Full Speed with Full Power	105
9.1	Specification Comparison of the Toyota Prius, SRM1 and the Designed SRM	154

Nomenclature

Symbol and Description		Units
2D	2 Dimensional	-
3D	3 Dimensional	-
a	Disk Radius	mm
A_b	Bearing Cross Sectional Area	mm ²
A_c	Cross Sectional Area of the Conductor	mm ²
A_{slot}	Stator Slot Area	mm ²
b	Radius of the Central Hole of Disk	mm
$B_{\text{cu-peak}}$	Peak Flux Density within the Conductor	T
d	Bearing Bore Diameter	mm
D	Bearing Outside Diameter	mm
B	Bearing Width	mm
B_{Peak}	Peak Flux Density	T
B_g	Air gap Flux Density	T
R_{bs}	Radius of the Bottom of the Stator Slot	mm
C_d	Drag Coefficient	-
D_a	Shaft Diameter	mm
d_c	Conductor Diameter	mm
d_w	Diameter of the Wire	mm
E	Young's Modulus	Pa
e	EMF	V

F	Pre-load Force	N
f	Frequency	Hz
F_c	Centrifugal Force	N
f_e	Electrical Frequency	Hz
f_f	Fundamental frequency	Hz
r_r	Rotor Radius	mm
f_n	First Natural Frequency	Hz
f_{ph}	Phase Switching Frequency	Hz
f_s	Switching Frequency of Supply	Hz
H	Rotor Pole Height	mm
h_r	Fillet Radius	mm
i	Phase Current/Constant Current	A
I_{rms}	RMS Phase Current	A
J	Current Density	A/mm ²
J_P	Polar Second Moment of Area	mm ⁴
K	Salient Pole Coefficient	-
k	Pre-load spring Stiffness	N/m
k_a	Anomalous Eddy Current Loss Coefficient	-
k_e	Eddy Current Loss Coefficient	-
k_h	Hysteresis Loss Coefficient	-
K_{hp}	Hybrid Ball Bearing Pair Stiffness	N/m
K_{hs}	Single Hybrid Ball Bearing Stiffness	N/m
K_{steel}	Steel Ball Bearing Stiffness	N/m
K_{Total}	Single Bearing Total Three Dimensional Stiffness	N/m
L	Self Inductance	H
l	Bearing to Bearing Distance	mm
L_a	Aligned Inductance	H

L_c	Total Conductor Length	mm
L_e	End Winding Length	mm
L_F	Full Rotor Length	mm
L_{Fe}	Active Rotor Length	mm
L_{max}	Maximum Inductance	H
L_{min}	Minimum Inductance	H
L_s	Stack Length	mm
L_{sh}	Shaft Length	mm
L_{st}	Stack Length	mm
L_u	Unaligned Inductance	H
m	Mass	Kg
MMF	Magnetomotive Force	A
N	Number of Turns	-
n	Rated Speed	rpm
N_p	Number of Winding Turns	-
N_r	Number of Rotor Poles	-
n_s	Steinmetz Constant	-
N_s	Number of Stator Poles	-
N_{st}	Number of Strands in One Conductor Turn of a Coil	-
P	Output Power	W
P_a	Anomalous Eddy Current Loss	W
P_{cu}	Copper Loss	W
$P_{cu-eddy}$	Eddy Copper Loss	W
$P_{Cu,prox}$	Proximity Loss	W
P_e	Eddy Current Loss	W
P_{Fe}	Core Loss	W
P_h	Hysteresis Loss	W

P_i	Input Electrical Power	W
P_o	Output Power	W
q	Number of Phases	-
R	Resistance	Ω
R	Stator Winding Resistance per Phase	Ω
r	Radial Distance From Centre	mm
R_c	Single Conductor Turn Resistance	Ω
r_c	Radius of the Rotating System	mm
R_e	Reynolds Number	-
R_{OD}	Rotor Outer Diameter	mm
R_p	Total Phase Resistance	Ω
S_e	Equivalent or Von Mises Stress	Pa
S_{OD}	Stator Outer Diameter	mm
t	Airgap Length	mm
T	Torque	Nm
t_r	Rotor Tooth Width	mm
Tr_D	Tie Rod Radius	mm
Tr_r	Tie Rod Radial Distance From Centre	mm
t_y	Stator Core Back Thickness	mm
ν	Poisson's Ratio	-
V_{tip}	Tip Speed	m/s
W_e	Input Electrical Energy	W
W_f	Field Stored Energy	W
W'	Co-energy	W
V_s	Supply Voltage	V
y_r	Rotor Yoke Outer Diameter	mm
y_z	Shaft Deflection	mm

y_{z0}	Maximum Shaft Deflection	mm
z	Axial Distance on the Shaft	mm
α	Rotor Active Length to Full Length Ratio	-
β_r	Rotor Pole Arc	Deg
β_s	Stator Pole Arc	Deg
δ	Deflection	mm
θ	Rotor Angular Position	Deg
λ	Rotor Pole Pitch	Deg
λ_{\max}	Maximum Rotor Slenderness	-
λ_s	Rotor Slenderness	-
μ	Viscosity of Air	P
η	Efficiency	%
μ_0	Permeability of Free Space	H/m
μ_r	Relative Permeability of the Conductive Material	H/m
ρ	Electric Resistivity	Ωm
ρ_{air}	Density of Air	K/m^3
ρ_c	Resistivity of conductor	Ωm
σ	Airgap Shear Stress	KNm/m^3
σ_θ	Tangential Stress of a Plate	Pa
$\sigma_{\theta h}$	Tangential Stress of a Disk with a Central Hole	Pa
σ_r	Radial Stress of a Disk	Pa
σ_{rh}	Radial Stress of a Disk with a Central Hole	Pa
τ	Sheer Stress	Pa
ψ	Flux Linkage	Wb
ω	Angular Velocity	rad/s
CNC	Computer Numerical Control	

DAQ	Data Acquisition
EDM	Electrical Discharge Machining
EPSRC	Engineering and Physical Sciences Research Council
EV	Electric Vehicle
FEA	Finite Element Analysis
FF	Fill Factor
HEV	Hybrid Electric Vehicle
ICE	Internal Combustion Engine
IM	Induction Motor
IPM	Interior Permanent Magnet
IPMSM	Interior Permanent Magnet Synchronous Motor
LCM	Lowest Common Multiple
NdFeB	Neodymium Iron Boron
PMSM	Permanent Magnet Synchronous Motor
SRM	Switched Reluctance Motor
TENV	Totally Enclosed Not Ventilated
VESI	Vehicle Electrical System Integration

Chapter 1

Introduction

This work focuses on developing a magnet free motor designed to meet the specification of the permanent magnet motor used in the third generation Toyota Prius. The Toyota Prius is chosen as it was the bestselling hybrid electric vehicle at the commencement of the thesis study. The volatility in the price of rare earth magnetic materials has created a demand for magnet free alternatives. Switched Reluctance Motors (SRM) are a great candidate as the rotor does not have brushes or any rare earth magnetic materials. In particular, high speed SRMs require less torque for a given power and hence a smaller size of motor which makes the design more cost-effective. SRMs are suitable for high speed applications as the rotor is robust with a simple structure. This thesis aims to push the rotor structural design to very high speeds relative to its size, which gives rise to significant mechanical stresses and implementation problems. The mechanical design of the motor is therefore of great importance. From an electromagnetic point of view, high speed operation results in an increase in losses particularly soft magnetic and AC winding loss that need to be mitigated. To achieve this an alternative approach to rotor design was needed to mitigate the high stresses involved. A novel approach to the rotor design has been implemented, the shaft has been removed from the rotor stack, removing an area of very high stress concentration. This includes removing the shaft bore from the laminations and using cheek plates to sandwich the laminations. These cheek plates each have their own extending shaft and the are secured using tie bars. This structure is a common topology used in flywheels. The implementation of a flywheel type topology to an SRM motor has not been studied before and therefore presents design challenges that are investigated in this work. This research resulted in the development and testing of a 50,000 rpm, 60 kW motor with a robust rotor allowing high speed, high power operation.

This thesis work is part of the Vehicle Electrical System Integration (VESI) Consortium which Newcastle University and London City University are two of the multiple academic and industrial partners. VESI is funded by The UK Engineering and Physical Sciences Research Council (EPSRC).

1.1 Overview

A review of existing research into SRMs is presented in chapter two. The review focuses on three major areas; the general operation of SRMs and the suggested modifications to improve the output, the research dedicated to design of an alternative SRM of the same specification to match the PM used in the Toyota Prius, and an overview of high speed electric motor design.

Chapter three provides the mechanical design methodology for a high speed SRM. The high speed operation of a large motor amplifies the mechanical stresses imposed upon the motor caused by the centrifugal force, as the stresses are directly proportional to the square of speed and radius. Furthermore, identifying the natural frequencies of the rotor is important in ensuring a safe operation as there is a risk of failure if the operational speed approaches the critical speed of the rotor. This high speed application necessitates the careful choice of a suitable bearing for a precise and safe operation. Different bearing types and mounting techniques are discussed in chapter three with the final choice of the bearings explained.

The operating principle of SRMs is discussed in chapter four, with a focus on the analytical electromagnetic design method. The methods for selecting the number of phases, choice of the stator/rotor tooth combination, the coil number of turns and the length of the air gap are discussed. Using an analytical method, the frame size, tooth width and core back width are calculated.

During chapter five, the mechanical constraints are investigated, this is carried out ensuring the rotor outer diameter is pushed to its limits before mechanical failure occurs, which in turn ensures the maximum possible output torque. A series of possible approaches to address the high stresses are investigated including the implementation of a flywheel type topology to the rotor. The choice of materials for different motor components are explained and the rotor vibration modes and their respective frequencies are estimated.

In chapter six the electromagnetic behaviour of the proposed motor is investigated. This for a high speed application must be taken into account in parallel with the mechanical design to ensure the rotor specifications are pushed to their limits before failure and to ensure the maximum electromagnetic output. This includes the static and transient output torque, as well as the calculation of losses such as AC copper loss and the iron loss. It is important to calculate the windage loss of a high speed SRM as it is proportional to the angular velocity cubed and the forth power of the rotor radius. The combination of the calculated losses is used to create an efficiency map with respect to the torque and the angular velocity.

In chapter seven the construction of the high speed SRM is presented. The process of building the stator, the rotor and the coils are explained in detail. The more

complex construction of the prototype rotors for the spin test is also presented. Extra stages are added to the spin test rotor manufacturing to ensure mechanical precision and alignment.

Chapter eight presents a series of tests to investigate the operation of the motor and to verify the Finite Element Analysis (FEA) results. The tests are performed in two parts: electromagnetic and mechanical tests. The electromagnetic test results are used to prove the output torque value obtained from the simulations. The mechanical tests are carried out by spinning the rotor up to 50,000 rpm whilst monitoring the vibration frequencies of the rotor and the bearing temperature.

Chapter nine provides a conclusion of this research work and suggests research areas for further investigation.

1.2 Publications

The following peer reviewed conference proceedings and publications are the result of this research work;

- (1) M Besharati, K R Pullen, J D Widmer, G Atkinson, V Pickert. “Investigation of the Mechanical Constraints on the Design of a Super-high-speed Switched Reluctance Motor for Automotive Traction” In: 7th IET International Conference on Power Electronics, Machines and Drives (PEMD) 2014, Manchester, UK, 2014.

Abstract - This paper presents a novel Switched Reluctance Motor (SRM) for automotive traction applications. The electromagnetic and mechanical simulation results of the proposed motor are presented for operation at 50,000 rpm. The SRM is designed to withstand the rotor stresses due to the centrifugal force whilst producing an output power of 60 kW. The simulation results confirm that the stresses forced on the rotor in the proposed topology are below the yield strength of the material with a safety factor of 1.2. Fatigue life may be an issue and will be investigated in the future. The high speed operation allows for a smaller overall size, which in turn leads to lower manufacturing costs. This combined with high output power makes this design a good candidate for use in mass production hybrid electric vehicles.

- (2) M Besharati, J D Widmer, G Atkinson, V Pickert, J Washington. “Super-High-Speed Switched Reluctance Motor for Automotive Traction” In: 2015 IEEE Energy Conversion Congress and Exposition (ECCE), 2015, Montreal, Canada.

Abstract - This paper presents a Switched Reluctance Motor (SRM) capable of running up to 50,000 rpm whilst producing an output power of 60 kW. The high speed operation allows for a smaller overall size, which in turn leads to lower manufacturing costs. It is demonstrated that, at very high speeds, merely shrinking the motor is not enough and certain mechanical considerations should be taken into account. A rotor with a flywheel type design that uses bolts to secure the laminations rather than feeding them onto a central shaft is introduced. Electromagnetic and mechanical simulation results for the motor are presented for key operating points, the results confirm that the stresses on the rotor in the proposed topology are below the yield strength of the material with a safety factor of 1.2. This combined with high output power might make a viable design for use in mass production hybrid electric vehicles.

- (3) M Besharati, J D Widmer, G Atkinson, V Pickert, K R Pullen, J Washington. “Design and Analysis of a High Speed, High Power SMR With a Flywheel Approach”. To be submitted to: IEEE Transaction on Energy Conversion.

1.3 Contribution to Knowledge

This thesis contributes to knowledge in the following areas:

- The mechanical design methodology of high speed, high power SRMs, the investigation of the mechanical constraints on high speed SRMs, implementing a flywheel topology to the rotor to address the high hoop stress (Chapters 3 and 5);
- The electromagnetic design methodology of a high speed SRM, including methods to improve the output torque and decrease the high electromagnetic losses rising from the high speed operation (Chapters 4 and 6);
- Construction of a high speed SRM including altering the existing techniques to wind the SRM coils, and manufacturing rotor to ensure maximum rotor alignment (Chapter 7).
- Development of an SRM to run at 50,000 rpm while producing 60 kW output power to replace the PM machine used in the Toyota Prius (Chapter 5, 6, 7 and 8);

Chapter 2

A Review of Switched Reluctance Motor Technology

In this chapter a review of existing research on Switched Reluctance Motors (SRMs) is presented. The review has three major focus areas:

- the general operation of SRMs and the suggested modifications to improve electromagnetic performance,
- research dedicated to design an alternative SRM to match the PM machine used in the Toyota Prius, and
- the design requirements of high speed electric motors.

For decades, interior permanent magnet synchronous motors (IPMSM) have been the favourite topology of choice for manufacturers of electric vehicles (EV) such as Toyota Prius, Nissan Leaf and GM Volt [1, 2]. Neodymium is the predominant rare-earth-material used in permanent magnets inserted in this type of motors. However, in 2009 the price of Neodymium and other rare-earth dopants, i.e. Dysprosium increased significantly [2, 3]. Fig. 2.2 shows the increase in the price of Dysprosium and Neodymium compared to that of Gold since 2010. This cost increase has reduced back to resealable levels in recent years, as shown is Fig. 2.1, but the resource uncertainty is still a clear issue, particularly when manufactures are committing to high volume production, as is the case with automotive applications, with millions of vehicles produced annually in countries with major automotive industry as shown in Fig. 2.3 [4].

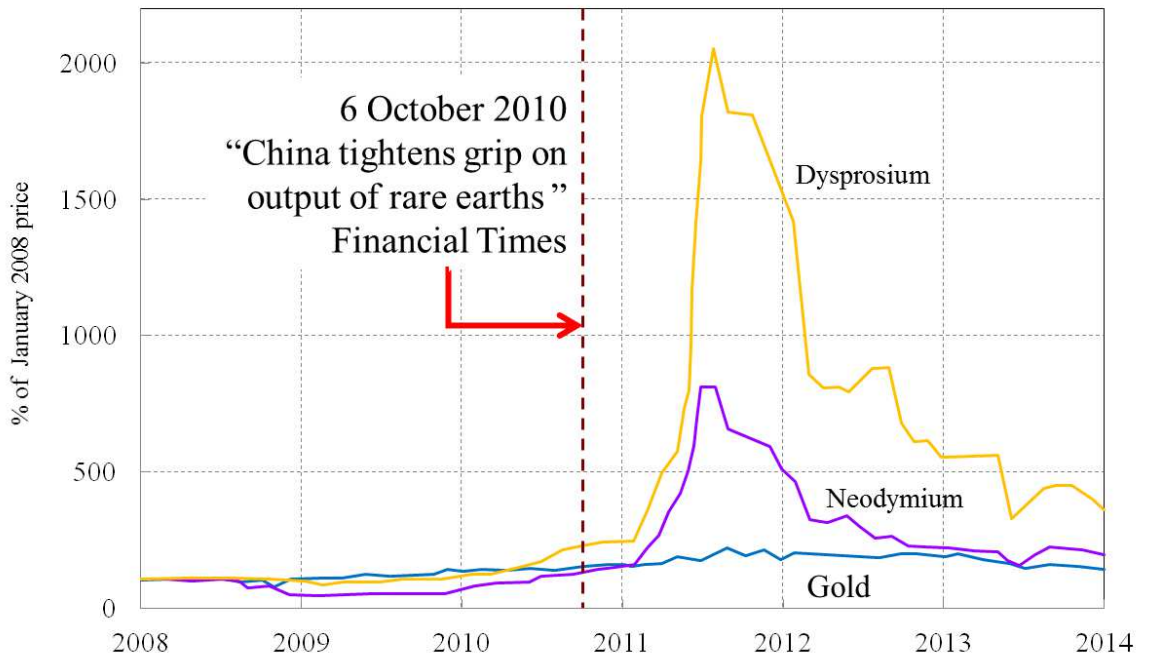
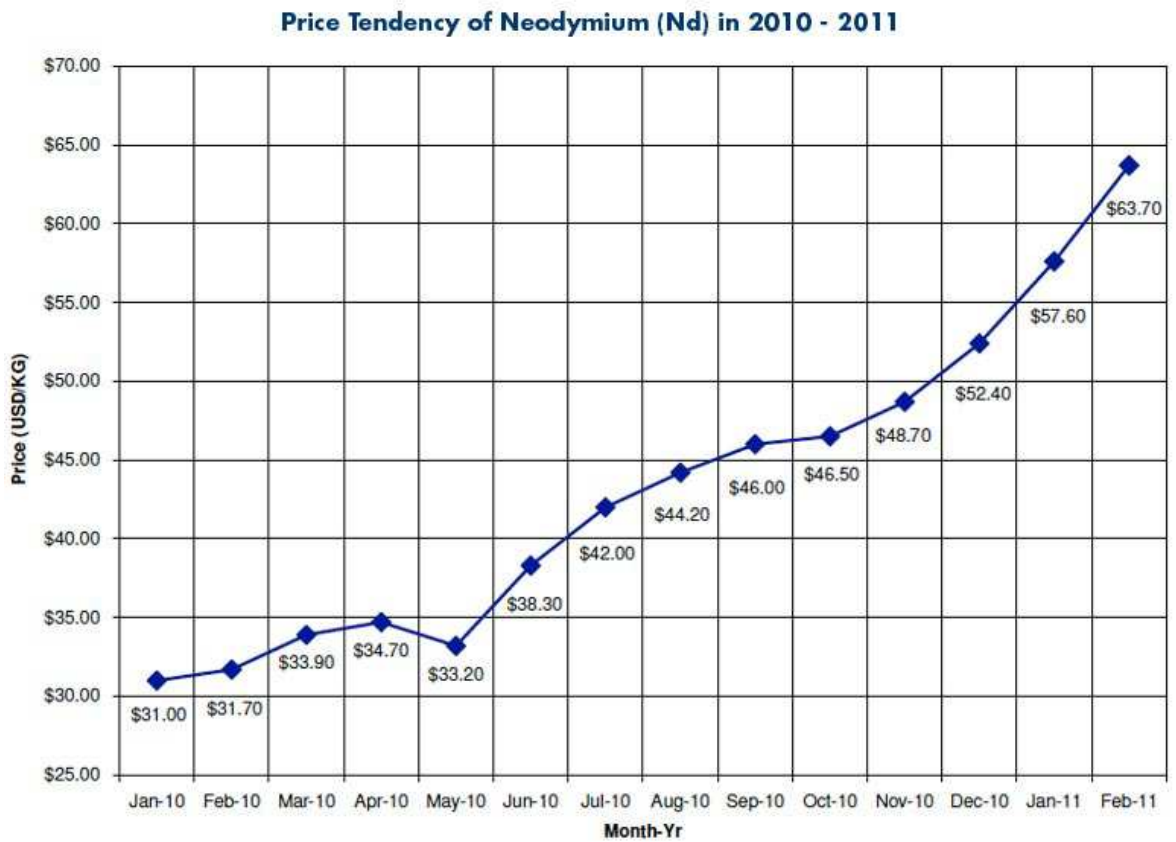


Figure 2.1: Rare Earth Metal Prices compared with Gold [2]



Pricing as of Feb. 15th, 2011.
 Data Source: China Rare Earth material market, subject to change; for reference only.

Figure 2.2: Rare Earth Metal Prices [3]

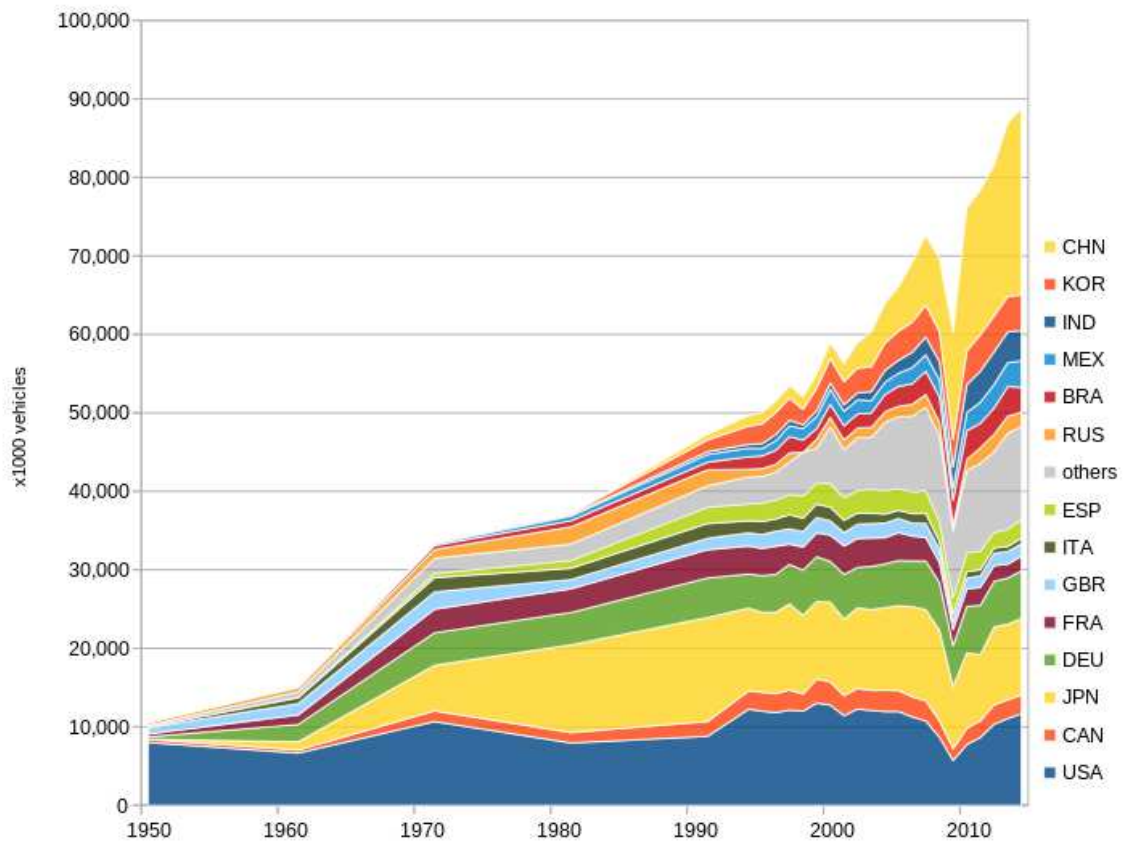


Figure 2.3: World Motor Vehicle Annual Production [4]

2.1 Why SRM?

The major factors in selecting electric motors for EVs or hybrid electric vehicles (HEV) are cost, weight and efficiency. Among the four major electric motor types (Switched Reluctance, Brushed DC, Induction and Permanent Magnet Machines) Switched Reluctance Motors (SRMs) are a good candidate to replace PM machines. Brushed DC machines, despite simple control technique requirements, are large and expensive for HEV applications. Furthermore, the brushes and commutators used in the DC machines add to the maintenance cost whilst reducing reliability. Induction machines, IMs, have higher power density and better efficiency compared to DC motors whilst being robust and cost effective. However, the heat dissipation in the rotor windings leads to lower power compared to PM motors.

SRMs have a wide speed range with satisfactory torque at low speeds. SRMs are usually lighter than IMs and DCs (for the same output power range) and have a better efficiency due to the reduced rotor losses. The simple structure of SRMs leads to lower manufacturing costs compared to the alternatives, making it suitable for mass production. Also, as an AC motor, shoot-through semiconductor failure

can not happen to SRMs which makes it perfect for applications where reliability is important [5]. The rugged structure of the rotor makes it of interest for high speed operation.

SRMs have not been investigated and implemented as vastly as PM machines and IMs [6]. SRMs are a viable solution as they can take advantage of perating under high temperature or high rotational speed, and cheaper power electronics as better technology is now available [7].

On the other hand, the torque density of SRMs is low and they experience high torque ripple. The salient structure makes SRMs inherently noisy. Also, SRMs require a non-standard converter compared to the more well-established motors.

The best-selling HEV is the Toyota Prius which employs a PM machine [8]. Therefore, the performance of this machine can be used as a reference for the design of competing machines based on SRM technology. Furthermore, there are some issues such as torque density that need addressing. One solution is to run the motor at a very high speed, which allows for a smaller size.

Increasing the motor speed while maintaining high output power is challenging. Both the structure of electrical machine and the power electronics should be compatible with high speed operation. Factors such as rotor strength, cooling, lubrication and vibrations should be carefully monitored. Overall, both rotor and stator should be designed for specific high speed application.

Conversely, iron losses increase with frequency. As a result, low iron loss materials are essential. In addition, it is challenging to remove the heat generated by the rotor. Thus, cheap and effective cooling is needed.

2.2 SRM Design Methods

Lawrenson [9] has described the fundamental design of SRMs. The number of phases, stator pole per phase, stator pole arc, rotor pole arc, iron loss and switching frequency are identified as some of the issues that have to be considered while designing SRMs.

The minimum number of rotor poles, N_r , and stator poles, N_s , for a given number of phases, q , can be calculated using Eq. (2.1).

$$\text{LCM}(N_s, N_r) = qN_r \quad (2.1)$$

Where LCM is the lowest common multiple. It should be mentioned the lower values of N_r , the lower the unaligned inductance.

Studies have shown that for self-starting reversible machines, the phase/pole combinations given in Table 2.1 serve perfectly [9]:

Table 2.1: Phase and Pole combination

Number of Phases	N_s	N_r
3	6	4
4	8	6
5	10	8

The basic requirement for the stator and the rotor pole arcs, β_s and β_r respectively, is described using Eq. (2.2);

$$\beta_s + \beta_r \leq \frac{2\pi}{N_r} \quad (2.2)$$

The switching frequency of the voltage applied to phase, f_{ph} , is given by Eq. (2.3):

$$f_{ph} = N_r \frac{\omega}{2\pi} \quad (2.3)$$

Where ω is the angular velocity. Consequently for a supply of q phases the supply switching frequency, f_s , can be expressed as Eq. (2.4);

$$f_s = qN_r \frac{\omega}{2\pi} \quad (2.4)$$

The design methods for SRMs are categorised into three categories; linear, non-linear and finite element method [10, 11].

In the non-linear method, the parameters are considered to be dependent on current with saturation effects included in the magnetic circuit. In this method the minimum and the maximum inductance is calculated using the magnetic circuit [12–20]. Extensive studies have tried to suggest different design procedures focusing on different geometrical aspects such as stator number of poles, rotor number of poles, pole pitch to pole arc ratio and air-gap length [21–25].

Recent advances in FEA software, the finite element analysis (FEA) has become more attractive for analysing SRMs leading into studies on meshing, boundary conditions, electromagnetic and control aspects of SRMs [26–28].

Investigating the effect of changing the geometrical parameter, is primarily done for the purpose of enhancing the output torque and reducing the torque ripple. In other

words, the machine output torque is considered as a starting point in optimizing the machine configuration. For instance, according to [29] a ratio between the rotor radius and stator radius between 0.57-0.63 will enhance the torque. [30] has demonstrated that an SRM with slightly wider stator poles will show a better torque characteristic compared to the same size SRM with narrower stator poles. Another way to decrease the torque ripple is having more than 4 phases. However, each phase needs two switching devices and two free wheeling diodes which results in the drive becoming much more expensive than the motor itself, unless alternative techniques are used to reduce the number of required electric components [31].

2.3 SRM Operation

SRMs have salient stator and rotor poles hence are referred to as doubly salient. In this type of motor, only stator poles (and not the rotor poles) are given simple windings around them, therefore saliency plays an important role in torque production. Also, opposite stator poles share the same phase and are connected in series via their coils. When a stator pole is excited, the magnetic circuit tends to have minimum reluctance by forcing the rotor poles to move towards the aligned position (maximum inductance). In generating mode, the opposite happens. If the rotor inter-polar axis is located on stator poles, the rotor is said to be unaligned with the stator. The aligned and unaligned positions are illustrated in Fig. 2.4. When the rotor pole is exactly at the unaligned or aligned position with a stator pole, the torque produced is zero. If the position of the rotor is at either side of an excited stator, a torque will be produced to restore the rotor to the aligned position. When at the aligned position, as the magnetic reluctance of the flux path is at its lowest, the phase inductance will be the highest. On the other hand, when at unaligned position the phase inductance (the slope of magnetization curve) will be the lowest due to the large air-gap leading to longer flux paths between rotor and stator. In other words, the produced torque tries to rotate the motor in the direction that inductance increases. However, this produced torque is independent from the direction of the current [9].

The torque can be improved by optimizing the physical characteristics of the motor design such as increasing the rotor pole width and reducing the air gap width as far as the manufacturing limits allow [32].

2.4 Torque Production

A continuous excitation of the stator phases in the clockwise direction creates a magnetic field which enables a steady rotation of the rotor in the counter clockwise

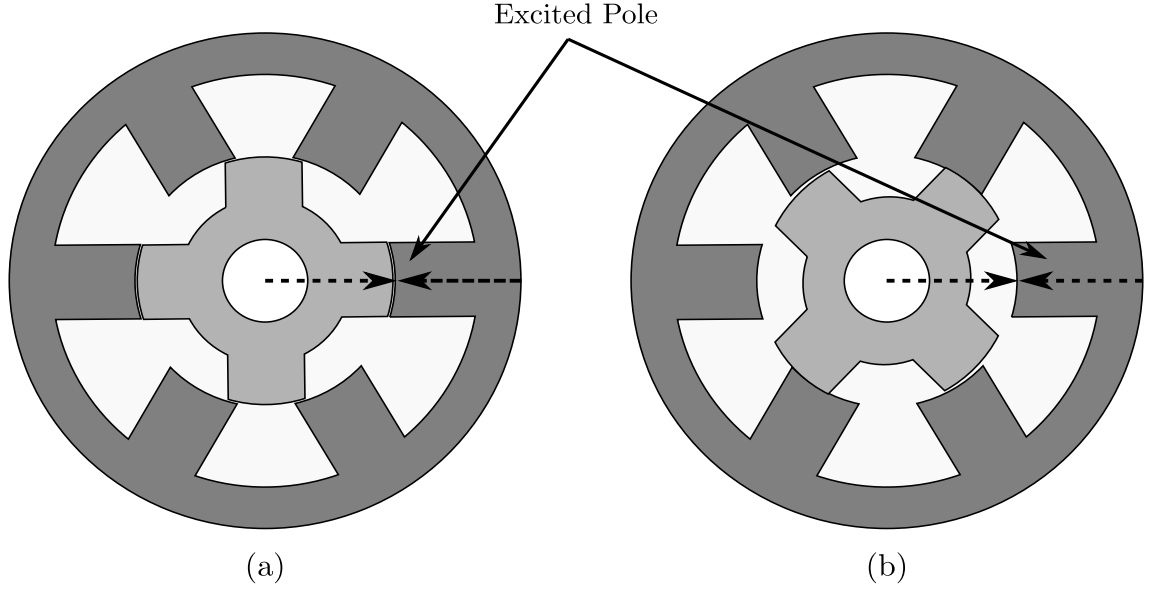


Figure 2.4: SRM Operation. a) Rotor Pole at Aligned Position with the Stator Pole. b) Rotor Pole at Unaligned Position with the Stator Pole

direction. The torque, T , at any rotor position is described using the co-energy, W_l , as given in Eq. (4.3), because of the magnetic non-linearity in saturation mode [33].

$$T(\theta, i) = \frac{\delta W_l(\theta, i)}{\delta \theta} \quad (2.5)$$

Where θ is the angular position of the rotor and i is the current flowing in the coil. The co-energy is directly dependent on the rotor position and the instantaneous current. The co-energy at all positions equals the area between the magnetization curves, which are shown in Fig. 2.5. Therefore, the co-energy can be found by taking the integral over that area as expressed in Eq. (2.6).

$$W_l = \int_0^i \Psi di \quad (2.6)$$

In the case of having no magnetic saturation in the motor, the magnetic curves will be straight, hence the co-energy equals the stored energy in the air-gap, W_f , and is given by Eq. (2.7).

$$W_f = W_l = \frac{1}{2} Li^2 \quad (2.7)$$

Here, L is the self inductance at any rotor position θ . Therefore, torque can be calculated using Eq. (2.8).

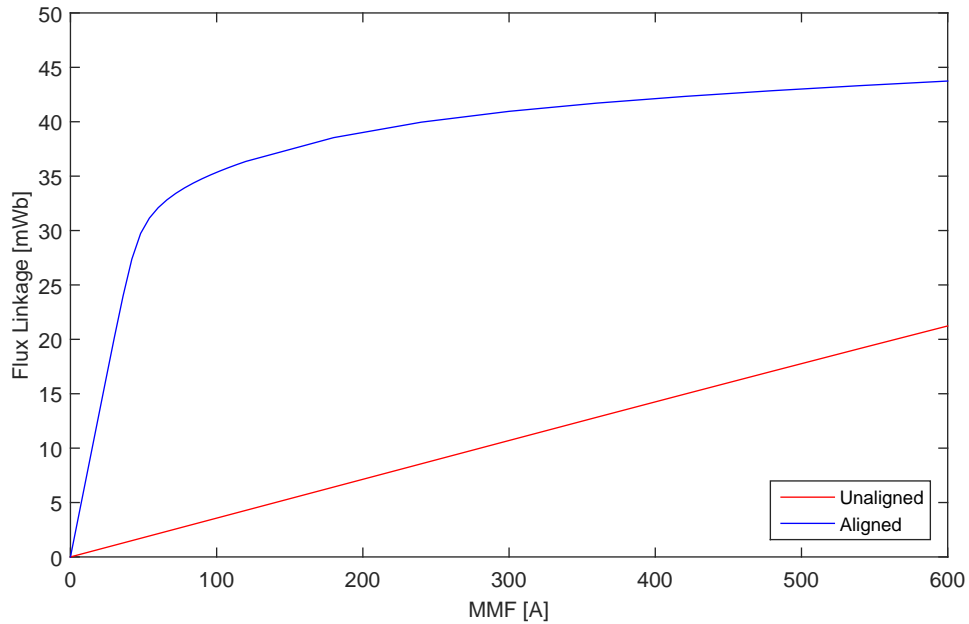


Figure 2.5: A Sample Magnetization Curve SRM

$$T = \frac{1}{2} i^2 \frac{dL}{d\theta} \quad (2.8)$$

It should be mentioned that the torque production is in direct relation with geometrical aspects of the motor, such as air-gap length and pole arc, which are limited by the frame size of machine. Furthermore, the B-H curve of the iron used in the lamination should also be considered as it determines when saturation occurs.

During each excitation cycle, four major inductance regions appear as shown in Fig. 2.6. These regions are;

Region 1: $0 - \theta_1$ and $\theta_4 - \theta_5$: In this region, as the stator and rotor are not aligned (overlapped), the flux path is mainly in air which leads to a constant minimum inductance. This inductance is called unaligned inductance, L_u . There is no contribution in torque production in these regions.

Region 2: $\theta_1 - \theta_2$: In this region the stator and the rotor poles start overlapping, therefore the flux flows through a path over the stator and the rotor laminations. This leads to an increasing inductance in relation to the rotor position. If at this moment the coils are excited by current flowing through them, a positive torque will be produced (i.e. motoring mode). Full alignment of the stator and the rotor poles ends this region.

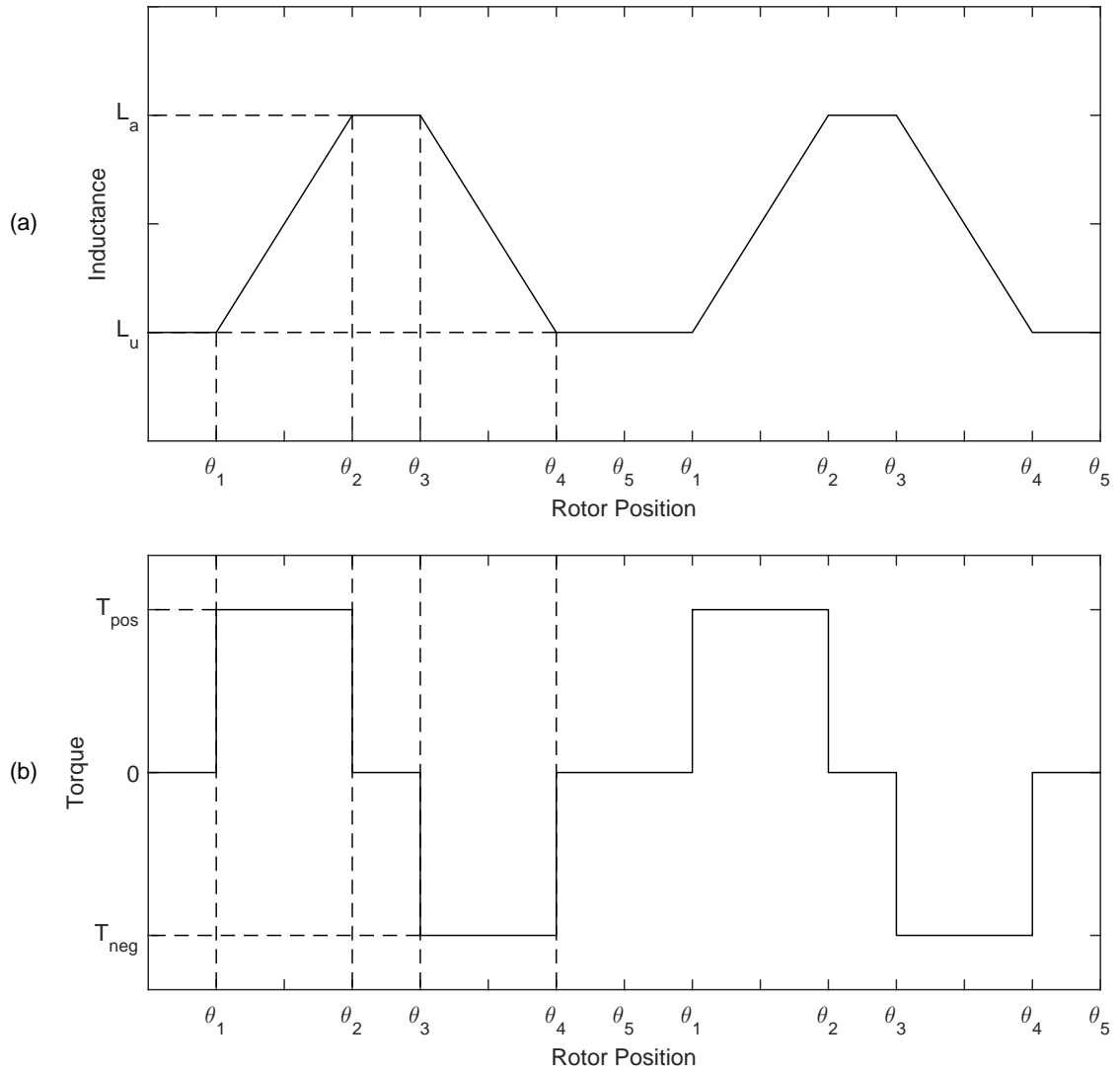


Figure 2.6: Excitation Cycle of a Single Phase a)Inductance profile of an SRM vs. Rotor Position. b)Torque profile of an SRM vs. Rotor Position [34].

Region 3: $\theta_2 - \theta_3$: Over this region, the inductance is at a constant maximum (aligned inductance, L_a), as the rotor pole position does not affect the complete overlapping. Like region 1, the constant inductance means there is no torque production in this region either, despite the presence of current in the coils.

Region 4: $\theta_3 - \theta_4$: This region is similar to region 2 with the difference that the inductance decreases here as the rotor pole moves away from the overlapping position. Decreasing inductance means negative torque can be produced in this region (i.e. generating mode).

In reality this inductance profile is not achievable as the saturation of the motor would curve the graph near the top. Furthermore, in order to reduce the torque ripple, every two succeeding phases will be excited in such a way that the inductance

in the second one starts while the inductance in the first is about to end.

2.5 Control of the SRM for High Speed Operations

The control of SRMs generally is more complicated than other types of electric motors. The non-linear inductance, and the rise up time of the excitation current requires special consideration for the drive. The rise up time of the excitation current becomes particularly important in high speed regions. The common control practice at high speed regions is advancing the turn on angle. However, it should be noted that if advanced too far, the falling current can cause excessive negative torque. Therefore, optimizing the advancing angle is essential in high speed drives [35].

2.5.1 Advancing The Inverter Commuting Angle

The SRM drive circuit uses an asymmetric bridge, unlike the regular H bridge used for other electric motors. There are some configurations proposed for the converter circuit which reduces the number of used devices while giving acceptable output [36]. A conventional drive circuit is shown in Fig. 2.7.

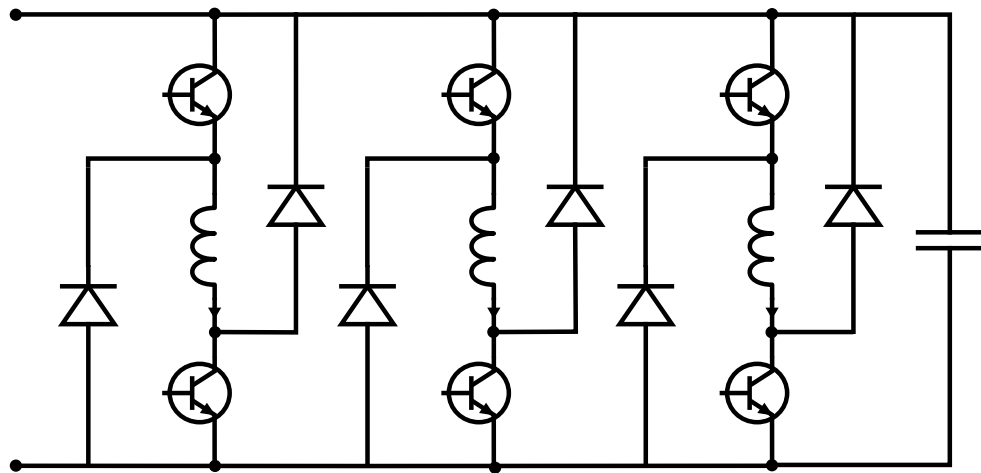


Figure 2.7: Asymmetric Bridge Converter

The flow of the current in each phase depends on one of three circuit operation modes [37]. The operational modes are illustrated in Fig. 2.8. In mode 1, both of the switches S_1 and S_2 are turned on. By applying the DC voltage V the current i flows in the phase winding. In mode 2, switch S_1 is off while switch S_2 is on. In this mode, the phase winding voltage V is zero but there is a decreasing inductance

current that flows in the free wheeling diode D_2 . In mode 3, both the switches S_1 and S_2 are off. Since the current decrease is not instantaneous, the current flows through the diodes D_1 and D_2 . Applying a reverse source voltage $-V$ reduces the phase winding current i rapidly. Therefore, this mode is used for rapidly reducing the current i near the aligned position.

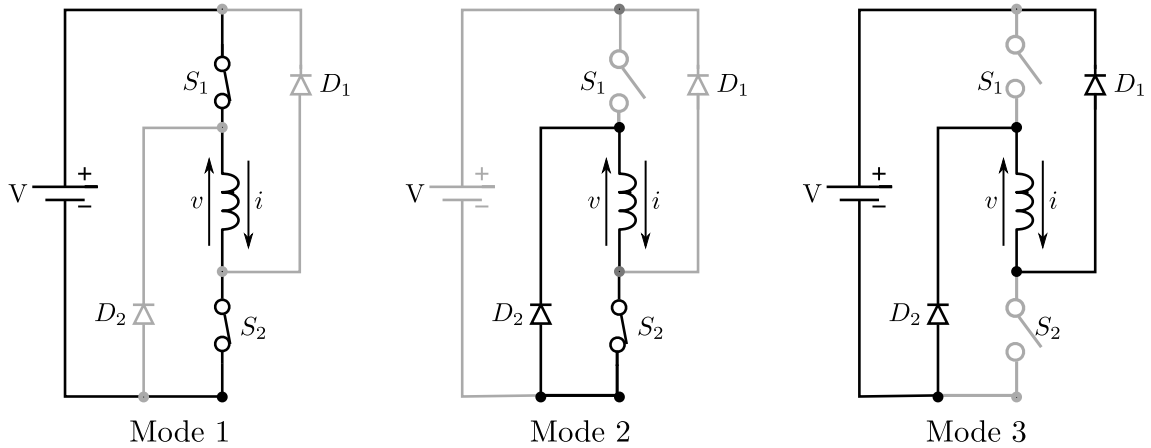


Figure 2.8: Conventional Drive Circuit Modes for an SRM [37]

The requirement for hybrid electric vehicle applications is the capability of producing a continuous power over a wide speed range. In SR motors, while operating at speeds below the base speed of the motor, the produced back emf is not large enough to overcome the current, therefore a simple chopping technique can be used to control the current. The current and voltage signals of an SRM while operating below the base speed is shown in Fig. 2.9 a.

After passing the base speed, the back emf increases to a level that can limit the current, as shown in Fig. 2.9 b. If at this point the phase is excited before its inductance increases, the current would have enough time to increase to a favourable level. This can be done by advancing the commuting angle of the inverter, as mentioned earlier. This technique permits maintaining a constant power while operating at speeds above the base speed.

The phases in SRMs are excited over the periods of one rotor pole pitch. In order to avoid excessive losses, the required time to deflux the motor is equal to the fluxing period. Therefore, advancing angles bigger than half of the rotor pole pitch are considered to cause motor instability. However, the instability would technically be dampened by different types of losses (including the copper loss, the resistance and voltage drop of the drive component).

Under these operating conditions, the total flux linkage during the excitation period would exceed the total flux linkage over the demagnetisation period. Therefore, a residual flux is present before the excitation of the phase and would

increase gradually until it reaches a steady state. Using a voltage control in the steady state allows an equal magnitude for the negative and positive voltage, leading to a constant mean flux during successive phase excitations (continuous current operation). Therefore, using this technique, would change the shape of the current from a single pulse to continuous current. Continuous current operation is illustrated in Fig. 2.9 c.

While in motoring operation, the production of a negative torque is unavoidable as the phase is excited while approaching a decreasing $dl/d\theta$. But the benefits of this technique in improving the motor output would overcome this insignificant negative torque [38]. Indicating the rotor position is important as it identifies which pole winding should be excited first.

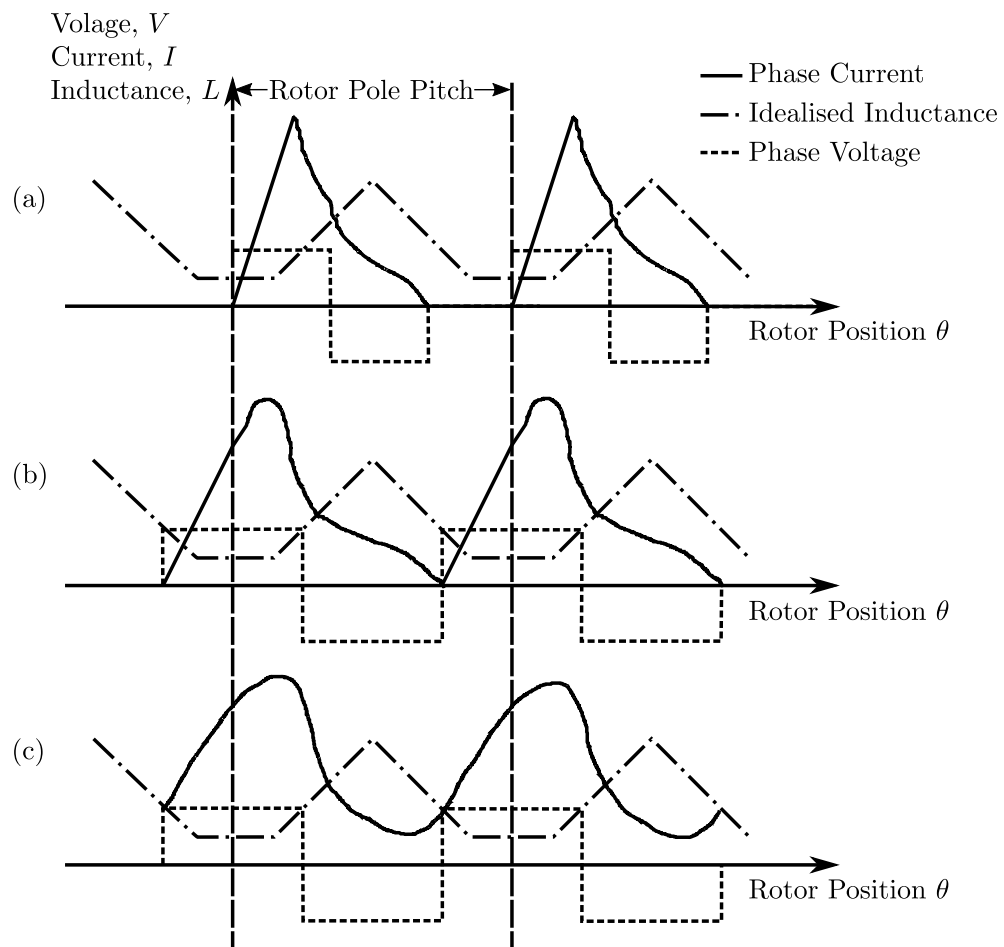


Figure 2.9: Single Pulse Mode to Continuous Current Operation. [38]

2.6 SRM Topologies

Like any other electric motors, many different topologies for SRMs have been introduced. Each one of these topologies are suggested to address a certain shortcoming of SRMs such as torque ripple or acoustic noise. However, not all of the novel topologies are suitable for high speed applications. Some of the more common topologies are discussed as follows.

2.6.1 Radial SRMs

The most common SRM topology is radial topology. This topology consists of a cylindrical rotor which is placed inside a cylindrical stator, where the flux linkage lines from stator poles towards rotor poles are in the radial direction.

This type of SRM is very easy to construct and uses simple rotor structure, which makes them suitable for high speed applications. Usually when considering the SRMs, it is accepted that the number of rotor poles should be smaller than that of stator poles [39]. Higher number of poles results in higher switching frequency and higher iron loss. Therefore, the conventional rotor and stator pole numbering is more suitable for this project. A simple drawing of a radial (conventional) SRM is shown in Fig. 2.10.

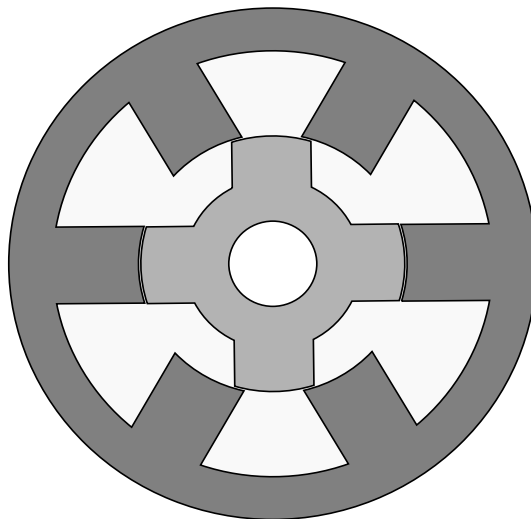


Figure 2.10: Cross Section View of a Radial SRM.

Research shows segmenting the stator may cause reduction in the manufacturing cost of the motor, it has negative effects on the torque due to the additional air gap that will be produced between the stator core back and teeth due to the manufacturing shortcomings [40]. Also, the segmental topology is not suitable for operation at

such high speeds. As a result, a non-segmented stator topology is considered for this work.

2.6.2 C-Core Stator SRMs

Improving the fill factor and ease of winding the coils calls for alternative stator topologies. C-Core stators offer more available slot space to accommodate the winding or permit using thicker wires for windings. Fig. 2.11 illustrates a C-Core SRM. This topology can improve the the efficiency and by stacking more models on top of each other, higher power can be achieved [41–43]. However, having a multilayer rotor effectively doubles the air gap length. This motor is going to have a significant copper loss as end windings is increased in length compared to the conventional type. Furthermore, having a long shaft rotated by multiple rotors is not suitable for high speed applications as long shafts usually do not perform flawlessly at high speeds due to the stresses and increased vibrations.

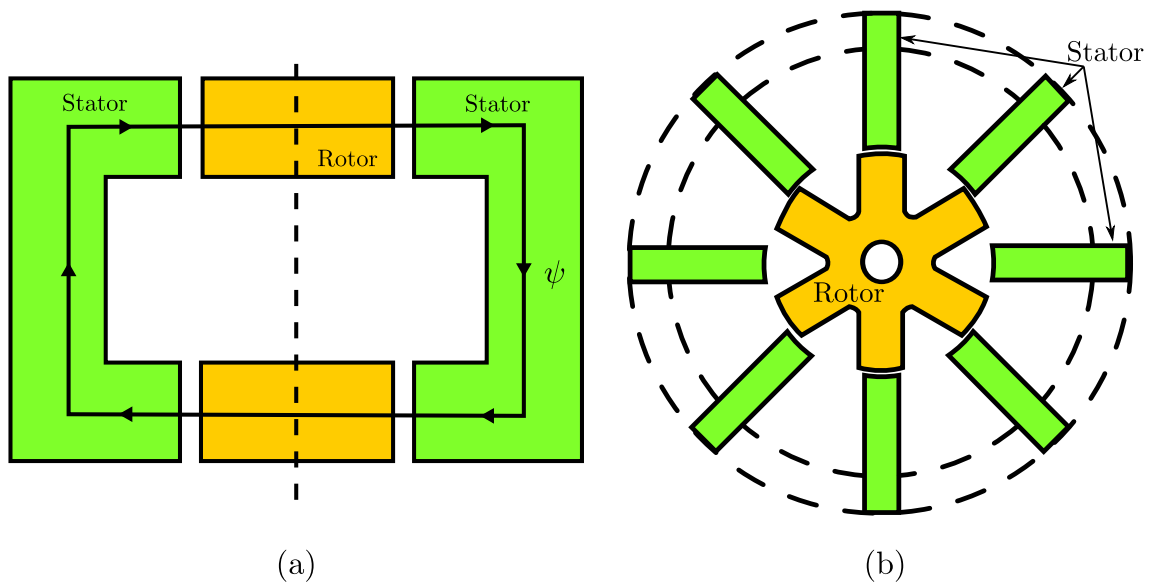


Figure 2.11: Schematic of a Multi Layer C-Core SRM. a) Flux Linkage Path. b) Cross Section View [41].

2.6.3 Disk Type (Pancake Shaped) SRMs

In this motor, the rotor is made of a material with small magnetic permeability in the shape of a disk, as shown in Fig. 2.12. The rotor poles are made by inserting a material with high magnetic permeability into the disk. The vibration and acoustic noise of SRMs are made by the radial component of the electromagnetic force. In this model that component is non-existent, hence, it leads to eliminating the

noise whilst having less torque ripple and greater power density [44]. However, the rotor structure is not suitable for high speed applications. Constructing this motor needs complicated methods in order to insert the rotor cubes inside the rotor disc. Furthermore, the sharp corners of the cubes impose stresses inside the rotor disc. The discrete distribution of the rotor poles around the disc would also add to the stresses. This rotor is likely to fail while running at high speed due to the severe rise in stress in between rotor cubes and rotor disc.

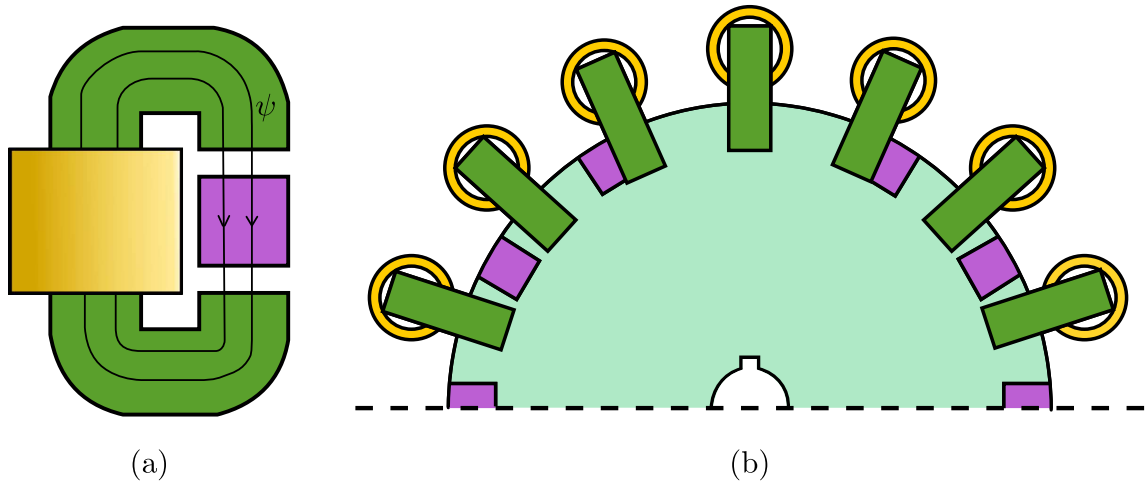


Figure 2.12: Pancake Shaped C-Core SRM. a) A Single C-Core. b) Cross Section View of the C-Core Rotor [44].

2.6.4 Hybrid SRMs

There are some SRMs that are a hybrid between the radial SRM and other motor types. The hybrid between SRM and permanent magnet is the most popular one. In this type of motors (especially in motors with small number of poles) just one piece of a permanent magnet material is used somewhere between two stator poles, which eliminates the need for a position sensor and helps the rotor poles to stop in that area. In [45] a new hybrid model is introduced in which at the tip of all the stator poles one piece of magnet is used, as illustrated in Fig. 2.13. It is suggested that this model has higher torque and better efficiency compared to a same size conventional SRM. It has shown good performance under full-load and over-load operation which makes it fit for electric vehicle applications. However, using magnets leaves less space for windings. Also, magnets are at the risk of demagnetization and motors which use magnets cannot operate at elevated temperatures or in harsh environments (which is an advantage of SRMs). Using rare-earth magnetic materials is not in line with the purpose of this project due to their increasing cost.

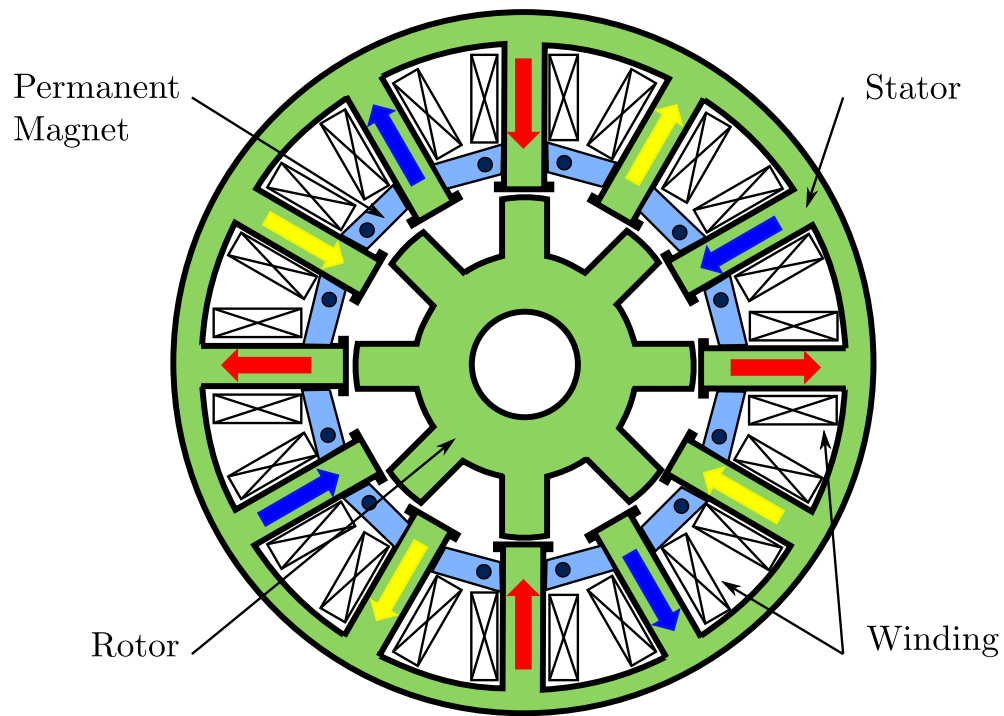


Figure 2.13: Cross-Section of a Hybrid SRM [45].

2.7 SRM in Automotive applications

The capability of operating wholly in constant power is an essential requirement of vehicle drive trains. The implementation of internal combustion engines (ICE) requires multiple gear systems in order to achieve the appropriate torque speed profile. However, properly designed and controlled electric motors can realize an extended range for constant power operation.

While designing an electric machine for HEVs the following should be carefully considered: 1) The constant power operation range, 2) The efficiency of the motor over this range, 3) The power factor over this range, 4) The over load capacity over short periods [46].

SRMs have been considered for different automotive applications for their robust structure, ability of operating at a wide range of speed and high temperature and their fault tolerant nature [47]. Overcoming the acceleration in a traction drive requires high torques at low speeds. The heat dissipation is mostly concentrated at the stator windings which makes cooling straightforward. The salient structure and large rotor shaft bore result in a lower rotor weight compared to an equivalent size PM motor. The salient structure of the rotor provides low torque to inertia ratio allowing fast acceleration (during starting) and deceleration (during emergency brakes). This characteristic of SRMs becomes important when considering road

safety. The advantages and disadvantages of SRMs over other electric motors and suggestions to improve the design method is discussed in [48].

Furthermore, an electric motor will be suitable for vehicle applications if it meets the short term overload requirements of the vehicle. The advantage of SRMs over e.g. induction motors is the lack of braking torque. Nevertheless, the overload abilities of SRMs depend on the amount of current (and how fast) that can be pushed into the coils against the rising back EMF. However, it should be mentioned that in real life the over load capability of the motor will be lower than the estimated ones as an overloaded motor will have a highly saturated core leading to a reduction in the torque and hence the power [49].

Kachapornkul et al. have suggested a 3-phase 15kW SRM for the propulsion system of an electric vehicle [50]. As the efficiency of the SRM is lower than that of a PM motor, efficiency improvement was investigated for this work by the selection of materials with low iron loss, machines design, increased fill factor and optimization of the voltage waveform.

2.8 Designing an SRM for Toyota Prius, University of Tokyo Experiment

The best selling hybrid electric vehicle at the commencement of this work was the Toyota Prius. The popularity of this model encouraged researchers to find magnet free alternative electric motors with the same output specifications. The research team at Tokyo Institute of Technology and University of Tokyo have carried out multiple projects to propose alternative SRMs to the PM machine used in the different generations of the Toyota Prius.

Hayashi and Takeno have investigated the efficiency improvement with respect to the implemented electrical steel for a 50 kW SRM with similar frame size, weight, rated current and voltage of the PM motor in the 2004 Toyota Prius [51, 52]. Three different electrical steel were studied for this work: 35A300 (Japanese Industrial Standards Denotion, known as 300 under British Standards) a general low loss silicon steel, 10JNEX900 or ‘Super Core’ a 6.5% silicon steel, and a layered block of amorphous alloy. The 35A300, 10JNEX900 and the amorphous alloy have a thickness of 0.35 mm, 0.1 mm and 0.25 mm, respectively. The comparison of the B-H characteristics of the three materials showed 35A300 has the best saturated flux density followed by 10JNEX900 and finally the amorphous alloy. Conversely, the high frequency iron loss graphs indicate the amorphous alloy and 10JNEX900 have 17% and 26% of the iron loss of 35A300 at 0.5 T. An SRM model was simulated for each one of the silicon steels and different efficiency

improvement techniques such as fill factor improvement and advancing the excitation angle were carried out. It was concluded that the amorphous alloy showed the highest efficiency, followed by 10JNEX900 and finally 35A300. This work also showed that improving the winding fill factor gave only 1% increase to the efficiency while optimizing the iron core design of the machine resulted in 5% increase. However, the amorphous alloy comes with a significant down fall of a high cost (almost 26 times that of 35A300) which makes it unsuitable for mass production. Therefore, efficiency improvement of a general low loss silicon steel via design techniques is the preferable solution.

In [51, 52] the authors tried to maintain the specifications of 2010 Toyota Prius. Therefore, the motors total axial length is kept equal to the length of interior permanent magnet (IPM) machine. Total axial length consists of the stack length and end winding lengths. Having more number of stator poles result in shorter end windings, therefore, the designs with higher number of stator poles end up having longer stack lengths.

The 2010 Toyota Prius requires a current density of $20 - 26$ A/mm² and a torque density of $35 - 45$ Nm/l for a duration of 18 seconds. Its efficiency at the highest point is 96% with a constant power operation of up to five times the base speed. The 2010 model has a torque of 400 Nm [53]. Selecting 10JNEX900 results in higher efficiency, however, torque improvement will be needed [54, 55].

2.8.1 Tapered Angles

Several approaches can be taken in order to enhance the output torque of the motor. Tapering the stator pole was used as a torque improvement technique. Tapering the stator poles smoothens the flux lines inside stator which results in better conversion loop energy and consequently higher maximum torque. An example of a stator tapered pole is illustrated in Fig. 2.14a. However, care must be taken to the extent of tapering the angle as big angles leave small spaces for winding.

Moreover, making use of a non-uniform air gap, as shown in Fig. 2.14b will result in eliminating the position sensor while widening the positive torque range [56]. This model, despite addressing the starting torque issue, would limit the motor to one directional rotation. Furthermore, the asymmetric air gap results in reduction in the maximum output torque.

Lower efficiency associated with SRMs, compared to the PM motors, is one of their biggest shortcoming which hinders their adoption for HEV applications. The second generation of the Toyota Prius has used a 50 kW IPMSM with a maximum torque of 400 Nm and an efficiency of 95%. Several approaches were taken to meet the high efficiency requirement. The choice of the silicon steel was carefully investigated

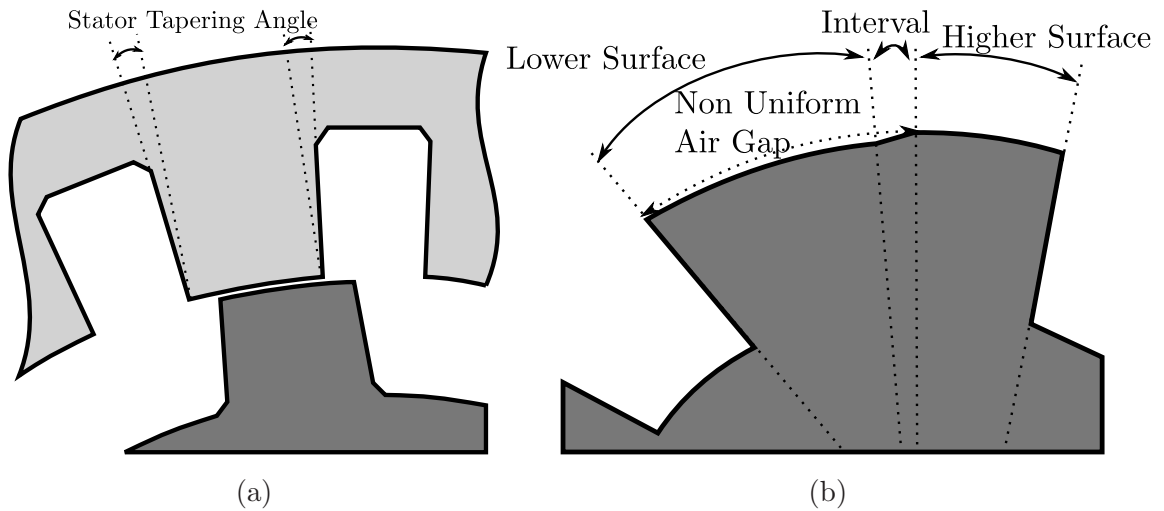


Figure 2.14: Torque Improvement Techniques. a) Tapering Stator Poles. b) Uneven Air Gap [56].

from the point of view of low iron loss and high torque density. During the material selection it was noted that the materials with high saturated flux density produced higher torque while materials with low iron loss result in a higher efficiency and a compromise was made in final selection. The torque density was improved via design improvement techniques such as increasing the number of stator poles, increasing the stack length and optimising the stator taper angle. The efficiency was found to be high at low torque with a medium to high operational speed [57–60]. The comparison of the IPMSM and the SRM are given in Table 2.2. However, increasing the number of poles is not always possible especially in high speed applications. Furthermore, the stack length is usually limited by the mechanical constraints or available motor space. Therefore, further techniques are required to improve the efficiency and torque density.

The research associated with replacing the PM used in the Toyota Prius models has continued by the release of the third generation of the model in 2009. The PM motor used in the third generation was more compact with higher rotational speed and improved output power. [61] has proposed an SRM with the same diameter and axial length while delivering torque, output power, efficiency and operation area competitive to that of the Toyota Prius. The torque improvement, like the previous works, was carried out by material selection and rotor design enhancement. The torque is directly proportional to the motor axial length, thus increasing the axial length results in an improved torque. Since the axial length of the motor is the sum of the stack length and the end winding length, by decreasing the end winding length the stack length was increased to maintain the constant axial length. The end winding are inherently shorter for concentrated short-pitch

Table 2.2: Comparison of the IPMSM in the Second Generation of Toyota Prius and a Competitive SRM

Parameter	Unit	IPMSM	SRM
Number of Poles		8	18/12
Stator Outer Diameter	[mm]	269	269
Stator Inner Diameter	[mm]	160.5	180
Winding Type		Distributed	Concentrated
Axial Length	[mm]	156	156
Winding Number of Turns		9	14
Fill Factor	[%]	56.7	57.2
Volume	[l]	8.92	8.92
Maximum DC Voltage	[V]	500	500
Base Speed	[rpm]	1200	1200
Full Speed	[rpm]	6000	6000
Torque at Base Speed	[Nm]	400	403
Torque Density at Base Speed	[Nm/l]	45	45
Maximum Power at Base Speed	[kW]	50	50
Copper Loss at Base Speed	[kW]	10	6.67
Iron Loss at Base Speed	[kW]	0.28	1.36
Efficiency at Base Speed	[%]	83	86
Current Density at Base Speed	[A/mm ²]	20	21.7

winding , compared to the distributed one used for the IPMSM. The end winding length, L_e is approximately calculated using Eq. (2.9) [61].

$$L_e = \frac{\pi R_{bs}}{2N_s} \quad (2.9)$$

Where N_s is the number of stator poles and R_{bs} is the radius of the bottom of the slot. Therefore, higher number of stator poles results in shorter end winding length. In order to ease the magnetic saturation, the optimization of the stator yoke width while maintaining the winding fill factor was also applied to improve the output torque. This was carried out by decreasing the winding number of turns. Other motor characteristics such as rotor outer diameter and stator pole taper angle also were altered to reach the target torque. The specification of the proposed SRM are compared to that of the third generation Toyota Prius in Table 2.3.

The phase winding number of turns is in inverse proportion with the efficiency, therefore should be carefully considered for SRM design for HEV applications [62]. Also, continuous current operation leads to efficiency reduction. The fill factor of a stator slot is calculated using Eq. (2.10).

Table 2.3: Comparison of the IPMSM in the Third Generation of Toyota Prius and a Competitive SRM

Parameter	Unit	IPMSM	SRM
Stator Outer Diameter	[mm]	264	264
Total Length	[mm]	108	108
Total Mass	[kg]	22.2	25.2
Fill Factor	[%]	54	56
Current Density	[A/mm ²]	18.8	23.9
Maximum DC Voltage	[V]	650	650
Torque at Base Speed	[N.m]	207	211
Torque Density at Base Speed	[N.m/l]	35	36
Full Speed	[rpm]	13900	13900
Maximum Power	[kW]	60	61
Maximum Power Density	[kW/l]	10.2	10.4
Copper Loss	[kW]	6.0	6.3
Iron Loss at Base Speed	[kW]	2.7	1.3
Efficiency at Base Speed	[%]	88	89

$$FF = \frac{N_p N_s (d_w/2)^2 \pi}{A_{slot}} \quad (2.10)$$

Where N_p is the winding number of turns per pole, N_s the number of strands in one turn, d_w the diameter of the wire and A_{slot} the stator slot area. It can be seen that to keep a constant fill factor, N_p should be increased whilst decreasing N_s . The number of turns is increased to achieve a target torque in applications where there is a current limit. Increasing the number of turns results in an increase in the motor back EMF which becomes an issue for high operational speeds. The shaft output power can still be maintained by applying a continuous current operation. Applying continuous current and increasing the number of turns results in producing negative torque and increased copper loss (due to higher rms and increased resistance due to higher number of turns) which leads to reduction in efficiency. Therefore a balance between the number of turns and the efficiency is required [62].

2.9 High Speed Motors

The market requirement is constantly towards improved efficiency and power density while reducing the manufacturing costs. The recent development in power electronics and electrical steel production has allowed researchers to move more

and more towards higher operational speeds for electric motors. This is especially of interest for direct drive applications where the need for a mechanical transmission system is omitted, resulting in lighter, more efficient systems with improved reliability and reduced maintenance requirements. High speed electric machines are particularly interesting for traction applications where reduction in weight and size are difficult to achieve.

Electric motors can operate at a wide speed range using accurate variable speed control. The interest for high speed electrical motors has increased in recent years. The high speed operation brings advantages like smaller size (hence reduced cost), higher power density and higher efficiency. Conversely, issues such as increased iron loss, requirement for expensive bearings, higher windage loss and increased mechanical stresses arise with higher speeds.

The operational speed of electrical motors depends on factors such as temperature, mechanical stress and critical frequencies. The magnetic and electrical loading, power and size of the machine also govern the mentioned factors. It has been demonstrated that a solid topology is usually preferred for the rotor of high speed motors, due to the mechanical robustness of such structure.

High speed motors should be defined as those which push the stress limits of the rotor components, rather than being defined as an absolute speed value. In this case, from mechanical design point of view, a high torque rotor with large volume and low speed can be equally challenging to construct as a high speed low torque rotor with a smaller volume.

The concept of dynamic speed is introduced by van Millingen et al [63], which is a numerical parameter described by Eq. (2.11):

$$n\sqrt{P} \tag{2.11}$$

Where n is the rotational velocity in rpm and P is peak power in kW. Eq. (2.11) is a figure of merit for high speed machinery, used as a guide number to assess possibility of dynamic challenges such as critical speeds, material stress, peripheral velocity and balance sensitivity [63]. Considering this figure of merit, a machine with a 1,000,000 $n\sqrt{P}$ is mechanically very difficult to engineer, whilst the manufacturing of machines with lower values of 500,000 – 800,000 is mechanically achievable with moderate difficulty [64].

A 2 MW 15,000 rpm IM is built using hoop stress relief cuts and an integrated joint boss, which results in the reduction of stress concentration. However, the laminations used for the rotor manufacturing are of high-strength aircraft-grade AISI 4130 alloy. Generally, cobalt iron which is significantly more expensive than

the common silicon iron, is used for the rotor construction of high speed motors and a low iron loss alloy such as NO20 for the stator [65]. The purpose of this work is to design a motor suitable for mass production in automotive applications which does not allow the use of expensive materials. In Fig. 2.15 the power-speed points are plotted for numerous high speed motors, where $\text{rpm}\sqrt{\text{kW}}$ are superimposed. The proposed SRM of this work is shown on the figure for the comparison purposes.

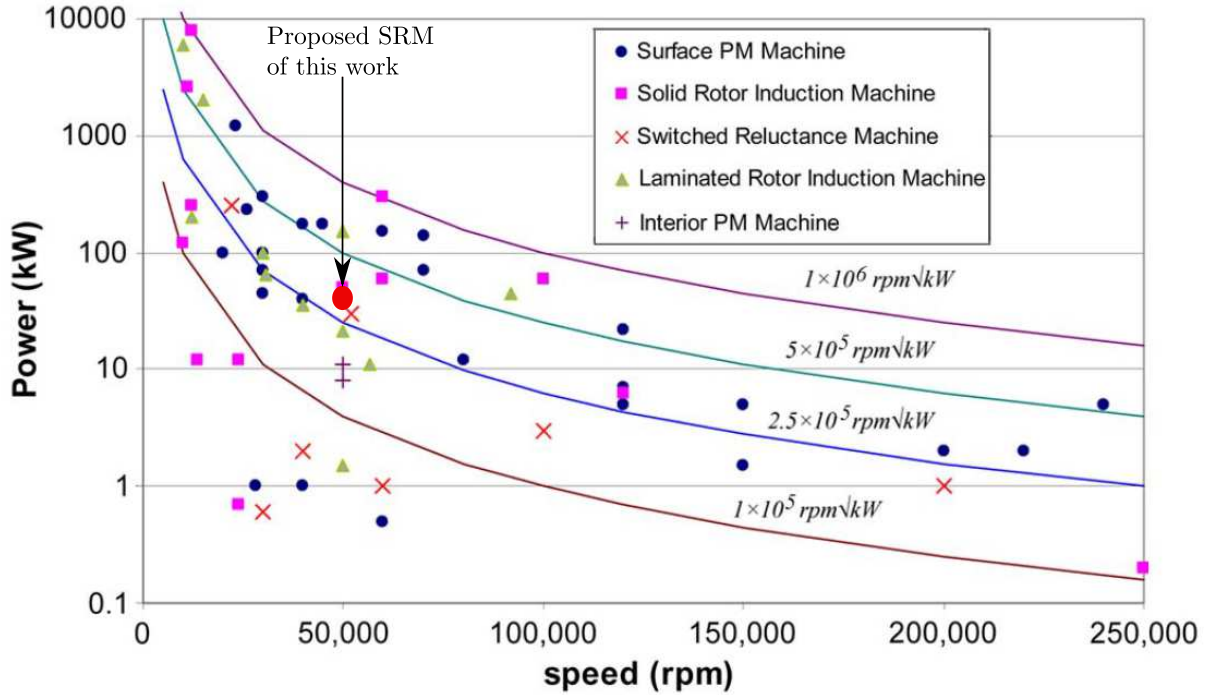


Figure 2.15: Speed vs Power Plot for different machine topologies by Gerada [65], with non-linear $\text{rpm}\sqrt{\text{kW}}$ correlations as proposed by van Milligen [63]

As classifying the electrical motors as ‘high speed’ or ‘high power’ can be misleading. Using the empirical formula demonstrated in Eq. (2.12), a border line is obtained in order to distinguish the ‘high speed’ and ‘super high speed’ terms. For instance a machine with a maximum speed of 60,000 rpm and rated power of 10 kW is classed as a high speed motor while motors running at faster speeds compared to it would be classed as super high speed motors [66, 67].

$$Pn^{3.3} \leq 6.2 \times 10^6 \quad (2.12)$$

Where P and n are the peak power in kW and Speed in krpm, respectively.

Fig. 2.16 shows the speed vs power plot for different machine topologies with a linear correlation. It can be seen from Fig. 2.16 that the proposed SRM of this work falls above the guide line, making it eligible for the super high speed class of motor.

However, the maximum permitted speed for each individual motor is defined by its mechanical stresses and thermal capabilities associated with the increased frequency. Also, tip speed, the tangential speed of the rotor at its outer surface, is used to define high speed as the size of the rotor is also taken into account in calculating this value [68].

Moghaddam introduces a high-speed index, to classify the limitations of electrical machines in high speed technology, as Eq. (2.14):

$$\omega P \tag{2.13}$$

By increasing the speed, the limiting factors for high-speed power capability takes different nature, resulting in changing the high speed index behaviour. Fig. 2.17 summarises the high speed index and rotor tip speed vs rotational speed of some 200 manufactured high speed machines [69]. As it can be seen, most of the machines fall between the orange and blue lines which are the Competitive Technical Limit (CTL) and Soft Technical Limit (STL), respectively. Regions, A, B and C are distinguished by blue, red and green ellipses, respectively, based on the behaviour of the high-speed index for different values of rotational speed, n . Using empirical relations, Moghaddam shows that:

$$P \propto R_{OD}^{2.6} \tag{2.14}$$

Where P is the machine output power is kW. While the empirical relations help deduce limits for existing state of the art, they present little information on how to achieve power limits. Nor are the relation vs particularly useful for evaluating power limits on novel machines, as can be deduced from Fig. 2.17 [69]. As it can be seen, the proposed SRM of this work is classed just above the CTL zone.

Induction machines are used in the majority of high speed applications as a result of their robustness and low maintenance requirements [70]. However, due to their high copper loss compared to the other electrical motors, they have a lower efficiency. Also, in a small size motor, there is limited space for conductors which leads to a relatively lower power density. The permanent magnet motors have a higher efficiency compared to induction machines or SRMs. But they have a larger rotor inertia. This causes extreme bearing load and shortens the bearing life.

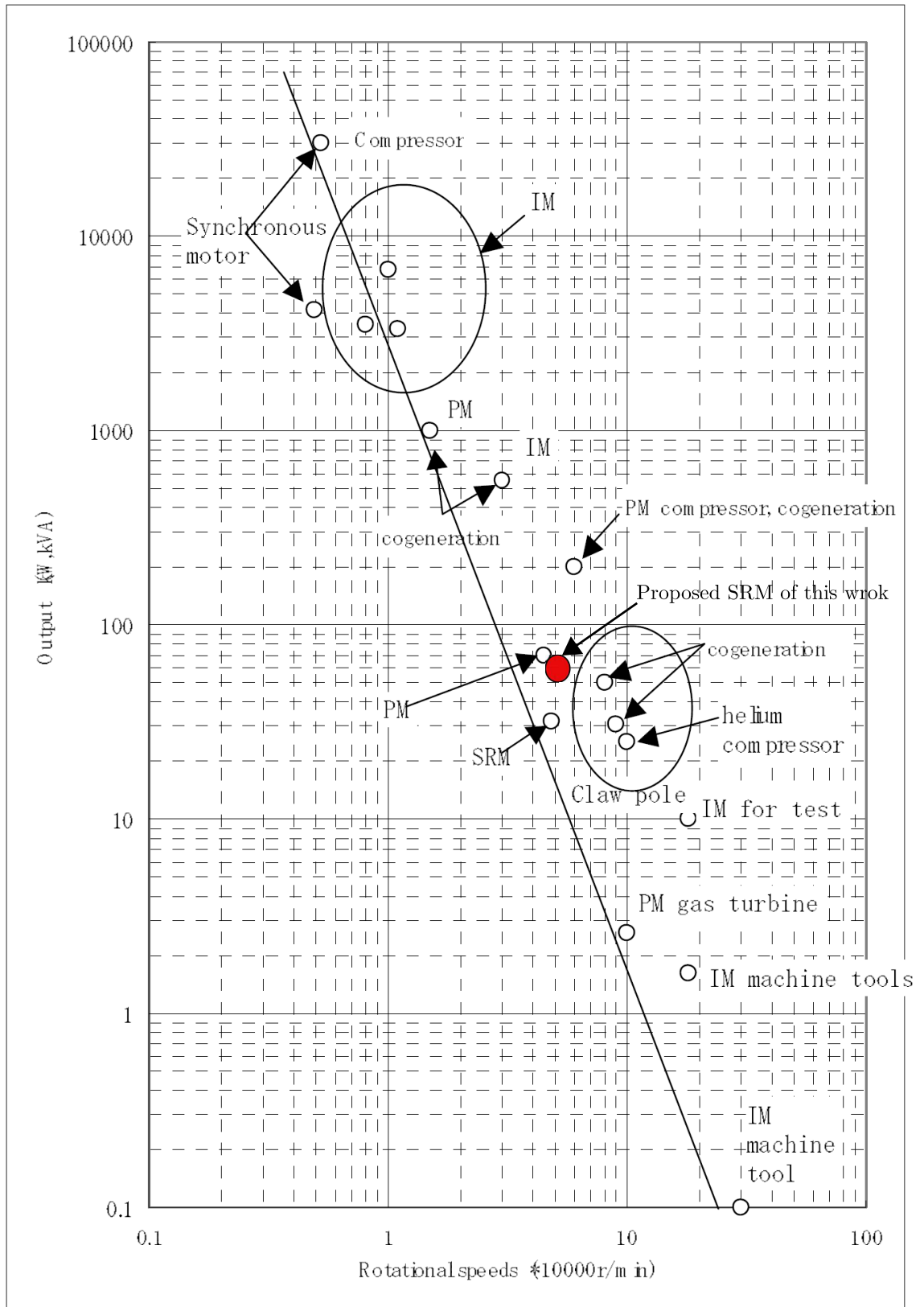


Figure 2.16: Speed vs Power Plot for Different Machine Topology by Rahman [67], with linear correlations as proposed by Maeda [66]

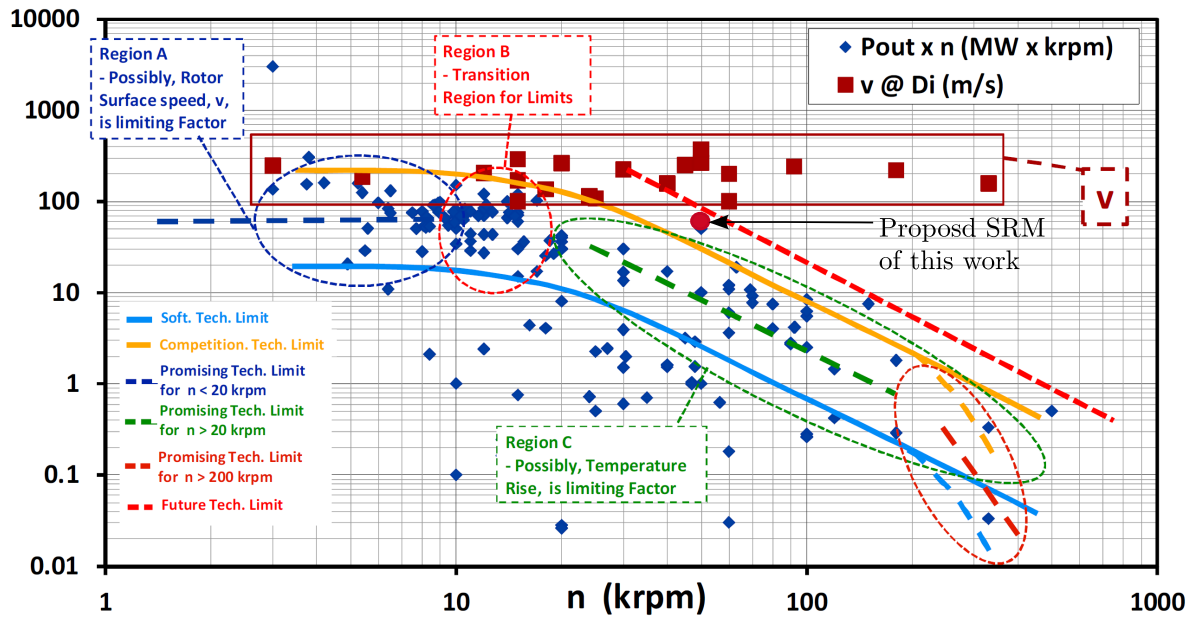


Figure 2.17: Plot of Speed vs High Speed Index by Moghadam for Various Machine Topologies [69].

In order to increase the efficiency in high speed operations, the electromagnetic losses (iron loss and copper loss) should be limited. For that, using laminations with low thickness (about 0.2 mm) and electrical steels with low specific loss index is essential. In addition, use of Litz wire for the winding can reduce the copper loss. Operation of high speed and super high speed motors require equal consideration for mechanical problems as electromagnetic ones [70]. The torque capability of the motor is affected at higher speeds which is dealt with by advancing the excitation angle. The Analytical design of a 50,000 rpm, 700 kW IM is demonstrated in [71], where power electronics considerations, use of Litz wire, use of low loss material for the rotor and the shaft are taken into account.

2.10 High Speed Switched Reluctance Motors

Several work has been carried out to design a suitable drive for high speed SRMs [72]. In [73] a high speed SRM is used for the spindle drive inside a dental drill. Here, attention was focused on the critical speeds of the rotor in order to avoid mechanical failures caused by external perturbations. Also, the choice of the bearings which are one of the main sources of the mechanical loss in very high speed applications is investigated.

[74] has designed a high-speed high power SRM for an aerospace application with an stator outer diameter of 6.35 inches and a stack length of 3.3 inches. The base

speed of the motor was achieved at 25,000 rpm. The motor poles would be heavily saturated, resulting in a high-power-density machine. Both the stator and rotor of the machine were oil cooled with fuel cooled windings. Cobalt iron was used in manufacturing the machine. However, despite achieving high power at high speeds, use of complicated cooling methods and expensive iron is not suitable for automotive applications.

A 22,220 rpm SRM with a power of 250 kW was designed and tested in [75,76]. The motor was a 12/8 topology with a diameter of 10.5 inches and a stack length of 15 inches weighing 124 pounds. Here vanadium-iron-cobalt was used as the magnetic steel and the stator, rotor and the windings are all oil cooled, which makes this motor to also be unsuitable for automotive applications.

The salient structure of rotor causes a significant increase in the windage loss. The loss caused by the fluid drag on a rotating body is called windage or air friction. With increasing popularity of the high speed motors, it is important to accurately predict the windage loss and apply all the possible precautions to reduce it. In order to address this issue, special rings or sleeves that are usually made of non magnetic materials are used to retain the rotor which in turn will experience eddy current losses inside them. The sleeves are usually made of Inconel or carbon fibre/epoxy with the carbon fibre resulting in less rotor loss which is a result of the eddy current flow due to the stator MMF harmonics, therefore care must be taken in choosing the material for the retaining sleeve [77].

Furthermore, in high speed applications it is common to implement a fillet radius at the intersection of the rotor teeth and the the rotor core back. This will significantly reduce the mechanical stress concentration at the rotor [78].

In [79] an SRM is designed to run at 750,000 rpm. In this work in order to address the issue of high drag losses, a sleeve made of carbon fibre is placed around the rotor, as shown in Fig. 2.18, providing a cylindrical surface. The spaces in between the rotor poles are filled with magnesium integral cast which is a light material and adds to the stiffness of the structure while reducing the windage loss. It is shown that the drag loss actually reduces if the air gap is increased up to 1 mm. It is also claimed that having 4 rotor teeth is favourable as it provides a double symmetric structure which in turn eliminated having different natural frequencies and stiffness in different planes. The stress that the edges of the salient poles inflict upon the sleeve is called the edge effect and can result in the sleeve's local failure. Therefore, it is important to ensure the tangential stress inside the bandage does not exceed the maximum yield stress, requiring precise sleeve design [80–82].

The design in [83,84] addresses the issue of high windage loss in an SRM running at 50,000 rpm. In this work, a flux bridge is added to the outer surface of the rotor, creating a cylindrical shape for the rotor as shown in Fig. 2.19. The flux

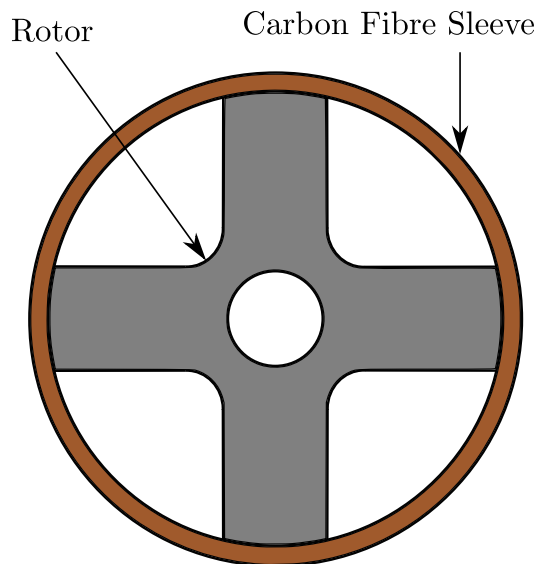


Figure 2.18: Rotor Designed for 750,000rpm Rotational Speed with Carbon Fibre Sleeves [77]

bridges in between each two adjacent rotor poles are supported by radial links. It is claimed that from the mechanical point of view the flux bridges are capable of with-standing the stresses caused by the centrifugal force whilst being thin enough to saturate to an extent to effectively act like air. Adding the flux bridge also results in rotor acoustic noises equal to the electric motors with cylindrical rotor by creating a cylindrical shaped rotor [85]. This techniques was combined with using an asymmetric air gap. This air gap would increase the aligned inductance while decreasing the unaligned inductance which would result in an improved torque for the same rotor specification.

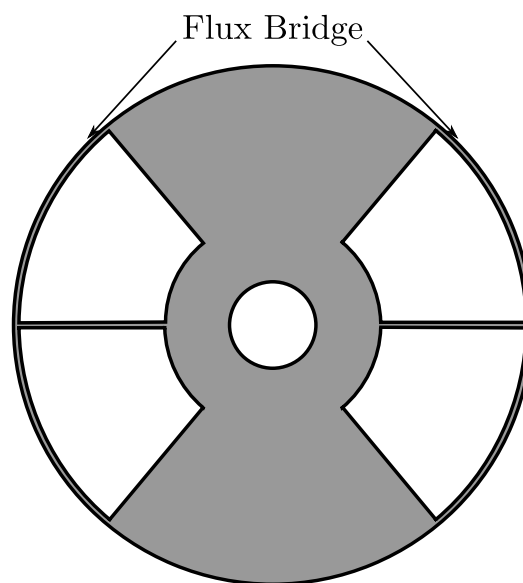


Figure 2.19: Rotor Designed for 50,000rpm Rotational Speed Using Flux Bridges [85]

If a high speed application employs hollow rotor, all the techniques used to mount the rotor on the shaft that include notches and key ways results in excessive stress concentration on that area. Therefore, glue works as an easy solution to lock the rotor to the shaft while avoiding a rise in mechanical stresses [81].

In high speed applications, the core loss P_{Fe} , which consists of the hysteresis loss, P_h , the eddy current loss, P_e , and anomalous eddy current loss, P_a , can be as large as the copper loss and is calculated using the Steinmetz equation as presented in Eq. (2.16).

$$P_{Fe} = P_h + P_e + P_a \quad (2.15)$$

$$= k_h f B_{Peak}^n + k_e (f B_{Peak})^2 + k_a (f B_{Peak})^{1.5} \quad (2.16)$$

Where k_h , k_e and k_a are the hysteresis, eddy current loss and anomalous eddy current loss coefficients, respectively. f is the frequency of the operation, B_{Peak} the peak flux density and n the Steinmetz constant. It should be noted that the methodology used in the FEA package is valid for no-sinusoidal waveforms, which is the case in SRMs [86].

The copper loss in high speed applications includes the DC winding and AC winding loss. The eddy current loss is mainly caused by the proximity effect caused by the varying magnetic field. For a wire with circular profile, the eddy current loss portion of the copper loss, $P_{cu-eddy}$, is estimated using Eq. (2.17).

$$P_{cu-eddy} = \frac{B_{cu-peak}^2 \omega^2 d_c^2}{32\rho} \quad (2.17)$$

Where $B_{cu-peak}$ is the peak flux density within the conductor, ω the angular velocity, d_c the conductor diameter and ρ the resistivity of copper [87].

In order to reduce the fundamental switching frequency at high speed applications, the lowest possible stator/rotor pole combination is often used. However, this causes issues such as high torque ripple and effects the self starting capability of the rotor. By applying a 4/2 combination [88] operates at 30,000 rpm while producing 0.2 Nm torque. A non-uniform air gap was implemented as shown in Fig. 2.20. This has flattened the torque waveform and widened its range, improving the self starting capability of the motor. Another advantage of this technique is reducing the acoustic noise.

In designing a rotor (or shaft) for high speed applications, it is vital to calculate the vibration frequencies and their shapes. The design speed of the motor should avoid the natural frequencies of the motor. However, the rotor can be accelerated fast

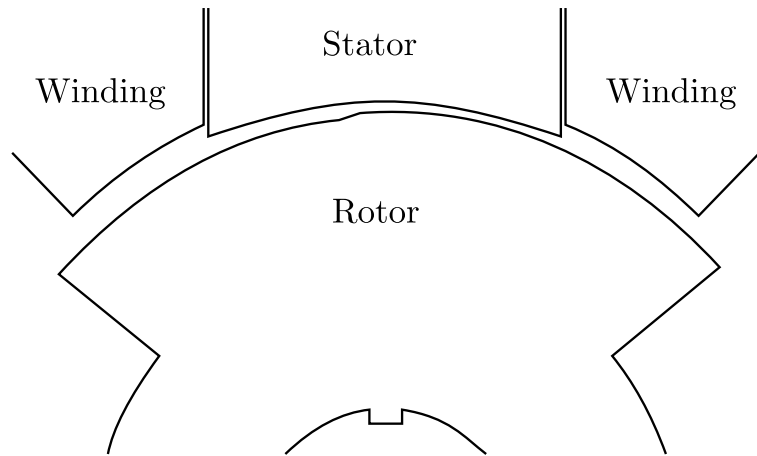


Figure 2.20: Non-uniform Air Gap in a High Speed SRM

enough to pass the speed associated with the rigid modes. Therefore, the shaft can be designed to operate at a speed between the rigid modes (rock and bounce) and bending mode. The rigid mode is proportional to the bearing stiffness, therefore reducing the bearing stiffness by techniques such as soft mounting reduces the two rigid modes of vibration [89, 90].

The noise or the mechanical resonance is created when the magnetic flux of an excited stator pole produces radial and/or circumferential electromagnetic forces on the excited pole, causing oval shaped deformation of the stator [91, 92]. It is important to avoid the modal frequencies of the stator occur simultaneously with the stator's natural frequencies, in order to avoid causing resonances which result in vibration and noise [93, 94]. Clearly SRMs still have several areas for improvement.

2.10.1 Benchmark SRM

The purpose of this work is to design an alternative SRM capable of meeting the specification the third generation Toyota Prius motor. In the previous section, the summary of the research carried out by University of Tokyo, to design such an SRM, was presented. However, as high speed, high power SRMs have not been investigated for hybrid electric applications before, it was decided to design the alternative motor to run at 50,000 rpm, which would result in a smaller more power dense design.

The design process started by scaling down the frame size of the SRM proposed by the Japanese research team, which has a maximum speed and output torque of 13,500 rpm and 207 Nm, respectively. This motor will henceforth be known as SRM1. The detailed specifications of SRM1 can be found in Table 2.4.

The scaling was carried out according to the relationship between power, torque and volume using Eq. (2.19), considering a 60 kW output power at 50,000 rpm.

$$P = \omega T \tag{2.18}$$

$$T \propto R_{OD}^2 L_s \tag{2.19}$$

It was defined that the motor torque has been scaled down by a ratio of 3.7:1 resulting in a knee point torque and speed of 55.89 Nm and 10,247 rpm, respectively. The rotor frame size had to be scaled down by a ratio of 1.5:1 on each physical measure.

Using the obtained ratio, the stator outer diameter, rotor outer diameter and the stack length were calculated to be 176 mm, 121 mm and 58 mm. Considering the conductor requirement, the fill factor is reduced to 45%. Furthermore, the high switching frequency resulted in selecting the 6/4 combination which is the lowest possible stator/rotor pole combination.

These values were used as a guide to start the design and further changes were made to meet the electromagnetic or mechanical requirements which will be discussed in detail in following chapters.

Table 2.4: Comparison of SRM1 and the Designed SRM

Parameter	Symbol	Unit	SRM1	Designed SRM
Stator Outer Diameter	S_{OD}	[mm]	264	176
Rotor Outer Diameter	R_{OD}	[mm]	182	121
Stack Length	L_S	[mm]	87	58
Maximum Power	P_{max}	[kW]	60	60
Maximum Speed	n_{max}	[krpm]	13.5	50
Torque	T	[Nm]	207	55.89
DC Link Voltage	V_{DC}	[V]	650	600
Fill Factor	FF	%	54	45
Stator/Rotor Teeth Combination	-	-	18/12	6/4

2.11 Summary

A review is presented in this chapter with three main focus areas; the operating principle of SRMs and the design techniques to improve the performance, summary of the existing SRMs to meet the specifications of the PM machine used in the Toyota Prius, and the design considerations of high speed SRMs.

SRMs operate based on the tendency of the magnetic circuit to move towards a position with minimum reluctance by forcing the rotor poles towards the aligned

position. The drive circuit of SRMs uses an asymmetric bridge unlike the H bridge used for other electric motors. Advancing the inverter commuting angle is commonly used particularly for speeds above the base speed.

SRMs have a simple structure, are easy to construct and cost effective. Magnet free SRMs are an attractive solution to replace the PM machines which are commonly used in HEV application. However, SRMs have a number of shortcomings such as high torque ripple, high acoustic noise and lower efficiency and torque density compared to PM motors.

Numerous techniques are used to address the shortcomings of SRMs. These techniques primarily focus on the improvement of the geometrical parameters such as the number of phases, airgap width, number of rotor and stator poles and pole pitch. Furthermore, many different topologies for SRMs have been used including; radial, c-core stator, disk type and hybrid SRMs.

The fault tolerant nature, robust structure, and ability to operate at a wide range of speeds and temperatures make SRMs suitable for automotive applications. The research team at the University of Tokyo have carried out an extensive research toward the design of an SRM to meet the specification of the PM machine used in the Toyota Prius. The research includes the investigation of a suitable low loss electrical steel, physical improvements including tapering the stator poles and the use of a non-uniform airgap.

The important aspects of the design of high speed motors are; reducing the aerodynamic loss, considering the critical speed and mechanical resonance, and finally diminishing the mechanical stress. It is common to implement a fillet radius at the intersection of the rotor teeth and core back to reduce the mechanical stresses. Moreover, to address the high windage drag, a sleeve is placed around the rotor to provide a cylindrical surface.

The frame size of the SRM designed by the University of Tokyo was scaled down according to the relationship between power, torque and volume. The scaled down dimensions are 176 mm, 121 mm and 58 mm for stator outer diameter, rotor outer diameter and stack length, respectively. These values were used as an initial guide to start the design. Further changes were made based on the electromagnetic or mechanical requirements which will be explained in following chapters.

Chapter 3

Mechanical Design Methodology

The aim of this project is to design a high speed high power SRM. Mechanical stresses imposed on a rotor are in direct proportion to the square of speed and radius. Consequently, running a relatively large rotor at high speeds amplifies the stress and overcoming the mechanical limits is arguably the biggest challenge in the design process. Furthermore, failure of the rotor will occur if the rotor natural frequencies coincide with the rotational speed. Therefore, designing a resilient, failure free rotor has the highest priority for high speed applications.

There are several factors limiting the maximum speed of all types of rotating bodies. The mechanical properties of the rotor material limit the speed, the maximum speed being the point as which the mechanical stress in the material is equal to its yield strength (with a relevant safety margin included). The critical speed is determined by the system rotordynamic properties, the aspect ratio of the rotor (ratio of radius to axial length), and the stiffness of the system that is dependent on the bearings and their positioning. Vibrations both resonant and self excited are very important in ensuring a safe operation. The purpose of mechanical design and the bearing design is to address the issue of the rotor vibrations by choosing the operational speed of the motor below the instability threshold whilst avoiding of the critical speeds.

Furthermore, choice of a suitable bearing is fatal to the precise and safe operation of the high speed motors as bearings are crucial components in high speed applications.

3.1 Mechanical Stresses

The majority of the stresses imposed upon a rotor are caused by the centripetal force. The centrifugal force is an inertial force in the radial direction which is caused by rotation. The directions of the coordinate system for stress analysis are illustrated

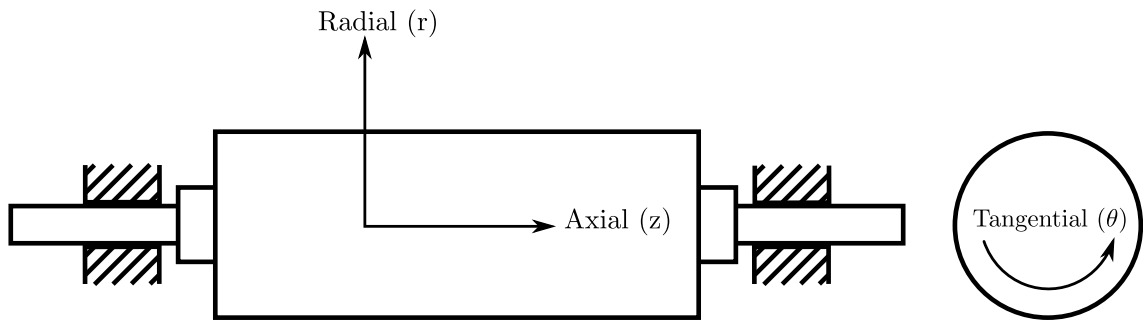


Figure 3.1: The Rotor Coordinate System for Stress Analysis

in Fig. 3.1. The centrifugal force is also used to describe the force reacting to the centripetal force. The value of this force, F_c , is calculated using Eq. (3.1).

$$F_c = m\omega^2 r_c \quad (3.1)$$

where m , ω and r_c are mass, angular velocity and radius of the rotating system, respectively. For any rotating system which has a simple structure and is not constrained, Eq. (3.1) can estimate the total force induced on the system radially.

The major stresses contributing to the total rotor stress are: Notch Effect and Tangential (Hoop) Stress.

3.1.1 Notch Effect

Objects that contain any form of indents, cracks, sharp angles. experience a rise in the stresses in that area despite their estimated average stress being below their yield strength. This is known as notch effect.

3.1.2 Tangential (Hoop) Stress

Any rotating plane sheet with a hole in the middle will experience a stress referred to as 'hoop stress' which is caused by the centrifugal force. Hoop stress is a tensile stress which is tangential to the circumference of the hole in order to repel the strain that would force the lamination (the ring) to lift off the shaft [95]. The highest concentration in a shape such as this will be on the hole in the middle. The hoop stress direction on the rotor of an SRM is illustrated in Fig. 3.2 where the central arrows indicate the direction of centrifugal forces. The geometrical design of the rotor should ensure that the generated hoop stress does not exceed the yield strength of the steel used in the rotor or the rotor will fail.

Hoop stress is directly proportional to the rotor radius squared and the angular velocity squared. Therefore, hoop stress act as a limiting factor for the maximum rotor radius.

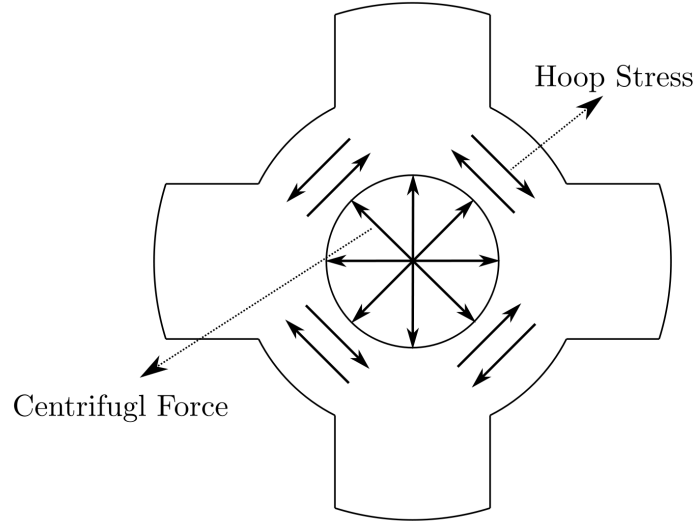


Figure 3.2: Hoop Stress Definition

3.1.3 Lamé Equation for Defining Stresses on a Disk

Since the rotor consists of a stack of laminations, each lamination can be assumed to be a rotating disk. Therefore, Lamé's equations for predicting the stresses on a rotating disk and thick walled pressure vessel can be applied to them [96]. This analysis will find the magnitude of the stress induced in different components of the rotor.

Lamé's stress equations for any point at a radial distance from the centre, r , within a solid disk are described in Eq. (3.2) for radial stress, σ_r , and Eq. (3.3) for the tangential stress, σ_θ .

$$\sigma_r = \frac{3 + \nu}{8} \rho \omega^2 a^2 \left(1 - \frac{r^2}{a^2}\right) \quad (3.2)$$

$$\sigma_\theta = \frac{3 + \nu}{8} \rho \omega^2 a^2 \left(1 + \frac{3\nu}{3 + \nu} \frac{r^2}{a^2}\right) \quad (3.3)$$

where ν is Poisson's ratio while ρ , ω and a are the material density, angular speed and the disk radius, respectively.

For disks with a central hole, Eq. (3.4) and Eq. (3.5) apply where b , σ_{rh} and $\sigma_{\theta h}$ are the radius of the hole, the radial stress and the tangential stress, respectively.

$$\sigma_{rh} = \frac{3+v}{8}\rho\omega^2\left(a^2 + b^2 - \frac{a^2b^2}{r^2} - r^2\right) \quad (3.4)$$

$$\sigma_{\theta h} = \frac{3+v}{8}\rho\omega^2\left(a^2 + b^2 + \frac{a^2b^2}{r^2} - \frac{1+3v}{3v}r^2\right) \quad (3.5)$$

Fig. 3.3 demonstrates the gradual change in tangential and radial stresses starting from the centre and moving towards the circumference. The values of σ_r , σ_θ , σ_{rh} and $\sigma_{\theta h}$ at the boundaries including centre, a and b are illustrated on Fig. 3.3.

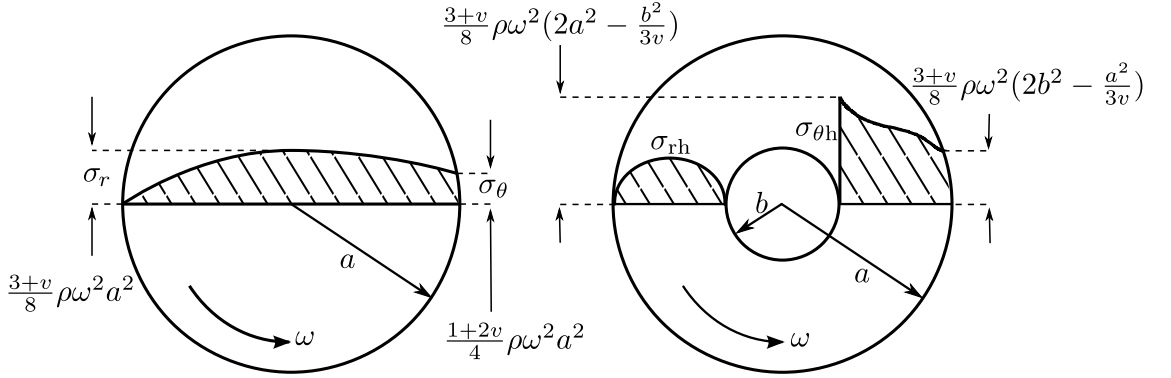


Figure 3.3: Radial and Tangential Stress Behaviour for a Generic Disk (Left) and a Generic Disk with a Central Hole (Right).

3.1.4 Simulation Assumptions

The aim of the analysis in this section is to estimate the magnitude of the stresses induced upon the rotor laminates. The main concern is regarding the size of the outer diameter of the rotor, whether it will withstand operating at the suggested speed, and finally if the proposed topology will be safe. For simplicity, some assumptions are applied to the model. It is assumed that all the contacting surfaces of the different rotor components are frictionless, allowing other external sources to be ignored. Since the rotor consists of a stack of laminations that are held together by glue, which has an insignificant axial stress, a single lamination needs only be considered in the analysis. This single lamination obeys the equations for a rotating disk as it is considerably larger in diameter than in thickness.

The stress value at any point of an elastic body should be maintained below the yield strength of the material in order to avoid failures or cracks. Von Mises, a theory on

material failure specifies a reference stress that acts as a basis for failure in elastic bodies. The resulting reference stress must be kept below the yield strength of the material at all points of the body over the whole range of speed.

It is essential to include the overspeed conditions to the mechanical analysis of the motor to avoid the mechanical failure of the rotor. As a result, the rotational speed used for the stress analysis has to be defined higher than the rated operational speed of the motor. Usually, a safety factor of 1.2 is applied for overspeed considerations which will be the case in this work. For the mechanical design and analysis of the rotor the overspeed will be used, and the rated operational speed will be used for stress analysis during the tests.

3.2 Rotor Vibrations

Vibrations occur in any rotating system and are caused when the centre of the system mass is not positioned at the rotational axis, i.e. when the system is not balanced. It is impossible to completely avoid imbalance because of the finite tolerances during manufacture, resulting from the limitations of the construction machines and techniques. Once rotating, this unbalanced mass experiences centripetal forces which in turn generate vibrations in the system, this is also known as whirling. The vibrations cause rotor deflection, which can reach dangerous levels, particularly if the rotor speed approaches critical/resonant frequencies. If the operation at resonant frequencies does not cause immediate failure by the rotor contacting the stator, then prolonged operation at this point will significantly reduce the lifetime of the system.

3.2.1 Rotor Slenderness (Aspect Ratio)

Addressing the rotor vibration issue is complicated and includes careful mechanical design of the rotor and bearing. The various resonant frequencies of the motor are estimated using numerical, analytical and finite element methods, with numerical and finite element methods having a higher precision compared to the analytical. As a result, analytical methods often tend to be used in early stages of design to predict the resonant frequencies, while the FEA methods are used at later stages to identify them precisely and optimise the design further.

In order to ensure stable operation at the maximum design speed [97], the maximum rotor slenderness, λ_{max} , can be calculated using Eq. (3.6). The slenderness ratio is used as a measure of stiffness and is the ratio of the length over diameter of the rotor.

$$\lambda_{max} > \lambda_s = \frac{L_F}{R_{OD}} = \frac{L_{Fe}}{\alpha 2r_r} \quad (3.6)$$

where λ_s , L_F and R_{OD} are the rotor slenderness, the full rotor length and the rotor outer diameter. α is the ratio of the active length, L_{Fe} , and the rotor length, L , as expressed in Eq. (3.7).

$$\alpha = \frac{L_{Fe}}{L} \quad (3.7)$$

3.2.2 Vibration Modes

For systems consisting of bearings and a shaft, the vibration modes should be carefully investigated [64] which are shown in Fig. 3.4:

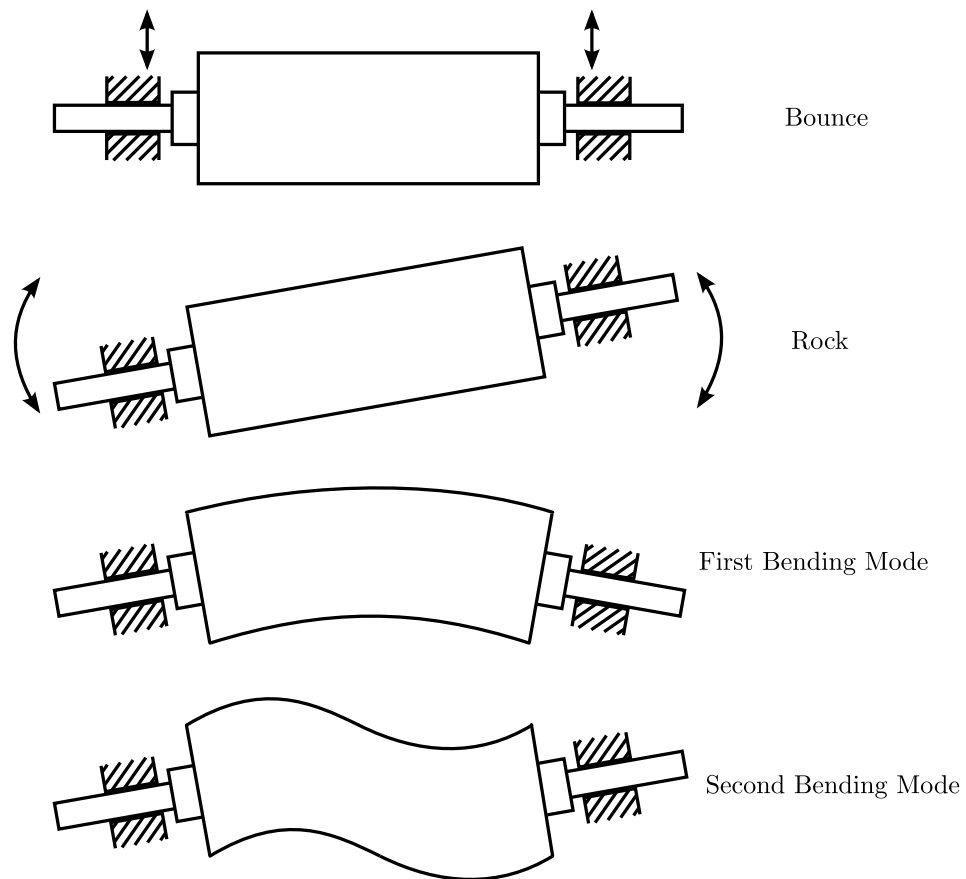


Figure 3.4: The Bounce, Rock, First and Second Bending Resonant Modes.

The first modes of vibration are either bouncing of the system parallel to the rotational axis or rocking of it between the bearings, which are caused by the spring like behaviour of the bearings.

The second vibration mode is the bending of the system in response to the transverse load force caused by the unbalanced mass. This deformation, which is also known as the bending mode, increases significantly as the transverse load oscillation proceeds towards a natural frequency of the system. The natural frequency of the system is an intrinsic property of the system based on its structure and stiffness. The natural frequency associated with the first bending mode is also known as the critical speed of the system, whose bending mode looks like half a sine wave [98].

The mentioned vibration modes also occur for the rotor system of the high speed electrical machines. The rotor design ideally avoids the vibration frequencies over its operating speed range. Constructing the most balanced system possible, or choosing a design speed below the resonant frequencies will do so. However, operating at speeds above the vibration frequencies is possible if the system deflection is maintained at its minimum. One way to do so is soft mounting the bearings. This will reduce the effective stiffness of the bearings which in turn significantly reduces the frequencies where rocking and bouncing modes occur defining a minimum threshold for the motor operating speed. Furthermore, if the system is accelerated rapidly throughout the resonant speeds, the system deflection can be limited allowing operation at higher speed ranges than the resonant frequencies.

The vibrations of the rotor are of two distinct types; resonant and self excited. An oscillating force, which is often the mass imbalance of the rotor, can cause the resonant vibrations if its frequency occurs at one of the natural frequencies of the rotating system. Additionally, self excited vibrations do not need any external force to occur, but they appear once the speed of the rotating system has passed a certain threshold which is identified by the intrinsic properties of the rotating system. Operating at self excited vibrations is practically impossible as they make the system unstable. On the other hand, if the rotor is capable of storing enough energy in the external dampers, the critical frequencies of the resonant vibrations can be passed with no failure. For this, soft mounting techniques are used which allow the speed to pass through the first two resonant modes.

The first critical frequency of the rotor is in direct relation with the shaft diameter and in inverse relation with the stack length and the rotor weight as these will increase the rotor lateral stiffness [99].

Finally, the gyroscopic moment can give rise to critical frequencies of the rotor. This effect is called the gyroscopic stiffening and appears due to an additional mass on the rotating object. If the rotor is not symmetrical, the centre of gravity does not meet at the centre of the shaft, resulting in gyroscopic stiffening.

Torque is proportional to the volume of the rotor. The outer diameter of the rotor is designed to be as small as possible in order to decrease the centripetal forces acting

on the rotor caused by the peripheral rotational speed. The axial length of the rotor can be increased in order to achieve a larger torque. However, the critical speeds should be carefully considered as they can cause mechanical failures.

In order to estimate the first critical speed, it is assumed the shaft is a clamped beam. The critical speeds (in revolution per minute) of the rotor correspond to its natural frequencies. The first natural frequency, f_n , can be obtained using Eq. (3.8).

$$f_n = \frac{60}{2\pi} \sqrt{\frac{48E\pi D_a^4}{64l^3m}} \quad (3.8)$$

where E is material's Young Modulus, D_a and l are the shaft diameter and the distance between the midpoint of the bearings, respectively, m is the mass of the shaft, and all are demonstrated in Fig. 3.5. Although here the presence of the rotor lamination is ignored, it is believed that the rotor lamination would increase the first natural frequency by having a larger structural stiffness [73].

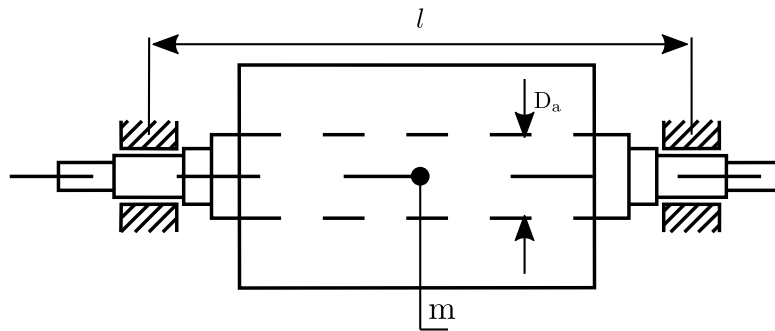


Figure 3.5: Main Parameter for Evaluating Critical Speed

3.2.3 Predicting the Critical Speeds using Rayleigh's Method

The simple structure of the rotor of an SRM means the rotor can be assumed to be a single rigid body of material,

Using Eq. (3.9) the shape function of the n^{th} resonant mode of a uniform beam with clamped ends can be predicted, where

$$y_z = y_0 \sin \frac{n\pi z}{L_{sh}} \quad n = 1, 2, 3... \quad (3.9)$$

where y_z is the deflection at a point at an axial distance of z on the shaft, L_{sh} is the shaft length and y_0 is the maximum shaft deflection. The laminated part of the

rotor has a larger radius and is much stiffer compared to the section of the shaft that the bearing is mounted on, causing the second moment of area to vary along the length of the rotor from maximum for the thicker radius to minimum for the thinner one. This affects the shape function, resulting in flattening along the active part of the rotor [64].

This method can provide a quick prediction for the critical speed of the rotor. The information included in the shape function consists of the shape information and the deflection magnitude and only the later is relevant for the purpose of this analysis. This shape form is highly dependent on the aspect ratio of the rotating system which is the ratio of the length over radius of the active part of the rotor. Therefore, a simple beam having a high aspect ratio would result in a sine wave form for the shape function. On the other hand, a disk having a low aspect ratio would have a trapezoidal form to it.

3.2.4 Predicting Critical Speed Using the FEA Method

The FEA method provides an accurate analysis of the critical speeds. This method allows the inclusion of bearings stiffness which helps in accurately predicting the resonant modes and the critical speeds. In this work only the results of the FE model are used.

3.3 Bearings

Any rotating system requires a set of bearings in order to maintain the rotational axis. Bearings may rotate or slide, or do both.

3.3.1 Bearing Types

Commercially available bearings are extremely restricted by the demands of the market in terms of their speed capabilities. However, growing interest in high speed applications for electric motors is expected to drive the market for higher speed bearings. Different combinations of bearings may also demonstrate different capabilities in dealing with the orientation of the load (axial or radial).

There is a vast range of types and configurations to choose from for the electrical machine applications. There are three major types of commercially available bearings:

- Magnetic bearings

- Air Bearings
- Rolling element (balls or cylinders) bearings

Using magnetic bearings can overcome the problems of limited shaft diameter and the need for lubricating the bearing by using magnetic forces, however their significant cost is their biggest downfall. Furthermore, active magnetic bearings involve a complex system including sensors actuators and control, resulting in a larger volume.

Air bearings use a thin layer of compressed air between the load and the bearing and are used mainly in applications where high speed or precision is required. The main disadvantage of this type of bearing is the requirement for compressed air, unlike the mechanical bearings, which leads to need for power consumption [100].

Ball Bearings are the most popular type which use rolling balls in a lubricated race way to bear rotating shafts with minimum friction. The frictional heat generation at the rolling element is related to its tip speed, therefore bearings suitable for high speed applications require a smaller diameter compared to lower speed bearings. Constant lubrication of the rolling part of the bearing, by for example using an oil pump, can remove the generated heat and reduce the wear by decreasing the contact area between the rolling and stationary parts of the bearing. This will increase the life time and service speed of the bearings.

3.3.2 Bearing Selection

In the process of bearing selection, different factors such as the lubricating method and the maximum nominal service speed for the lubricating method must be assessed. This narrows down the suitable bearing types and once the bearing is selected, its inner race diameter will be determined by the shaft's diameter.

The bearing size is based on the shaft diameter. Bearings with large inner diameters have a lower life as the rotational speed is increased. As a result, the shaft diameter should be as small as possible to permit a longer bearing life. However, the shaft diameter is determined by the output torque. As the temperature of the bearings rises it might be necessary to cool the bearings by pumping lubricant into them in order to reduce the temperature difference between the inner and outer rings of the bearing. The viscosity of grease and oil, which are the major lubricating materials used in bearings, limits the maximum operating speed of the bearing. For high speed applications grease and for super high speed applications, oil is the best lubricant.

In high speed applications, special attention should be given to the bearing choice because they are the only components in contact with the rotor. High speed bearings

need to operate reliably at high speeds and high temperatures with minimum noise whilst having acceptable stiffness. Therefore, in high speed applications hybrid rolling bearings are used. This type of bearings has one inner and one outer ring in between which balls made of high stiffness and low density ceramic (e.g. Si_3N_4 silicon nitride) are placed.

The bearings used in this work are of angular contact type. A simple schematic of them is shown in Fig. 3.6. D is the bearing outer radius, d is the bearing inner radius and B is the bearing width. In this case a pre-load washer is used to apply axial pre-load. However, this type of bearing comes with a higher mechanical loss compared to magnetic or air bearings. This mechanical loss is in direct relation to the rotational speed and the frictional torque.

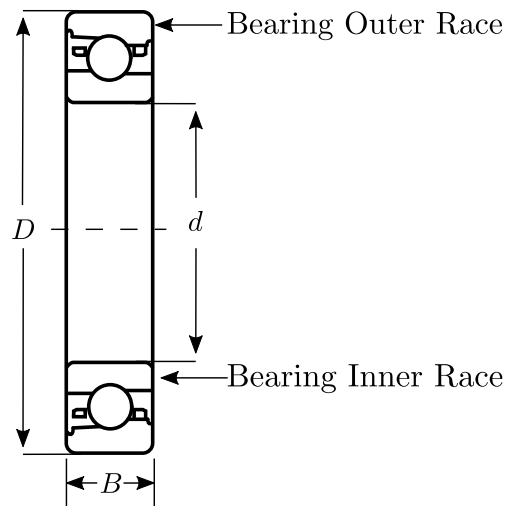


Figure 3.6: Single Angular Contact Bearing.

3.3.3 Bearing Mounting Types

The next critical step after choosing the bearing is mounting it on the shaft and in the housing. The tolerance of the shaft and housing along with the dimensions for mating shoulders are specified by the manufacturers and should be adhered to. Using the correct amount of lubrication is crucial in achieving the full life of the bearings. Excessive lubrication results in overheating, on the other hand, inadequate lubrication leads to excessive wear and eventual failure. Different applications require different types of lubrications; however, pre-lubricated, sealed bearings are available.

If the bearings have higher stiffness compared to the rotor, they are called hard mounted and conversely if they have lower stiffness they are called soft mounted.

Hard mounting is used for applications where precise position is required. On the other hand, for applications which precise location for the rotational axis is not necessary and larger displacements can be tolerated, soft mounting is used. Soft mounting allows easy passage over the natural frequencies of the system. Although, in hard mounted cases the bearings can be assumed stiff and their compliance ignored, in soft mounted cases the bearing compliance needs to be included [101].

Angular contact bearings can bear loads in the axial and radial direction. In applications where a high global stiffness along with high axial and radial loads are needed, a back to back connection is preferable. In applications where high axial loads are needed the tandem connection is preferred. For a back to back connection, the side of the bearings where the outer race has a wider surface are arranged to face each other. If the wider side of the bearing outer race is facing the shorter side of the next bearing, it is a tandem connection. Back to back and tandem connections are illustrated in Fig. 3.7.

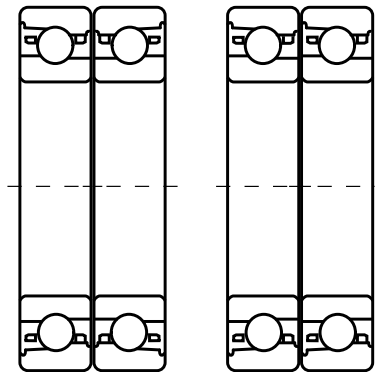


Figure 3.7: Angular Contact Bearing Connections, Back to Back (Left) and Tandem (Right)

For prototype manufacturing for this work a single bearing was deemed sufficient. Care needs to be taken in mounting a single bearing on the rotor as the balls will be pushed out of their place or ‘de-raced’ if mounted the wrong way. The side faces of the outer race of the angular contact bearings have different lengths. Each bearing is mounted on either side of the rotor with the shorter side of the outer race facing the rotor. In this way, the movement of the rotor only presses the balls toward the longer side, avoiding de-racing and bearing failure.

3.3.4 Pre-load

Preload is applied in applications where high precision is required. The pre-load increases the rigidity of the rotor which in turn decreases the unwanted bearing

displacement. This can be achieved by implementing a pre-load spring. Pre-load springs come in conical or waved washer shapes. The pre-load spring selection is based on the design applied pre-load force which will be explained later.

3.3.5 Bearing Specification

After carefully considering all the aspects involved in the bearing selection, an angular contact ball bearing is employed for this work. This is due to greater robustness and general smaller size of ball bearing coupled with their independence of any auxiliary equipment. This particular type of bearing has ground surfaces making it suitable for any given mounting configuration. The full specification of the selected bearing is presented in Table 3.1.

Table 3.1: Bearing Specification

Specification	Type	Symbol	Unit
Manufacturer	SKF	-	-
Type	High Precision Angular Contact	-	-
Ball	Ceramic Coated Hybrid Ball	-	-
Row Number	Single Row	-	-
Lubricant	Grease	-	-
Rated Speed	68,000	n	[rpm]
Bore Diameter	20	d	[mm]
Outside Diameter	37	D	[mm]
Width	9	B	[mm]

3.4 Shaft

The shaft is a rotating part of the electrical machines that transfers the mechanical power generated to the load. The process of shaft design should consider avoiding operation at, or near the natural frequencies. The shaft design process includes determining the rotational velocity, the torque, the position and dimensions of the other components attached to the shaft specially the location of the bearing, the forces posed on the shaft, and finally selecting the right material.

Designing the shaft as short as possible helps in reducing the deflection and bending moments while increasing the critical speed. The stress raisers should be placed as far as possible from high-stress points of the shaft. Hollow shafts are used in

applications where better stiffness to mass ratio and higher natural frequencies are required.

Power can be transmitted from one shaft to another via a coupling. These can be rigid or flexible. Rigid couplings allow no relative motion between the shafts. Despite the high risk of stresses in this type, they can be useful in applications where accurate alignment is essential. On the other hand, flexible couplings allow axial, regular and angular misalignment to some extent.

The cross sectional area of the shaft is proportional to the torque being transferred. When designing a motor to run at high rotational speeds, the outer diameter of the rotor must be as small as possible in order to decrease the centripetal forces acting on the rotor. Consequently, the axial length of the rotor tends to increase in order to achieve the required output torque. However, when increasing the rotor axial length, the critical speeds need careful consideration. The shaft of high speed machines should be made of a magnetic steel with a high yield strength.

The minimum shaft diameter, can be estimated using Eq. (3.10) where T , J and τ are torque, polar second moment of area and shear stress, respectively. r is the radial distance from centre. This expresses the torsion in a beam.

$$\frac{T}{J_P} = \frac{\tau}{r} \quad (3.10)$$

For a beam with a solid circular profile, J_P is calculated using as Eq. (3.11).

$$J_p = \frac{\pi}{2}r^4 \quad (3.11)$$

Combining Eq. (3.10) and Eq. (3.11) the minimum allowable radius for the shaft is obtained using Eq. (3.13) the result of which is presented in Table 3.2

$$\frac{2T}{\pi r^4} = \frac{\tau}{r} \quad (3.12)$$

$$r = \sqrt[3]{\frac{2T}{\pi\tau}} \quad (3.13)$$

However, given the mechanical stresses imposed on the shaft, a 20% increase was considered for the shaft diameter to ensure extra robustness. Finally, taking into account the measurements of commercially available bearings and the coupling requirements, a shaft radius of 10 mm is considered for the design.

Table 3.2: Torsion in Shaft Parameters

Parameter	Symbol	Unit	Value
Torque	T	Nm	56
Shear Stress	τ	MPa	20
Minimum Allowable Shaft Radius	r	mm	5.6

3.4.1 Tip Speed

As no retaining sleeve will be used, a maximum rotor tip speed of 250 m/s is applied to determine the upper limit of the operational speed [102,103]. Eq. (3.14) expresses the tip speed as, V_{tip} , a function of angular speed, ω , and rotor radius, r_r .

$$V_{\text{tip}} = \omega r_r \tag{3.14}$$

For the operation speed of 5236 rad/s (50,000 rpm) and a radius of 45.5 mm, the tip speed is equal to 238.2 m/s, indicating a feasible set of dimensions for future investigation.

3.5 Balancing

Although the manufacturing process is carried out to a tight tolerance, an imbalance is unavoidable. This creates a whirling force that is defined in Section 3.2.

The imbalance can be significantly reduced using a balancing machine. The motor application will define the balance quality grade. The permissible centre of gravity displacement for the operational speed can be identified using a look up table and material removed to re-balance.

3.6 Acoustic Noise

In some applications reducing acoustic noise is very important. The same technique for dealing with the critical frequencies applies for the acoustic noise. The stator should be designed to achieve the maximum possible natural frequency and minimum possible harmonic components caused by the magnetic radial force for the stator. The target is to achieve a dominant mode frequency above the audible frequency range. Higher mode frequencies can be achieved by making a thicker stator back iron. However, a thicker back iron will result in a lower power

density because of the reduced iron utilisation. Also, in cases where there is limited space for the motor, increased stator back yoke results in a smaller available area for the coils leading to a higher current density and also higher thermal diffusion distance from the coils to the ambient.

3.7 Windage Loss

In high speed SRMs, a high viscous drag appears in the air gap, P_{drag} which causes power loss that can be estimated using Eq. (3.15), where K is the roughness coefficient of the rotor surface, C_d is the rotor drag coefficient, ρ_{air} is the air density, ω is the rotor angular velocity, r_r is the rotor radius and L_s is the stack length [79, 104].

$$P_{\text{drag}} = KC_d\rho_{\text{air}}\pi\omega^3r_r^4L_s \quad (3.15)$$

The detailed investigation into the windage loss of the motor will be presented in Chapter 6.

3.8 Conclusion

In this chapter, the mechanical design methodology of an SRM has been discussed. High operational speeds impose mechanical constraints on the rotor. Therefore, the biggest challenge of the design process is addressing the mechanical constraints. The mechanical constraints, which are in direct proportion to the square of speed and radius, limit the outer diameter (by means of stress concentration) and the length of the rotor (by means of vibration frequencies and the first bending mode in particular).

In rotating systems, due to manufacturing constraints, it is impossible to precisely match the centre of the mass to the centre of rotation. The increasing rotational velocity, which acts at the centre of mass, results in bowing of the shaft caused by centrifugal force. The increase in the shaft bow exaggerates the eccentricity which in turn further increases the centrifugal force. This can be diminished by balancing the system and optimization of the geometrical parameters of the system.

One way to deal with the vibration issue is to accelerate the shaft fast enough to pass through and beyond the first natural frequency before the amplitude of the vibrations become significant, passed this point, the shaft can be operated at a speed larger than the natural frequency.

The choice of bearing is particularly important for this work due to the high operational speed and consequently the required precision. Different bearing types were discussed. High precision angular contact hybrid bearings were selected for this work, whose specification were provided.

The rotor tip speed has been used to determine an upper limit for the operational speed. For the operation speed of 5236 rad/s (50,000 rpm) and a radius of 45.5 mm, the tip speed is equal to 238.2 m/s. This result falls well below 250 m/s which is used as a rule of thumb to ensure a safe design speed.

The minimum shaft diameter needed to transfer the required torque is calculated. Adding 20% to the radius to increase the robustness and considering the commercially available bearings and the coupling requirement, a 10 mm radius is considered for the shaft.

Chapter 4

Electromagnetic Design Methodology

This work focuses on designing an alternative SRM to replace the third generation Toyota Prius motor. This is done by scaling down the frame size of an existing SRM, with the same specification as the PM, denoted as SRM1, the process of which was provided in Section 2.10.1. The detailed specifications of SRM1 can be found in Table 4.1.

Table 4.1: Detailed Specifications of SRM1

Parameter	Symbol	Unit	Value
Stator Outer Diameter	S_{OD}	[mm]	264
Rotor Outer Diameter	R_{OD}	[mm]	182
Stack Length	L_S	[mm]	87
Maximum Power	P_{max}	[kW]	60
Maximum Speed	n_{max}	[rpm]	13,500
Torque	T	[Nm]	207
DC Link Voltage	V_{DC}	[V]	650
Fill Factor	FF	-	0.54
Stator/rotor teeth combination	-	-	18/12
Weight	W	[kg]	25.2
Iron Loss	P_{Fe}	[kW]	1.3
Copper Loss	P_{Cu}	[kW]	6.3
Efficiency	μ	[%]	89

The general principle of SRM operation is presented in this chapter. The methods for selecting the number of phases, choice of the stator/rotor teeth combination, the coil turns and the length of the air gap is discussed. Using the analytical method, the rotor outer diameter, rotor pole pitch, tooth width and core back width is calculated.

4.1 Introduction to SRMs and their Operation

Reluctance machines produce torque by the tendency of their rotor to move towards a position to maximise inductance of the excited windings. If the phase is excited while its inductance is increasing, it is in motoring operation mode. On the other hand, exciting the phase with a decreasing inductance results in a generating operation mode.

4.1.1 The Aligned Position

The arrangement where the central axes of a pair of rotor poles are exactly aligned with the central axes of the stator poles of one phase is called the aligned position. In this position the magnetic reluctance of the flux path is at its minimum, or conversely inductance is maximised. It is in the aligned position that the stator and rotor teeth are most likely to become saturated. If a phase in the aligned position is excited, no torque will be produced as the inductance is already at its maximum. However, if the rotor is positioned either side of the aligned position, the rotor will move towards the maximum inductance position and in doing so will generate torque.

4.1.2 The Unaligned Position

The arrangement where the rotor interpolar axes are exactly aligned with the central axes of the stator poles of one phase is called the unaligned position. If the phase in the unaligned position is excited, no torque will be produced. If the rotor is placed at either side of the unaligned position, a torque is produced which will rotate the rotor towards the next aligned position. Since the flux leakage is larger at the unaligned position, compared to the aligned position, the saturation is significantly smaller.

4.1.3 SRM Operation Principle

The direction of the rotor movement and hence the torque is independent from the direction of the current or the flux linkage, but instead on the sign of the rate of change of inductance with position. The torque acts in a direction towards the nearest aligned position. As a result, to produce a positive torque in motoring operation mode, the rotor needs to be positioned in the forward direction between an unaligned position and the next aligned position. In other words, to operate in motoring operation mode, the phase should be excited while rotor is in the unaligned position and unexcited while in the aligned position. The flux then needs to be

reduced to zero before the rotor pole has completely left the stator one, otherwise a negative torque (braking torque) is produced. To achieve a full rotor revolution, each phase needs to be excited a number of times equal to the rotor pole number.

Instantaneous Torque

The torque production process of an SRM is explained in detail in [33, 34]. Current passing through a coil sets up a magnetic flux around the coil. It is not possible for all of this flux to pass through intended magnetic path, a portion of the magnetic flux not used for any work is called flux leakage. During the phase excitation period (on time) part of the energy input from the supply is stored in the magnetic circuit of the coil (stored field energy, W_f) and part of it is converted to mechanical work (co-energy, W'). The input electrical energy, W_e , is shown as the shaded area in Fig. 4.1 and can be expressed as per Eq. (4.1).

$$W_e = W_f + W' \quad (4.1)$$

The coenergy, W' , is the area between the magnetisation curve at any position and that of the unaligned position which can be expressed as Eq. (4.2), and is visualised in Fig. 4.1.

Flux Linkage

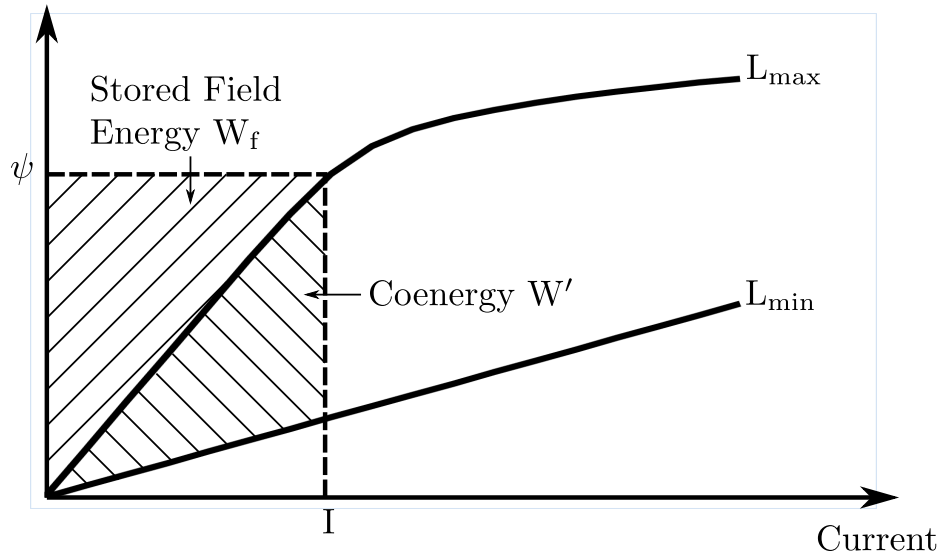


Figure 4.1: Coenergy and Stored Field Energy

The energy acquired from the supply before the turn off, that is not converted to mechanical work, W_f , is stored in the magnetic field at aligned position and sent back to the supply at turn off.

$$W' = \int_0^i \psi di \quad (4.2)$$

If a phase is excited using a constant current, i , over a short rotation angle, the produced mechanical work is equal to the rate of change of co-energy with respect to the rotation angle.

The torque produced by exciting one phase at any given rotor position is described in Eq. (4.3).

$$T = \left[\frac{\delta W'}{\delta \theta} \right]_{i=const.} \quad (4.3)$$

In the case of a constant current with an inductance that varies linearly with rotor position, the electromagnetic torque of an SRM can be rewritten as Eq. (4.4) where i is the excitation current and $L(\theta, i)$ is the inductance which is dependent on saturation and position [105].

$$T = \frac{1}{2} \frac{dL(\theta, i)}{d\theta} i^2 \quad (4.4)$$

This equation can only be used to express the torque before the motor enters saturation. It can be seen that the torque is proportional to the square of current, allowing any direction of current to produce a unidirectional torque.

4.1.4 Equivalent Circuit

In order to create a basic equivalent circuit for an SRM, the mutual inductance between phases is ignored as it is negligible. The supply voltage is expressed in Eq. (4.5) as the sum of the resistive voltage drop and the rate of change of flux linkage with time.

$$V_s = R_p i + \frac{d\psi(\theta, i)}{dt} \quad (4.5)$$

where R_p is the phase resistance and ψ is the phase flux linkage and is defined as a function of current and inductance in Eq. (4.6).

$$\psi = L(\theta, i) i \quad (4.6)$$

Substituting Eq. (4.5) in Eq. (4.6) gives the supply voltage, V_s , as the sum of resistive voltage drop, inductive voltage drop and the induced emf as shown in Eq. (4.7). The basic equivalent circuit is visualised in Fig. 4.2 [34].

$$V_s = R_p i + L(\theta, i) \frac{di}{dt} + \frac{dL(\theta, i)}{d\theta} \omega i \quad (4.7)$$

Therefore, the induced emf is given as Eq. (4.8).

$$e = \frac{dL(\theta, i)}{d\theta} \omega i \quad (4.8)$$

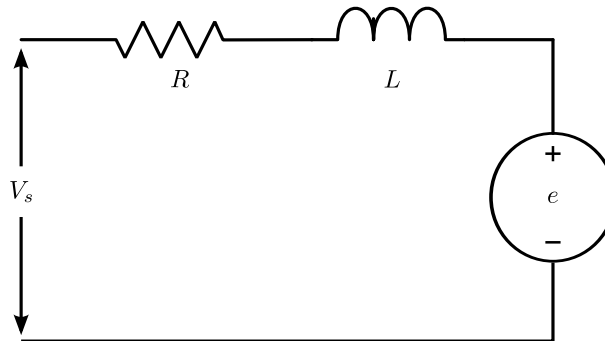


Figure 4.2: Equivalent Circuit of a Single Phase

4.2 Design Investigation

When designing electromagnetic motors, numerical methods, analytical methods and finite element analysis (FEA) methods are commonly used. Compared to numerical and analytical methods, FEA is generally more accurate and, with developments in computer technology, is the dominant method. However, the other methods are still used in the early stages of the design process, as they can reduce development time. In this work, some of the physical features of the motor were calculated using numerical methods in the early stage of the design. The FEA method was then used to precisely calculate the electromagnetic aspects and optimise the physical specifications.

The losses in high speed electric motors are a major concern. Due to the high frequency nature of the high speed operation, losses associated with frequency such as iron loss and skin effect will rise. Using thin laminated material reduces the iron loss. Also, using interwoven Litz wire can reduce the skin effect and proximity loss (AC loss) issues. The major factor that influences the copper loss is the current

density, regardless of the number of turns. Although increasing the stator pole height allows more area for the winding and hence reduces the copper loss, it comes with increased magnetic core loss.

4.2.1 Number of Phases

The preferred number of phases depends on the application. Numerous factors are involved in the choice of number of phases. Starting capability and directional capability improves for number of phases above one. Higher number of phases increase the reliability of the motor as becomes tolerant of a single phase failure. A three phase machine has higher power density compared to a two phase machine. However, higher number of phases also means a requirement for a greater number of power electric components, which inherently increases the total cost and reduces reliability. Furthermore, in high speed applications, the efficiency is improved by reducing the core loss which can be done by reducing the fundamental frequency and ultimately the number of phases. In applications where high speed SRMs are used, such as aerospace, a three phase system is favoured over a four phase one as it reduces the size and the losses while maintaining thermal robustness.

If the number of phases increases the mean torque will increase by increasing the number of strokes per revolution resulting in a decrease in torque ripple. It is important that the choice of number of phases guarantees sufficient starting torque. It is known that in the case of a three phase motor (or more) the rotor and stator tooth width can be designed in a way that at any given position there is at least one phase which produces torque [106]. Also, a higher number of rotor poles causes the saliency ratio, which is the ratio between minimum and maximum inductance, to decrease which in turn results in lower output torque. For this work 3 phases are considered.

4.2.2 Stator/Rotor Teeth Combination

It is necessary to determine the stator/rotor tooth number at the beginning of the design process. Typically for the design of high speed SRMs the stator/rotor tooth number combination is chosen to be as small as possible in order to reduce the fundamental switching frequency to its lowest possible value. This frequency can be obtained using Eq. (4.9) where N_r and n are the rotor pole number and the rated speed in rpm, respectively.

$$f_e = \frac{N_r n}{60} \quad (4.9)$$

A low stator/rotor tooth combination has a negative effect on the electromagnetic design especially on the output torque. The reduction in the torque is compensated by increasing the rotor size.

As shown in Table 4.1, the stator/rotor tooth combination of SRM1 is 18/12. For this work, a 6/4 combination is selected as it is the lowest possible for a three phase motor. However, this results in a reduction in output torque. As a result, the scaled down dimensions were modified to achieve the required output.

4.2.3 Analytical Design

The design ratios of radial SRMs are well established. These describe the different geometrical aspects of the motor and are chosen to consider various characteristics of the motor e.g. torque, acoustic noise, torque ripple, unaligned inductance, etc. In [33,34] Krishnan and Miller have provided the detailed analytical design process of the SRMs which is used to create a guide for some of the major physical specifications of the motor, as follows.

The rotor outer diameter, R_{OD} , should be about 60% of the stator outer diameter, S_{OD} , as is expressed in Eq. (4.10).

$$R_{OD} = 0.6S_{OD} \quad (4.10)$$

Equation Eq. (4.11) expresses the rotor pole pitch, λ , as the ratio of circumference to number of rotor teeth.

$$\lambda = \frac{\pi R_{OD}}{N_r} \quad (4.11)$$

The ratio of the rotor tooth width to the pole pitch is very important in the design of SRMs. Having the rotor pole pitch, the rotor tooth width, t_r , can be calculated from Eq. (4.12).

$$t_r = (0.3 \sim 0.4)\lambda \quad (4.12)$$

As only about half of the flux in each tooth passes through the stator yoke in each direction, the stator yoke, t_y , does not need to be wider than 60% of tooth width as per Eq. (4.13).

$$t_y = 0.6t_r \tag{4.13}$$

There is no need to calculate the stator tooth width and core back width as the rotor and stator can have equal tooth widths and core back thickness. The calculated values for the geometrical dimensions of the motor are presented in Table 4.2.

4.2.4 Coil Design and Number of Turns

The diameter of each conductor of a coil of winding is chosen based on the fill factor and the slot area. The permitted current density can be defined by the choice of the cooling method. Typical current density values in respect to different motor cooling methods include; 4.7 – 5.4 A/mm², 14.0 – 15.5 A/mm² and 23.3 – 31.0 A/mm² for totally enclosed not ventilated (TENV) motors, external blower through cooled motors and liquid-cooled motors, respectively [107]. The stator outer diameter can be increased to allow more slot area to reduce current density, if there are no size limitations [20].

Beyond the base speed, which is the minimum speed that can produce the maximum power, the back emf rises to a level that limits the current, torque and therefore reduces the power. In order to reduce the back emf and implement conventional discontinuous current operation at higher operational speeds, a lower number of turns is considered resulting in a boost in the output power. However, this would come with a torque reduction at lower operational speeds which in turn results in an increase in the rating of the inverter’s silicon and the drive cost.

The high speed operation of motor requires a high electrical switching frequency. High switching frequencies cause high levels of AC losses in the conductor. In order to address this issue, Litz wire is used. This type of wire takes its name from Litzendraht the German word for braided. Litz wire consists of several strands of woven thin insulated conductor and offers lower proximity loss and skin effect, when compared to a solid conductor.

Litz wire selection considered the calculated skin depth at 3.3 kHz (which will be explained in following chapters), a simple winding process and the commercially available Lits wires. A Class F, 155°C rated, red heavy polyurethane-nylon (MW80-C) wire was selected which consists of 5 × 3 × 33 (or 30) strands of wire. Given the 50% fill factor, the available copper area of a slot is equal to 25.04 mm². This meets the copper area provided by the Litz wire which is 25.08 mm² nominally. The finished coils do not use the supplier’s maximum recommended current density of 0.25 mm²/amp for windings which necessitates the cooling of the

litz construction in some manner. Finally, the wire design requires a voltage rating of 600 V. This requirement was met by means of using appropriate thickness for the slot isolation. A voltage rating is usually included to the Litz construction by using a tape layer or an extruded layer, which was not required for this work.

4.2.5 Air Gap

In high speed SRMs the core loss and the windage loss are higher. The air gap width substantially affects this. A large air gap would require high MMFs to achieve the same flux, hence large copper loss. On the other hand, a narrow air gap requires a level of precision that makes manufacturing difficult, and viscous drag is larger [79]. For high speed SRMs it is common to use an air gap of 0.2 – 0.3 mm. For this work, an air gap of 0.3 mm was chosen to ease the manufacturing of the prototype.

4.3 Motor Specification Investigation

The rotor dimensions; for tooth height, tooth width and core back thickness are similar to the stator. The rotor outer diameter is finalised using stress analysis which will be presented in chapter 5. This suggests the initial SRM design which is shown in Table 4.2.

Table 4.2: Detailed Specifications of SRM

Parameter	Symbol	Unit	Value
Stator Outer Diameter	S_{OD}	[mm]	176
Stator Core Back Thickness	t_y	[mm]	15
Rotor Tooth Width	t_r	-	25
Air gap Width	t	[mm]	0.3
Rotor Outer Diameter	R_{OD}	[mm]	105
Stack Length	L_s	[mm]	58
Maximum Power	P_{max}	[kW]	60
Maximum Speed	ω_{max}	[krpm]	50
Torque	T	[Nm]	56
DC Link Voltage	V_{DC}	[V]	600
Fill Factor	FF	-	0.5
Stator/rotor teeth combination	N_s/N_r	-	6/4
Number of Turns	N	-	8
Number of Phases	q	-	3

4.4 DC Voltage

The phase voltage in SRMs is proportional to the number of turns of each winding and the magnetic flux per tooth. Keeping the motor dimensions and air gap width fixed, the magnetic flux per pole is proportional to the voltage that is applied across that winding and inversely proportional to the number of turn of each coil.

It is therefore the case that output torque of an SRM can be controlled by adjusting the voltage to number of turns ratio. For instance, after finding a suitable number of turns for the required fill factor, the voltage can be varied to reach the desired torque [79].

4.5 Conclusion

The electromagnetic design methodology and operating principles of a high speed SRM were discussed in this chapter.

The design process began with scaling down the geometrical parameters of an existing SRM, which has same specifications as the PM machine used in the Toyota Prius, with a ratio of 1.5:1. This was obtained considering a maximum speed of 50,000 rpm whilst maintaining an output power of 60 kW.

Next, the resulting values were processed using analytical methods to indicate the values for the other major geometrical parameters. The rotor outer diameter, the stator core back thickness and the rotor tooth width were calculated in this way to be 105 mm, 15 mm and 25 mm, respectively.

The high speed operation imposes a number of requirements on the electromagnetic aspects of the design process. An airgap width of 0.3 mm was considered for this work, which is common for high speed SRMs. The high speed operation also results in a high switching frequency, therefore 6/4, which is the lowest stator/rotor pole combination for a 3 phase machine, was selected.

For a high speed application, the back emf rises to a level that limits the current and consequently the torque, a trade off between the supply voltage and the number of turns on the coil, as they are inversely proportional. Using a lower number of turns for the coil reduces the back emf, resulting in an increase in the output power. As a result, 8 turns of conductor for each coil windings were selected. In order to address the high AC copper loss which is caused by the high speed application, Litz wire is implemented in this work.

Chapter 5

Mechanical Design Investigation

When designing high speed machines, the mechanical constraints (the stresses and the natural frequencies) have higher priority when compared to the thermal or electromagnetic ones. In order to develop as much torque as possible, the physical dimensions of the rotor, especially the outer diameter, are chosen to be as close to the mechanical limit as possible. As a result, it is vital to investigate the rotor reaction as precisely as possible. Ensuring the robustness of the rotor for the design speed is the main challenge of this work.

Various approaches to address the mechanical constraints for different types of electrical machine have been taken. The process usually consists of predicting the stresses using an analytical model, then confirming this using Finite Element Analysis (FEA). In this work, the the analysis is carried out using only the FEA method.

In this chapter, the mechanical constraints will be investigated for the rotor of a radial (conventional) SRM. This motor is designed to replace an existing SRM, SRM1, that has the same output specifications, outer diameter and stack length as the PM machines used in the Toyota Prius. Some of the specifications of SRM1 is given in Table 5.1.

The mechanical stresses imposed on the rotor are simulated here. The notch effect and hoop stress are the major causes of the mechanical stresses. Suitable approaches to address each one of these are suggested and simulated. This leads to a new rotor topology for an SRM which applies a flywheel topology to the rotor. The proposed topology will be analysed for high speed operation with different rotor specifications investigated.

Decisions over the choice of materials are explained. This along side the estimate of the rotor stiffness is used to calculate the vibration frequencies and determining the vibration modes.

Table 5.1: Detailed Specifications of SRM1

Parameter	Symbol	Unit	Value
Stator Outer Diameter	S_{OD}	[mm]	264
Rotor Outer Diameter	R_{OD}	[mm]	182
Stack Length	L_S	[mm]	87
Maximum Power	P_{max}	[kW]	60
Maximum Speed	n_{max}	[rpm]	13,500
Torque	T	[Nm]	207
Stator/rotor teeth combination	-	-	18/12
Weight	W	[kg]	25.2

5.1 FEA model for Mechanical Analysis

It is common for high speed permanent magnet rotors to be contained within a prestressed sleeve which prevents the surface mounted magnets from lifting off the rotor. In high speed SRMs, this technique is also used despite the lack of magnets, it reduces the large windage loss of SRMs by providing a smooth airgap surface. This can also be achieved by using a flux bridge [79,83]. However, adding this sleeve does increase the magnetic air gap resulting in a reduced electromagnetic performance.

5.1.1 Simulation Assumptions

ANSYSTM software was used to study the rotor mechanical stresses. The physical properties of the electrical steel including material density and isotropic elasticity (Young's Modulus and Poisson's ratio) were required input for the FEA model. These data were found on the material data sheet. The contact area between different rotor components are assumed to be frictionless. However, this assumption should be made with the effects of Poisson's ratio in mind. Poisson's ratio is a measure that defines the expansion of a material under a compressive force, in the directions that are perpendicular to the axes of the compressive force. It is known that Poisson's ratio effects can lead to significant strains in the axial direction in high speed motors. Assuming a frictionless contact results in unconstrained rotor components in the model, which in turn will not undergo any stress in the axial direction. However, as the Poisson ratios of the different rotor components are the same and they are under the same stress magnitude, the assumption of frictionless contact is possible [64].

An elastic body subjected to different loads in three directions would require a three dimensional stress system. Each single point inside the rotating body is undergoing

stresses in different directions with changing stress magnitude from point to point within the object. It is possible the combined stress at each point exceeds the material's yield strength, despite the principal stresses acting on the object in the x, y and z directions being below the yield strength. The Von Mises criteria is the equivalent stress of the three principal stresses, which is described as Eq. (5.1)

$$(S_1 - S_2)^2 + (S_2 - S_3)^2 + (S_3 - S_1)^2 = 2S_e^2 \quad (5.1)$$

where S_e is the equivalent or Von Mises stress with S_1 , S_2 and S_3 being the principal stresses in different directions. Therefore, Von Mises stress is merely a criterion to determine the equivalent stress at each point, not a real stress. The stress analyses from here-forth will only consider the Von Mises stress.

5.2 Design Process

It was explained in Section 2.10.1 how the motor was scaled down. The physical measurements of the motor were then calculated using an analytical method. During this process, the stator/rotor tooth number was reduced from 18/12 to 6/4 to avoid a high switching frequency and resulting iron core loss. As a result, the initial electromagnetic analysis showed the scaled down motor could not meet the specified torque requirement of the project. This can be compensated by increasing the rotor active length from 58 mm to 95 mm.

The rotor topology and material need to be investigated closely for the rotor stress which in turn can limit the permissible size of the rotor and its electromagnetic capability.

In this chapter the stress concentration on the rotor is studied and improved. This is carried out while ensuring the final design will meet both the electromagnetic output of the motor and rotor safety factor. From an electromagnetic point of view, the output torque is the subject of the investigation, while the maximum stress and the resonant frequencies are the investigated mechanical constraints. The electromagnetic and mechanical improvements are carried out using the FEA methods. The rotor component materials and the maximum speed are the given conditions for the mechanical analysis, which define the maximum allowable radius for the rotor. These findings go hand in hand with the torque requirement of the design. Having made the required improvements on the length of the rotor to achieve the target torque, the design is analysed for the resonant vibrations to identify the critical speed. The more detailed electromagnetic analysis is to follow in the next chapter.

5.3 Mechanical Analysis

Determining the stresses induced by the centripetal force on the rotating parts is crucial, as if yield strength is exceeded, failure or permanent deformation will occur. The maximum stress tolerated by the material before failure is called its yield strength, which is a property of the material stated by the material manufacturer. Usually during the design process the total maximum stress due to rotation is maintained below the yield strength. This can be done either by designating a safety factor or by fatigue analysis. The latter requires knowledge of the duty cycle, and as this information was not provided by the supplier due to customer confidentiality, the former was adopted for this test.

Two aspects of the rotor's mechanical behaviour are investigated; the mechanical stresses and the resonant frequencies.

5.3.1 Conventional SRM Rotor Topology

The electrical steel used for a high speed rotor needs to have high yield strength to be able to tolerate the high mechanical stresses associated with the high speed operation. Therefore, after consulting the manufacturer (Cogent Steel) M250-35HS electrical steel was chosen for this work. This material is suitable for high speed applications and has a guaranteed yield strength of 400 MPa and a typical yield strength of 450 MPa [108].

The mechanical analysis started by running the stress analysis on an SRM rotor with a conventional topology. For this model, only one rotor lamination was considered in the simulation as there is no shear stress present (apart from the possible shear caused by the glue that is very small and negligible). As the rotor is not using a retaining sleeve, any need for adding compressive forces is eliminated. The simulations solved for the equivalent stress and the total deformation. However, the maximum principle stress was also observed for all the simulations. The stress map is illustrated in Fig. 5.1 which showed a maximum equivalent stress of 1210 MPa concentrated at the sharp corners at the bottom of the rotor teeth (caused by the notch effect) followed by stress concentration around the shaft bore (caused by the hoop stress).

5.3.2 Addressing The Notch Effect

The maximum equivalent stress is concentrated around sharp corners at the bottom of the rotor teeth, as a result of the notch effect. The common practice to address this issue is to add fillets to the sharp corners, however, the analysis showed adding

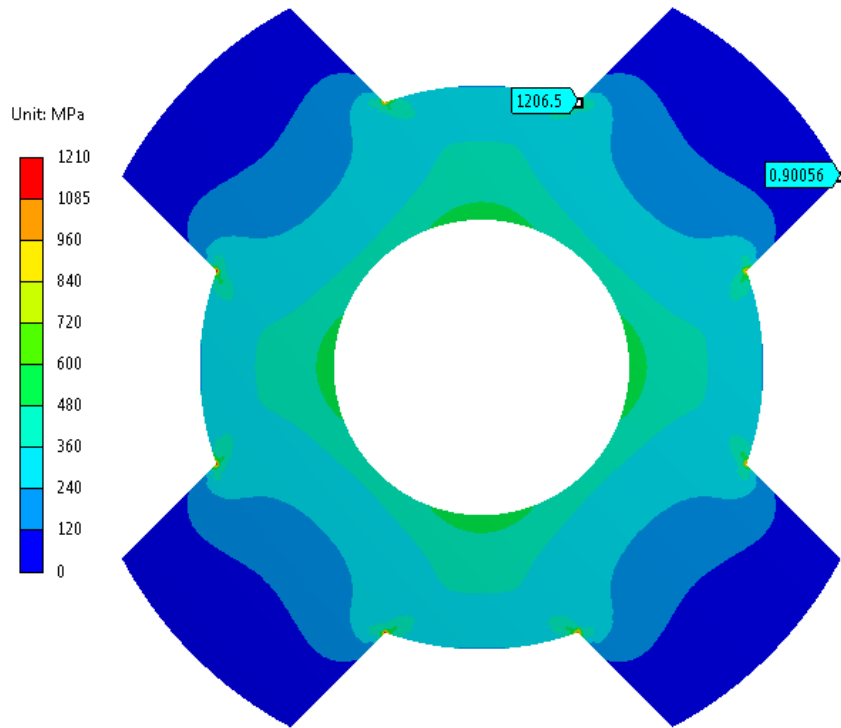


Figure 5.1: Stress Analysis of a Conventional SRM Rotor

two fillets to the bottom of each slot on either side increases the number of sharp angles in each slot (the start and end point of each fillet), and hence does not help the stress.

To combat this issue, a tangential curve was used to connect every two adjacent teeth, providing a smooth path whilst removing any sharp corners. The stress analysis showed a maximum equivalent stress of 511 MPa, which can be seen in Fig. 5.2. The stress magnitude was still higher than the allowable 450MPa. This stress is concentrated around the shaft bore and is caused by the hoop stress. Therefore, other topologies for the rotor were required.

5.3.3 Addressing The Tangential Stress

It can be seen from Fig. 5.2 that the maximum stress was concentrated around the shaft bore. This excessive stress was caused by the hoop stress. In order to reduce the hoop stress, a fly wheel topology is applied to the rotor.

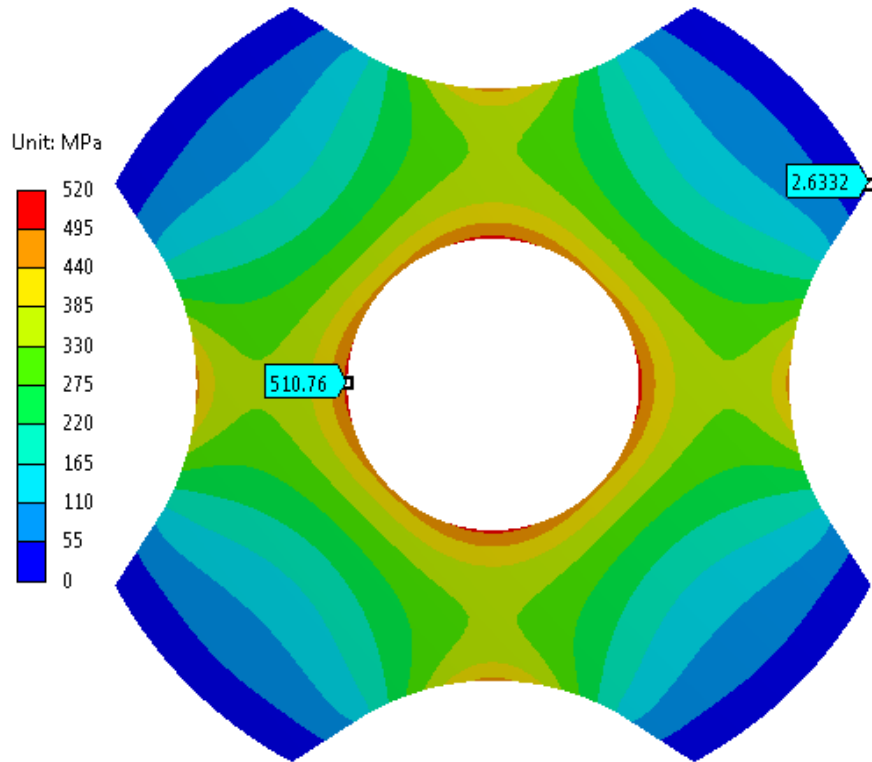


Figure 5.2: Stress Analysis of a Conventional SRM Lamination with Added Fillets

5.3.4 Flywheel Structure

The idea to use a flywheel structure to the rotor is taken from a patent by Prof. Keith Pullen [109]. A simple schematic a flywheel is shown in Fig. 5.3. This method completely removes the shaft bore where the hoop stress is concentrated and uses cheek plates and tie rods to sandwich the laminations.

However, the shape of the tie rod cuttings has a direct impact on the equivalent stress on the laminations. The Pullen patent suggests a number of overlapping circles for the tie rod cuttings. These circles are distributed on a tangential direction, as shown in Fig. 5.4, and are claimed to significantly reduce the equivalent stress. However, the proposed cutting shape for the tie rods were found not to be suitable for the SRM rotor topology since, compared to a cylindrical flywheel, an unbalance is introduced to the rotor structure due to the presence of the rotor poles. Therefore, a simple circular cutting shape was found to be sufficient for the tie rod cuttings.

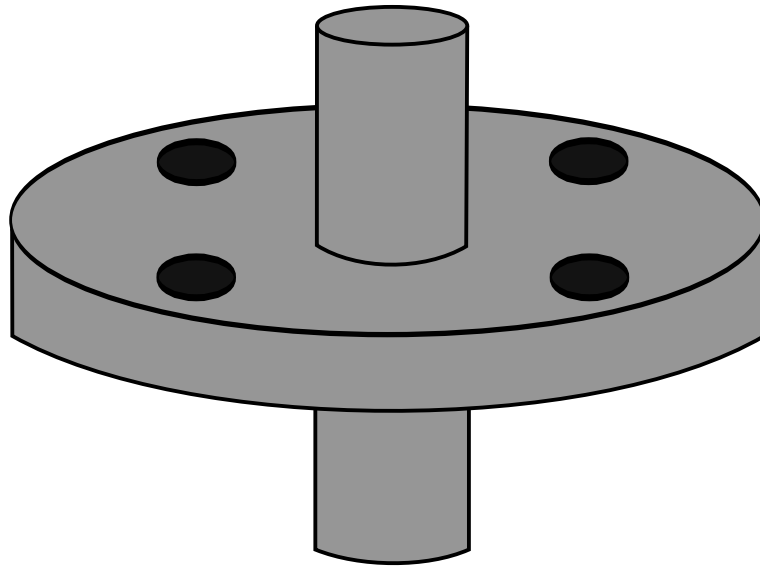


Figure 5.3: Flywheel Simple Schematic

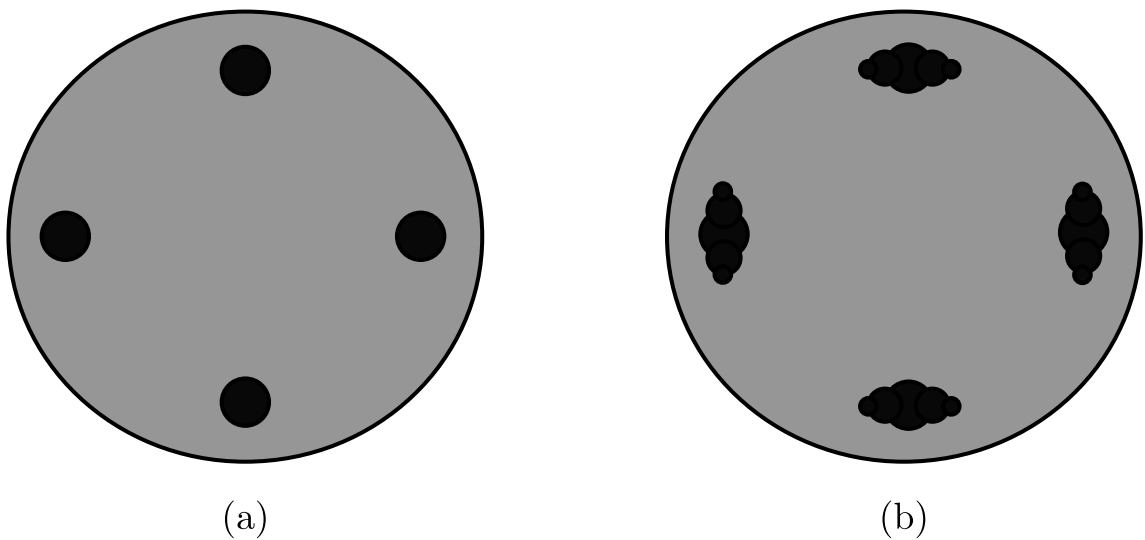


Figure 5.4: Comparison of the the a) Circular Tie Rod Cutting and b) The Overlapping Circle Cutting Shape as Proposed by Pullen

A simple schematic of the proposed topology is presented in Fig. 5.5. In the proposed topology, the laminations do not have a shaft bore. Instead, they are sandwiched between two cheek plates which are bolted together using tie bars. Each one of the cheek plates has its own external shaft extending along the rotating axis that is used to transfer the torque to the load.

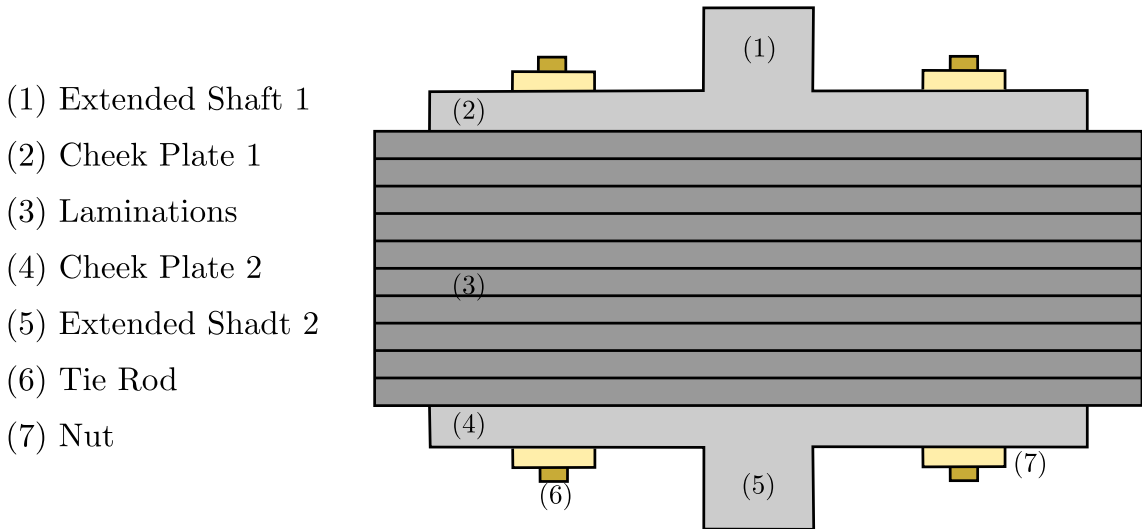


Figure 5.5: Rotor Simple Schematic with a Flywheel Structure

5.3.5 Physical Features of the Proposed Model

Next, the physical dimensions of the proposed rotor design were investigated closely for their effect on the mechanical stresses. A final design which ensures the lowest possible stresses in the rotor can then be achieved. The parameters subject to investigation are illustrated in Fig. 5.6.

Tie Rod Cutting Diameter and Location (Tr_D and Tr_r)

To keep the cheek plates and laminations together tie rods are used. In order to feed through the laminations, a cut needs to be made. The rods themselves also have to be thick enough to sustain the forces applied to them by the rotating laminations.

The location and shape of the tie rods therefore has been investigated. If placed closer to the rotor outer diameter, they will be close to the varying magnetic field and susceptible to eddy current induction, which will give rise to heating and loss. On the other hand, moving them closer to the center of the rotor will lead to increased mechanical stresses on the laminations. The shape of the holes also affects the hoop stress. Simulations showed circular cuttings would have the lowest stress concentrated around them. The number of the cuttings has been chosen to be equal

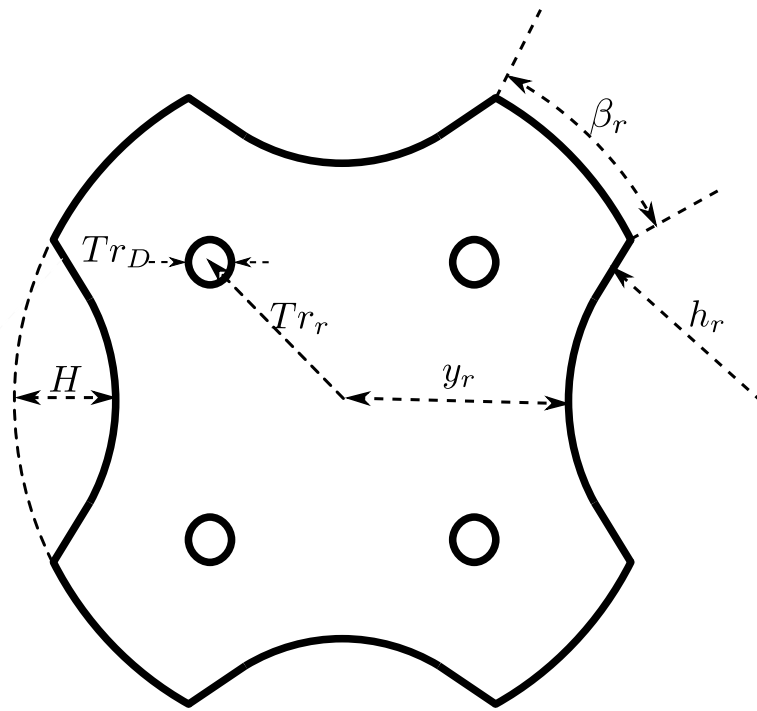


Figure 5.6: Detailed Drawing Dimensions of The Proposed Rotor

to the rotor teeth number to ensure symmetry, hence lower stresses. If the rods are too small in diameter, they will not withstand the applied forces. Without any tie rod holes, an equivalent stress of 239 Mpa is obtained via simulation on a lamination with no shaft bore. Adding the holes increases the stresses, however, Fig. 5.7 shows the stresses seem to vary little with increases in hole diameter. Considering the yield strength of the tie rod material, a 6 mm diameter is selected. The location of the tie rod cutting is investigated and shown in Fig. 5.8, for a given diameter of 6 mm. It is decided to locate the tie rod holes 26 mm radially from the rotor centre as they will be safely away from the rotor teeth and the changing field whilst maintaining the equivalent stress below the yield strength of the laminations. This ensures the minimum possible equivalent stress.

Fillet Radius(h_r)

The radius of the tangential curves added to the base of the rotor teeth has been also investigated. It was expected that smaller radii would experience lower stresses however, this reduces the rotor tooth height, leading to higher flux leakage. The optimum value of the fillet size is given in Table 5.3. It should be mentioned that the centre of the radius is assumed to be fixed in the space and only the value of the radius is changed.

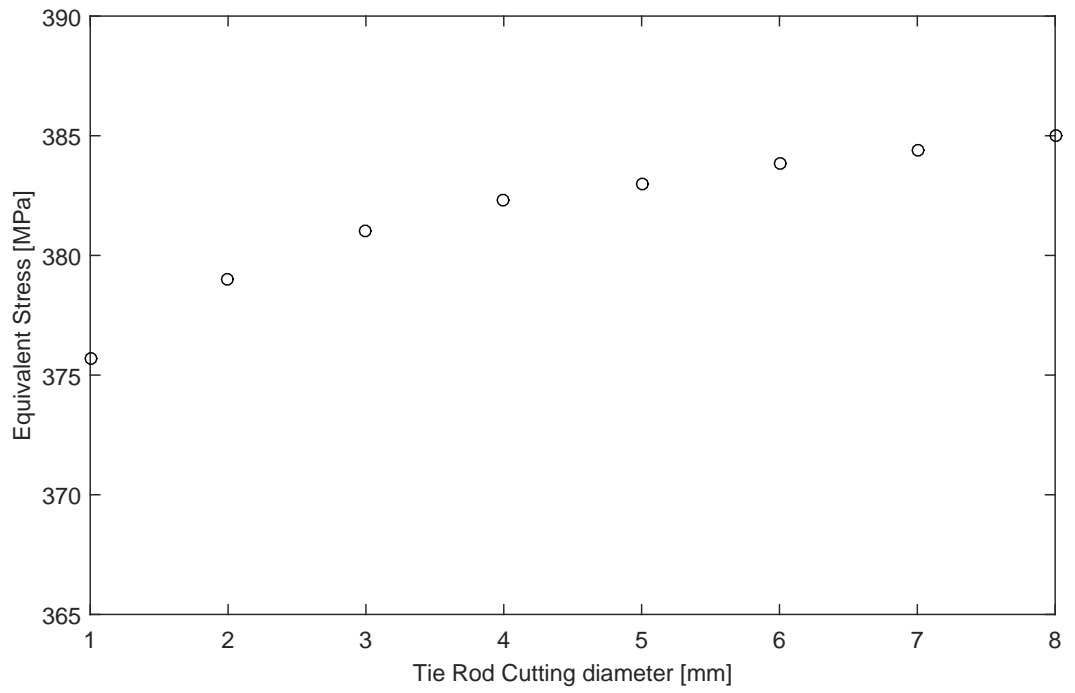


Figure 5.7: Tie Rod Cutting Diameter Vs. Equivalent stress

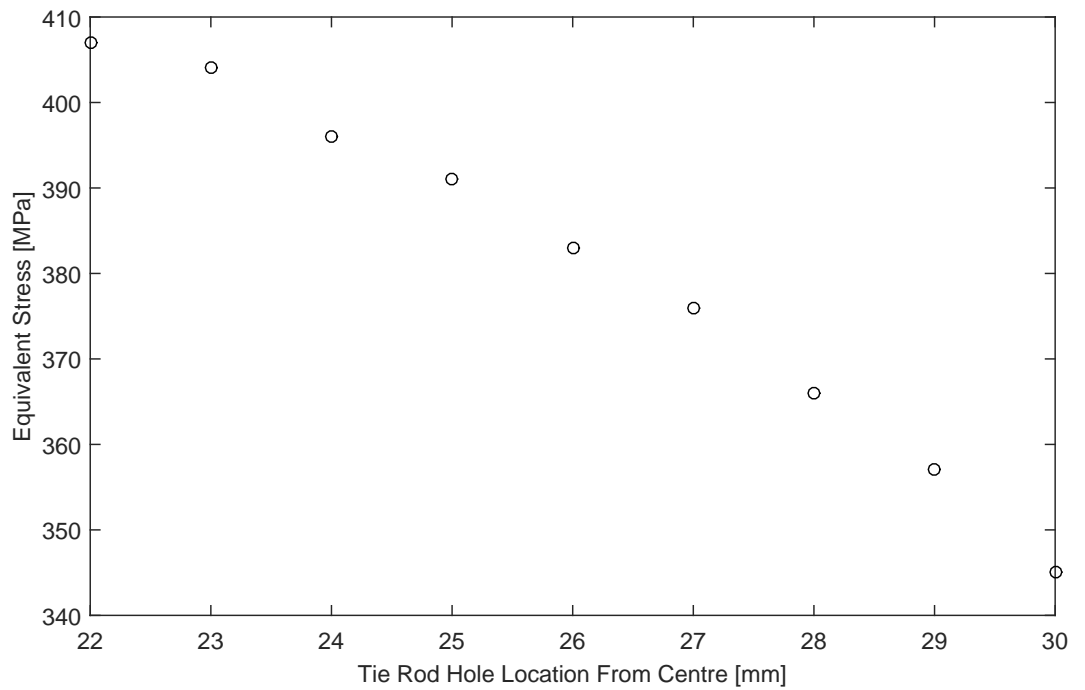


Figure 5.8: Tie Rod Location From Centre Vs. Equivalent stress

Rotor Pole Arc (β_r)

The rotor pole arc is another physical feature of the rotor to be investigated. Changes to rotor pole arc will have the largest effect on the electromagnetic behaviour of the machine. Therefore, the optimization process considered both the mechanical stress and the output torque simultaneously. As shown in Fig. 5.9 increasing the rotor pole arc up to $34^\circ C$ increases the torque. However, any increase beyond this point results in a reduction in the output torque as the rotor tooth comes in close proximity to the stator tooth of the next phase.

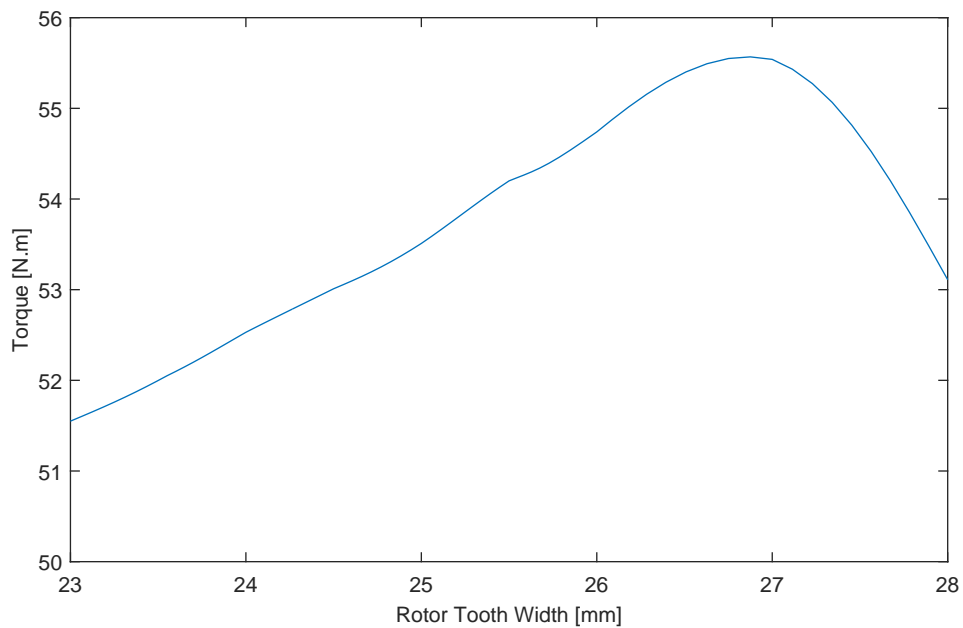


Figure 5.9: Rotor Tooth Width Vs Torque

Rotor Outer Diameter

It is important to identify the maximum allowed diameter for the rotor. The motor output torque is in direct proportion with the square of the rotor diameter. However, increases in the diameter also dramatically increase the stresses. Therefore, it is favourable to increase that parameter to its limits. After identifying the optimum values for various physical features of the rotor, the maximum rotor diameter, considering the safety factor, was identified. The optimised values are presented in Table 5.3.

Rotor Component Materials

The choice of the materials for the analysis and manufacturing was an important step of the design process. The proposed motor consists of several components whose material was carefully chosen as their yield strength was critical for the requirement of the high speed application. The cost, availability and manufacturing requirements were other factors to consider for selection process. The selected materials for different rotor components and their respective yield strength are presented in Table 5.2. The detailed description of the materials used in the design will be presented in Chapter 7.

Table 5.2: Materials Used in The Motor Construction

Part	Material	Yield Strength
Rotor Lams	M250-35HS	450
Tie Rods	A286	580
Cheek Plates	Nitronic 50	690

FEA Simulation Results of Proposed Model

The proposed design was analysed for the mechanical stresses, while ensuring the optimised rotor could deliver the required output torque. As it can be seen from Fig. 5.10 the maximum stress of 382.5 MPa was at the cuttings, which was below the yield strength leaving a safety factor of 1.2.

Proposed Model 2

A design with no shaft in the rotor caused concern over satisfying alignment for all the rotor components. Therefore, a second design was required for the mere purpose of alignment comparison. For this, a small shaft with 10 mm diameter was added to the design. As alignment was the only purpose of the added shaft, it would only extend 15 mm into the cheek plates on either side. The mechanical analysis showed a maximum stress of 433.7 MPa concentrated around the shaft bore, as it is shown in Fig. 5.11.

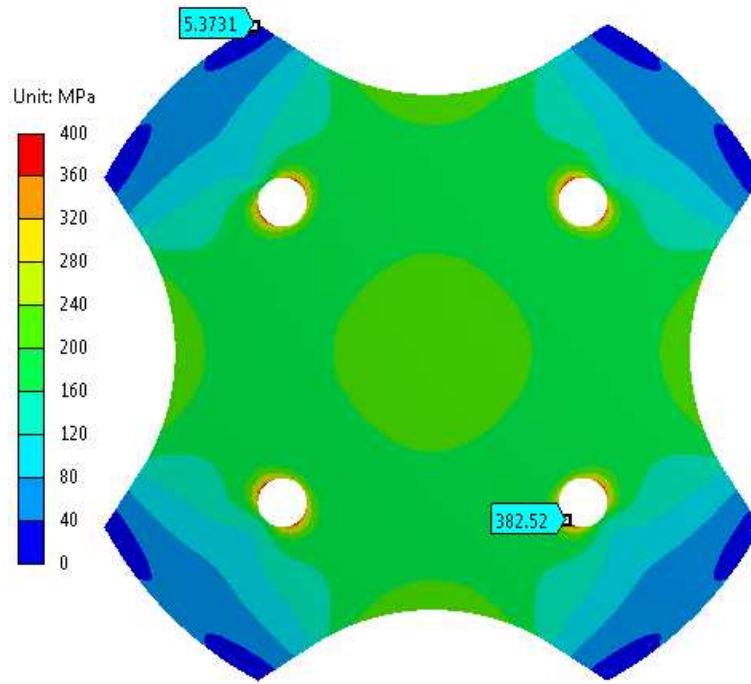


Figure 5.10: Stress Analysis of the Proposed Rotor

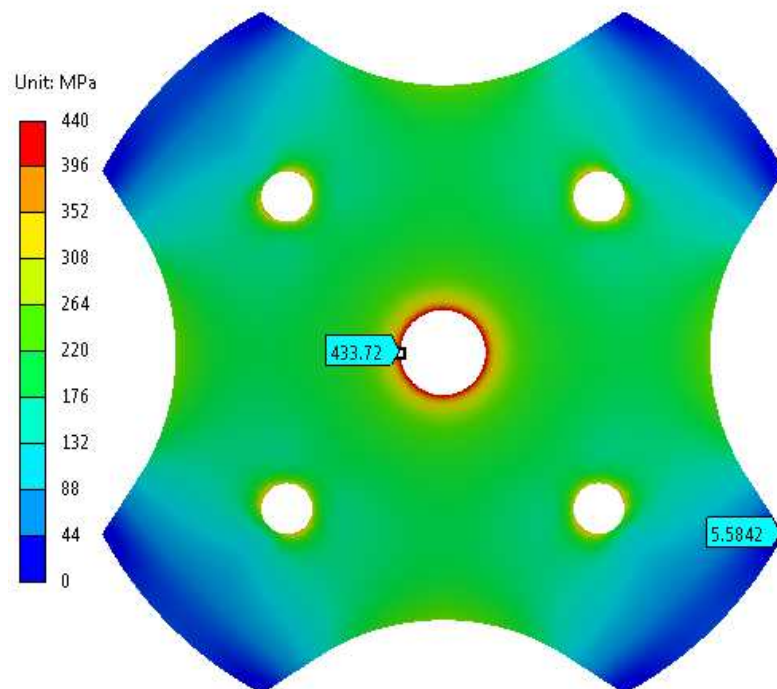


Figure 5.11: Stress Analysis of the Proposed Rotor with a Shaft Hole

The final values for various physical features of the proposed rotor can be find in Table 5.3 .

Table 5.3: The Optimised Rotor Physical Specifications

Parameter	Denoted Symbol	Unit	Value
Rotor Outer Diameter	R_{OD}	[mm]	91
Rotor Yoke Outer Diameter	y_r	[mm]	32
Rotor Pole Height	H	[mm]	13.5
Tangential Curve Radius	h_r	[mm]	26.5
Tie Rod Diameter	Tr_D	[mm]	6
Tie Rod Distance From Centre	Tr_r	[mm]	26
Rotor Pole Arc	β_r	[Deg]	34

5.4 Vibration Frequencies

It is important to ensure the design speed of the motor remains below the critical speed. The modelling of the rotor assumes it is a solid lump of steel. The stiffness of the bearings needed to be adjusted. This is an important factor in determining the vibration modes and their respective frequencies.

5.4.1 Bearing Stiffness

The bearing stiffness is a criteria determining the deflection or deformation magnitude in a bearing under load. It is defined as the ratio of load to deflection and can vary by the type, size, design, material, contact angle and pre-load class of the bearing.

A high precision angular contact hybrid ball bearing is selected for this work. The typical stiffness of the chosen bearing type obtained from the manufacturer is $18.6 \text{ N}/\mu\text{m}$ for a pair of steel bearings. However as they are hybrid bearings with ceramic balls, the stiffness has been adjusted. The calculation process is as follows;

$$K_{hp} = K_{steel} \times \text{Ceramic Ball Coefficient} \tag{5.2}$$

$$= 18.6 \times 1.1 = 19.98 \text{ N}/\mu\text{m} = 19980 \text{ N}/\text{mm} \tag{5.3}$$

$$K_{hs} = \frac{K_{hp}}{2} \tag{5.4}$$

$$= \frac{19980}{2} = 9990 \text{ N}/\text{mm} \tag{5.5}$$

where K_{hp} , K_{steel} and K_{hs} are the stiffness of a pair of hybrid bearings, the stiffness of a steel bearing of this size and the stiffness of a single hybrid bearing.

The total stiffness of the bearing considers all three dimensions and is inversely proportional to the cross section area of the bearing. The selected bearing has a diameter of 37 mm and is 9 mm wide. The total three dimensional stiffness of the bearing is shown in Eq. (5.7) which was used as the input data for ANSYSTM, where K_{Total} is the total three dimensional stiffness of the bearing and A_b is the bearing cross sectional area..

$$K_{Total} = \frac{K_{hs}}{A_b} \tag{5.6}$$

$$= \frac{9990}{37 \times 9} = 30 \text{ N/mm}^3 \tag{5.7}$$

5.4.2 Vibration Modes

After adjusting the stiffness, the modal analysis was carried out for a fully assembled motor. Modal analysis is used during the design process to identify the vibrations characteristics of the motor including the natural frequencies and the vibration mode shapes. Table 5.4 summarises the first ten vibration modes and their respective frequencies.

Table 5.4: The Vibration Modes and Their Frequencies

Order	Type	Frequency[Hz]
1.	Rock	1.3811e-002
2.	Bounce	85.634
3.	Bounce	85.634
4.	Bounce	127.72
5.	Rock	177.62
6.	Rock	178.68
7.	Bend	3747.4
8.	Bend	3748.2
9.	Torsion	10331
10.	Bend	11750

The critical speed would be the first bending mode that occurs at 3747.4 Hz, which is significantly above the design speed of 50,000 rpm (833 kHz) , it should not therefore be a problem. The first rock and bounce modes can be overcome if the motor speeds up fast enough without spending a significant period of time around that region.

Also, soft mounting technique will be applied to the bearings which reduces the first rock and bounce modes significantly, allowing the machine to speed up and pass over them quickly.

5.4.3 Spring Pre-Load

The rigidity of the bearing can be altered by applying a pre-load. The magnitude of the force for light, medium and heavy pre-load were provided by the bearing manufacturer. The selected bearings are an angular contact type with a light pre-load. The stiffness of the pre-load spring, k , was calculated to be 30 N/mm, using its data sheet [110] and Hook's law.

The bearing manufacturer's suggestion for a light pre-load is 26 N. Eq. (5.9) shows the calculated deflection for a light pre-load.

$$\delta = \frac{F}{k} \quad (5.8)$$

$$= \frac{26}{30} = 0.86 \text{ mm} \quad (5.9)$$

In practice, the required pre-load was applied to the pre-load spring by taking off the magnitude of deflection from the designated space for the spring washer as illustrated in Fig. 5.12. this can be done during the design of the housing by only allocating the width of the pressed spring washer.

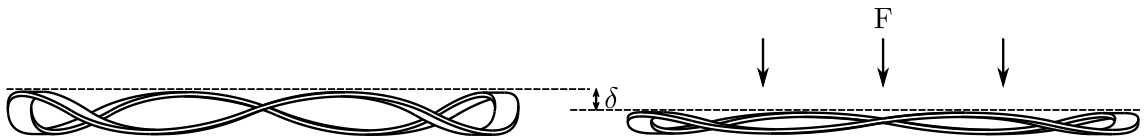


Figure 5.12: Deflection of a Pre-load spring

5.5 Conclusion

The mechanical design process started with the results of analytical calculations for the initial frame size of a high speed SRM to replace the PM motor in the Toyota Prius. This was carried out by scaling down the frame size of an existing SRM which was proposed to replace the PM machine whilst having the exact same specification. Next, a radial SRM was designed based on the calculated frame size. The output torque of this design was analysed using FEA and the further optimised to meet the required torque, the results of which will be presented in the next chapter. In

the next stage, the rotor design was analysed for mechanical stresses which are very important in high speed rotors. A Combination of the notch effect and the hoop stress caused the maximum stress of the rotor to exceed the yield strength of the rotor lamination material, therefore a different approach was required for the rotor.

A topology common to flywheels has been applied to the rotor. The central shaft, which was deemed to be the main source of the hoop stress, has been completely removed and instead a set of tie rods and end plates used to support the laminations. The materials for the stator and the rotor lamination are selected from the low iron loss range whilst having high yield strength so M250-35HS, A286, and Nitronic 50 were chosen for the rotor, the bolts and the cheek plates, respectively.

The mechanical analysis was carried out for various rotor features of the new design such as the location and size of the cutting holes for the tie rods and the rotor pole pitch. The maximum rotor radius considering the safety factor was identified as 91 mm. The final values of the different rotor geometrical features, which ensured a maximum stress below the yield strength for the rotor, were also presented considering a safety factor of 1.15. Applying a smaller radius and number of poles compared to the scaled down model, resulted in torque reduction. The rotor length was increased from 58 mm to 95 mm in order to meet the torque requirement of the machine.

The electromagnetic design and analysis of the motors will be discussed in detail in the next chapter. In conclusion, a design suitable for an operational speed of 50,000 rpm which can produce 56 Nm was proposed in this chapter.

Chapter 6

Further Electromagnetic Design Investigation

This chapter focuses on the electromagnetic design methodology which, for a high speed application must be taken into account in parallel with the mechanical design described in Chapter 5. Using analytical methods, the main physical features of the motor, such as frame size, number of phases, number of poles, etc. have been defined and presented in Chapter 4.

The design of the rotor in particular has been presented in the mechanical design chapter, where it has been ensured that the rotor is pushed to its limits before failure. This has been checked against electromagnetic simulations to see if the performance of the machine has been compromised by these changes.

The electromagnetic specification of the proposed motor will now be investigated in more detail for the instantaneous and transient output torque with the help of FE models. Operating at high speeds increases the AC copper loss and the iron loss. The increase in the AC copper loss is due to the skin effect and the proximity loss, these effects are investigated and suitable solutions are applied to reduce them.

Windage loss also increases with speed as is proportional to the angular velocity cubed. The toothed structure of the rotor adds further to the windage loss which makes windage an important component of the total loss for this application, this will be calculated using analytical methods.

Finally, the calculated losses are used to estimate the efficiency of the motor at a range of loading points and presented as an efficiency map.

6.1 Rotor Structure Development

Before presenting the electromagnetic analysis of the proposed motor, it is important to electromagnetically optimise the value of the physical features of the motor. The development process of the rotor topology, from the mechanical point of view, was described in 5.3.5, where the impact of varying various rotor features on the equivalent stress of the laminations was studied.

It is also essential to investigate the implications of the proposed flywheel structure on the motor output from the electromagnetic point of view. The major rotor features, that will have a direct impact on the motor output, are the rotor tooth width t_r , the radius and location of the tie rod cutting Tr_D and Tr_r , and the radius of the tangential line at the bottom of the rotor teeth, h_r . The value of the tie rod diameter will not have a significant influence on the electromagnetic performance of the motor, therefore it was sufficient to find the optimum value only through the mechanical analysis.

6.1.1 Rotor Tooth Width (t_r)

Changes to rotor tooth width will have the largest effect on the electromagnetic behaviour of the machine. The optimization process has to consider both the electromagnetic and mechanical impact of varying the tooth width. As shown in Fig. 6.1 increasing the rotor tooth width up to 27 mm increases the torque. However, any increase beyond this point results in a reduction in the output torque as the rotor tooth comes in close proximity to the stator tooth of the next phase.

6.1.2 Tie Rod Cutting Location (Tr_r)

If the tie rods are placed too close to the rotor outer periphery, they will be close to the varying magnetic field and susceptible to eddy current induction, which will in turn give rise to the iron loss and heating. On the other hand, placed close to the centre of the rotor will result in increased mechanical stresses on the rotor laminations. The location of the tie rod is investigated against the maximum output torque and the results are shown in Fig. 6.2 for a fixed tie rod diameter of 6 mm. As it can be seen, varying the location of the cuttings from 20 mm to 29 mm away from the rotor centre has a small impact (0.1 Nm) on the output torque. This is likely to be caused by disturbing the path of the magnetic flux and creating saturation around the area of the tie rod cutting. Finally, the tie rods are located at 27 mm relative to the centre of the rotor.

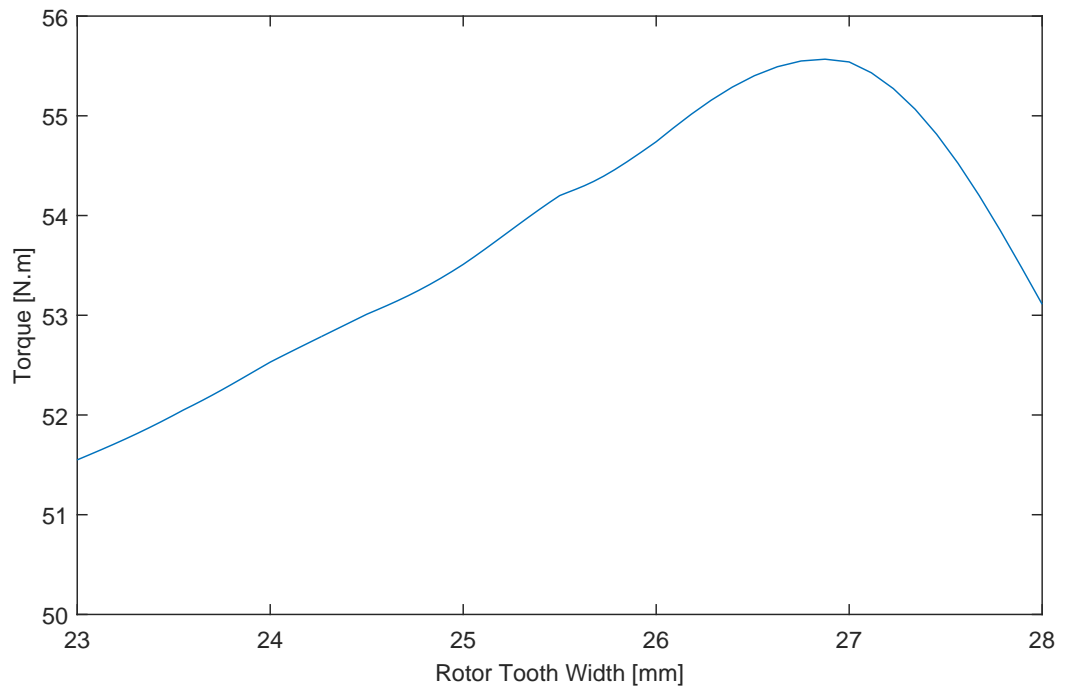


Figure 6.1: Rotor Tooth Width Vs Torque

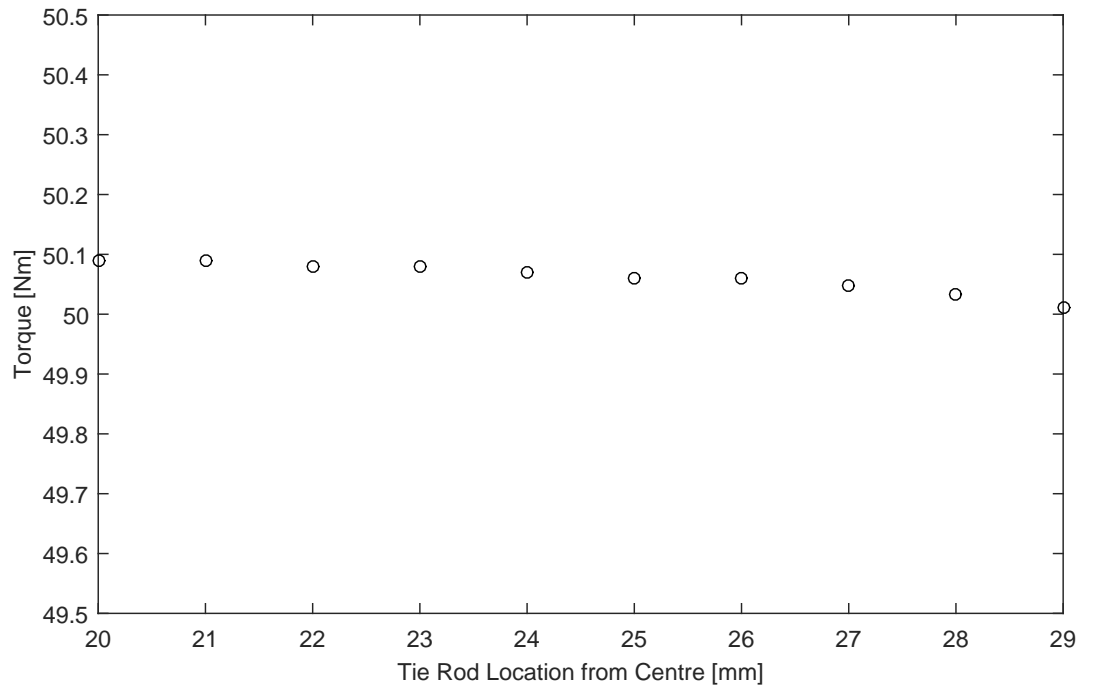


Figure 6.2: Investigation of the Optimum Value for the Tie Rod Location

6.1.3 Diameter of the Fillet at the Bottom of Rotor Tooth (h_r)

The study of the fillet at the bottom of the rotor teeth were carries out assuming the center of the fillets were fixed points in the space and the diameter would vary relative to these centres. The analysis shows increasing the diameter from 72 mm to 81 mm would result in a reduction in the output torque, as presented in Fig. 6.3 . This is caused by reduction of the available rotor back iron which in turn leads to the expansion of the saturated areas. A diameter of 72 mm was deemed sufficient as a smaller diameter would be susceptible to flux leakage.

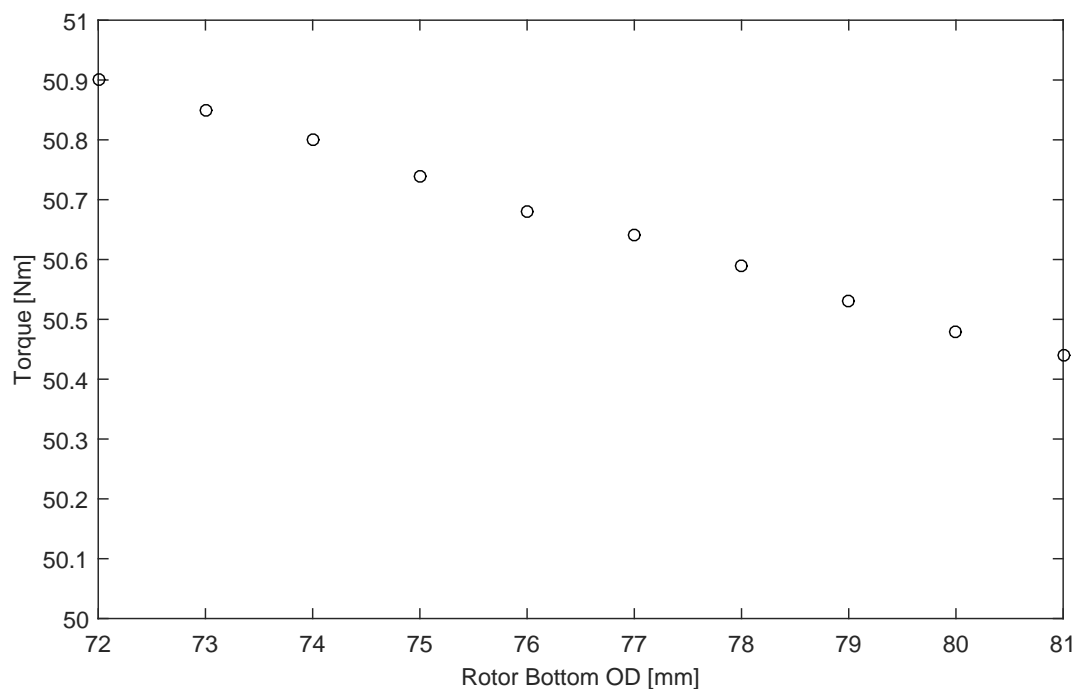


Figure 6.3: Investigation of the Optimum Value for the Rotor Bottom Outer Diameter

6.2 Static Simulation

In order to fully analyse the performance of a motor, a dynamic (transient) simulation is required, however a good way to foresee the dynamic operation is to analyse the static operation of the motor. This technique is particularly beneficial as static simulations require significantly shorter computation time. The static characteristics of the motor can be obtained using the magnetisation curves and torque vs angle profile [25].

6.2.1 Two Dimensional FEA Simulation Results

An FE model has been designed using Infolytica Magnet to simulate the motor in two dimensions (2D) from an electromagnetic point of view. 2D analysis allows short simulation run times even for models with a fine mesh ensuring more precise results. 2D analysis was used during the mechanical design stage whilst physical features of the rotor were being examined for the lowest operational stresses. The model is shown in Fig. 6.4.

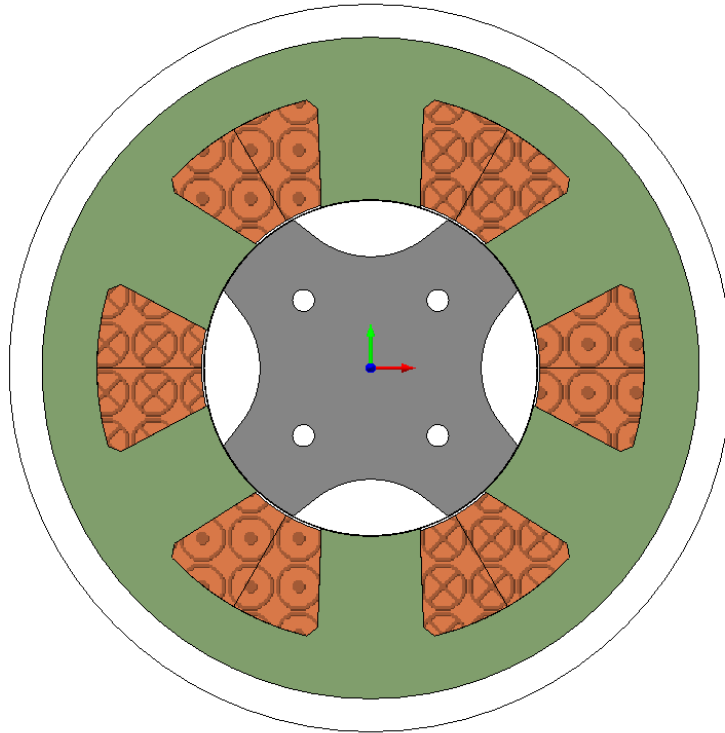


Figure 6.4: Model Used for 2D Static Simulation

In order to avoid producing negative torque, at any given time only one phase is excited. Only when the current starts to decrease in that phase, will the current increase in the following phase. This is done to avoid the rotor approaching a position with decreasing inductance. The direction of the current in the windings is illustrated in Fig. 6.5.

The magnetic field solution of the motor at aligned position is plotted in Fig. 6.6. The black lines show the flux path from stator pole to rotor pole, through the rotor back iron and the opposite rotor pole, and back to the opposite stator pole. It can be seen that the saturated areas are the bottom of the stator teeth and around the tie rod cuttings. Also, it can be seen that the tie rods of the rotor poles that are not in the aligned position will be effected by the varying but smaller magnetic field.

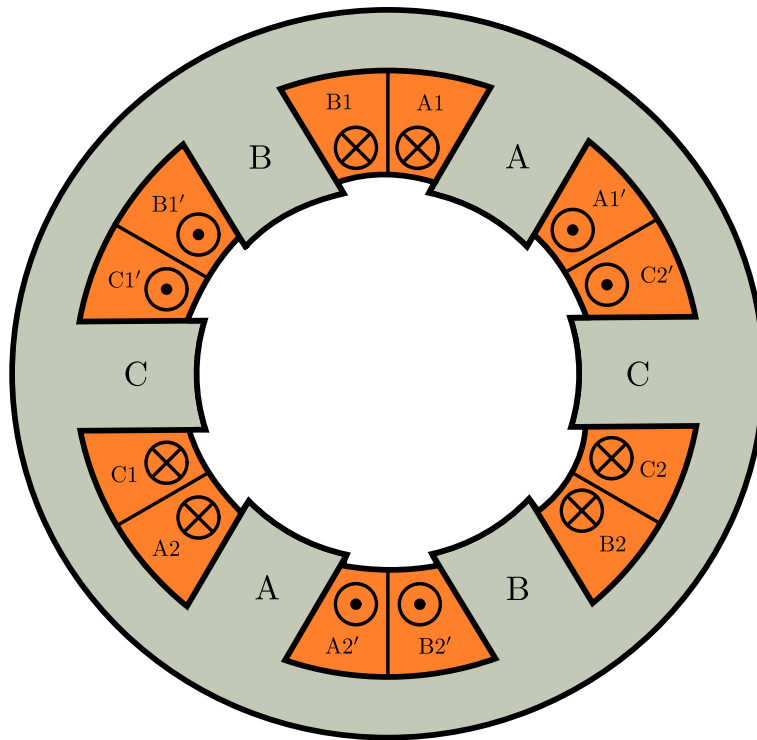


Figure 6.5: Winding Current Direction

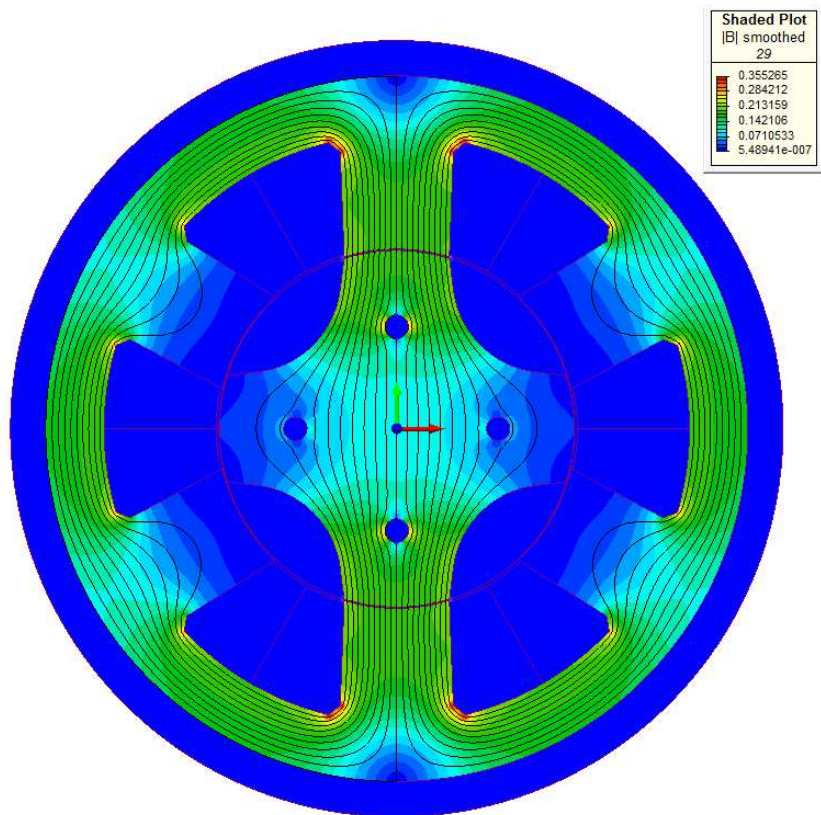


Figure 6.6: Flux Density of the Motor and the Flux Path in Aligned Position

In order to show the effect of magnetic saturation on the iron in the motor, the magnetisation curves at several rotor positions have been calculated and are shown in Fig. 6.7. The current is applied to one phase, made up of two coils, with each coil having eight turns. To create the curves a range of currents from 0 to 600 A were used, and rotor was rotated in steps of 15° electrical from 0° to 180°. The knee of the curves shows where the motor enters saturation at each rotor position with saturation being higher in positions where the teeth are aligned.

The magnetisation curves of the motor at the aligned (180°) and unaligned (0°) positions are the focus of the simulation as the torque produced is directly related to the co-energy. Co-energy can be calculated by integrating the area enclosed by these two curves. The peak torque from the FEA simulation was calculated as 66.00 Nm at full current.

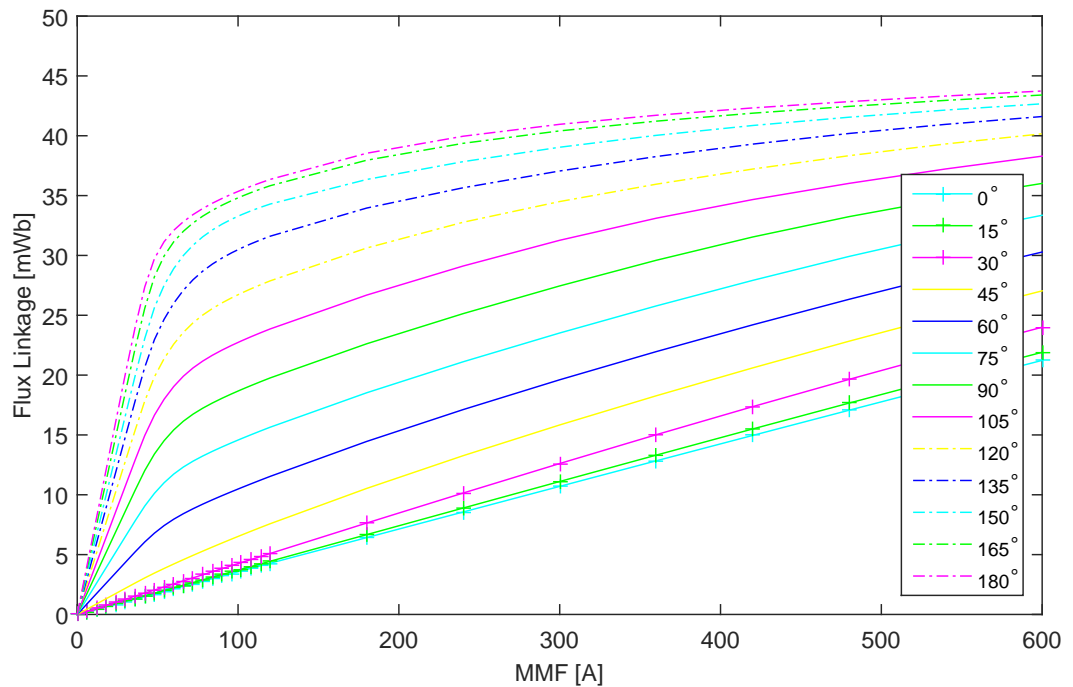


Figure 6.7: Expanded Magnetisation Curve

6.2.2 Three Dimensional FEA Simulation Results

The same conditions for number of turns and current were applied to the Three Dimensional (3D) model. The 3D model is more representative of the real machine as it takes into account the effect of the end winding. In order to save on the computation time, only one quarter of the machine was modelled for this section. The model is shown in Fig. 6.8.

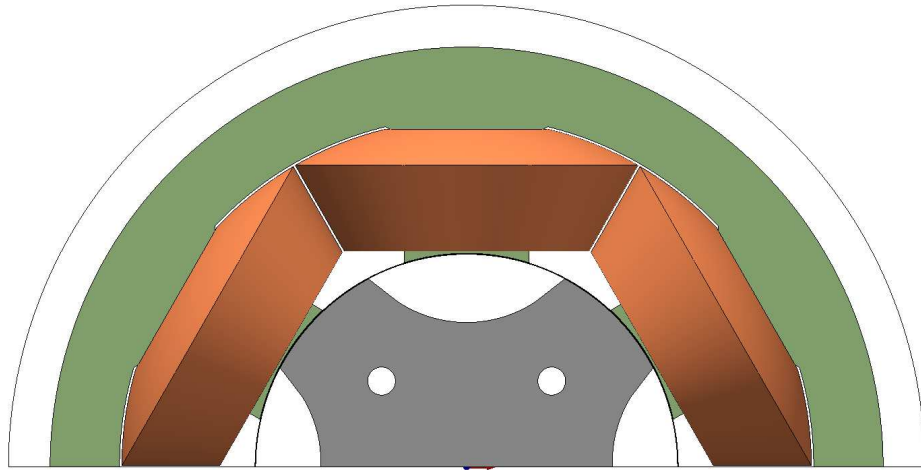


Figure 6.8: Model Used for 3D Static Simulation

Fig. 6.9 shows the magnetisation curves from the 3D model and compares them with those obtained from the 2D model. Using the co-energy, the peak torque from FEA analysis was calculated to be 63.77 Nm at full current. There is 3.3% difference between the 2D and 3D simulation which can be attributed to the end winding effect. However, it also shows that end effect for a machine of this aspect ratio is limited. The difference can also be caused by calculation errors rising from different meshing methods used in the 2D and 3D models.

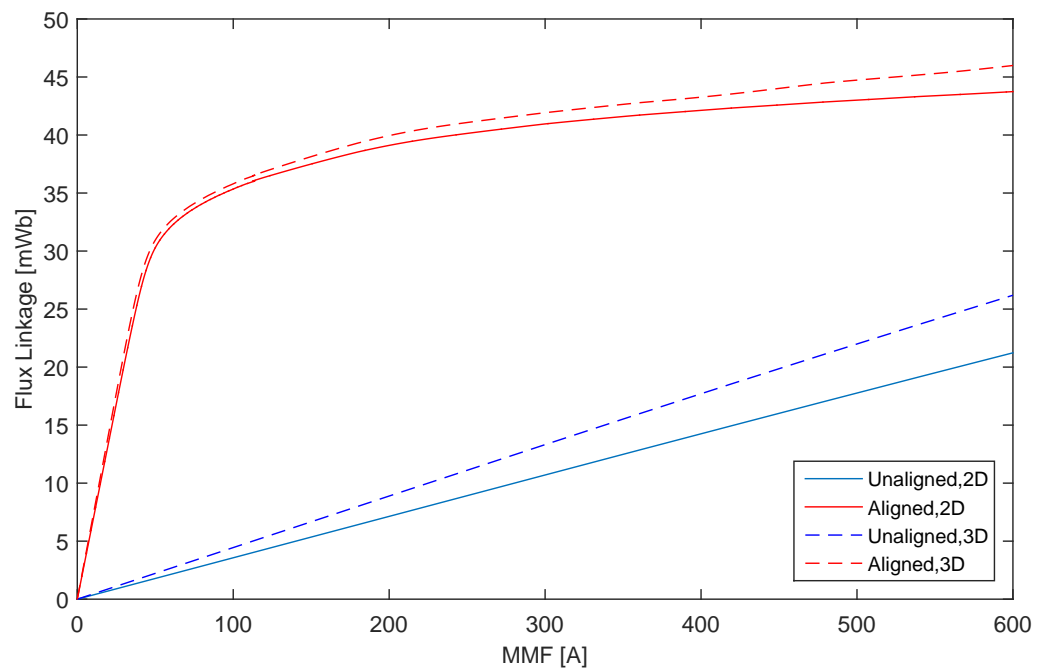


Figure 6.9: Comparison of Magnetization Curves for a 2D and 3D FE Model

The same model was used to create the torque vs angle profile of the motor which

is shown in Fig. 6.10. Each curve represents the torque at a certain magnitude of MMF for a range of rotor positions. Current was applied in steps of 60 A from 0 A to 600 A (equal to an MMF of 0 to 4800 A) and the rotor rotated in steps of 5° electrical to create the profile. The curves at higher currents become skewed due to significant saturation.

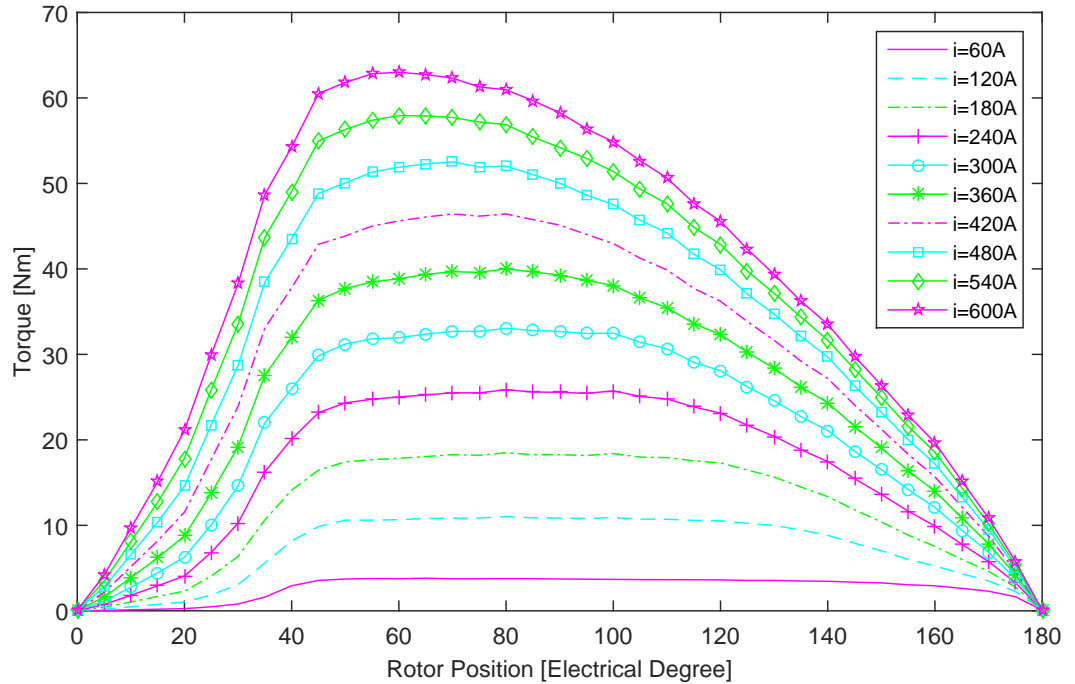


Figure 6.10: Torque Vs. Rotor Position Using the 3D FEA Model

6.3 Dynamic Simulation

The dynamic (transient) simulations are of interest as they predict the behaviour of the motor more accurately, taking into account losses and current shape. The majority of losses such as the iron loss and the ohmic loss can be calculated using the dynamic simulations. The dynamic simulations were run at the base speed and the full speed of the motor.

6.3.1 Dynamic Simulations at Base Speed

Like other electrical motors, the speed where the back EMF rises enough to be equal to the bus voltage is called the base speed. At this point the rated power of the motor is also realized if the rated current is applied. Base speed is also the maximum speed that the motor can provide the maximum torque. Therefore, torque analysis

at this speed shows the maximum torque output of the motor under given voltage constraints.

The base speed was calculated by scaling the SRM1 model to be 10,250 rpm. It was rounded to 10,000 rpm giving the rotor a ratio of 5:1 final speed to base speed. At low speed it is the current that needs to be limited and hence current control is used at low speeds and square wave current waveform was applied to this model. As it can be seen from Fig. 6.11 a maximum phase current of 600 A is used in order to provide an MMF of 4800 A.

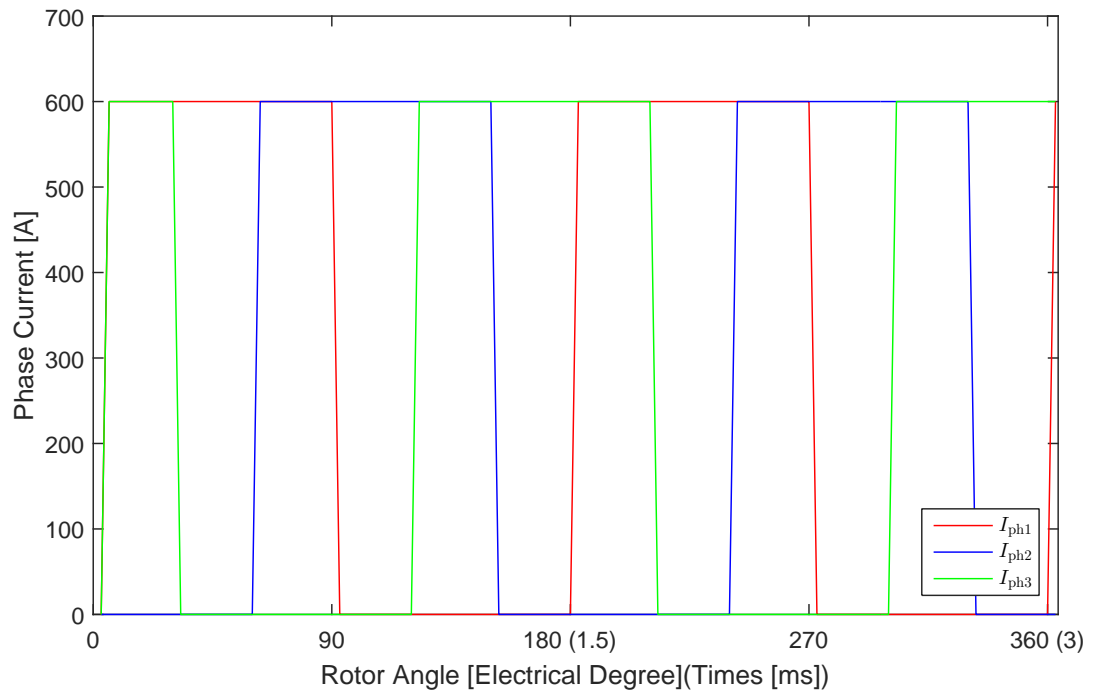


Figure 6.11: Square Wave Phase Current Used for Control at Base Speed

Advancing the switching angle was also used to further increase the torque. A range of angles have been evaluated from 0° to 90° electrical degrees as shown in Fig. 6.12, it was found that an advance angle of 20° at base speed maximised the torque output. Fig. 6.13 shows the torque waveform, at base speed with full current, over the period of one electric cycle, where an average torque of 55.60 Nm is achieved.

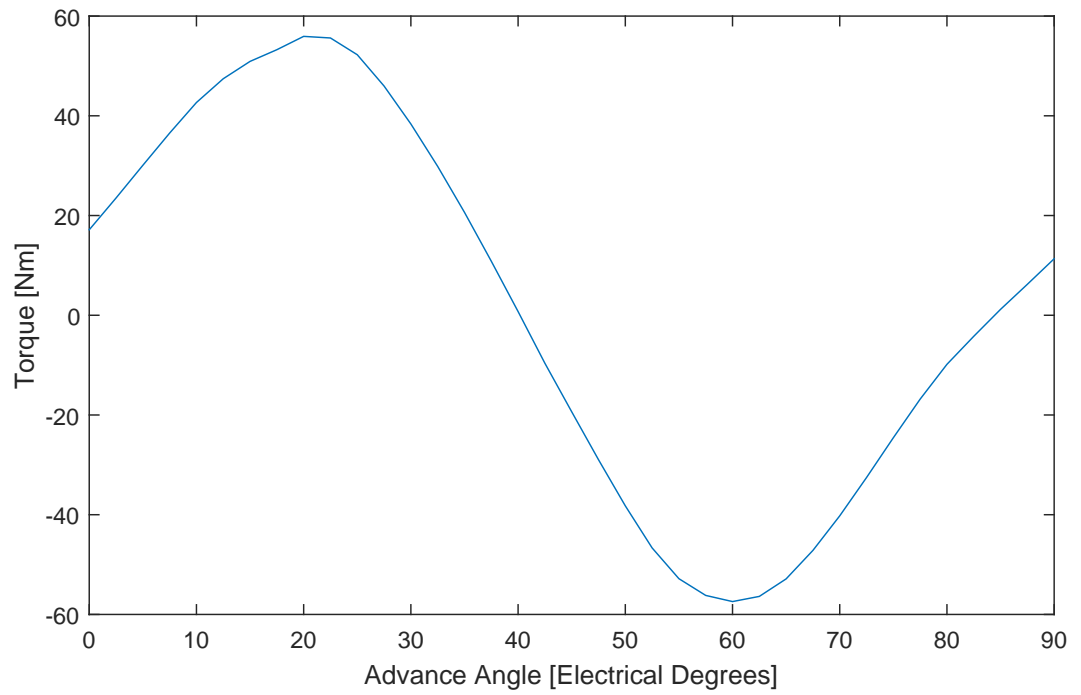


Figure 6.12: Advancing the Stator Excitation Angle

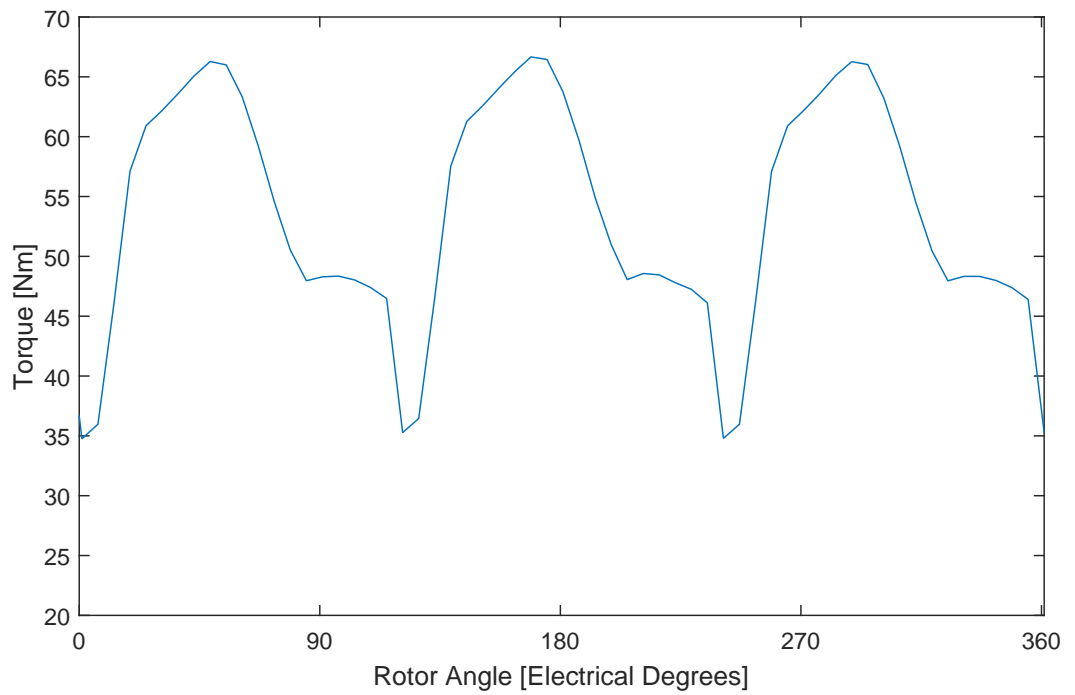


Figure 6.13: Transient Torque Vs. Rotor Position at the Base Speed

6.3.2 Dynamic Simulations at Full Speed

During the scaling down process it was calculated that a torque of 11.45 Nm is required to maintain an output power of 60 kW whilst running at the full speed of 50,000 rpm. Simulations show an MMF of 1200 A is enough to generate the required torque at full operational speed. A square wave current was used in stator phases to obtain this MMF, which is shown in Fig. 6.14. To improve the torque, a range of angles have again been evaluated. It was found that an advance angle of 30° at the maximum operational speed maximised the torque output. Fig. 6.15 shows the torque waveform at full speed from which the average torque is calculated to be 11.44 Nm.

It has been shown that from the electromagnetic aspects, the motor meets the torque requirements.

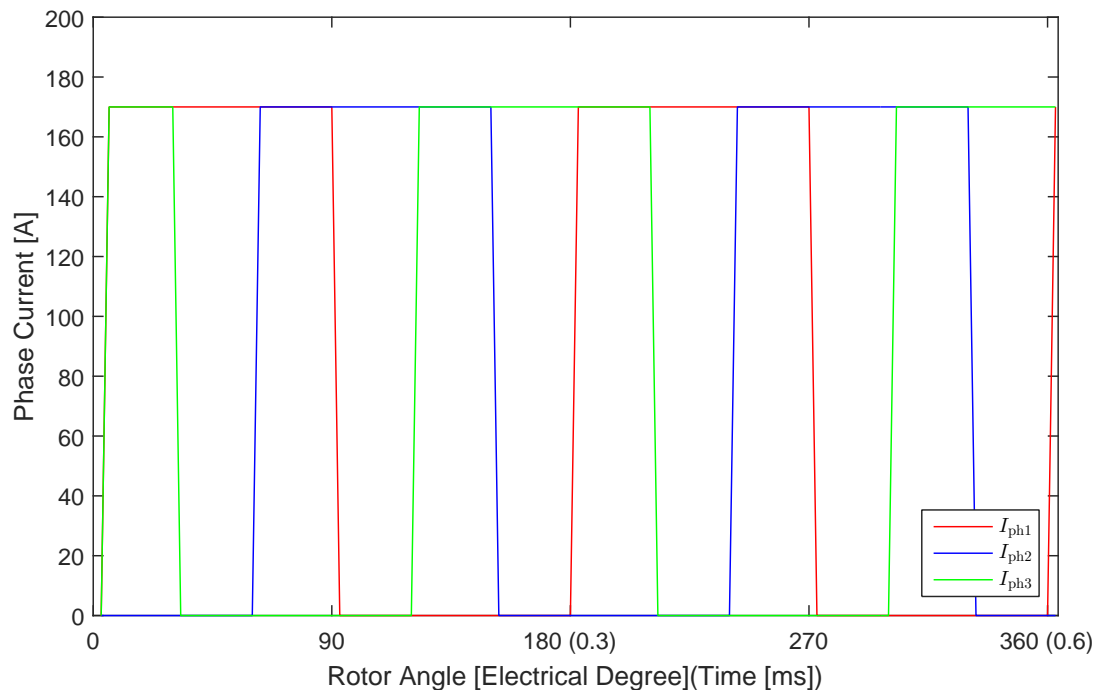


Figure 6.14: Square Wave Phase Current Used for Control at Full Speed

6.4 Losses

Heat dissipation is a very important factor in design of electric motors. Various losses contribute to the machine total loss from electromagnetic point of view including DC winding loss, AC winding loss and core loss. The mechanical components of loss are the windage loss and the bearing friction loss.

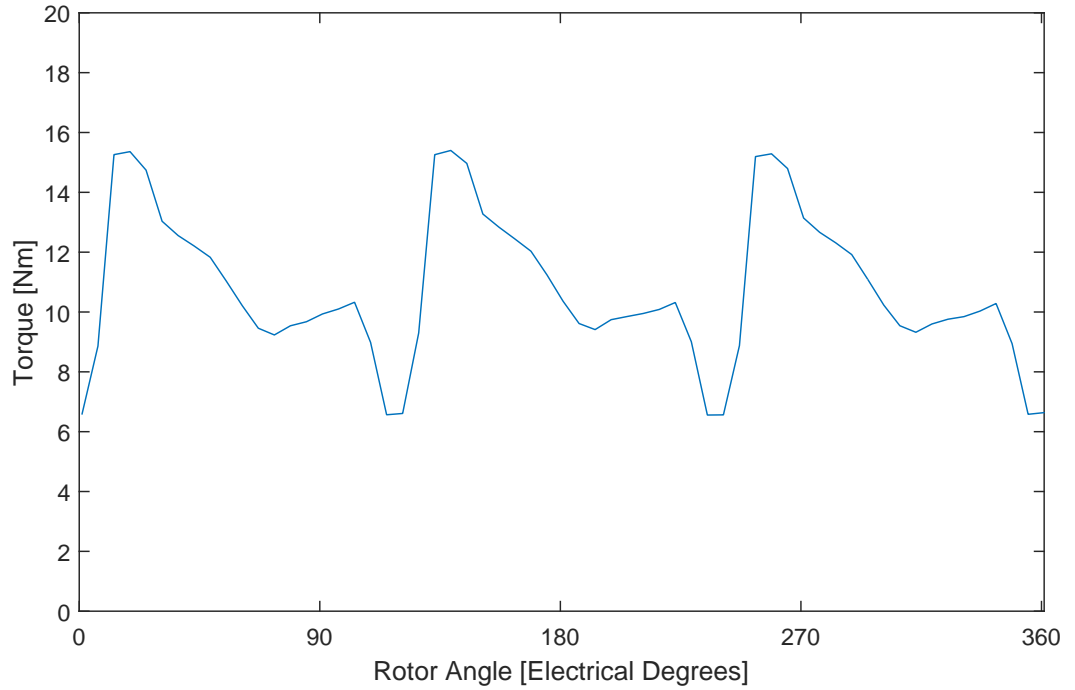


Figure 6.15: Transient Torque Vs. Rotor Position at Full Speed 50,000 rpm

6.4.1 DC Winding Loss

The copper loss, P_{cu} is usually the main source of loss in the motor and can be expressed as Eq. (6.1) where q is the phase number. I_{rms} , the rms phase current and R_p , the stator winding resistance per phase.

$$P_{cu} = qI_{rms}^2 R_p \quad (6.1)$$

These are calculated using Eq. (6.2) and Eq. (6.3), respectively.

$$I_{rms} = \frac{i}{\sqrt{q}} \quad (6.2)$$

$$R_p = \rho \frac{L_c}{A_c} \quad (6.3)$$

Where L_c is the total conductor length and A_c is the cross sectional area of the conductor.

6.4.2 AC Winding Loss

At low speeds, the winding loss can be assumed to be equal to the DC loss that would be present with a DC current. As the fundamental frequency increases with an increase in the operational speed a significant AC loss can exist. Two major factors contribute to the AC loss in the windings;

- The skin effect.
- The proximity copper loss.

Skin Effect

As Faraday's law explains, a current flowing within a conductor creates external and internal magnetic field. If the current alternates over time, the magnetic fields also alternate. In this case, the internal magnetic field induces eddy currents within the conductor. The flow path of this current is located toward the centre of the conductor and in the opposite direction to the source current. However, its return path is located towards the circumference of the conductor and in the same direction as the main current as illustrated in Fig. 6.16.

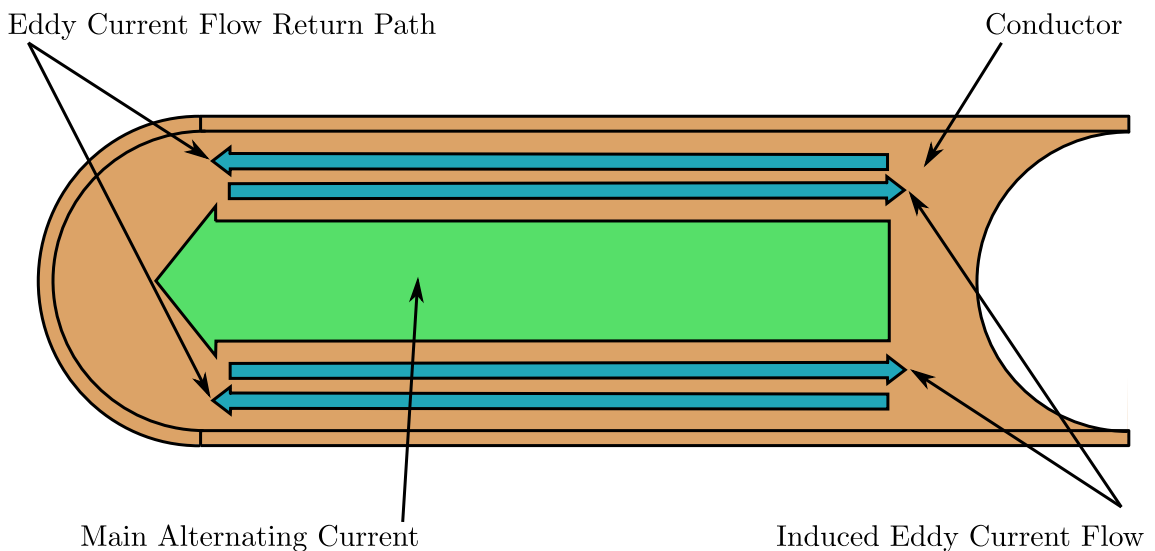


Figure 6.16: Skin Effect

As a result of this, the main current is redistributed over the area from the outer surface of the conductor and as deep as the conductor's skin depth, δ_{sd} , towards its centre, this depth can be calculated using Eq. (6.4) where ρ_c is the resistivity of the conductive material, f the fundamental frequency, μ_r the relative permeability of the conductive material and μ_0 the permeability of free space.

$$\delta_{sd} = \sqrt{\frac{2\rho_c}{f_f\mu_r\mu_0}} \quad (6.4)$$

If the diameter of the conductor is significantly larger than its skin depth, all other parts of the conductor except that within the skin depth remain unused which wastes the copper area and copper itself. The skin effect therefore causes the operating cross section of the conductor to diminish, increasing the effective resistance which in turn increases the copper loss. For an operational speed of 50,000 rpm the skin depth of 1.14 mm is calculated.

Proximity Effect

The alternating magnetic field produced by a conductor carrying an alternating current is affected by adjacent alternating current carrying conductors. Eddy currents are induced within each conductor that oppose the alternating magnetic field generated by the other. The flow direction of the induced eddy current will add to the main current on the furthest side of each conductor and subtract from it on the nearest. The net current is illustrated in Fig. 6.17 for two conductors in close proximity. This phenomenon increases the resistance and thus the ohmic loss in the external conductors and is known as proximity effect [111].

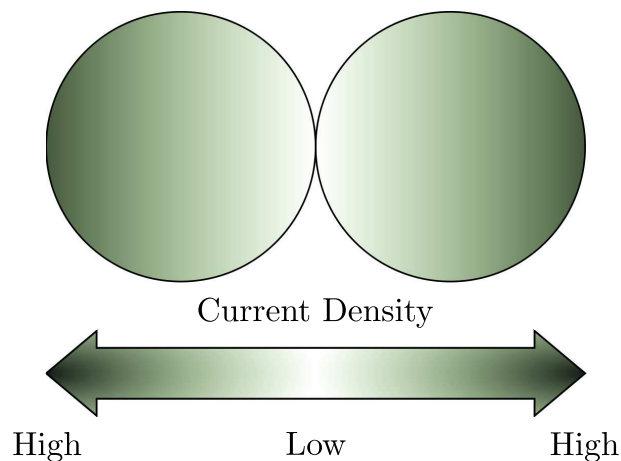


Figure 6.17: An Example of Proximity Effect

When there are more conductors, as in a normal slot in a motor this effect worsens as the alternating magnetic field of each conductor influences every single conductor. Conductors in the centre of the slot are least affected, as the proximity effect caused by the conductors either side of them cancel. However, conductors towards the outside of the coil are influenced as they have more conductors to one side than

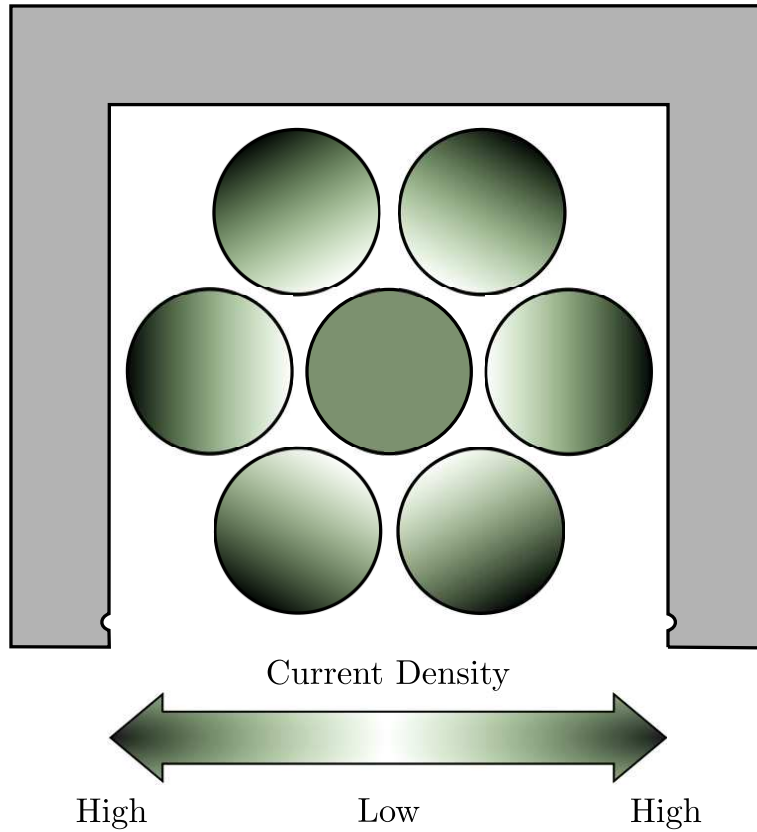


Figure 6.18: Proximity Effect in an Electrical Machine Coil

the other, which means there is an overall proximity effect in the conductor. An example of this current redistribution is shown in Fig. 6.18.

The proximity loss, $P_{\text{Cu,prox}}$ can roughly be estimated using Eq. (6.5).

$$P_{\text{Cu,prox}} \sim J^2 f_f^2 r_r^3 \quad (6.5)$$

where J is the current density, r_r is the rotor radius and f_f is the fundamental frequency.

An FE model was used to investigate the proximity loss on the conductors inside the machine slot, when the appropriate current was applied at full speed. The repositioning of the current within the conductors of the winding, when the rotor is approaching the aligned position, is illustrated in Fig. 6.19. Here, it can be seen that the current redistribution occurred more for the conductors near the opening of the slot (conductor 8) compared to those near the yoke (conductors 1,2 and 3). This is due to the stray fluxes and the higher magnitude of magnetic flux near the tip of the stator teeth compared to that near the yoke.

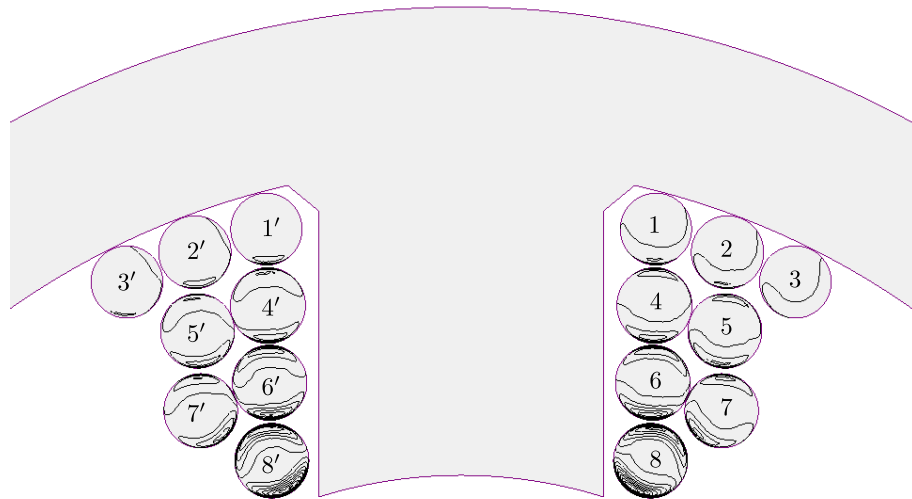


Figure 6.19: Current Density in the Conductors of a Coil Inside the Slot

Effect of Litz Wire on AC Winding Loss

The use of Litz wire can reduce the copper loss due to the skin effect, allowing it to be ignored as the conductor diameter is small in comparison to the skin depth [97]. In this case the diameter of the conductors is 0.2 mm compared to the skin depth of 0.14 mm. Therefore, copper loss due to skin effect can be ignored, therefore the total winding loss can be assumed to be equal to the DC winding loss. The use of Litz wire has one major disadvantage which is reduced utilisation of the slot area due to the woven structure, however in high frequency applications Litz is a requirement [112].

The current density in conductor 8 for a square wave of applied current has been plotted in Fig. 6.20. Results are shown assuming both a solid and stranded conductor. Conductor 8 has been chosen as it is closest to the airgap and influenced most by the proximity effect. It can be seen that in the case of a solid conductor, the proximity effect redistributed the current to a peak density of 470 A/mm². The peak occurs immediately after exciting the coil but settles down immediately. The same model considering a finely stranded Litz wire shows an even current density distribution equal to 16 A/mm² over the whole period of excitation.

The copper loss resulting from the proximity effect in each conductor is shown in Fig. 6.21. As expected, conductor 8 experiences the highest loss at 5.7 kW. However, using finely stranded Litz wire reduced the loss significantly. The ohmic loss is plotted in Fig. 6.22, showing each conductor has a uniform loss.

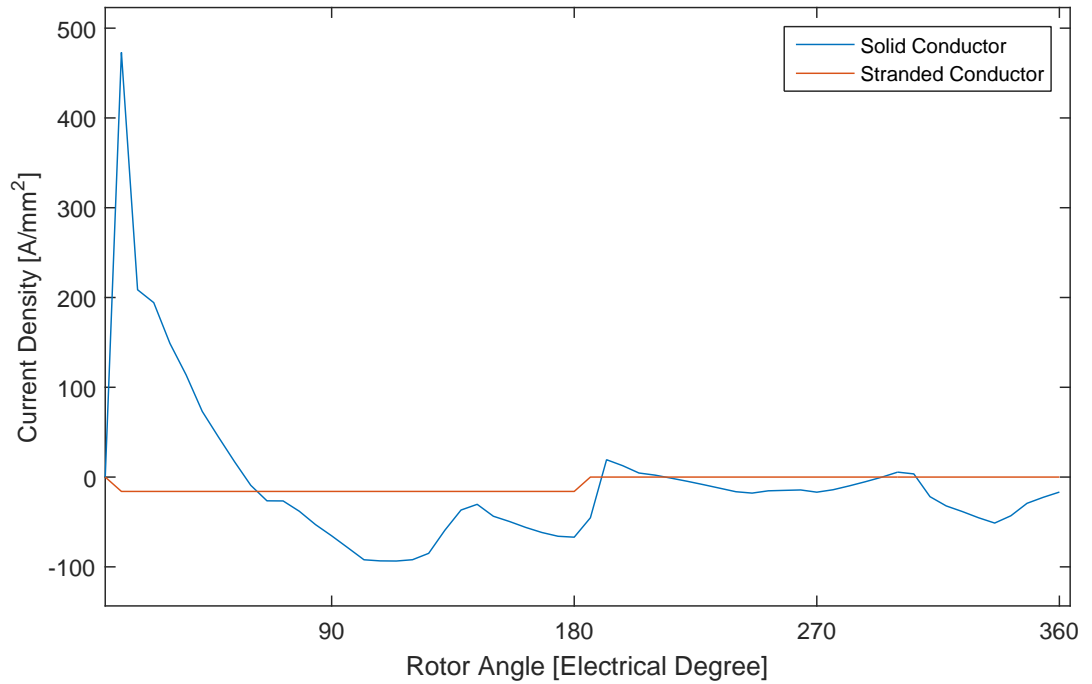


Figure 6.20: Comparison of Current Density in A Solid vs Finely Stranded Conductor

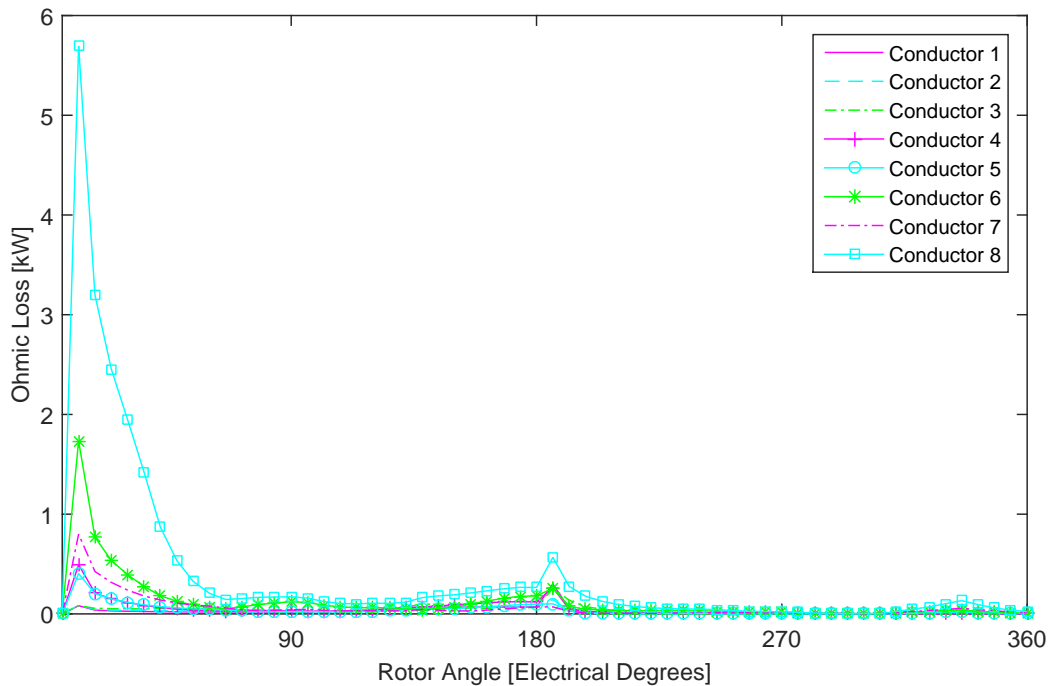


Figure 6.21: Ohmic Loss in the Solid Conductor

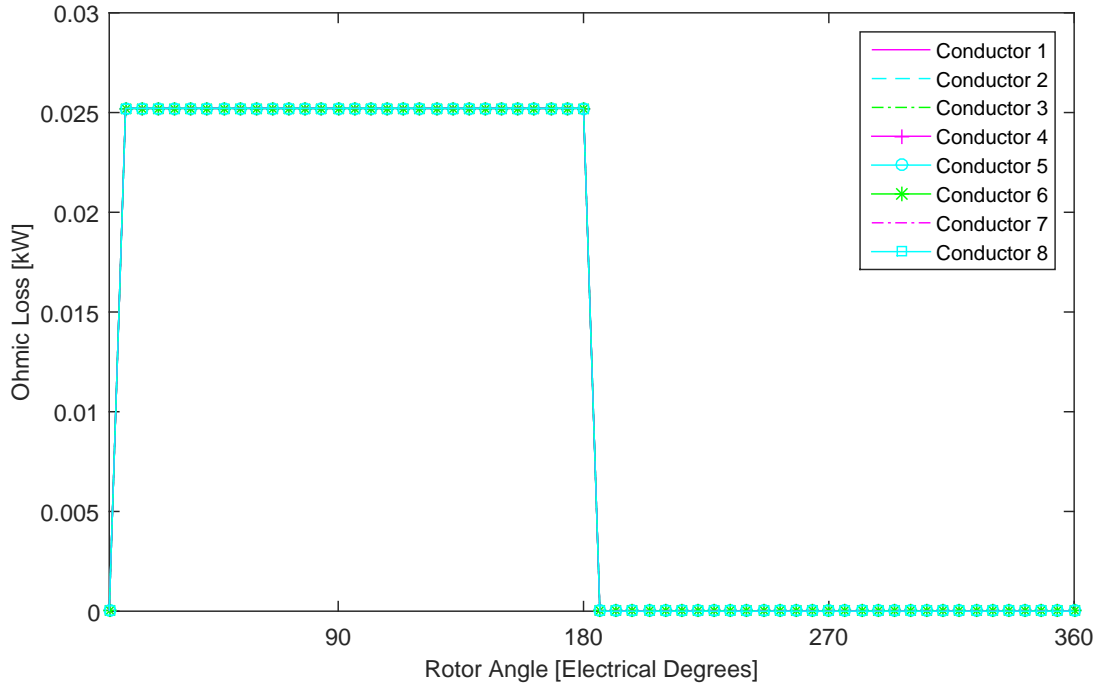


Figure 6.22: Ohmic Loss in the Finely Stranded Conductor

6.4.3 Iron Loss

The iron loss in machines, P_{Fe} with high rated switching frequencies is proportional to the square of peak flux density, B_{Peak} and the square of the fundamental frequency, f , as shown in Eq. (6.6).

$$P_{\text{Fe}} \propto f^2 B_{\text{Peak}}^2 \quad (6.6)$$

Hysteresis and eddy current losses are the main sources of iron loss in SRMs. For a given flux density the hysteresis losses increase linearly with frequency, whilst the eddy current losses increase with the square of the frequency. Traditionally, in order to address these losses laminated silicon-iron stator and rotors are used. The frequency of the machine is defined by the number of rotor poles, as a result fewer number of rotor poles will result in lower iron loss. The minimum rotor pole number for a three phase SRM (four poles) was considered for this work to reduce the fundamental frequency. Also, the electrical steel used for the rotor and stator were chosen from a low iron loss range. Hargreaves *et al.* in [113] say “more manufacturing processes equals more iron loss”, therefore, an increase in the iron loss due to the manufacturing process is inevitable.

6.4.4 Eddy Current at Tie Rods

From the electromagnetic aspect, saturation of the rotor lams around the tie rod cuttings and creation of eddy currents at the tie rods are some of the concerns of implementation of the flywheel structure. Fig. 6.23 demonstrates the magnetic field solution at full design speed. As it can be seen, the area of the tie rod cuttings that are in the flux path have started to saturate. However, when the rotor was completely at aligned position, the flux density did not exceed 1.7 T.

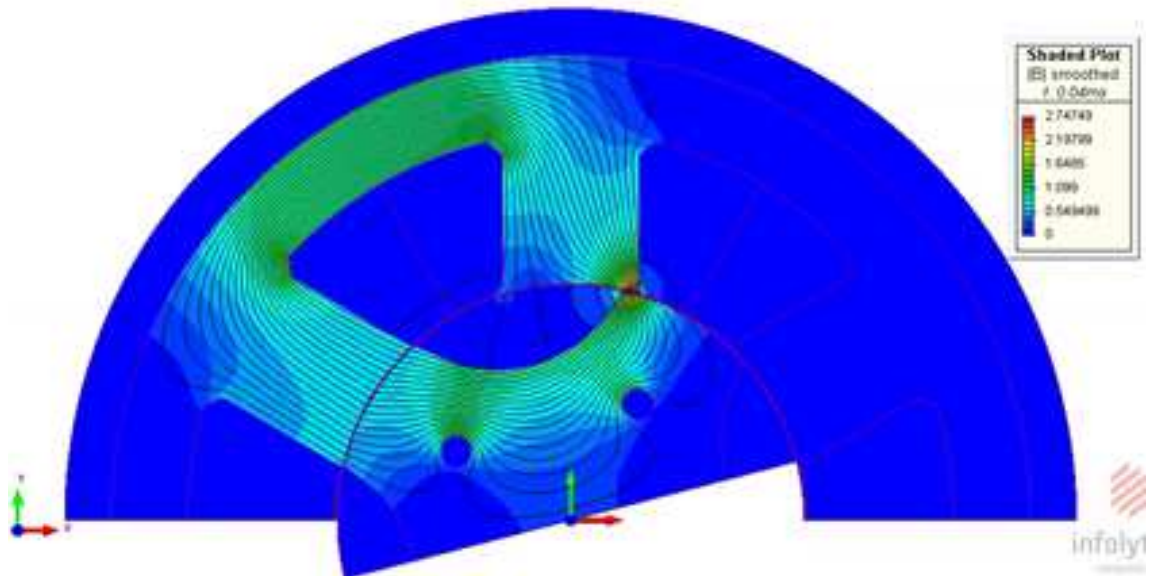


Figure 6.23: The Magnetic Field Solution at Full speed

Furthermore, despite using stainless steel for manufacturing the tie rods, which is a non-magnetic material, the conductive nature of the rods will still create possible paths for the eddy currents to flow. Fig. 6.24 presents the current density at the tie rods for one electric cycle. It can be seen that a maximum current density of 7.21 A/mm^2 was created. This underlines the necessity to use non conductive materials for tie rod manufacturing, such as high yield strength plastic or carbon fibre, to avoid excessive loss at the tie rods.

6.4.5 Windage Loss

SRMs also experience mechanical losses (bearing and windage loss) in addition to electromagnetic losses (iron and copper loss). In high speed SRMs the high viscous drag that appears in the air gap causes power loss, also known as windage loss.

The rotor saliency in SRMs leads to a windage loss higher than that normally found in other electric motors. Several approaches have been suggested to deal with this

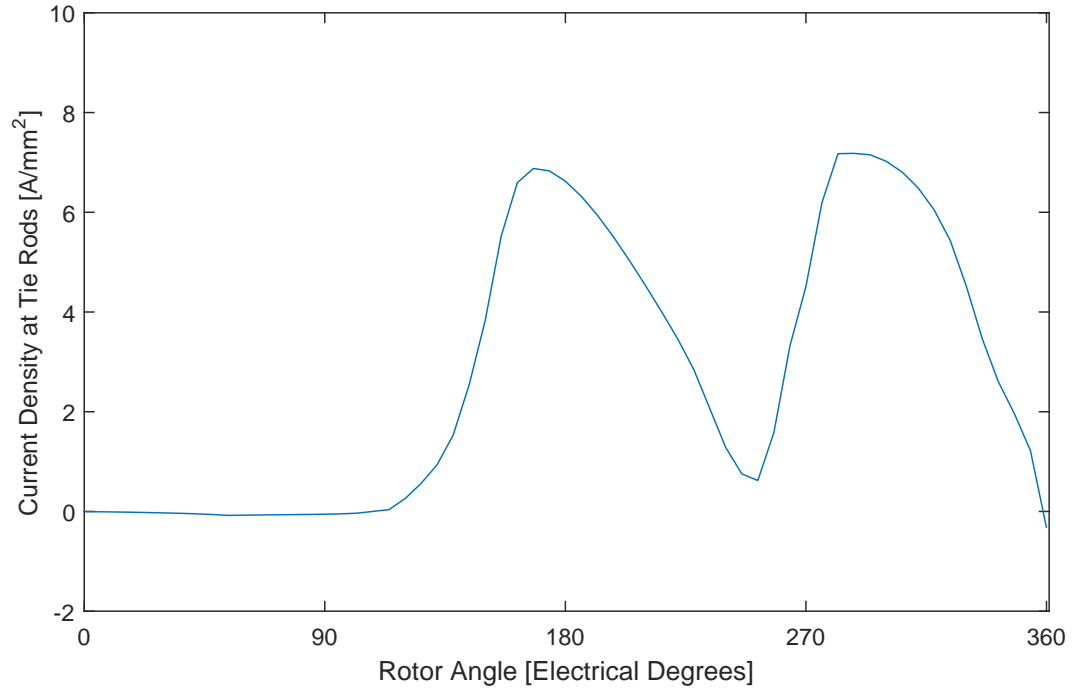


Figure 6.24: The Current Density Caused by the Eddy Current at Tie Rods

issue. Adding moulded epoxy in between the rotor poles is a possible approach. Although the performance of the motor even at high speeds is not compromised in this way, this approach adds a few more steps to the simple manufacturing process of a conventional SRM and hence increases the cost. Another approach is to add a rib in between adjacent rotor poles [114]. From aerodynamic point of view, this rotor resembles a cylindrical rotor hence the windage loss is dramatically reduced. However, this approach results in torque reduction especially if the ribs do not saturate fully, it also adds to the mechanical constraints.

The Reynolds number, R_e , is used to describe the drag coefficient at the surface of the rotor and can be expressed as Eq. (6.7). Where r_r is rotor radius, t is the air gap length and ω is the angular velocity, μ is the viscosity of air which is equal to $18 \mu\text{Pa}$, ρ_{air} is the density of air and is equal to 1.2 kg/m^3 at the room temperature and pressure [115].

$$R_e = \frac{r_r t \omega}{\frac{\mu}{\rho_{\text{air}}}} \quad (6.7)$$

The drag coefficient, C_d , is given in Eq. (6.8) [115].

$$\frac{1}{\sqrt{C_d}} = 2.04 + 1.768 \ln(R_e \sqrt{C_d}) \quad (6.8)$$

The Reynolds number increases in proportion to the angular velocity whilst the drag coefficient reduces. These two equations are important in determining the windage loss of a rotor. The windage loss for a cylindrically shaped rotor, P_w , is expressed by Eq. (6.9) [115].

$$P_w = \pi C_d \rho_{\text{air}} r_r^4 \omega^3 L_{\text{st}} \quad (6.9)$$

Where L_{st} is the stack length and ρ_{air} is the air density. Since the rotor of an SRM is not cylindrical an additional coefficient is required. Eq. (6.10) estimates the additional windage loss due to the pole saliency.

$$P_{\text{wp}} = (K - 1) \pi C_d \rho_{\text{air}} r_r^4 \omega^3 L_{\text{st}} \quad (6.10)$$

Where K is the salient pole coefficient given as a function of the rotor pole depth, H , and the rotor radius, r_r , in Eq. (6.11).

$$K = 8.5 \left(\frac{H}{r_r} \right) + 2.2 \approx 4.72 \quad (6.11)$$

According to the equations presented the saliency in this particular rotor, for the given rotor radius and rotor pole height, produces 3.72 times more windage loss compared to a cylindrical rotor with the same rotor radius [115]. The windage loss of the proposed rotor is presented in Fig. 6.25 where it is compared against the windage loss of the same outer radius cylindrical rotor. The calculations show a windage loss of 64.54 W and 5.214 kW (8.7% of output power) for the salient rotor, at the base speed of 10,000 rpm and full speed of 50,000 rpm, respectively. At full speed a cylindrical rotor would only produce 1.4 kW of windage loss (2.3% of output power), which shows the importance of applying windage reducing techniques and their effect on efficiency improvement.

In order to measure the mechanical loss (combination of the bearing and windage loss) of the SRM, without exciting the SRM coils, the shaft is rotated and the torque is measured using a torque transducer. The product of this measured shaft torque and the rotational velocity of the rotor gives the mechanical loss. Only the windage loss estimate obtained from the FEA method was considered for this work as the test set up was not suitable for this purpose.

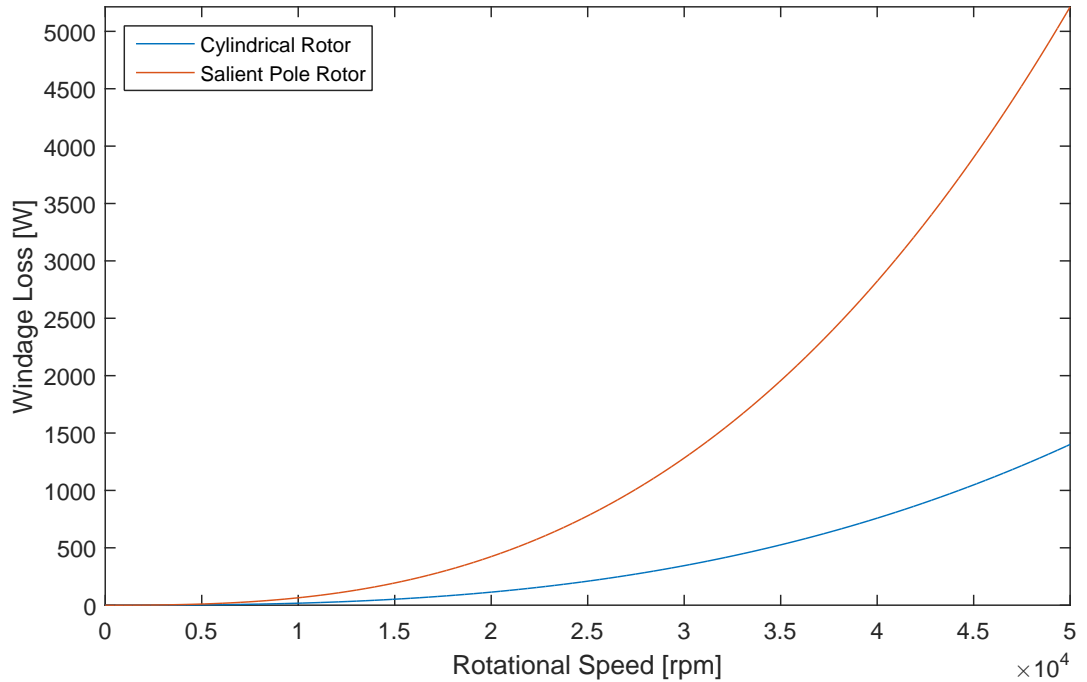


Figure 6.25: Windage Loss Comparison of a Cylindrical and Salient Pole Rotor

6.5 Efficiency Map

The efficiency, η , using the shaft output power, P_o , and the input electrical power, P_i , can be expressed as Eq. (6.12).

$$\eta = \frac{P_o}{P_i} \quad (6.12)$$

The resistance of a single turn of conductor, R_c , is calculated as 0.0464 m Ω . The total resistance of a single phase, R_p , is given by Eq. (6.15) where N is the number of turns of a coil of windings.

$$R_p = R_c \times (N)^2 \times \text{No. Coil per Phase} \quad (6.13)$$

$$= 0.0464 \times 10^{-3} \times 8^2 \times 2 \quad (6.14)$$

$$= 5.939 \text{ m}\Omega \quad (6.15)$$

For the copper loss component, only the DC copper loss is included in the efficiency calculation as the AC copper loss is considered negligible by using the Litz wire. Having the phase resistance, the DC winding loss is calculated using Eq. (6.1). The iron loss, made up of eddy current loss and hysteresis loss for both the stator

and rotor was obtained for every current and operational speed point using the FE model. At base speed, the rotor's total contribution to iron loss was 563.55 W, while the stator's total contribution was 1233.45 W. On the other hand at full speed, the rotor's and stator's total contribution to iron loss were 2170.56 W and 4220.52 W, respectively. As the majority of this loss is concentrated at the stator, use of a suitable liquid cooling system, preferably oil, can address the temperature rise caused by the iron loss at the stator. The liquid cooling can not be used on the rotor as it will give rise to the windage drag. Nevertheless the dissipated heat at the rotor can flow through the shaft. This makes implementation of a cooling system for the bearings even more necessary. The magnitude of the three major losses for base speed and full speed are given in Table 6.1.

Table 6.1: Loss Type Contribution at Base Speed and Full Speed with Full Power

Loss type	Symbol	Unit	Base Speed	Full Speed
DC Winding Loss	P_{cu}	kW	3.33	0.22
Iron Loss at Rotor	P_{rFe}	kW	563.54	2170.56
Iron Loss at Stator	P_{sFe}	kW	1233.45	4220.52
Total Iron Loss	P_{Fe}	kW	1.79	6.39
Windage Loss	P_{wp}	kW	0.06	5.21
Phase Current	I_{ph}	A	600	150

At base speed, the DC winding loss, the iron loss and the windage loss make up 64.2%, 34.5% and 1.3% of the total loss, making the DC copper loss the major contributor. At full speed, the DC winding loss, the iron loss and the windage loss make 1.8%, 54.1% and 44.1% of the total loss, making the iron loss the major contributor followed by the windage loss.

The calculated losses were used to calculate the efficiency map of the proposed machine which is presented in Fig. 6.26. The peak efficiency of the machine is 93.7% at 15,000 rpm, 60 kW with a torque of 36.6 Nm.

Fig. 6.27 shows how the efficiency map would look if windage loss reducing techniques were applied. The peak efficiency is increased to 94.0% at 17,500 rpm, 60 kW with a torque of 32.7 Nm. The areas with high efficiency have been increased, with the losses at high speed being reduced significantly.

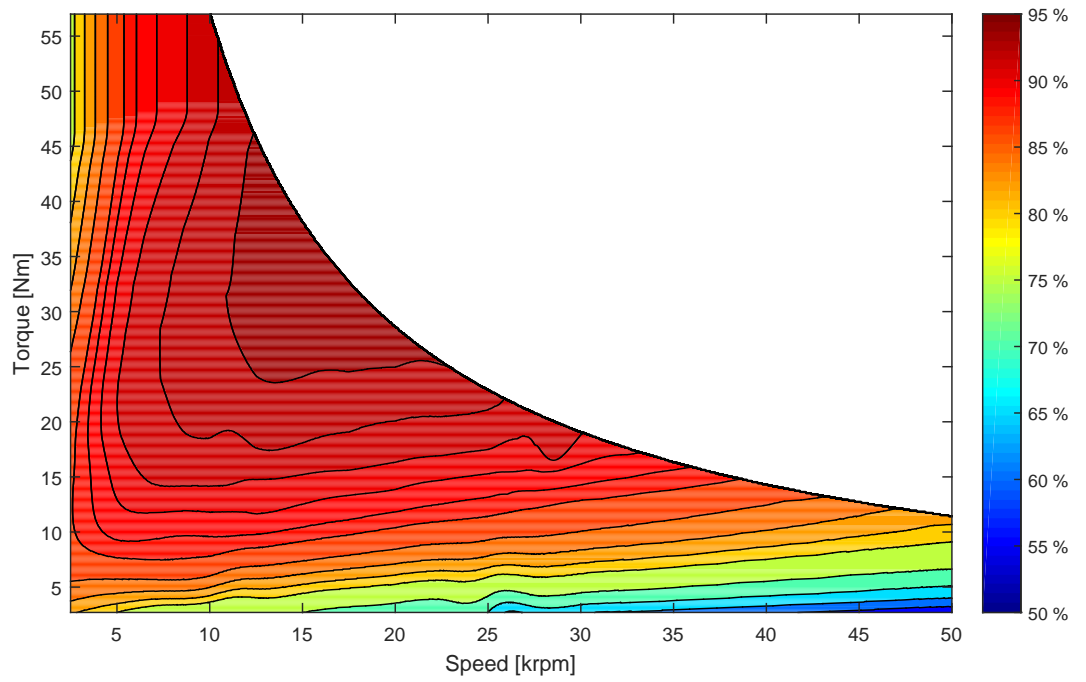


Figure 6.26: Efficiency Map Considering a Salient Pole Rotor

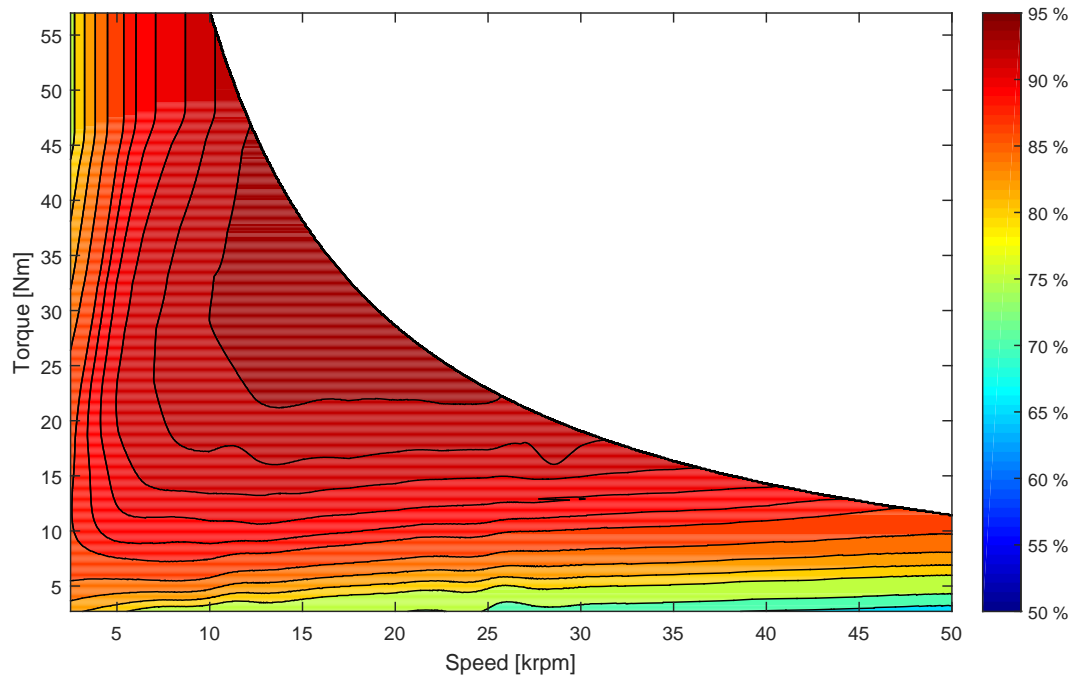


Figure 6.27: Efficiency Map Considering a Cylindrical Rotor

6.6 Conclusion

The electromagnetic behaviour of the motor has been analysed for various aspects of the motor. Peak torques of 66.00 Nm and 63.77 Nm were calculated from the 2D and 3D FEA of static models, respectively. The 3.3% difference being due to inherent calculations errors of FEA rising from different meshing methods as well as the end winding erect. Static models are very useful at the early stages of the design process as they save computation time whilst providing reliable results. 2D FEA was used to study all the other electromagnetic aspects. An average torque of 55.6 Nm is achieved from the 2D dynamic simulation.

Simulations were used to analyse the major electromagnetic aspects of the operation such as the ohmic loss, the AC winding loss, the skin effect and the proximity effect. The DC winding loss for the full rated current was calculated to be 3.3 kW for the winding design using Litz wire.

AC winding loss increases significantly with frequency operation, due to the skin effect and the proximity loss. The skin depth of the copper is 1.14 mm at 50,000 rpm (833.33 Hz). By choosing a finely stranded Litz wire, with a strand radius of 0.2 mm, the waste of copper due to skin effect is prevented. Further analysis was carried out to identify the iron losses of the motor, showing a loss of 1.79 kW and 6.39 kW at the base speed and full speed, respectively.

The windage loss in a toothed rotor is higher than other purely cylindrical electric motors and dramatically increases with speed as it is in proportion to the speed cubed. Analytical calculations show a windage loss of 5.21 kW at the full speed of 50,000 rpm, which could be reduced, by for example filling the rotor gaps with epoxy, to 1.79 kW.

The calculated losses were used to create an efficiency map for the motor which shows a peak efficiency of 93.7% at 15,000 rpm, 60 kW with a torque of 36.6 Nm.

In conclusion, an SRM was presented in this work which can produce 56 Nm while being capable of running up to 50,000 rpm, resulting in an output power of 60 kW.

Chapter 7

Prototype Construction

In this chapter the construction of the high speed SRM is presented. First the process of building the stator is discussed. Whilst, a common technique is used to construct the stator laminates, an alternative technique was required to shape the coils and mount them on the stator teeth. This technique provided a satisfactory fill factor with the potential for an increased fill factor.

Secondly, the more complex construction of the prototype rotors for the static and spin test are then presented; one with an aligning central shaft and one without. Due to their high operational speed, special attention is given to mechanical precision required.

7.1 Static Test Prototype

It is possible to ascertain most of the machine performance from static test. The university has no suitable test chamber available to test the motor at 50,000 rpm. There was also the lack of a suitable drive for a dynamic test for this machine. Despite the simple SRM rotor structure, new construction techniques were developed to meet the requirements of high speed operation. The detailed construction process follows.

7.1.1 Stator Laminations

The lamination stack was created using electrical discharge machining (EDM) otherwise known as wire erosion. The stator lamination material is grade NO20, a non-oriented, fully processed electrical steel with a 1 μm coating of Suralac7000 insulating coating on each side. The material is supplied in 2 m \times 1 m sheets, which were cut to 240 mm square in order to fit in the wire erosion machine. As the thickness of each sheet is 0.2 mm, to construct a 95 mm long stack, 475 sheets

were required. No bonding or glue was used in the stator lamination stack instead a keyway in the case and on the laminations was sufficient for them to retain their position. Glue can also inhibit the wire erosion process as it is non-conductive and without it the stacking factor of the laminations was 99%. The complete stack of 475 laminations was cut in one operation, once cut each stator lamination was cleaned to remove corrosion caused during EDM. A single stator laminate is shown in Fig. 7.1.



Figure 7.1: One Stator Laminate

In order to ensure axial alignment and a high stacking factor, the laminations were compressed in a hydraulic press to a pressure of 4 tonnes. The finished stator was placed inside the case as shown in Fig. 7.2.

Finally, to secure the lamination stack to the case, a locking ring was used between the stack and the machine end cap, as shown in Fig. 7.3. The design of the ring allows enough space for the end winding while keeping the laminates in place.



Figure 7.2: Stack of Stator Lamination in the Case



Figure 7.3: Stator Lamination Lock Ring

7.1.2 Slot Insulation

Sheets of Nomex aramid thermal insulation paper with a thickness of 0.25 mm and a maximum operating temperature of 300°C were placed inside the slot before inserting the coils. The sheets were cut to leave enough over hang to wrap completely around the coil in the slot, and into the gap between adjacent coils sharing the same slot. Plastic slot wedges (Tufnol) were slid into the stator tooth opening to provide a barrier between the coils and the air gap.

7.1.3 Coils

In Section 4.2.4 the design of the Litz wire was explained in detail. Manufacturing the coils using this wire proved to be more difficult than expected. The issue was down to the thickness of the wire and the small slot area and small slot opening demanding an alternative technique to simple hand winding to achieve the required fill factor.

It is common when making prototypes to manufacture the windings by feeding them through the slots and around the stator teeth by hand. This technique was ruled out for several reasons. First, the slot area and the available space inside the stator bore was too small for the technician's or author's hand to fit in and move freely whilst holding the wire. Second, the thickness of the Litz wire caused it to create large bows when bent around the corners, creating long end windings. These bows would extend inside the slot wasting the slot space.

Finally, pressing the finished coil turned out to be a vital stage of manufacturing the coil by removing the air within the strands and ensuring the goal fill factor, which can not be achieved by mere hand winding.

As a result, it was decided to press and then hand wind the coils in order to achieve the best possible fill factor. A set of bobbin jigs were made with a rectangular profile. The longest side of the rectangle was equal to the slot depth and the shortest side was equal to the half of the slot opening ensuring that two coils made using this jig would pass through the slot opening. The parts of the bobbin jig are shown in Fig. 7.4. The rectangular profile area of the jig was large enough to fit 5 of the required 8 turns in.

The inside of the bobbin was covered with mould release in order to ensure easy release of the cured coils. The structure was then secured in place in a lathe. The coil could then be wound by rotating the bobbin around its centre whilst one end of the wire was held tight over it with the other end being fed through the system, which also made it easy to count the turn numbers. Each row of wire was covered with a two part epoxy resin, consisting of Araldite LY 5052 epoxy and Aradur 5052



Figure 7.4: Coil Forming Bobbin

hardener. The low viscosity of the resin allowed it to reach all the surfaces inside the Litz wire giving a solid finish.

Next, the whole coil was wrapped inside several layers of electric tape in order to keep the wires in place until the glue set. The jig was completed with two parts either side of the coil which were pushed in place and secured using clamps, applying a compressive force to the coils. Afterwards, the assembled bobbin was placed under 4 tonnes of pressure in a hydraulic press overnight whilst the resin set, the pressure removed a significant amount of air within the Litz wire strands.

Finally, the electric tape and the bobbin jigs were manually removed from the coil before mounting the coil on the stator tooth. Using this technique resulted in block form coils that could be slipped onto the stator teeth over the insulation. The resulting coil is shown in Fig. 7.5.

Once all 6 coils were pressed, they were checked visually for any sign of damage to the wire or the enamel, if no faults were detected then it could be mounted on the stator. Once all coils were mounted slot wedges were inserted into the stator tooth grooves in order to hold the coils in place. These strips were cut from glass fibre laminated plastic (Tufnol) with a thickness of 1.5 mm. Once all 6 coils were secured in place, the remaining 3 turns were added to each coil by hand by feeding the end of the cable through the space in between each two coils. This process was repeated three times, filling the triangular space in between the coils until the goal of 8 turns was reached.

As it was essential to monitor the thermal behaviour of the coils, 3 thermocouples were added in order to monitor the temperature inside the coils. These

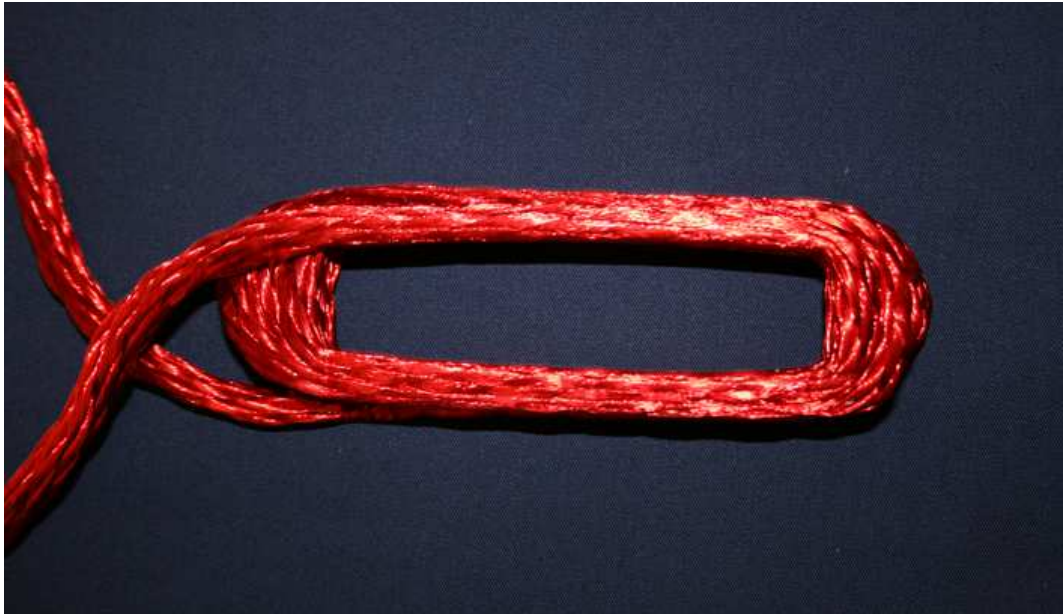


Figure 7.5: Pressed Coil with 5 Turns

thermocouples are PTFE insulated with an exposed welded tip suitable between.

One of the thermocouples was inserted inside the coil during the pressing stage to monitor the temperature inside the coil, one was placed in between two coils occupying one slot in order to monitor the temperature rise in the middle of the slot and the last was placed on the over hanging wire to monitor the thermal behaviour of the end winding.

The goal fill factor of 40% was ensured using this process. It is believed with more practice and improved design of the bobbins or by pressing 5.5 turns it would be possible to achieve 9 turns (a fill factor of 45%). Fig. 7.6 shows the finished coils mounted on the stator coils, the Nomex in between the coils and Tufnol slot wedges can be seen.

In the next stage, in order to stop the end winding from falling into the rotor bore, each was individually secured using tying cords. The ends of the coils were placed in heat shrink cable sleeving tubes to protect the enamel from any damage caused by handling. As can be seen in Fig. 7.7 all the terminations of the coils came out from one end in order to keep the manufacturing of the end caps and the set-up of the test rig simple.

Whilst on the static test rig the coils of diametrically opposed stator poles were connected in series, as illustrated in Fig. 7.8, which in turn would allow one complete phase to be excited for the purpose of the static test.



Figure 7.6: Coils, Nomex and Tufnol Insulations



Figure 7.7: Tying Cords, Heat Shrinks and Thermal Coupling

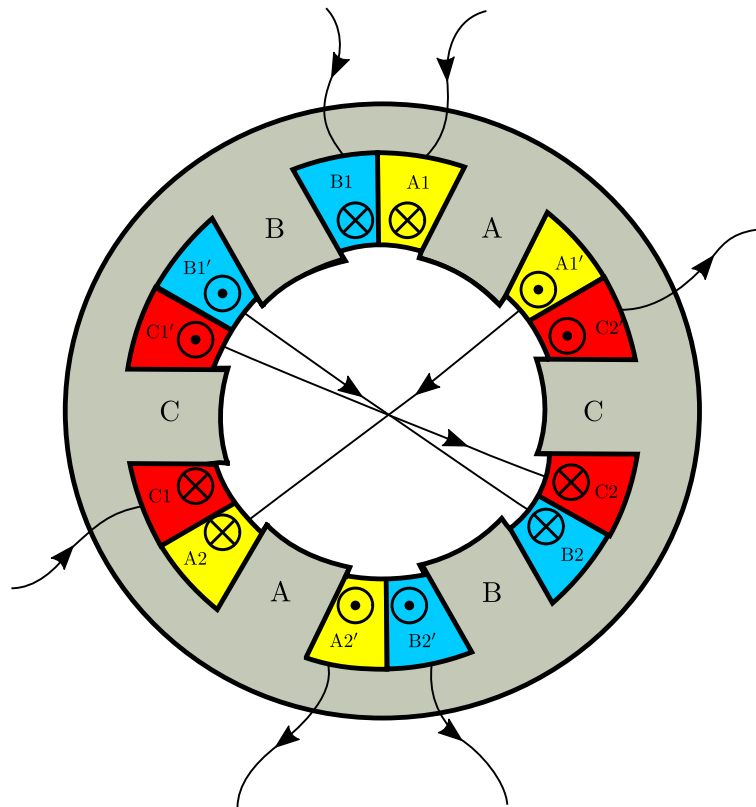


Figure 7.8: Phase Winding Series Connection

7.1.4 Rotor Laminations

A stack of M250-35HS non-oriented, fully processed lamination electrical steel sheets was used for manufacturing the rotor. This grade of electrical steel is particularly suited for high speed applications, having a high yield strength. As with the stator laminations, each side is coated with a $1 \mu\text{m}$ layer of Suralac7000 insulation.

In order to build a 95 mm stack, 68 sheets of this 0.35 mm thick lamination were required with four rotor segments cut from each of the sheets and stacked together to produce the final rotor axial length. A smaller stack height was used as in this case the stacks were glued. This is included in order to ensure flatness of the rotor as will now be discussed, but makes it more difficult to wire erode such a large stack.

Laminations are not perfectly smooth and cannot be guaranteed to be even in thickness, neither will the coatings be of uniform thickness. This non-uniformity can accumulate, resulting in a lamination stack that is not flat. To address this issue, half of the rectangular sheets were cut in one orientation with the rest rotated by 90 degrees. The final stack could then be made by stacking these alternately in order to randomise non-uniformity.

Gluing of the stacks using Ultimeg 2002 epoxy resin was used as a second measure to ensure rotor flatness. The stack of 68 laminations was clamped in between two aluminium plates with four spacers of 22.75 mm length to set the height of the stack. The stack was placed in the oven at 300 °C for three hours for the glue to cure. From resulting block four rotor biscuits were cut using EDM, these could then be stacked together to produce the final rotor lamination stack. The rotor laminations were cut with a radius 1 mm larger than required for the finished machine. The extra material could then be skimmed later to ensure the concentricity of the rotor. This process was carried out once for the rotor without the central shaft, and a second time with a 10 mm diameter shaft hole. One cut laminate of each rotor is presented in Fig. 7.9a and Fig. 7.9b for the rotor with and without the central shaft, respectively.



(a) Rotor Laminate without the Shaft Hole (b) Rotor Laminate with a Shaft Hole

Figure 7.9: One rotor Laminate of Each Rotor Topology

7.1.5 Cheek Plates

The cheek plates were made from a 76.20 mm diameter cylinder of austenitic, nitrogen strengthened nickel alloyed stainless steel bar (grade Nitronic 50 annealed ASTM A276/ASTM A479). This is material with high mechanical strength and reasonable machinability. A CNC milling machine and EDM were used to manufacture the cheek plates. The sharp corner where the shaft of the cheek plate meets the end plate itself was carefully machined with a large fillet radius in order to reduce stress in this area. The mechanical analysis indicates a negligible effect of applying corner radii. A cheek plate can be seen in Fig. 7.10, the four holes for the tie rods can be seen along with space for the nuts to sit such that they do not protrude out from the cheek plates.



Figure 7.10: Fully Manufactured Cheek Plate

Bearing Locating Ring

The addition of a fillet on the base of the shaft on the cheek plate required the addition of a flat surface for the bearing to accurately locate. A 5 mm thick ring was manufactured with a 5 mm radius on one side, equal to the size of the cheek plate fillet. The outer diameter of the part of this ring that touches the bearing was equal to the outer diameter of the bearing inner ring to avoid any friction between the balls and the ring. As can be seen from Fig. 7.11 this is achieved by making a step on the flat side of the ring leaving an outer diameter of 24 mm on that side.

7.1.6 Tie Rods

The tie rods, which are shown in Fig. 7.12, and the small aligning shaft were manufactured from grade A286 solution annealed aged ground steel. The tie rods were manufactured from a 600 mm long bar of diameter 8.19 mm. The required 6 mm diameter was obtained using a centre-less grinding technique, the tie rods were then cut to as length of 150 mm. Using the CNC machine, an M6 thread with 1 mm pitch and 0.6 mm depth was added to the either end of the tie rods.

The locating shaft was made from a 200 mm long bar of diameter 11.36 mm, which was ground to 10 mm.



Figure 7.11: Bearing Locating Ring on the Rotor



Figure 7.12: Rotor Tie Rods

7.1.7 Rotor Assembly

The rotor components were assembled and the structure placed in a lathe to add the final touches to the rotor components. However, at this point the shafts of the cheek plates could not be made to align and each shaft was nearly 1 mm off centre. This was caused by the construction process and due to the strain that was put on the tie rods during the assembly process. Therefore, manufacturing the rotor required further refinement as described in the following section.

In order to address the alignment issue, it was decided not to fully finish the construction of the rotor components before assembling them.

Cheek Plates Manufacturing Ensuring Rotor Alignment

In the second attempt, the cheek plates were made using the CNC and the lathe, however, the extending shaft was not machined to the exact diameter, instead having a 1mm larger diameter. The front and back view of this cheek plate is presented in Fig. 7.13a and Fig. 7.13b, respectively.

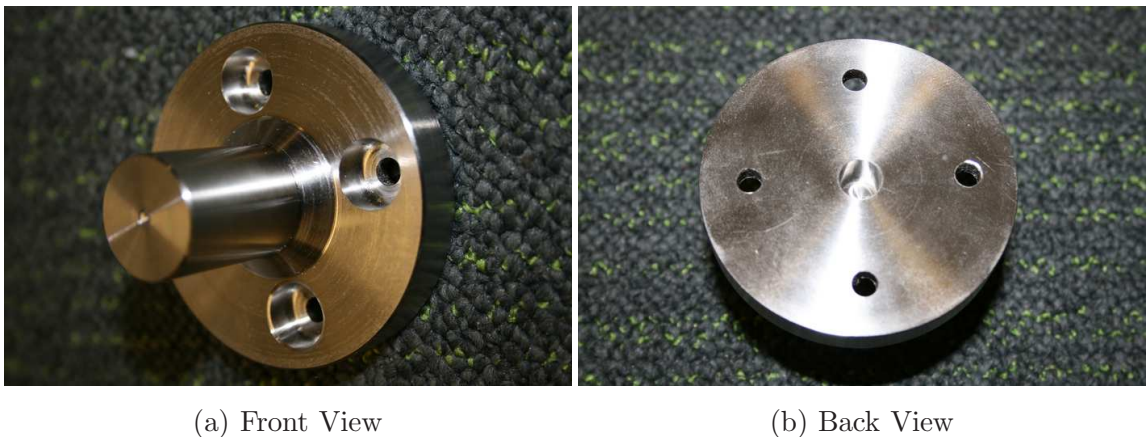


Figure 7.13: Roughly Made Cheek Plate

In the next stage, the laminations and cheek plates were mounted on the tie rods. The threads were added in a way to allow them to extend 2 mm inside the cheek plate. This will give a margin for the nut to fasten tight enough and press the cheek plates along with the laminates, which in turn leads to a robust structure for the rotor. The rotor was placed in lathe and turned to remove the excess 1 mm from the lamination diameter to bring it to the correct size. The cheek plate's shaft was then turned down to 20 mm diameter. Following this technique allowed the rotor to turn true to the centre and facilitated the alignment of all of the rotor components.

Bearing System Assembly

The bearing locating rings were then mounted on the shaft. Fig. 7.14a and Fig. 7.14b show the side view and the top view of the final result, respectively.



(a) Assembled Bearing Placing Ring

(b) Rotor Side View

Figure 7.14: Static Rotor

In the next stage, the bearing was mounted on with a transition fit. This structure, as shown in Fig. 7.15, was ready to be mounted into the end caps in the case.



Figure 7.15: Bearing Assembled On the Rotor

7.2 Modified Construction for Spin Testing

At this stage two rotors were manufactured in order to compare the alignment of the cheek plates and the rotor lamination stack. The first had a 10 mm diameter central locating shaft and the second no shaft at all, with all other features being identical.

For the spin tests the load side of the rotor shafts had to be turned to 5 mm diameter and 15mm long. This was to allow mounting the compressor wheel which will be explained later. An aluminium housing was made for the rotor to sit in, combined with two end plates which together act as a dummy stator.

7.2.1 Soft Mounting Bearing

As explained in the previous chapters, if the rotor is accelerated fast enough, it can pass over the first rock and bounce vibration modes. Research shows soft mounting the bearings can drastically reduce the frequencies of the rock and bounce vibration modes, facilitating quick transition over them.

The soft mounting was implemented by adding an O’ring around the bearing. A Viton 75-compound O’ring with an outer diameter of 61 mm, inner diameter of 55.25 mm and a cross section area of 2.3 mm was obtained.

Two bearing housings were manufactured for each bearing, each of the bearings sits in the centre of the housing with two O’rings wrapped around the outside of each housing. As can be seen in Fig. 7.16, the O’rings were placed inside two grooves on the outer surface of the housing. The O’rings were compressed between the housing and the end caps to 75% of their cross section in order to adjust the stiffness of the bearing system.

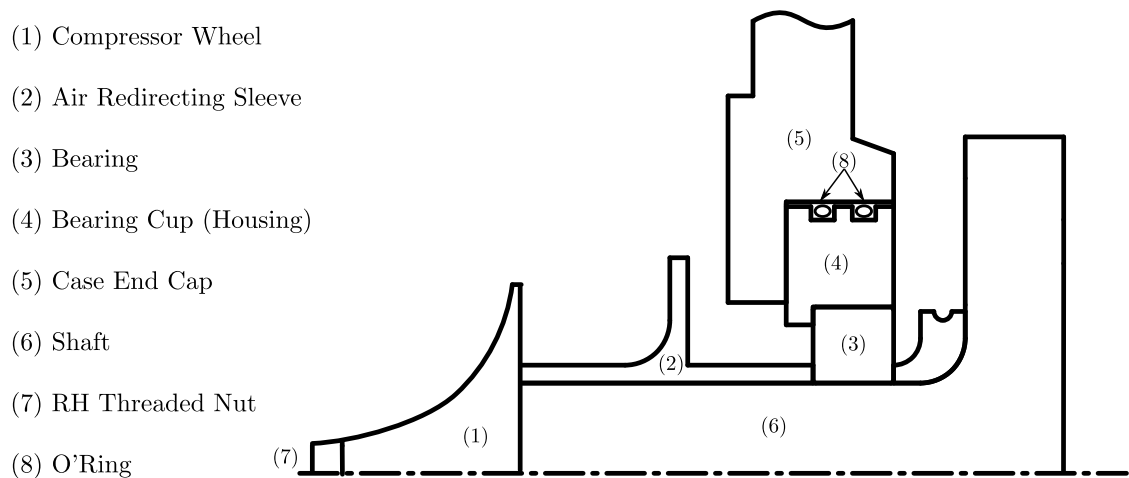


Figure 7.16: Soft Mounted Bearing System

7.2.2 Probes

Three different types of probes were to be used during the spin test; a magnetic encoder, a thermocouple and an accelerometer. The magnet used by the encoder was mounted on a hole drilled into the non-load side of the rotor shaft. The encoder was bolted on the case end cap observing the required distance from magnet advised by the manufacturer.

It is necessary to monitor the bearing temperature as high temperatures lead to bearing failure. A thermocouple probe was potted in to the side of bearing cups so it was in contact with the outer race of the bearing.

Finally, to measure the vibrational frequencies of the rotation, an accelerometer has been placed as close as possible to the bearing. A long stud was manufactured that was screwed into a threaded hole on one of the bearing housing parts. One end of the stud sits directly on the outer race of the bearing with the accelerometer probe screwed to the other end. Fig. 7.17 and Fig. 7.18 show the final assembly of the high speed prototype rotor from different angles.



Figure 7.17: Fitted Magnet on the Rotor Shaft, Potted Thermocouple and Accelerometer Stud



Figure 7.18: Fitted O’rings on the Bearing Cups

7.2.3 Balancing

The high speed of the machine demands professional balancing of the rotor. First, the balance quality grade was determined by using a lookup table. The balance quality grades are classed based on the motor application. After consulting with the balancing company and considering the weight and size of the rotor a G1.0 grade was selected. Next, using a second look up table, the maximum permissible residual unbalance (from ISO 1940/1) was determined for the possible over speed of 60,000 rpm. A $0.2 \mu\text{m}$ centre of gravity displacement was identified for design speed of the rotor. This information was used to balance the rotor which was carried out by a professional balancing company. Material was removed from the cheek plates of the motor to provide the balance, the resulting rotors showed minimal sign of alteration, validating the manufacturing techniques that were implemented to ensure alignment for rotor components.

7.2.4 Spin Test Drive Technique

London City University agreed to carry out the spin test using their high speed test chamber. The test rig uses compressed air as the prime mover for the high speed test. In this way, the rotor can spin up without requiring an electric load. As a

result, there is no need for the stator, instead a cylindrical tube was built to act as a dummy stator to maintain the air gap size and provide protection in case of a failure.

An air compressor drives the machine. Compressed air can be controlled to allow limited pressure over a limited period of time, providing a controlled drive for the spin test. If the mounted compressor runs in reverse, it will act as an air turbine. For this, the compressed air is fed from the exhaust and let out from the inlet tube. Fig. 7.19 shows the compressor volute.



Figure 7.19: Volute of The Compressor Wheel, The Side Tube is Exhaust and the Middle One is the Inlet.

The compressor wheel has an outer diameter of 41 mm and a 4 mm diameter shaft, it is capable of running at 250,000 rpm. However, mounting the compressor wheel required extra attention.

As the compressor wheel has a low mass, it has been mounted directly to the rotor shaft, and overhung from the bearings without causing any rotor dynamic problems. A 5 mm diameter hole was drilled at the center of the wheel. The nose of the wheel was ‘faced off’ to make it shorter and allow more material for a connecting nut. The wheel was then locked to the shaft with a right hand threaded nut and glued using Loctite.

The turbine volute was mounted directly onto the end caps of the dummy stator. Fig. 7.20 shows an air redirection sleeve that was placed between the bearing and the

compressor wheel. The sleeve serves two purposes; first the curved surface guides the compressed air out to the atmosphere providing extra protection for the bearing, and second the cylindrical part locks the bearing in place stopping it from wobbling. The assembled system was used for the spin test at the City University.



Figure 7.20: Air Redirection Sleeve

7.3 Case and End Caps for Static Test

The case and the end caps are machined from grade AW6082-T6 Aluminium alloy using a lathe and a CNC milling machine. The end caps were covered with slot lining paper in order to provide insulation from the end winding.

7.4 Final Assembly

With one end cap bolted to the stator the pre-load washer was inserted into the cavity for the bearing. The complete rotor assembly including bearings was then mounted into the case, with the second end cap placed on the case. The second end cap was manufactured in such a way as to allow the coil terminations to come out of the case on one side. A disk was manufactured from black nylon in order to provide a platform for the coil terminations to connect to the power supply to. The

coil terminations were clamped using M6 bolts and screwed to the inner side of the plate. Finally, the plate was mounted on the end cap and the end cap is screwed to the case.

The motor was mounted on the test rig as can be seen Fig. 7.21, where the torque transducer and the rotary table can be seen connected to the motor.

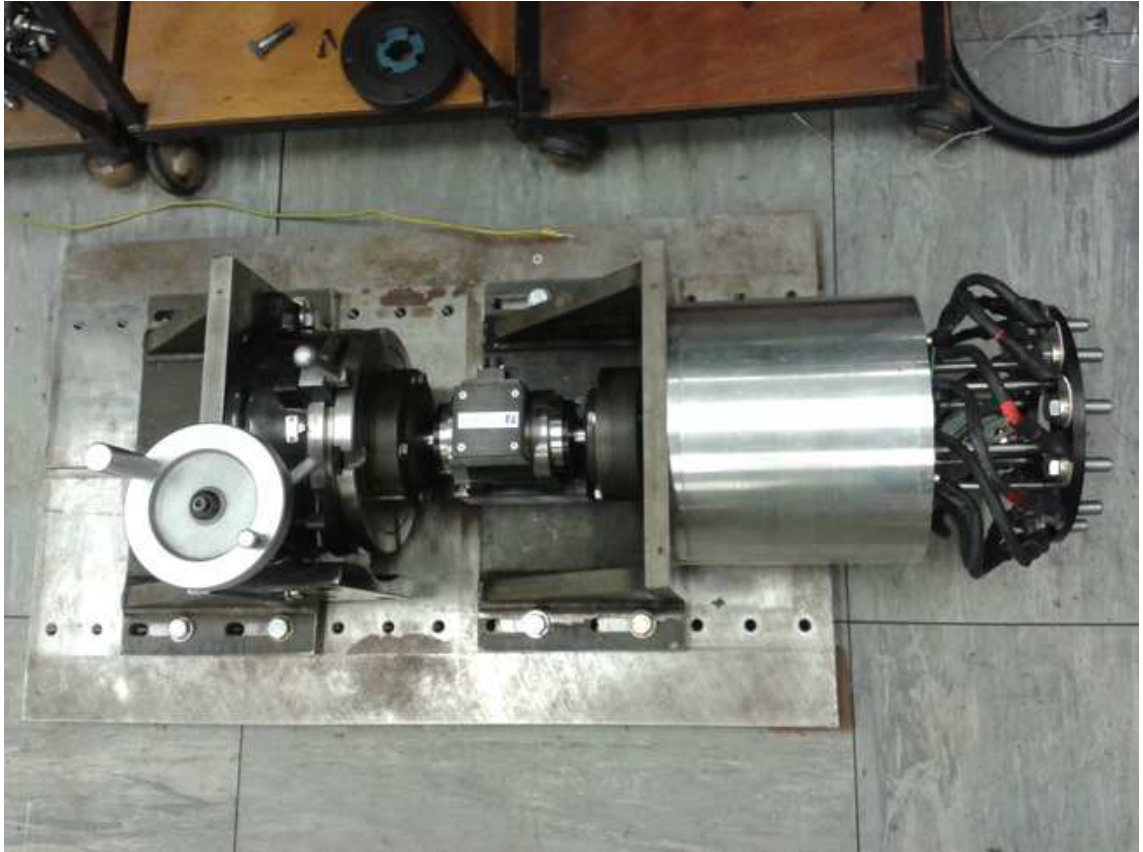


Figure 7.21: Static Test Rig

7.5 Conclusion

The manufacture of the two high speed rotors using the flywheel type technology has been presented, the rotors are similar, apart from the addition of a 10 mm central shaft.

The high operational speed required careful manufacture of the rotor. In order to achieve a uniform thickness on the rotor lamination stack, the laminates were stacked in alternating directions and then glued to a specified height.

It was found that fully manufacturing the rotor components separately and then assembling did not give a satisfactory result, due to mis-alignment of the cheek plates. As a result, the laminates were cut with an extra millimetre on their

diameter, the cheek plates were partially made, and all of the rotor components were assembled on the lathe. The rotor was then finished on the lathe, resulting in an assembly with good alignment.

Manufacturing the stator proved to be more simple, with no glue and the whole stator was cut in a single operation from a stack of NO20 using EDM.

Having a non-segmented stator, however, made the winding process more difficult. A completely pre-made and pressed coil was not suitable due to the small slot opening. Furthermore, the use of Litz wire made it difficult to hand wind the coils whilst achieving an acceptable fill. As a compromise 5 turns were wound around a bobbin and pressed using a hydraulic press. The resulting coils were then mounted on the insulated stator teeth. The remaining 3 turns were then hand wound and a fill factor of 40% was achieved. However, it is believed that further development and more accurate pressed coils can increase the fill factor to 45%.

Chapter 8

Testing and Analysis

In previous chapters the design methodology of a high speed, high power SRM was presented. The electromagnetic behaviour of the proposed motor was simulated focusing on the output torque and the increased losses that are caused by running at high speeds.

The mechanical constraints imposed on a high speed rotor, caused by the centripetal force, were investigated and the maximum mechanical stress imposed on the rotor and the vibration frequencies calculated.

In this chapter a series of tests are presented which were designed to investigate the operation of the motor and verify the results of the FEA. The tests are divided into two sections: electromagnetic and mechanical tests.

To test torque production a static test rig was set up at Newcastle University. The static test results are used to prove the output torque value obtained from the simulations, by creating a torque vs rotor position profile. Flux linkage vs current curves have also been created to be compared to the simulation data from design verification. The thermal performance of the motor was tested to ascertain the thermal torque limit.

A flywheel topology is used for the rotor which leads to reduction of the mechanical stresses and particularly the hoop stress. The mechanical test is used to investigate the feasibility of the novel approach to the rotor topology. The mechanical part of the tests was run at the high speed test chamber of London City University as part of the VESI project.

8.1 Electromagnetic Tests

To verify the torque and thermal properties of the machine a series of static tests were carried out:

- Measurement of DC resistance.
- Flux linkage with respect to rotor position and current.
- Static torque with respect to current and rotor position.
- Temperature rise in various points of windings with respect to time.

The results of these tests have been used to verify the design process and to provide confidence in any future research following this work.

In order to test the torque of the motor a static torque test rig was required. The test rig consisted of a rotary table dividing head, coupled to a 100 Nm Magtrol torque transducer, which was then connected to the shaft of the machine. The rotary table allows fine position adjustment of the rotor position. The torque transducer is accurate to within 0.01% of its rated value and therefore can provide a very accurate torque measurement at the rated torque of 56 Nm. The output of the torque transducer is a 0-5 V signal, which was fed into a data acquisition unit, along with the current measured via a current clamp. The torque and current are logged by the acquisition unit at every test point. All the required equipment was connected considering the safety measures suggested by the manufacturers and required by the university. The full set up schematic can be seen in Fig. 8.1 while Fig. 8.2 shows the rotor mounted on the base plate, whilst coupled to the rotary table via the torque transducer. The procedure and results of each test are as follows.

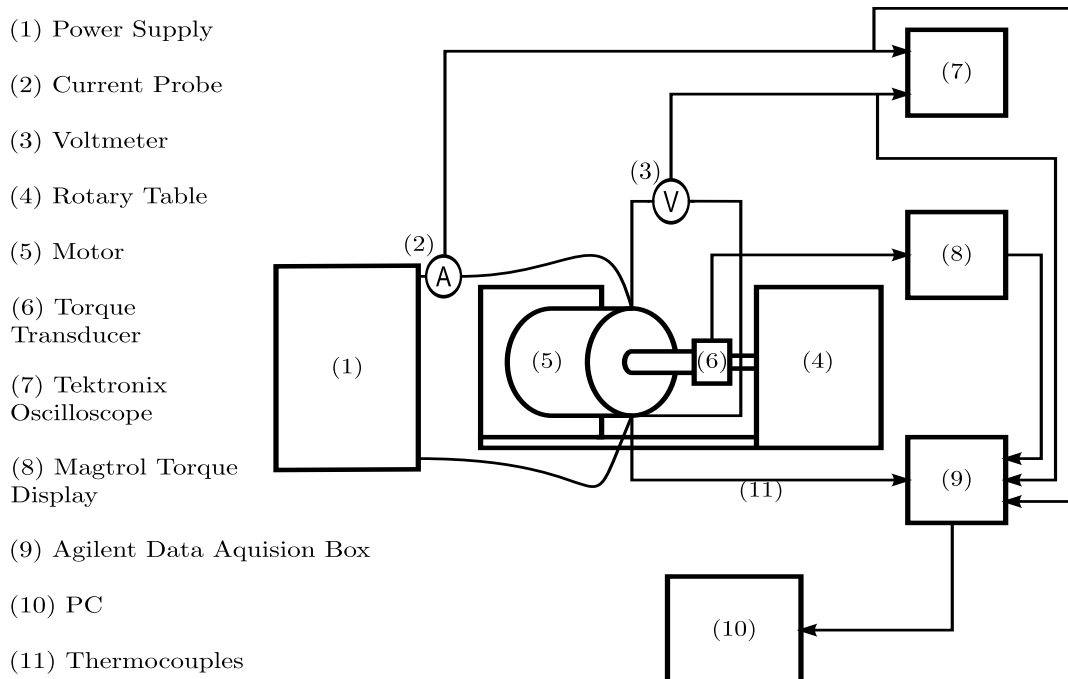


Figure 8.1: Static Test Set Up

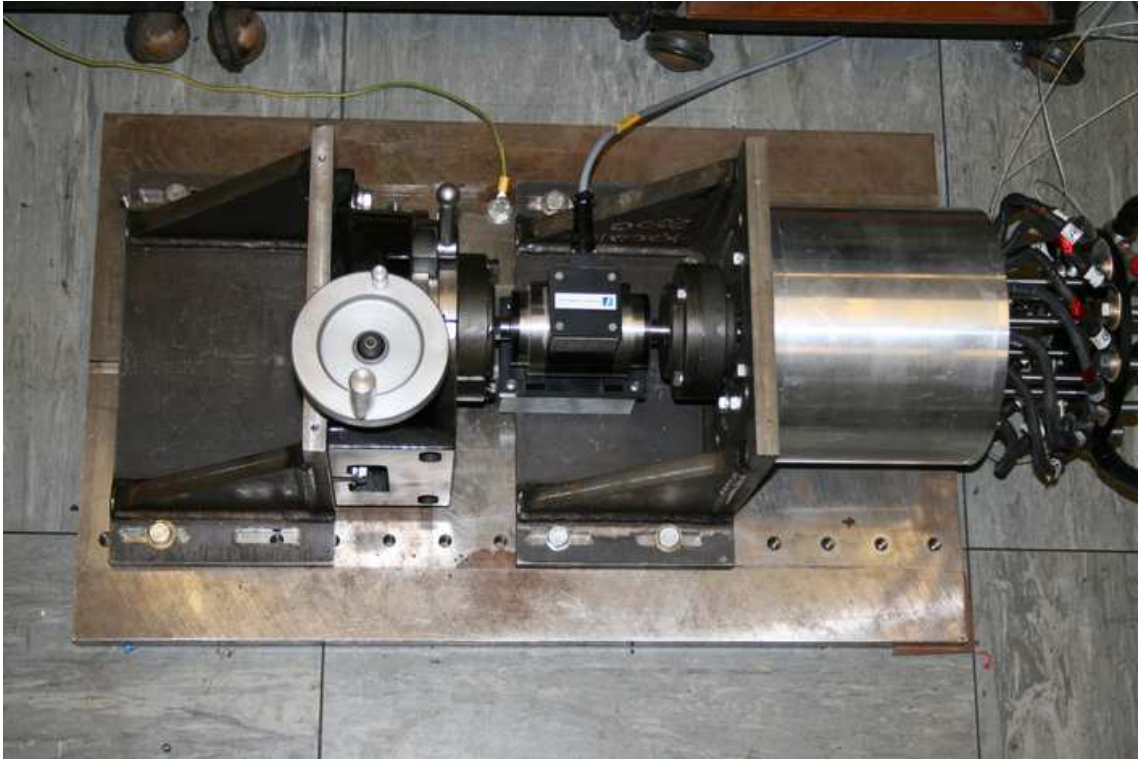


Figure 8.2: Rotor Mounted on The Test Rig and The Rotary Table

8.1.1 DC Resistance

The DC resistance of the windings was calculated using Ohm's law. Since the temperature affects the winding resistance, the voltage was applied for short periods of time, which maintained the winding temperature at or around the room temperature.

A low voltage was applied to the winding and the resulting current measured, the resistance was measured as $5.83 \text{ m}\Omega$ per phase. This result is within 1.5% of the calculated phase resistance of $5.93 \text{ m}\Omega$. The test circuit is shown in Fig. 8.3.

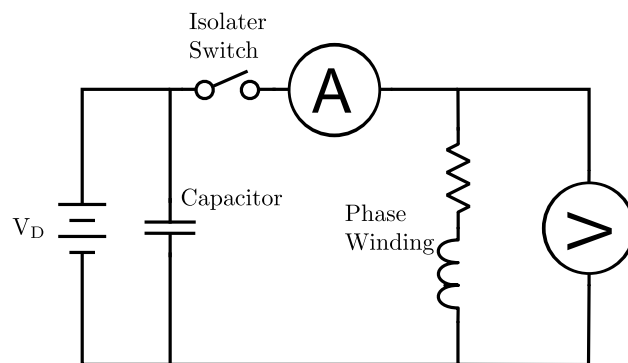


Figure 8.3: DC Resistance Test Test Circuit

8.1.2 Flux Linkage

Using the static test rig, voltage pulses were applied to the motor and the rise and fall time of the voltage transients were recorded and the data processed using a MATLAB script to create the flux linkage vs current for all rotor position.

The script works based on locating the initial rise and fall of the transient and also calculates the resistance during the steady state period of the pulse. The measured voltage can be expressed as Eq. (8.1).

$$V = iR + \frac{d\psi}{dt} \quad (8.1)$$

The flux linkage vs current for the rising and falling was calculated by integrating the corresponding voltage over the period of rising or falling as expressed in Eq. (8.2).

$$\int V - iR = iL = \psi \quad (8.2)$$

Data Processing

A test circuit was set up using a 60 V, 600 A Regetron power supply. Calculating the required voltage using the SRMs equivalent circuit showed no more than 5 V was required. Setting the voltage for any larger voltage magnitude left a significantly large overhead for the voltage resulting in a faster rise for the voltage and failure of the power supply. A function for a current pulse was written for the power supply, which applied enough voltage for 600 A over a period of 100 ms.

A digital oscilloscope was used to read the data from the voltage and current probes whose data sample rate was carefully set with respect to the length of one voltage pulse. The sample rate and resolution of the oscilloscope are inversely related, although a high sample rate gives a better resolution for the measured data, it will require a significantly longer computation time. For this experiment, it was decided to use a sample rate 250 kS/s for 0.4 s, giving 100 k data points.

Noise Filtering

There is a significant overshoot on the rising part of the voltage signal, which existed for all phases and in every rotor position. After the overshoot the signal settles down at 3.5 V. This signal was filtered to remove noise for use in the rest of the process. The measured voltage and current pulses are displayed in Fig. 8.4. Fig. 8.4a shows a single voltage pulse. Fig. 8.4b displays a single current signal corresponding to the input voltage signal shown. The current signal was also filtered to remove noise.

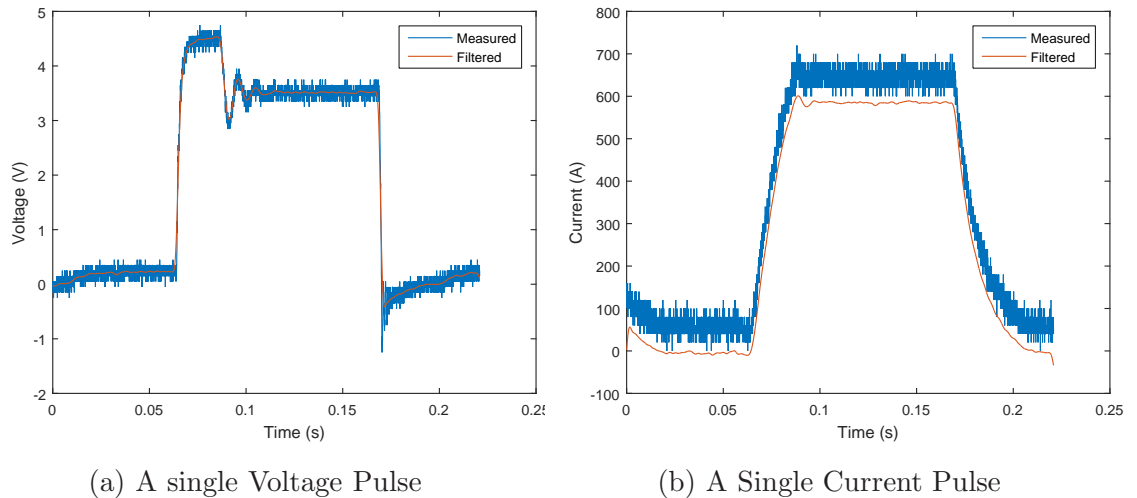


Figure 8.4: The Voltage and Current Pulses Used to Calculate the $\psi - I$ Curves

Identifying the Start and End Points of the Transient

The start and the end point of the transition period for the rising and falling periods, as shown in Fig. 8.5, were identified. This determines the start and the end of the time interval over which the rate of change of the voltage is calculated (shown as blue lines). The green line indicates the steady state interval over which the resistance of the phase was calculated. Identifying the intervals is the most important part of the data processing, as inaccurate values for the start and end points result in incorrect flux linkage curves or inaccurate minimum values for the flux linkage.

Compiling the Flux Linkage Curves

Using the calculated data for the start and end point of the intervals, and inputting the data contained within these points into Eq. (8.2), the $\psi - I$ curves for the rising and falling transients were created which are shown in Fig. 8.6. The rising and falling curves are slightly different. It is believed that the slight difference was caused by the different levels of noise present during each transient. The filtering and the process of identifying the start and end point of each transient have also affected the final result. It is also possible that the shaft deflects a small amount during excitation causing the values to be measured at slightly different rotor positions. This influences when the current reaches the steady state, which in turn affects the $\psi - I$ calculations, the tests however were repeated with the same result so it is the case that this is the best accuracy that will be achieved using this particular test set up.

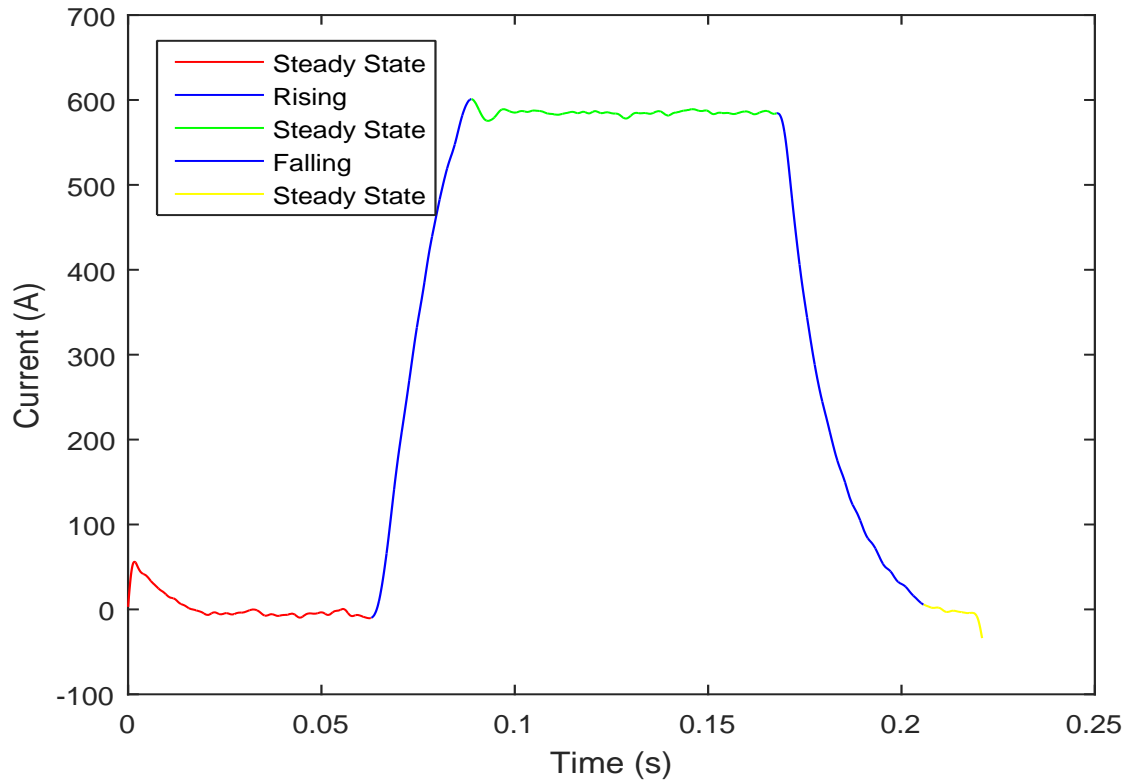


Figure 8.5: The Start and End Points of The Rise and Fall Transients

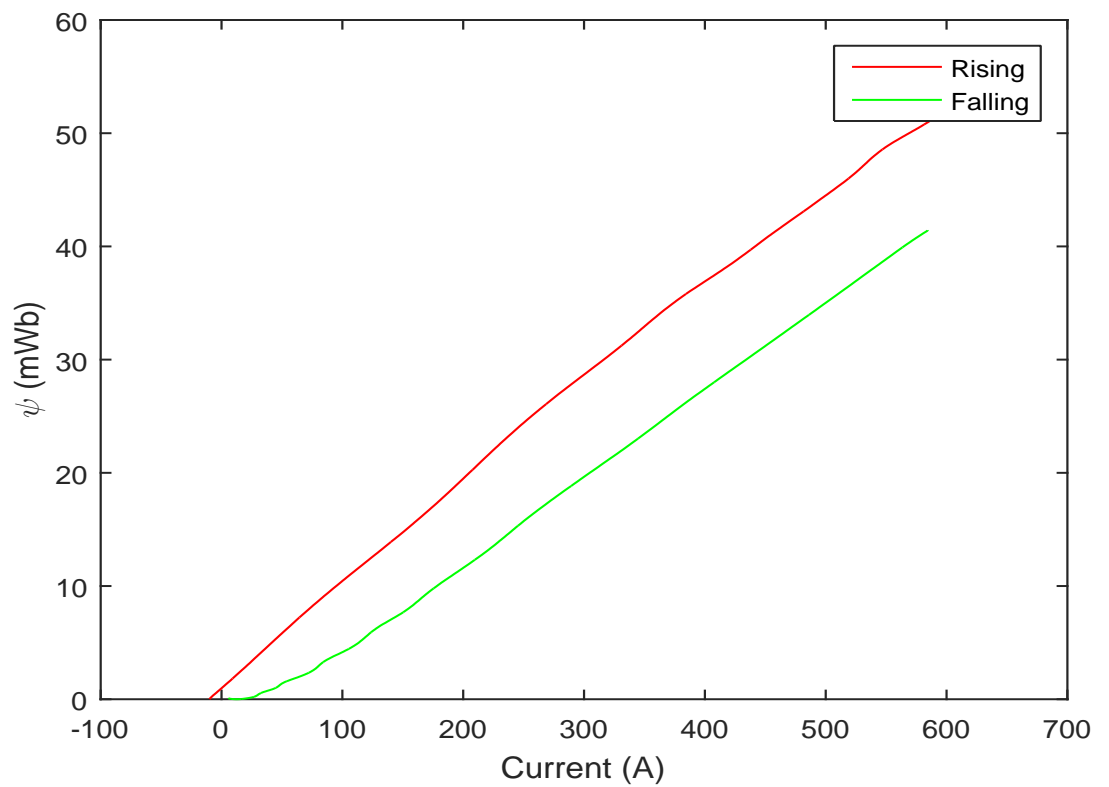


Figure 8.6: Generic Flux Linkage vs Current

The aligned and unaligned positions were determined by applying a constant current and finding the positions where zero torque was produced. Since the torque is produced as a result of movement of the rotor between these positions the flux linkage vs current curves at the aligned and unaligned positions are of interest.

Fig. 8.7 shows the $\psi - I$ curves created using the measured data and compares it with those created using FEA which are not significantly different for all three phases. However, a small discrepancy between the test and FEA curves can be seen. For the aligned curves, the test motor has entered saturation at a lower magnitude of flux linkage. This could have been caused by the small overshoot in the signal however, changing the magnitude of voltage overhead or the rise and fall time of the pulse did not remove the overshoot. The permeability of the electrical steel could be affected by the manufacturing process, or simply not as good as was modelled in the first place. The laminations used for the prototype were cut using the wire erosion machine which has a very long manufacturing time. This could result in a reduction in the quality of the electrical steel. Furthermore, all the produced batches of electrical steel do not have the exact specifications of the product that are provided in the data sheet and used in the simulations. This has been investigated by lowering the permeability of the lamination in the simulation by 5%, the difference in the $\psi - I$ curve can be seen in Fig. 8.8. With the new material properties, the simulated machine reached saturation at the same point as that measured from the prototype. Also, the measurement errors, the inaccuracy in identifying the rise and fall points and the sensitivity of the filtering process can all result in the difference between the simulation and test results. Therefore, the discrepancy between the $\psi - I$ curves is not considered an issue.

8.1.3 Static Torque

In order to measure the static torque, a rotary table, which locks the rotor at a precise angular location, and a 100 Nm torque transducer were used for an expected peak torque of 56 Nm from the simulations. The torque was measured every 3° mechanical and the torque and current logged by the acquisition unit at every point.

The 600 A 60 V Regetron power supply was again used for this experiment. The power supply was set in current control mode to give a maximum of 600 A. Voltage and current are measured more accurately using the a data acquisition unit, coupled to the machine through a differential voltage probe and current clamp. Since the prototype motor is a 6/4 SRM, a 90° mechanical rotation of the rotor is equivalent to a full electrical cycle. Therefore, regardless of the position of the rotor, a 90° rotation on the rotary table is enough to study the torque data of any given excited stator phase.

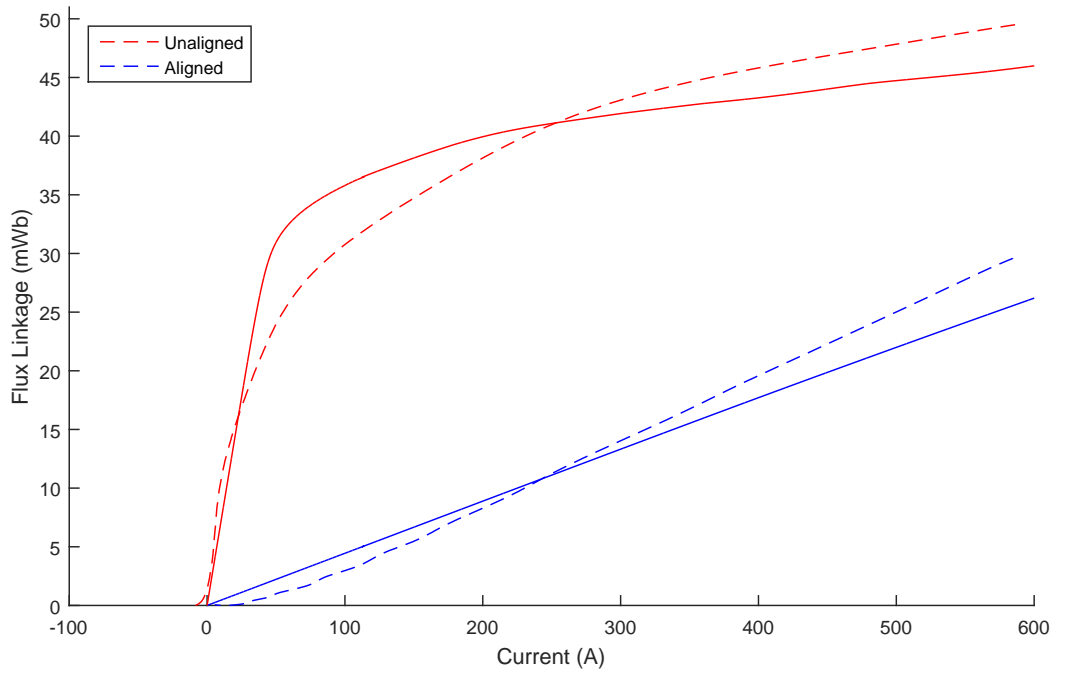


Figure 8.7: Flux Linkage vs Current

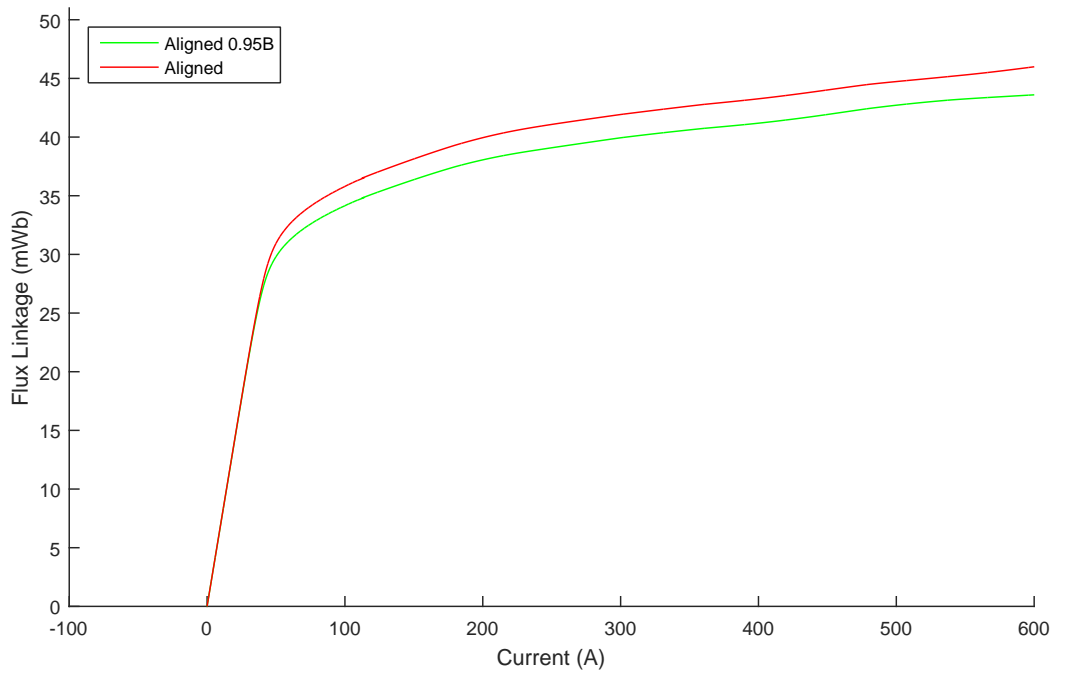


Figure 8.8: Effect of Reduced Permeability on the Aligned Curve

A pulse function code was created for the current starting from 0 up to 600 A in steps of 60 A. This function sets the current to zero between the measurement intervals, which eliminated the need for a switch. Fig. 8.9 presents the torque waveform over a full electrical rotation for varying values of current. It can be seen that the peak torque at full rated current is 58.06 Nm. This is 8.9% less than the 63.77 Nm peak torque estimate obtained from the FEA.

There were thought to be a number of possible causes for this discrepancy such as the air gap being slightly larger than expected. However, analysis showed that even a 10% increase in air gap width would reduce the torque by less than 1% so this was certainly not the case. The same sensitivity analysis used for the flux linkage measurement was applied to the torque. A 5% reduction in the permeability of the rotor lamination results in an 8% reduction in the output torque.

At this point the rotor stacking factor of 99% was taken into account, this leads to a 1% reduction in output torque.

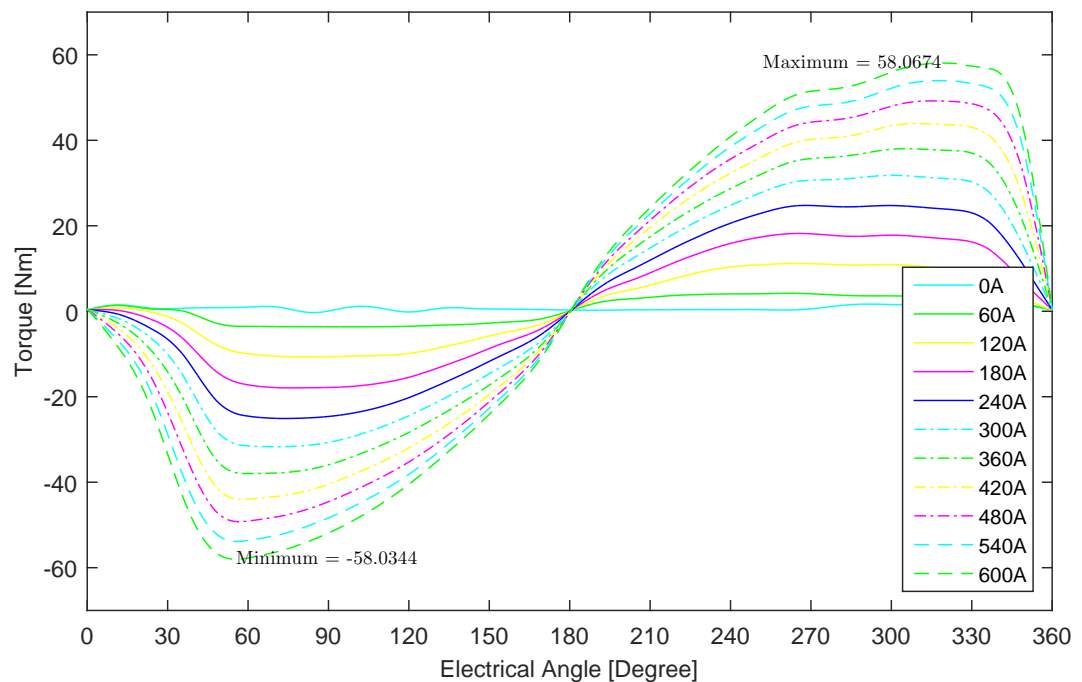


Figure 8.9: Static Torque Result

The torque was simulated considering a 5% reduction in the quality of the lamination and the stacking factor of the laminations. The results are compared to that of the test which are shown in Fig. 8.10. A very good agreement can be seen which validates the simulation results. This adds more confidence to the idea that the differences in the flux linkage characteristic are more dependent on the measurement accuracy and data processing.

After identifying the aligned and unaligned positions for one stator phase, this test was repeated for the other two phases which were found to have the same performance.

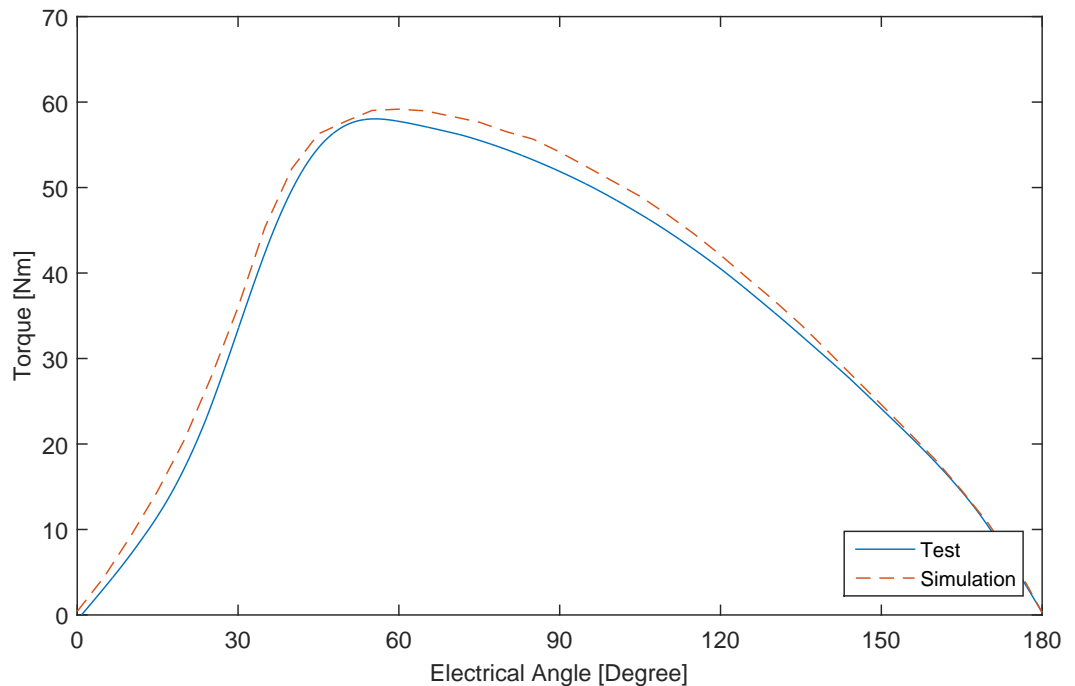


Figure 8.10: Static Torque Comparison Between Test and Simulation Results taking into account reduced lamination quality.

8.1.4 Thermal Behaviour

The primary limiting factor in design of electric machines is the thermal capability of the machine. The machines temperature limit is directly related to the losses which are in turn proportional to the magnetic loading, electric loading and operational speed.

For this test, the same circuit as the two previous tests was used. As all three phases experience the same rms current and hence should heat up by the same amount all six windings were connected together in series with the terminations connected to the power supply. Due to the lack of an implemented cooling system, full rated current could not be used for this experiment. Instead, 150 A was used which is equivalent to a square wave with a peak of 212 A.

The increase in temperature was observed in three points on the windings: inside a coil, in between two coils and inside one of the end windings whilst also observing the ambient temperature [116]. The temperature was recorded every 2.5 s for three hours until the steady state was reached. The results are shown in Fig. 8.11.

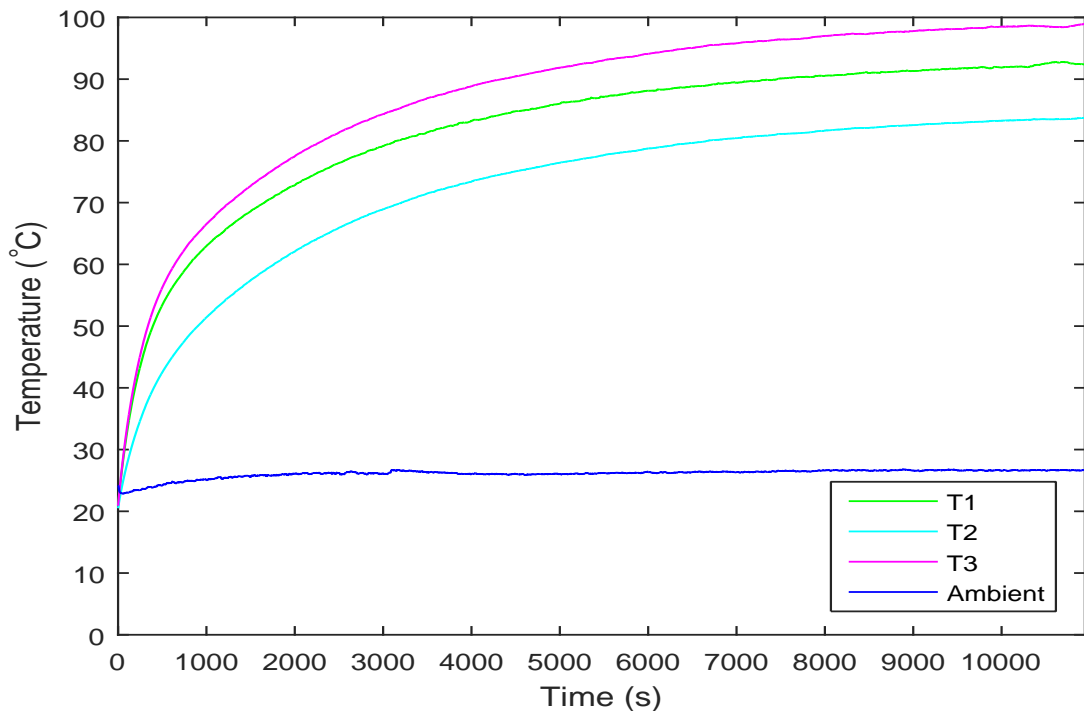


Figure 8.11: Thermal Test Result

The maximum design temperature of the motor is 155° . The maximum recorded temperature was 98.9° , as the power loss in the windings is related to the square of the current the motor could take another $\sqrt{1.57}$ times the current. Therefore, without using a cooling system, a maximum rms current of 188 A (equal to the peak current value of 266 A) could have been used before exceeding the design temperature. This would result in a current density of 7.63 A/mm^2 , which is a suitable value for air cooling. The heat dissipation caused by the iron loss is not included here and would lead to a lower current loading than calculated in this case.

8.2 Mechanical Tests

The spin test was carried out at London City University. Due to the high energy present at high speed operation, the test was carried out in a high speed chamber with concrete reinforced walls. Sand bags were also added to absorb the impact during possible failure.

An air compressor was used as the primary drive for the spin test. The stator was replaced with a cylindrical tube of identical size to provide support and mimic the drag effect of the real stator. The compressor wheel was directly mounted on the rotor shaft and secured using a right hand threaded nut. The volute of the

compressor then was fitted in place on the load end cap. The compressed air is applied in reverse, causing the system to work as an air turbine.

8.2.1 Test Set Up

For this test, an accelerometer, an encoder, a type K thermocouple and an NI USB data acquisition box (DAQ) were used. The encoder was an RM44AC™ magnetic encoder suitable for a maximum speed of 60,000 rpm. The magnet part of the encoder was glued on the shaft, allowing the measurement of the rotational speed. The accelerometer is an MTN/1130 series Monitran accelerometer with a frequency response of 2 Hz to 15 kHz. A stud was manufactured and screwed on the bearing housing cup to make sure shortest distance between the bearing and the accelerometer and to prevent any possible movement.

In order to read and log the data measured by the probes, a LABVIEW program was created to interface the probes and data acquisition box. The accuracy and validity of the logged data was inspected before installing the probes on the rotor. A signal generator was used to apply sinusoidal signals with an amplitude of 2.2 V and 20 V to the encoder and the accelerometer inputs of the DAQ, respectively while they were connected to the data box. After verifying the accuracy of the LABVIEW code, the probes were installed on the rotor. Next, a small volume of compressed air was used to run the compressor wheel at low speed to study the performance of the probes and the LABVIEW file in situation.

The motor was then transferred to London City University for mechanical testing. Fig. 8.12 shows the probe set up and the contribution of London City University in providing equipment for the test rig. Fig. 8.13 shows the test set up in the test rig of London City University. The motor was clamped to the test table using G clamps and sand bags were used to provide extra stability to the table.

The set up was rotated using a small volume of air to ensure the probes and rotor operate correctly.

8.2.2 Spin Test Results

The capability of the motor to maintain mechanical integrity was verified by running the motor up to 50,000 rpm. Two rotors were manufactured for the spin test; Rotor 1, has a central locating shaft of 10 mm diameter, Rotor 2, has no shaft.

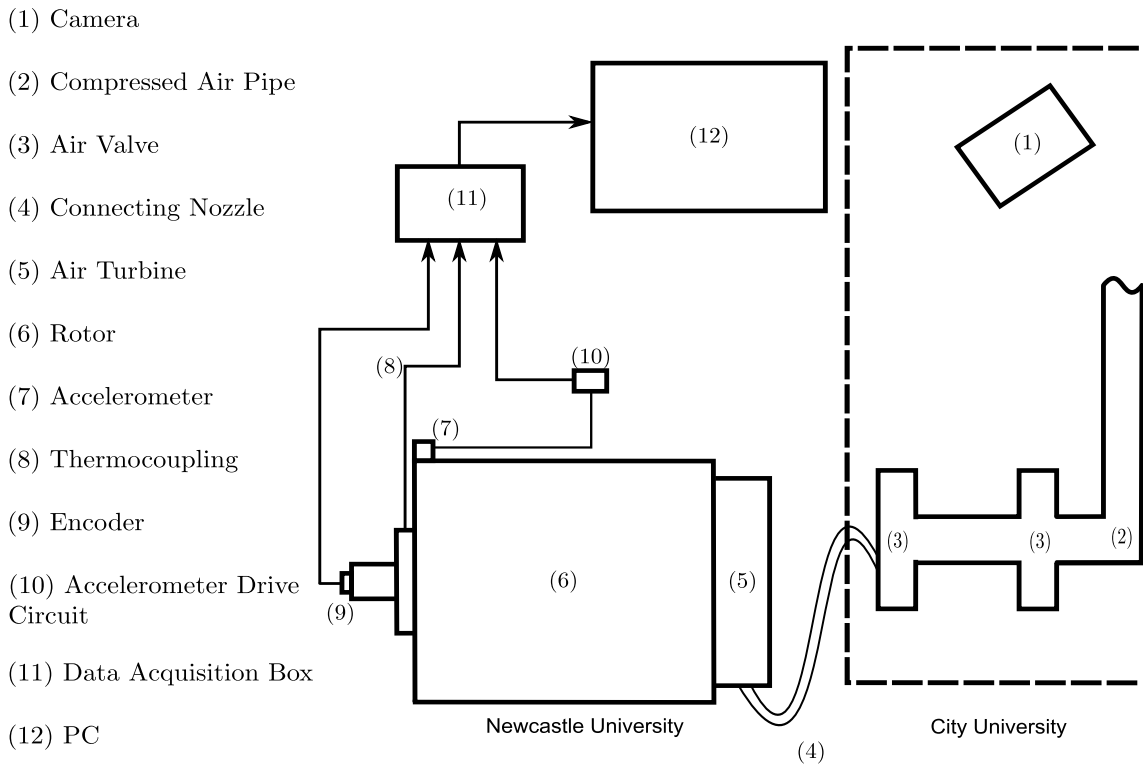


Figure 8.12: Mechanical Test Set Up



Figure 8.13: Mechanical Test Rig and Set Up

Rotor1

With a central shaft, Rotor 1 was deemed to have the more robust structure of the two prototype rotors, however during the balancing operation no differences between the two were observed.

Fig. 8.14 shows the rotor speed against time. The rotor was successfully spun up to 53,000 rpm after which the air flow was cut to allow the rotor to decelerate under its own losses. There were no signs of mechanical failure, however, the test duration was not long enough. Longer test times will require the implementation of complex bearings and cooling systems.

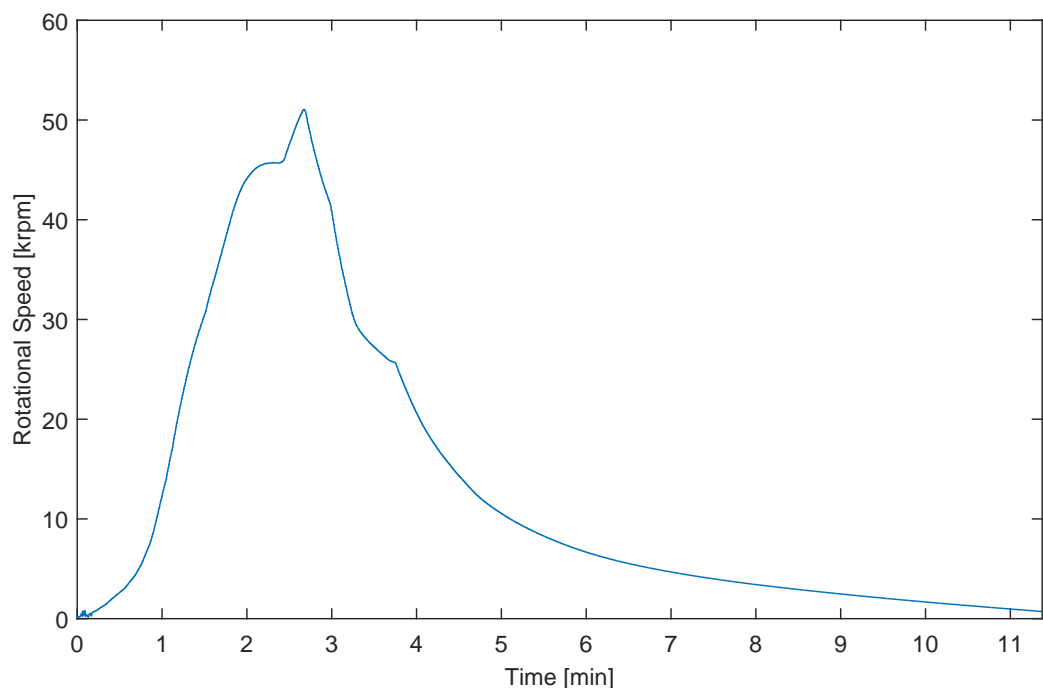


Figure 8.14: Speed Test Result of Rotor1

However, due to the mechanical losses of windage and bearing friction, the temperature at the bearings increases by 26 °C, as shown in Fig. 8.15. This underlines the need for a suitable cooling system for the bearings.

The vibration frequencies of the rotor were monitored during the spin test. To ensure the rotor vibration frequencies remained below the critical speeds and to allow immediate termination of the test if excessive vibration occurred. The vibration measurements are affected by the air flow, the compressor wheel operation and the test bed. Using the current test rig results in having too many components contributing to the resonant frequencies, therefore it would be difficult to identify the resonant frequencies of this operation. As a result, the vibration measurements of the rotor are not included in this work.

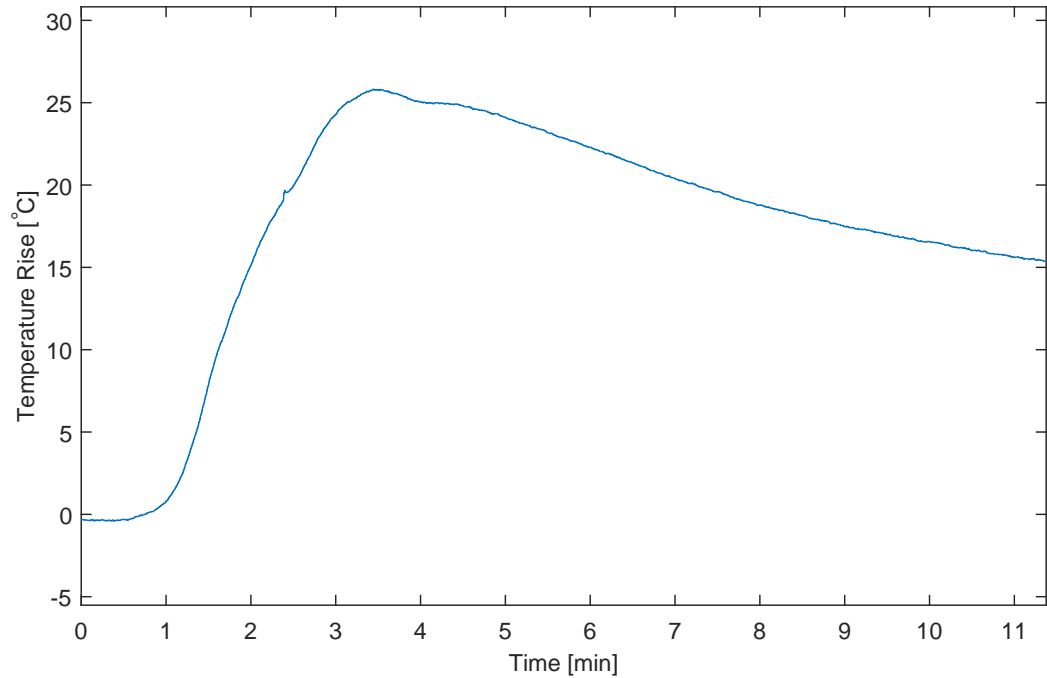


Figure 8.15: Temperature rise of the bearing of Rotor1

The test was repeated multiple times and the full operation speed was maintained for a duration to ensure the structural feasibility of the rotor. However, during one of the initial tests, a piece of debris hit the compressor wheel, leaving a minor damage as shown in Fig. 8.16. The debris could have been some of the glue used on the volume modifications. This damage still allowed the rotor to be spun up however, the resonant vibrations while maintaining at full speed were increased.



Figure 8.16: Evidence of Damage on the Compressor Wheel

Rotor2

Due to the damage to the compressor wheel, the rotor was only spun up to full speed briefly. Fig. 8.17 shows the motor at 51,000 rpm before the air flow was cut off. Again, no sign of mechanical failure was observed for this rotor.

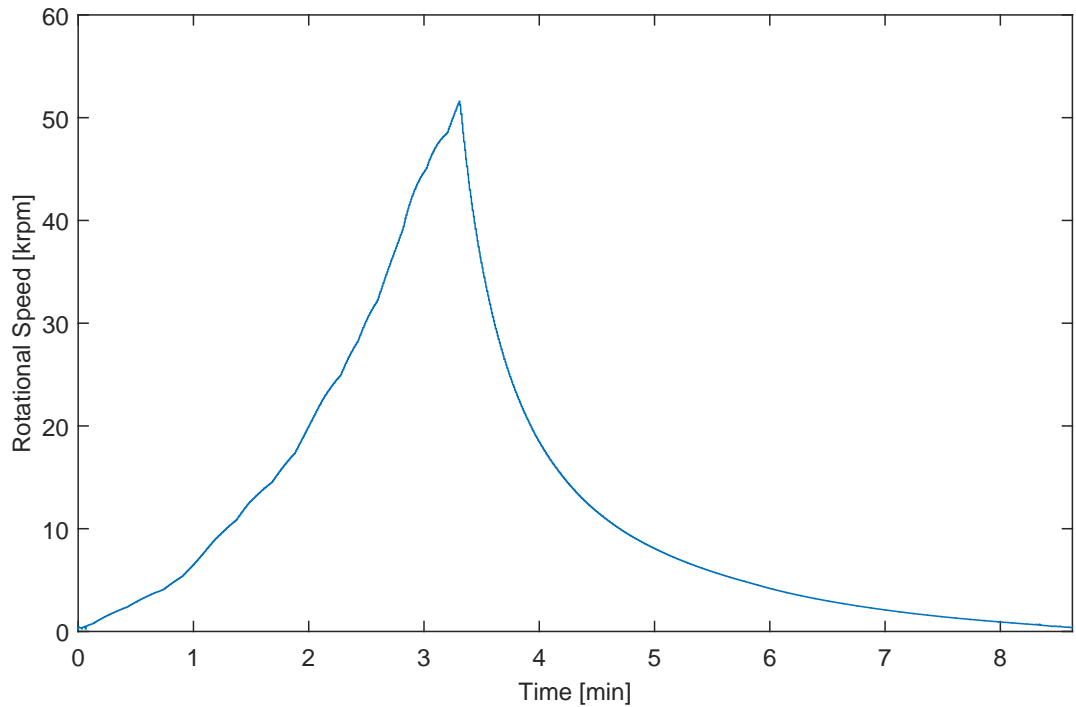


Figure 8.17: Speed Test Result of Rotor2

The temperature at the bearings experienced an increase of 33 °C as shown in Fig. 8.18.

In order to obtain the magnitude of the windage drag and the bearing friction loss, it could be possible to add a clutch between the compressor and the rotor and disengage the clutch once the full speed is achieved. This allows the rotor to decelerate independently. The bearing friction and the windage drag losses can be calculated from the deceleration speed as they are in proportion to the speed and the square of speed, respectively. This was not considered during this project but is an interesting area for future study.

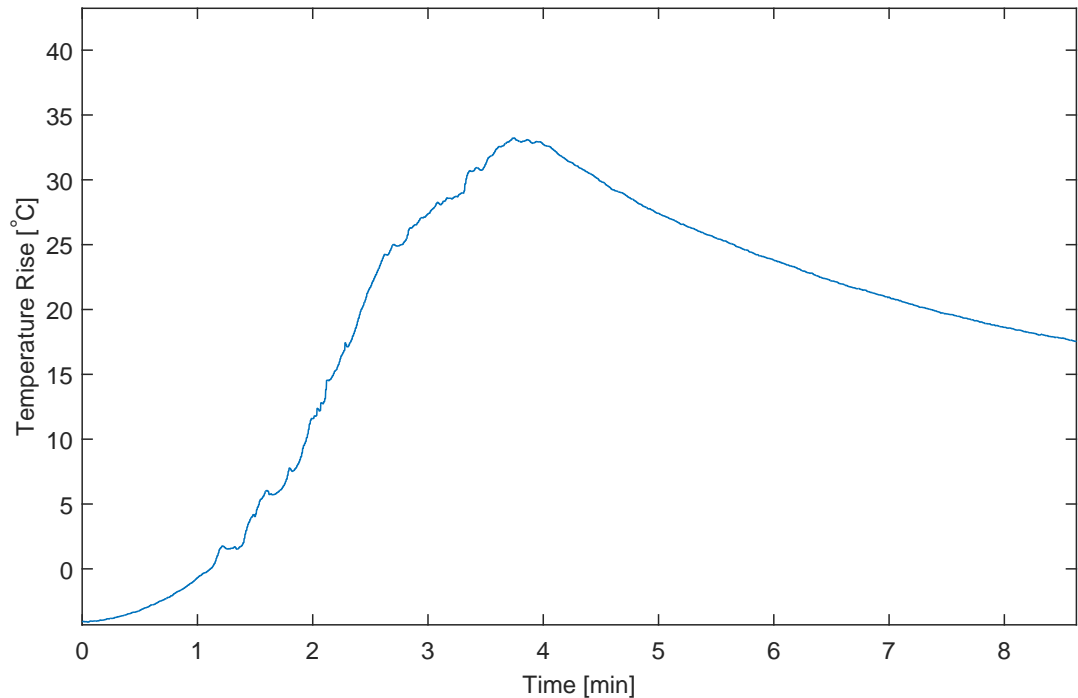


Figure 8.18: Temperature rise of the bearing of Rotor2

8.3 Conclusion

The practical tests results were presented in this chapter. The tests were carried out in two groups: the electromagnetic tests and the mechanical tests.

The electromagnetic performance of the motor was investigated using a series of tests at Newcastle University. Various test set ups were designed to carry out each of the tests.

A test circuit was designed and implemented on the test rig to measure the DC resistance of the motor. The results also helped in identifying the maximum required voltage for the next static tests.

The next SRM characteristic to identify was the flux linkage vs current profile. The concept of this test was to use the SRM voltage equation to create the flux linkage curves. A short current pulse of full rated current was applied at the aligned and unaligned positions. By integrating the rate of change of voltage during the transition period the flux linkage vs current curves were created. The results were compared to the flux linkage curves obtained from the FEA. It was found that by reducing the permeability of the laminations by 5% in the simulation a better agreement, especially in the saturation flux was found. Other differences in the characteristic were attributed to measurement errors and

limitations in the script used for the calculation, this was confirmed by the good match found between simulation and results of the next test.

The test rig was then adjusted to perform a full current test aimed at creating the torque vs rotor position profile. The torque vs rotor position profile was created for a full electrical cycle for a range of currents starting from 0 A to 600 A in steps of 60 A. The peak torque at full current was identified as 58.06 Nm. The aligned and unaligned positions were also identified using this type of test as they are the positions where zero torque is produced. The test technique and the implemented equipment were explained. Again a simulation between measured results and a simulation with 5% reduced permeability for the lamination materials was conducted. The results of this simulation showed very good correlation with the results of the measured prototype.

The thermal behaviour of the machine was then measured. Due to the lack of an implemented cooling system, a constant current of 150 A was used instead of the full rated current. This test was carried out over a period of three hours and the results verified the design thermal capability of the motor.

The mechanical tests were carried out using the high speed test chamber at London City University. A compressed air system was used as the primary drive for the test. Therefore, a no load test setup was designed and built. The operational speed of the motor was monitored using a magnetic encoder. Both of the prototype rotors were successfully spun over the design speed of 50,000 rpm. During the test the vibration frequencies of the bearings and the bearing temperature were monitored to avoid possible failure. No signs of mechanical failure were seen during the spin tests. Although this proves the feasibility of the applied topology for this application, further tests with longer duration are required to fully assure the rotor can maintain its structural integrity over long periods of operation. The longer steady state operation of the motor will require the implementation of complex bearings with cooling systems.

Chapter 9

Conclusion

9.1 Introduction

The simple structure of SRMs makes them robust, and their magnet free nature consequently makes them cost effective. The rotor of an SRM is free from any winding or permanent magnet material which makes the technology a good candidate to replace PM motors, while achieving an acceptable power density. Furthermore, the rugged structure of the rotor makes them suitable for high speed applications.

The main focus of this thesis has been to design a high speed, high power SRM to meet the specifications of the PM motor used in the Toyota Prius. In order to push the limits of power density, a 50,000 rpm, 60 kW SR motor has been designed, manufactured and tested.

Due to the high operating speed of this motor, whilst still having a sizeable diameter, it was necessary to take into account both the mechanical and electromagnetic design simultaneously. For simplicity the design methodology for each constraint will be presented here separately.

9.1.1 Electromagnetic Design Process

Prior to the work presented in this thesis a design investigation into an SRM to replace the PM machine found in the Toyota Prius was conducted by a research team at the university of Tokyo. The work of this research team involved the design of a 13,500 rpm SRM (SRM1) that produced 207 Nm of torque, this machine was summarised in Chapter 2. In this work it was proposed to increase the speed of the machine whilst producing the same 60 kW output power as the Prius PM machine and the Tokyo SRM machine (SRM1).

To achieve a guideline for the motor frame size, the design process began by scaling down the machine according to the sizes of Tokyo SR machine, SRM1. The

required geometrical properties of the motor, such as the stator outer diameter, the rotor outer diameter and the stack length were calculated using analytical methods to be 176 mm, 105 mm and 58 mm, respectively. A stator/rotor tooth combination of 6/4 was selected in order to reduce the electrical frequency, keep the iron loss of the machine low and reduce the power electronic converter PWM switching frequency requirements. The initial dimensions of the motor generated using analytical methods were then implemented in FEA models to more accurately identify the electromagnetic output of the motor.

9.1.2 Static Simulation

Initial FEA investigation of the machine dimensions obtained by analytical calculation showed that to produce the required torque, the length and diameter of the rotor needed to be altered to 95 mm and 91 mm, respectively. The resulting FE model, when solved for static torque showed that the motor produced a peak torque of 66.09 Nm when simulated in 2D and 63.77 Nm in 3D. The 3.3% difference between the two simulations being due to the end effects, which are not considered in the 2D simulation and the difference in mesh quality between a 2D and 3D simulation.

Static simulations are very useful in the early stages of the design process because they produce reliable results in a short time frame. However simulating a more realistic performance of the machine required transient simulations. When supplied with a square wave current under dynamic conditions the motor was simulated to produce an average torque of 55.6 N.m at the corner speed of 10,000 rpm whilst keeping within the specified voltage limit of 600 V.

9.1.3 Dynamic Simulation

Dynamic Simulations also allow calculation of the electromagnetic losses in the machine which are categorised as DC copper loss, AC copper loss and Iron loss. The DC copper loss of the machine at full rated current of 600 A was calculated to be 3.3 kW. The AC loss required more investigation into the design of the winding, a short study on the influence of skin effect and proximity loss on the winding was conducted. The conclusion was that, unsurprisingly a coil of 8 turns of a solid copper conductor would produce significant losses nearly fourteen times that of the DC copper loss. A stranded conductor therefore needed to be used of radius less than the 1.14 mm skin depth of copper at 833.33 Hz. A simulation using stranded conductor showed that the loss in the conductors was reduced to the extent that the loss in the coils was equal to the DC copper loss in the windings. For the final

design 8 turns of litz wire were chosen. The litz wire contains 750 strands with a diameter of 0.2 mm, each much smaller than the skin depth of the copper.

Iron loss was calculated by the FEA software using manufacturer's data applied to the Steinmetz equation on a per harmonic basis.

Windage loss in a toothed structure such as an SRM is a concern, particularly as windage loss is proportional to the cube of the speed. The windage loss was calculated using a previously developed model, and was found to be 5.21 kW at 50,000 rpm. Compared to a smooth cylindrical rotor this loss was 3.72 times higher. Measures can be taken to reduce the windage loss by, for example, filling the gaps between teeth with an epoxy material to give a smooth surface. It is also thought that by increasing the end plates of the rotor to the same diameter as the outer diameter of the rotor teeth then the windage loss will be reduced although this is a subject for further investigation.

Using the data calculated for copper loss, iron loss and windage loss an efficiency map of the motor was created. The peak efficiency of the motor was 93.73% at 15,000 rpm and 60 kW, which could be increased to 94% at 17,500 rpm, 60 kW by using a cylindrical rotor, which pushes the overall high efficiency points to higher speeds. The main benefits of a cylindrical rotor were found at the highest speeds where the windage and iron losses are dominant, in these areas the efficiency can be increased. The cylindrical rotor for an SRM can be imitated by filling the inner pole gaps with epoxy or the use of flux bridges between the rotor tips.

9.2 Mechanical Design Process

9.2.1 Mechanical Stresses

The majority of the stresses imposed on a high speed rotor are caused by centrifugal force, which is an inertial force in the radial direction and is directly proportional to the square of the angular velocity of the rotor.

A tip speed of 250 m/s was used as a rule of thumb, based on the output power and design speed of the motor, to determine an upper limit for the operational speed. The rotor tip speed at 5236 rad/s (50,000 rpm) with a radius of 45.5 mm was calculated to be 238.2 m/s. This falls below the guide upper limit, which indicated the possibility of safe operation.

Considering a conventional SRM rotor there were found to be two main causes of stress on the laminations of the rotor;

- Notch Effect: The rise in the stresses around any indents, cracks, and sharp angles of a rotating body.

- **Tangential (Hoop) Stress:** The stress concentration around the central hole of a rotating disk. The hoop stress limits the maximum operational speed and the maximum rotor outer diameter.

The notch effect was relatively simple to alleviate, through the removal of sharp angles by the use of fillets. In the case of this machine these fillets needed quite a large radius so that the teeth of the machine joined the fillet at a tangent, removing any possible sharp edge. Having a too small a radius results in reduction in the rotor pole height and hence a decrease in output torque. Removing the influence of the notch effect reduced the rotor peak stress of 1208 MPa, located near the corner of one of the tooth bodies, to 511 MPa located at the inner diameter of the rotor. This was still too high considering the typical lamination yield strength of 450 MPa.

Hoop stress was the cause of the peak stress at the inner diameter of the rotor with fillets. The hole at the inner diameter of the rotor has a minimum possible size when a shaft is fed through it, that size is the diameter of the shaft required to transfer 55 Nm. The minimum shaft diameter was calculated using the torsion in a beam equation to be 11.2 mm. As a safety factor and to provide more robustness 20% extra was added to the diameter. When the shaft is being designed, bearing availability also needs to be taken into account. The closest diameter among commercially available bearings is 15 mm. However, the shaft needs to be designed slightly larger to accommodate for a chamfer against which the bearing is pressed. Therefore, a 17 mm diameter would be the smallest possible. For this work the size of available couplings was also considered, which meant that the shaft size would be 20 mm rather than the 17 mm shaft that would be chosen in reality.

A rotor lamination with a 17 mm diameter hole for a shaft was simulated. It showed that the maximum stress was 470.1 MPa at the inner diameter of the lamination, this was above the guaranteed yield strength of the stator lamination, of 400 MPa. Therefore, it was not possible to have a shaft through the centre of the rotor to transfer torque. An alternative approach to the configuration of the rotor was considered.

One way to completely remove the hoop stress on the inner diameter of the rotor lamination is to have no hole at all. This means that with no through shaft another method of holding the rotor laminations together was required. A topology commonly applied to flywheels was applied to this rotor. This involved adding bolts and tie rods through the rotor, and connecting them to cheek plates at the ends to sandwich the laminations together. The cheek plates then have an extending shaft used to transfer the torque to the load.

The new design required extra investigation from both a mechanical and electromagnetic point of view. The number, size and position of the holes for the

tie rods was analysed for the minimum stress yet maximised torque. It was found that aside from the addition of the rod holes in the first place, there was little difference in the motor performance based on the size and position of the holes. Therefore a symmetrical set of four holes was chosen such that they can lay under each of the teeth of the rotor. At this point other minor design specifications such as the rotor tooth arc and rotor tooth height were investigated both mechanically and electromagnetically to achieve an optimized design.

The final design, including the tie rod hole cuttings with a diameter of 6 mm located at a radial distance of 26 mm from the centre, showed a maximum stress of 382.5 MPa at an over speed of 60,000 rpm, which is below the guaranteed yield strength of the material (400 MPa). This is a safety factor of 1.15 against the yield strength of the laminations, and a safety factor of 1.7 for operating at 50,000 rpm, ensuring a safe rotor design to operate at 50,000 rpm.

9.2.2 Rotor Vibration

Vibrations cause deflection in the rotor, and if spun at natural frequencies, the rotor deflections can reach dangerous levels. The rotor design ideally avoids the vibration frequencies over the full operating speed range.

Furthermore, soft mounting of the bearings reduces the effective stiffness, allowing operation beyond vibration frequencies. If the rotor is accelerated rapidly through speeds associated with the rock and bounce mode, the system deflection can be limited allowing operation beyond those resonant frequencies.

The frequencies of the rotor were calculated using modal analysis on the complete rotor including tie rods, cheek plates and taking into account bearing stiffness.

9.3 Prototype Construction

The stator of the machine was produced out of a stack of NO20 grade silicon iron laminations, a typically low iron loss material. The laminations were wire eroded in a stack without being glued together, and then stacked in the case and located by means of the keyway in the lamination and stator housing. The absence of glue gave a higher stacking factor that would have been achieved for a glued stack.

It would have been possible to manufacture the stator teeth in segments, allowing the coils to be wound individually on to the teeth of the machine and then slotted together on the stator, as has been the subject of other machines constructed [117]. However this was not considered for this work as the main aim was to produce a high speed rotor. Furthermore, segmenting the stator teeth risks adding a small

air gap in between the segments. As a result, obtaining a high stator fill factor with small slot openings and litz wire was a challenge. Like wise, using segmented rotor poles, in which the pole modules are inserted in a rotor back iron with low permeability [118,119], is not an option for high speed motors where the robustness of the rotor structure has the highest priority.

To make the coils, 5 turns were initially wound around a bobbin and pressed using a hydraulic press. The resulting coils were then mounted on the insulated stator teeth. The remaining three turns were then hand wound, achieving a slot fill factor of 40%.

The high operational speed required careful manufacture of the rotor. The rotor laminations were of grade M250-35HS which is suitable for high speed applications due to its typical yield strength of 450 MPa. When stacking the laminations it was the case that they were not of uniform thickness. In an attempt to achieve a uniform rotor length the laminations were stacked in alternating directions, glued and cured in the oven using clamps and spacers. The laminations were wire eroded with a millimetre larger diameter than the finished rotor. The cheek plates were machined to an almost finished state then assembled along with the tie rods and the laminations. The rotor machining was finished on the assembled rotor in order to ensure the components were concentric.

Due to possible difficulties in the alignment of the rotor cheek plates using only the tie rods through the laminations, a second rotor was constructed. The second rotor had a small locating shaft of 10 mm diameter running through the centre of the laminations. This shaft diameter is small enough to avoid significant hoop stress, yet allows more certainty in the alignment of the rotor components. The shaft is not however capable of transmitting full load torque, and simply located in holes cut out in the cheek plates.

Bearing selection is a crucial part of the design process of a high speed motor. There are three major types of commercially available bearings: magnetic bearings, air bearings and rolling element (balls or cylinders) bearings. Ball bearings were used here as they eliminate the auxiliary equipment needed for control and operation of magnetic and air bearings. For a 20 mm shaft diameter and 50,000 rpm there was a limitation on the available bearings. A set of high precision angular contact bearings were chosen for the project. The bearings are ceramic coated hybrid ball bearing type with a rated speed of 68,000 rpm with a grease lubricant.

The spin test of the rotor was performed at London City University using a compressed air system to drive. It was required to build a separate housing for the motor consisting of a cylinder with two end plates to hold the bearings. The rotor was suspended inside the housing and a compressor wheel attached to the end of the shaft. It was with the compressor wheel attached that both rotors were

balanced by removing a small amount of material from the cheek plates. Although a shaft was added to one rotor to aid alignment, no practical differences were noticed in the balancing of the two rotors.

Also included in the test setup was an accelerometer to measure the vibrations of the rotor, an encoder to measure the speed and a thermocouple to measure the temperature of the bearings.

9.4 Motor Testing

The motor tests were carried out in two groups: the electromagnetic tests and the mechanical tests. The electromagnetic performance of the motor was verified at Newcastle University, using various test set ups. The mechanical tests were performed at London City University.

9.4.1 Electromagnetic Tests

The required facilities of a 50,000 rpm 60 kW high speed test chamber were not available at Newcastle University. However, assessment of electromagnetic performance was carried out via a series of static tests.

The flux linkage versus current characteristic of the motor was created by applying short current pulses in the aligned and unaligned positions. By integrating the SRM voltage equation, the flux linkage could be calculated. The results showed a good match with the FEA simulation, with the differences attributed to poorer than expected material characteristics and limitations in the measurement method.

The static torque versus rotor position was measured on a static test rig for a full electrical cycle and currents between 60 A and 600 A, in steps of 60 A. The peak torque at full current was measured to be 58.06 Nm. The measured torque was lower than that expected from FEA simulations by 8.9%. An investigation into the possible causes of the lower torque was carried out. Although there is the possibility that the airgap is larger than expected this was ruled out as a possible cause of the lower torque as it would require double the airgap size to reduce the torque by only 5%. Instead it is more likely that lower than expected lamination performance is to blame, with only a 5% reduction in material properties in the simulations leading to the same drop in torque. This is a more than possible reduction in material properties due to manufacturing or simply a worse than normal batch of laminations. This is before taking into account that the simulation of the motor will not be without inaccuracies in the calculations. A simulation with reduced material properties was conducted and the results matched very well with the measurements of the prototype machine.

The thermal behaviour of the machine was tested over a period of three hours and the results verified the design thermal capability of the motor. However, due to the lack of an implemented cooling system, a constant current of 150 A (equivalent to a square wave of peak of 212 A) was used instead of the full rated current. An RMS phase current of 424 A would be required to produce full rated torque, less than three times the current density used in the static test with no cooling method applied. It is possible to greatly increase the cooling capability with either water or oil cooling it is expected that if they were applied the full rated current could be realised.

9.4.2 Mechanical Tests

The mechanical tests were carried out using the high speed test chamber at London City University. A compressed air system was used as the primary drive for the test. Therefore, a no load test set up was designed and built.

A LabVIEW program was written that took in the outputs of the accelerometer, magnetic encoder and temperature sensors. The program analysed the inputs and displayed the results in real time so that the speed of the rotor could be seen as well as if the vibrations of the rotor were becoming too high.

Both rotors were successfully spun up to over the design speed of 50,000 rpm. During the test the vibration frequencies of the bearings were monitored. The temperature of the bearings was also monitored to avoid excessive temperature rise and failure. No sign of mechanical failure was observed. However, the duration of this test was not long enough to ensure no failure would occur after long periods of operation. A longer test duration will require more detailed bearing design, implementation of complex bearings and use of some type of a cooling system for the bearings.

9.5 Comparison to Motors with Similar Specification

The culmination of this research has been the successful design, construction and testing of a high speed, high power SRM capable of 60 kW at 50,000 rpm, using a flywheel topology approach for the rotor. Although, the tests have verified the design and indicated the possibility of full-load, full-speed operation, it should be noted that the spin test was carried out for a short period of time and under specific conditions. Table 9.1 provides a comparison with the design SRM1 produced by Tokyo university, and the third generation of Toyota Prius. The high speed machine is smaller, whilst providing the same power, the weight of the machine has reduced

from 25.2 kg to 18 kg. The result is a higher efficiency machine with a power to weight ratio 1.39 times that of the original machine.

It should be mentioned that compared to the other state of the art motors that were mentioned in Chapter 2, the proposed motor of this work does not implement the expensive iron-cobalt lamination, but uses the lower cost NO20 and M250-35HS for manufacturing the stator and the rotor. The bearings used for the prototype of this work were from angular contact ball bearing type, which are from a lower cost range compared to the magnetic or air bearings used in high speed motors. No exotic material or expensive manufacturing technique was used for the design or construction of the prototype. The results of this work give confidences in design and manufacture of a high speed high power SRM and provide the grounds toward further study regarding different aspects of such motors.

Table 9.1: Specification Comparison of the Toyota Prius, SRM1 and the Designed SRM

Parameter	Symbol	Unit	Toyota Prius	SRM1	SRM
Stator Outer Diameter	S_{OD}	[mm]	264	264	185
Rotor Outer Diameter	R_{OD}	[mm]	-	182	91
Stack Length	L_S	[mm]	50	87	95
Maximum Power	P_{max}	[kW]	60	61	60
Maximum Speed	n_{max}	[krpm]	13.9	13.9	50
Torque	T	[Nm]	207	211	56
DC Link Voltage	V_{DC}	[V]	650	650	600
Fill Factor	FF	-	0.54	0.56	0.4
Stator/rotor teeth ratio	N_r/N_s	-	-	18/12	6/4
Max Torque Density	TD	[Nm/l]	35	36	22
Max Power Density	PD	[kW/l]	10.2	10.4	23.5
Specific Power	$P - W$	[kW/kg]	2.7	2.4	3.33
Specific Torque	$T - W$	[Nm/kg]	9.3	8.4	3.11
Mass	W	[kg]	22.2	25.2	18
Iron Loss	P_{Fe}	[kW]	2.7	1.3	1.79
Copper Loss	P_{Cu}	[kW]	6.0	6.3	3.3
Efficiency	η	[%]	88	89	91.36*
Airgap Shear Stress	σ	[kNm/m ³]	-	45.73	44.99

*The mechanical losses are not included in the calculation of the efficiency.

9.6 Recommendations for Future Research

The work described in this thesis is one step toward the implementation of an operational high speed high power SRM. The following recommendations for further research are put forward:

1. Research on “ The Control of High Speed, High Power SRMs for Automotive Applications ” culminating in the design, construction and testing of a 60 kW SRM drive and controller.
2. Research on “ The Windage Loss Investigation of High Speed, High Power SRMs with a Large Cheek Plate Approach ” culminating in the calculation and measurement of the windage loss of the SRM rotors with and without a cheek plate size of that of the rotor. Use of a clutch to disengage the compressor wheel from the rotor and investigating the bearing friction loss.
3. Detailed design of the bearing system, including alternative bearing types suitable for high speed applications and a choice of cooling system for the bearings.
4. Further mechanical tests focusing on the spin test, including increasing the total test duration, increasing the duration of operating at full speed and use of X-ray scans for the detailed study of the rotor for structural failures.
5. Measuring the vibration frequencies of the rotor over the full range of the operational speed.
6. Research and development of a full load, full speed dynamometer test rig.
7. Performance measurements up to full load and full speed.
8. Design and construction of a cooling system suitable for the respective current density.

Appendix A

Photographs and Mechanical Drawings

Mechanical drawings, note scale on drawings no longer accurate due to thesis page formatting.



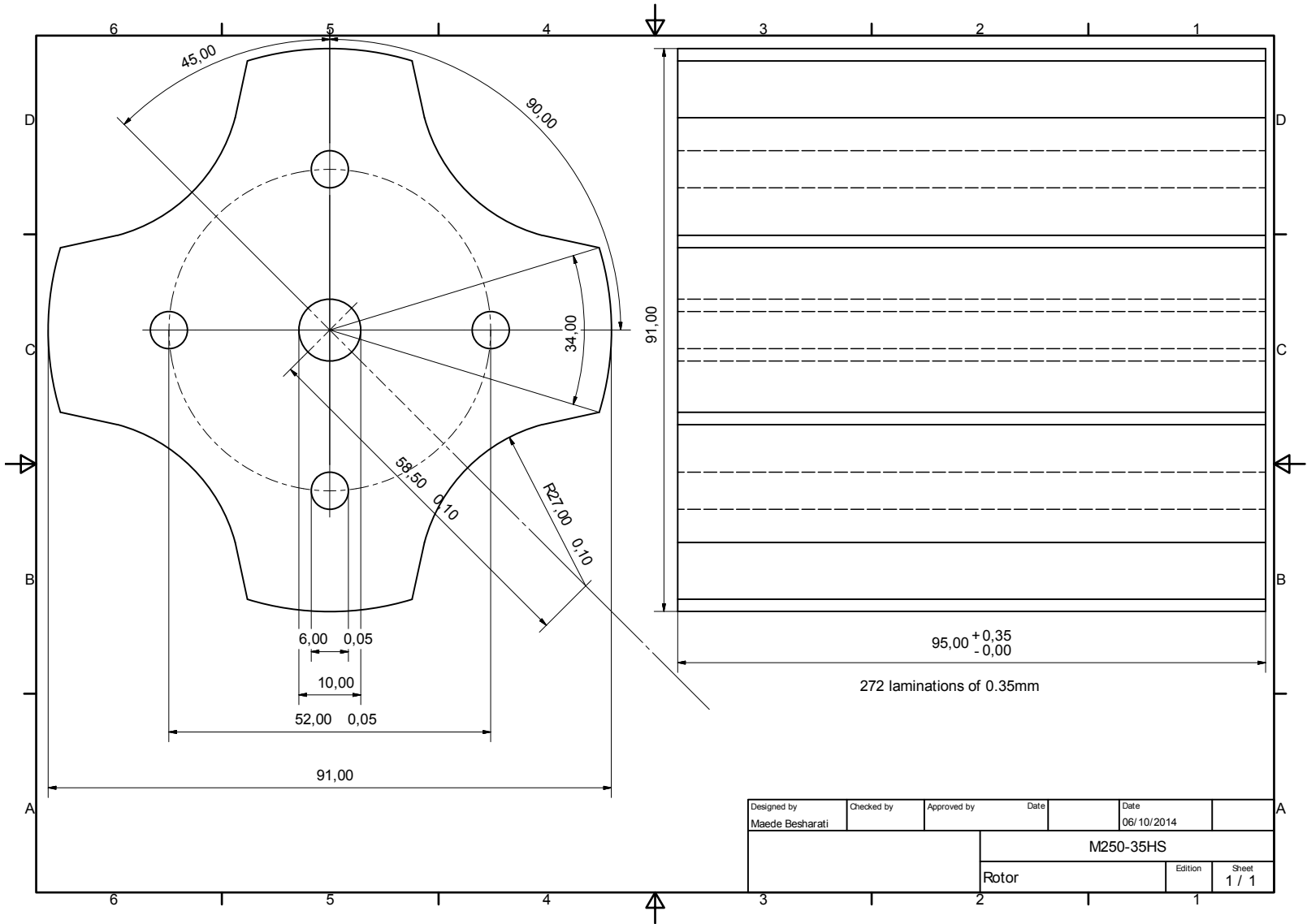
Figure A.1: Wire Erosion Machine



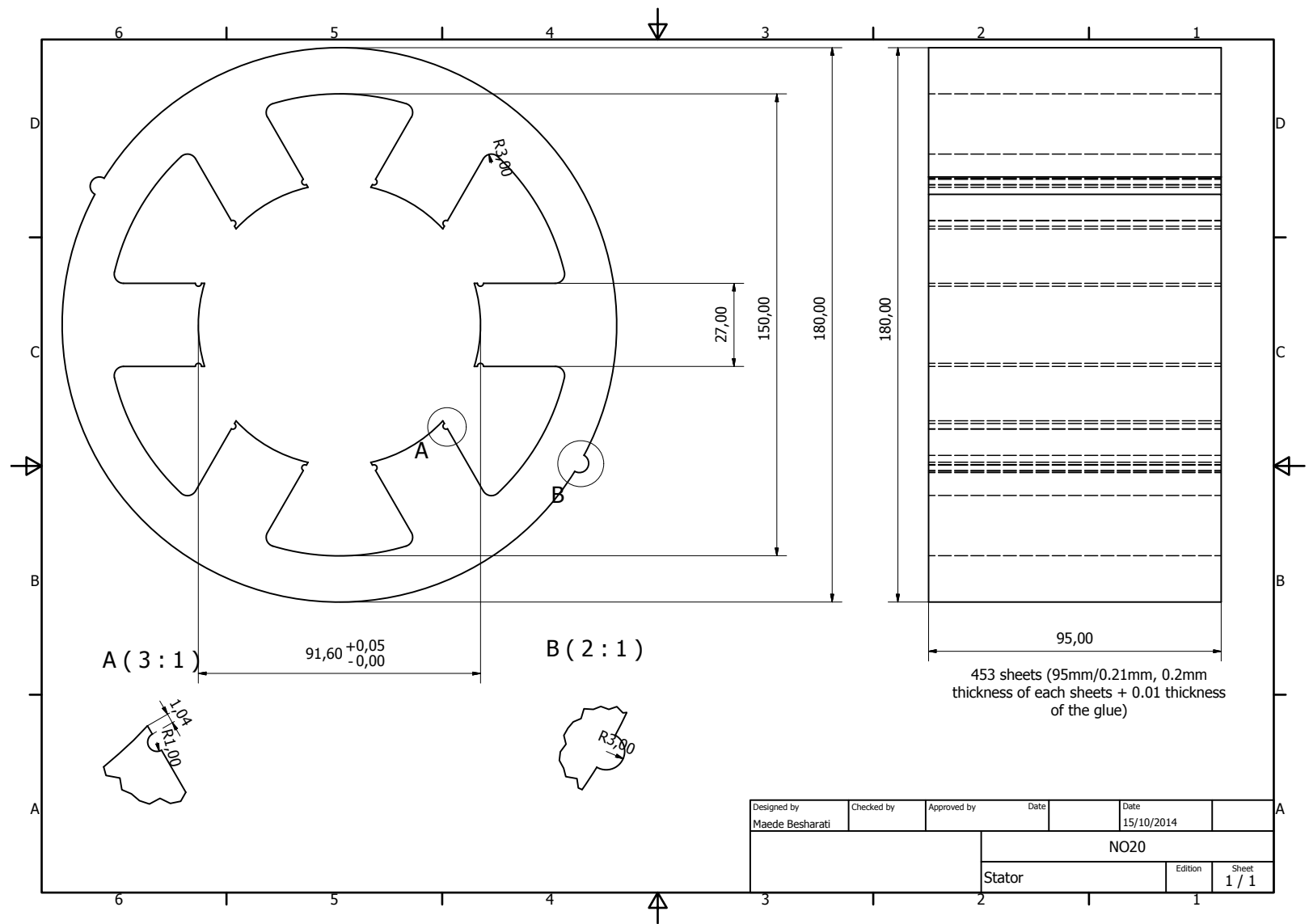
Figure A.2: Stator Inside the Case

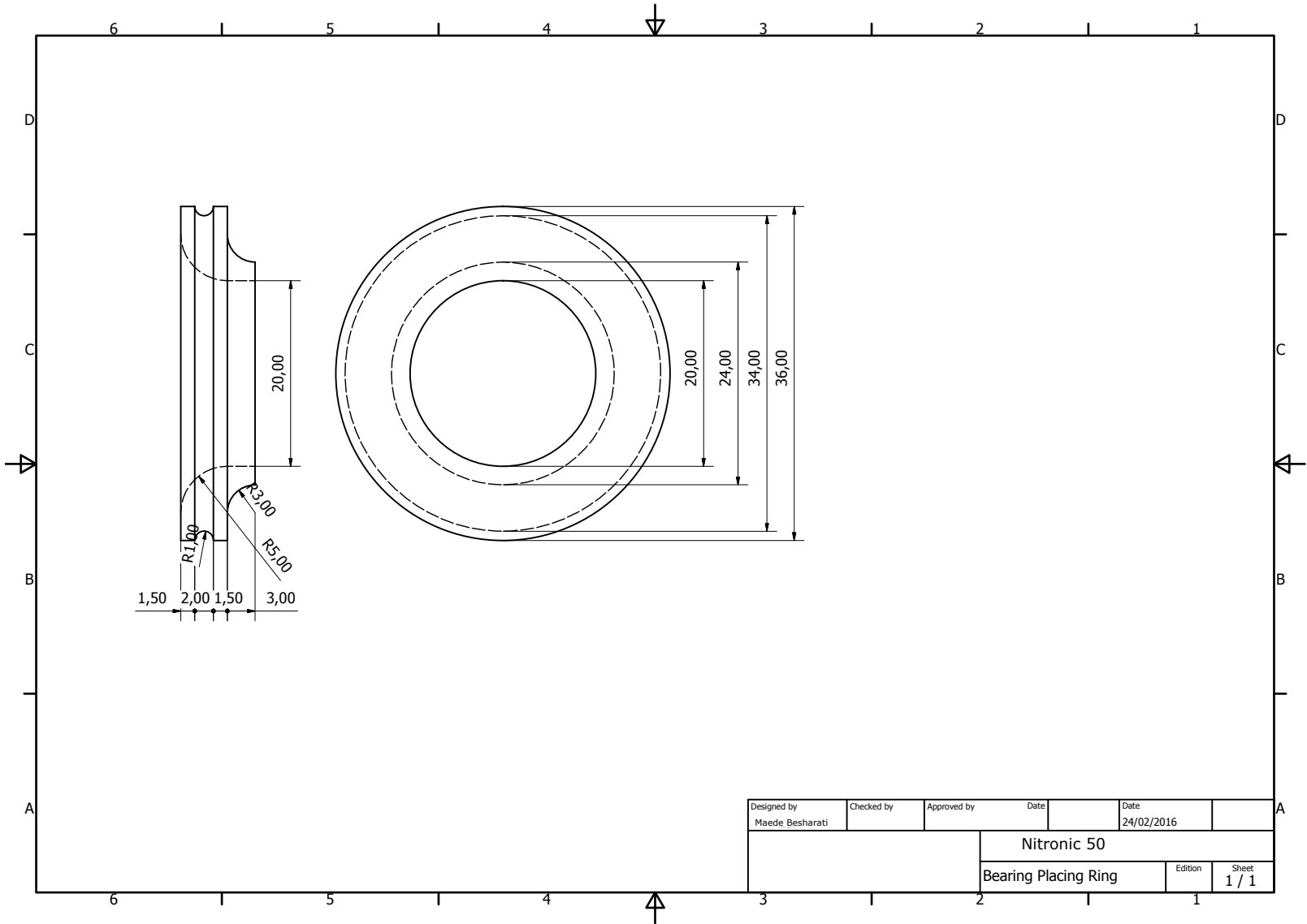


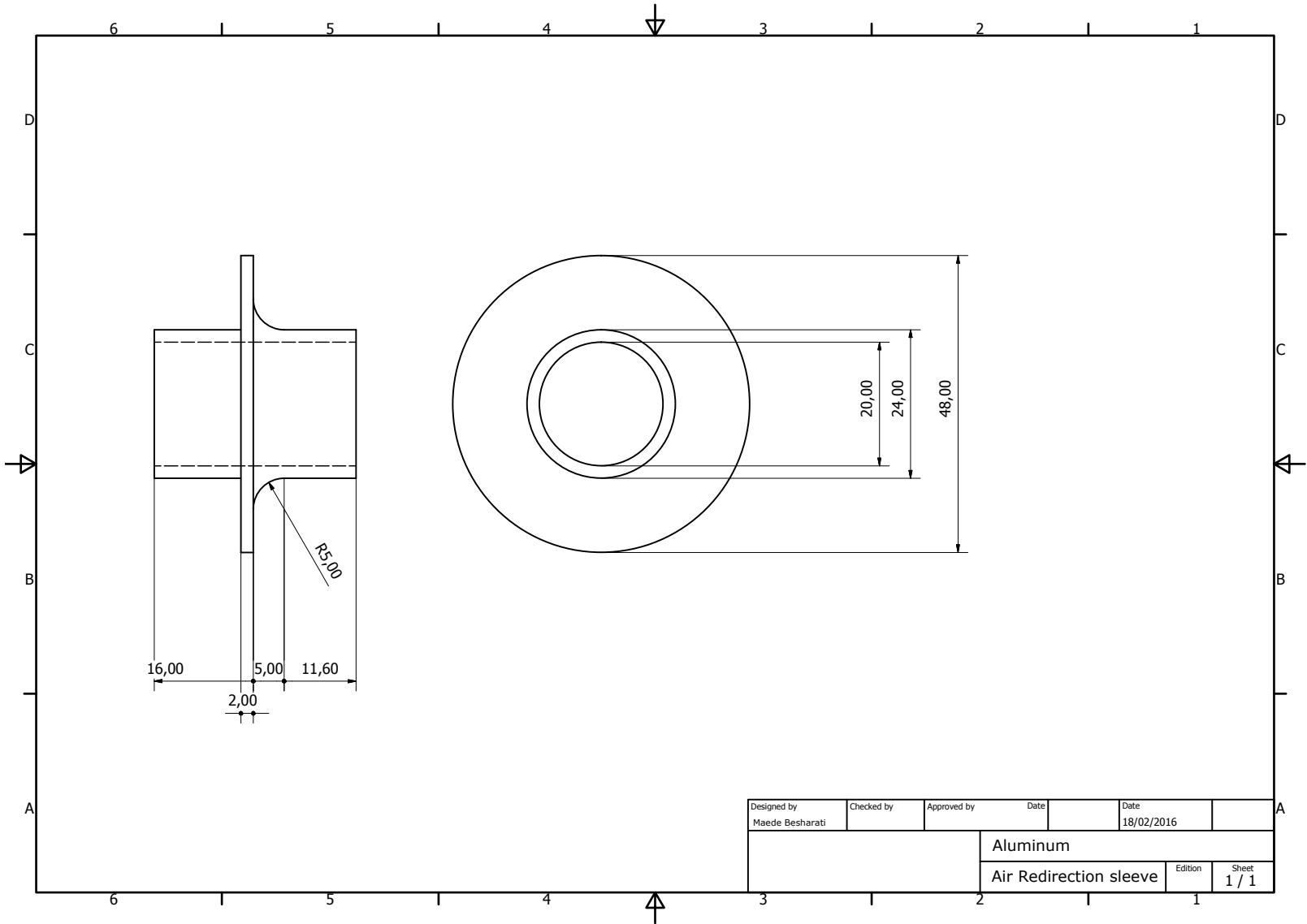
Figure A.3: End Windings

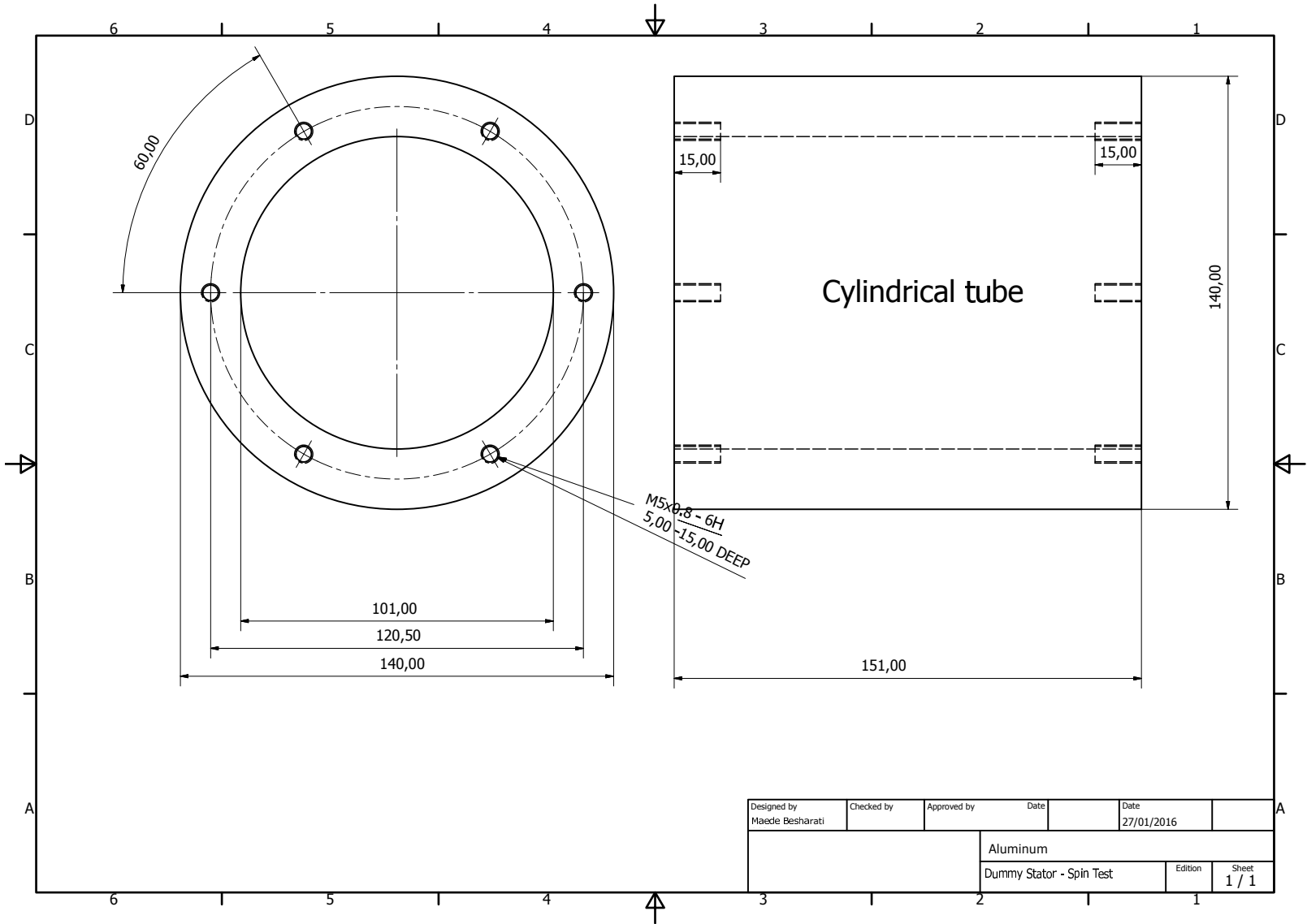


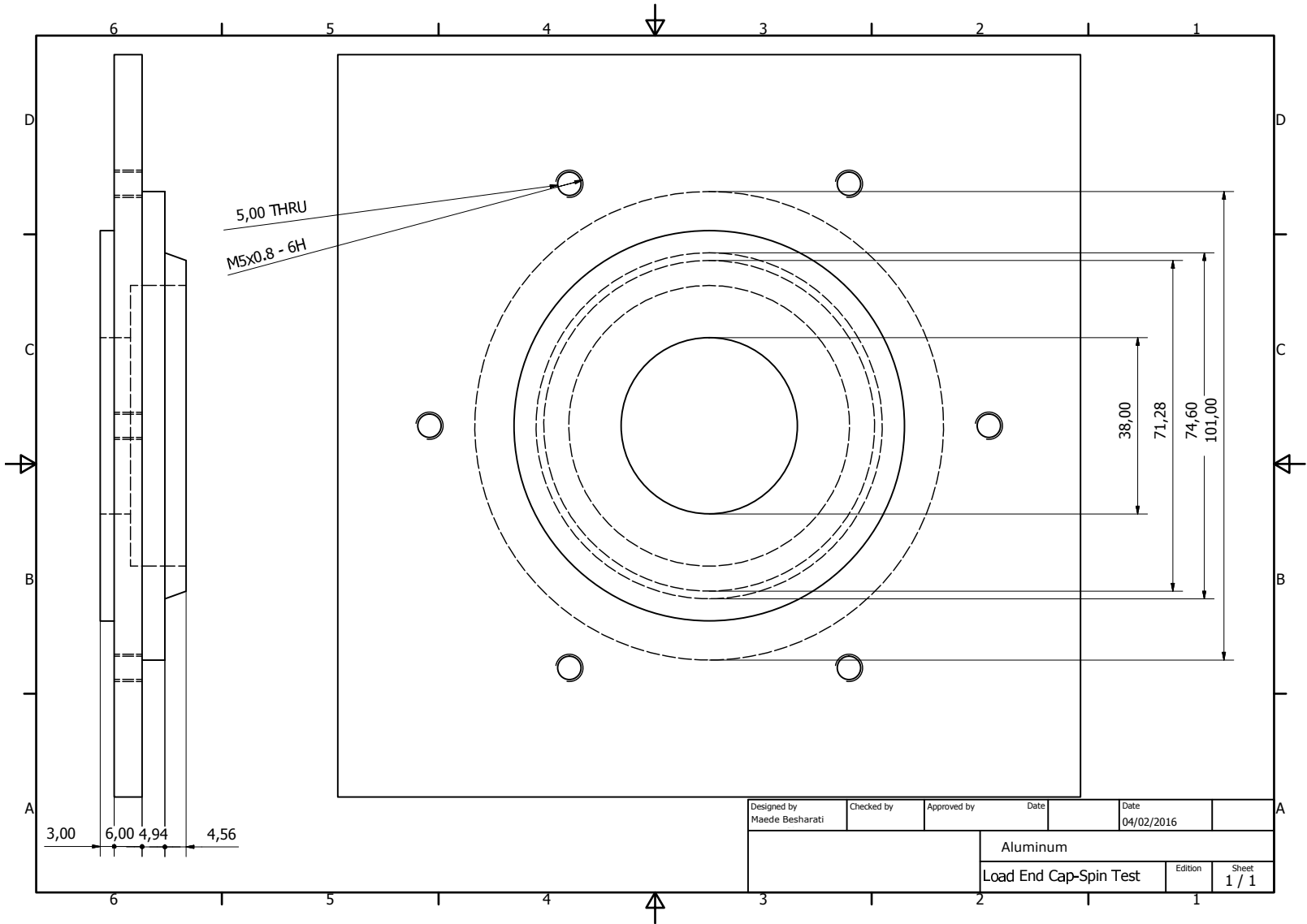
160

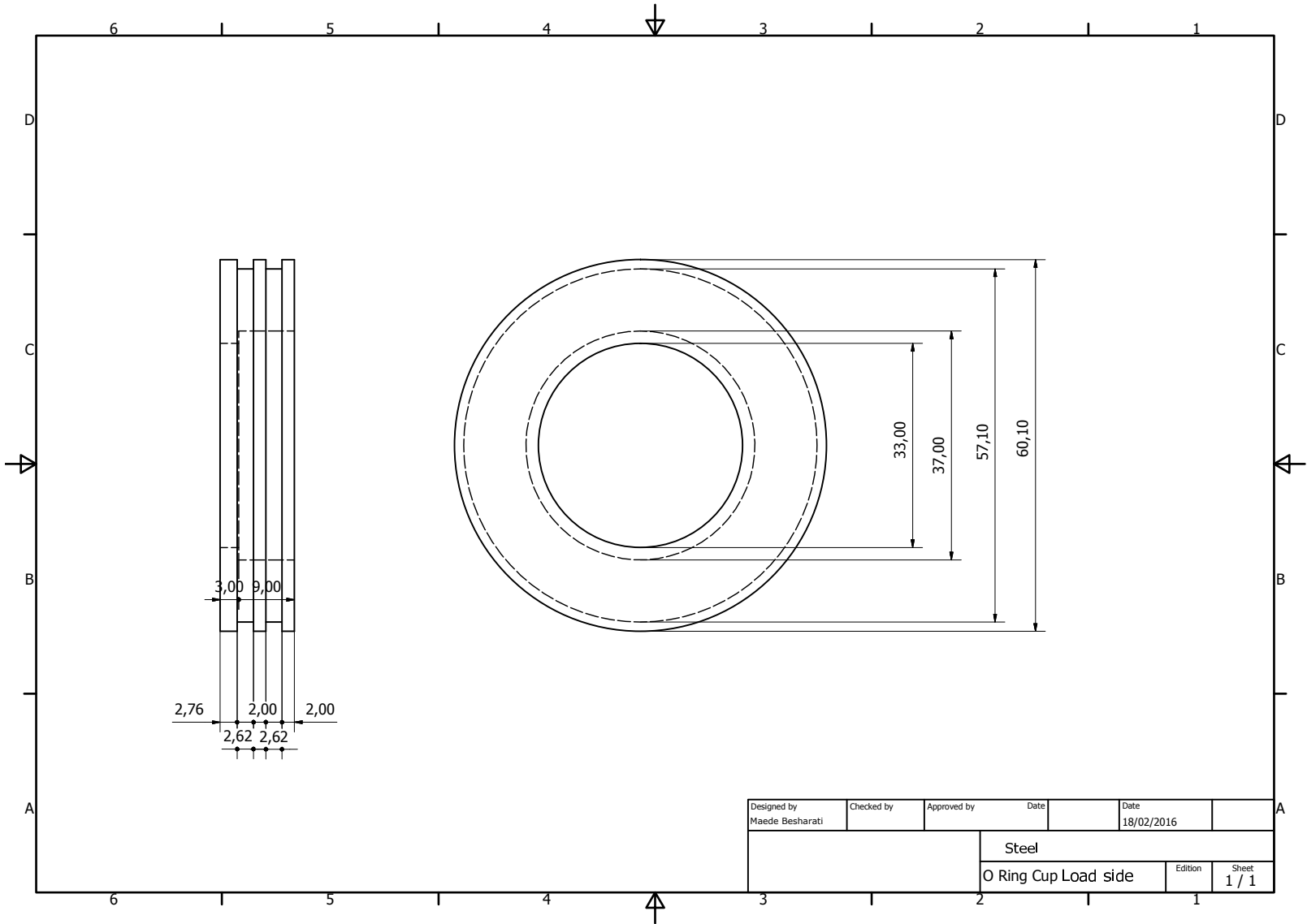




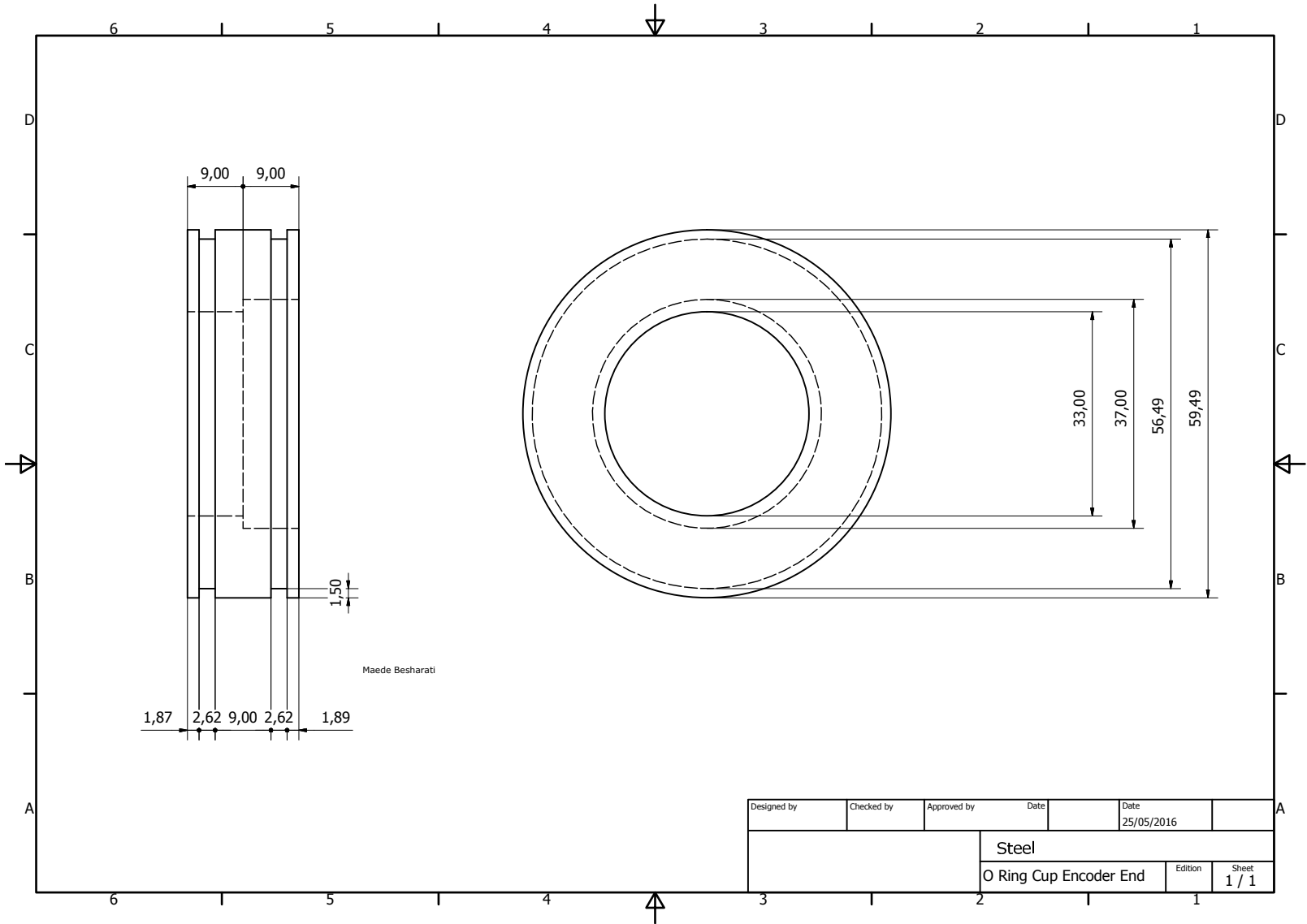


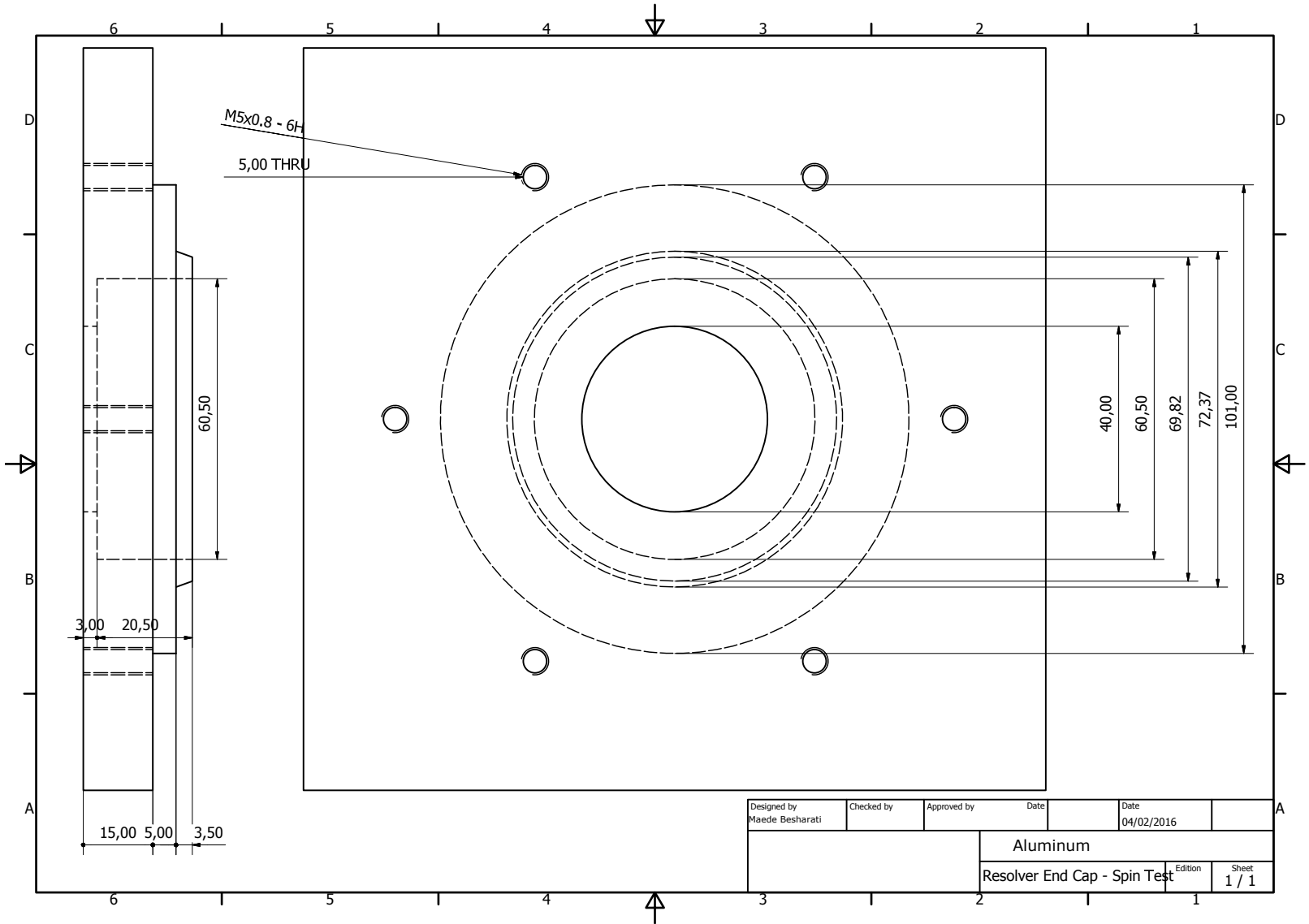


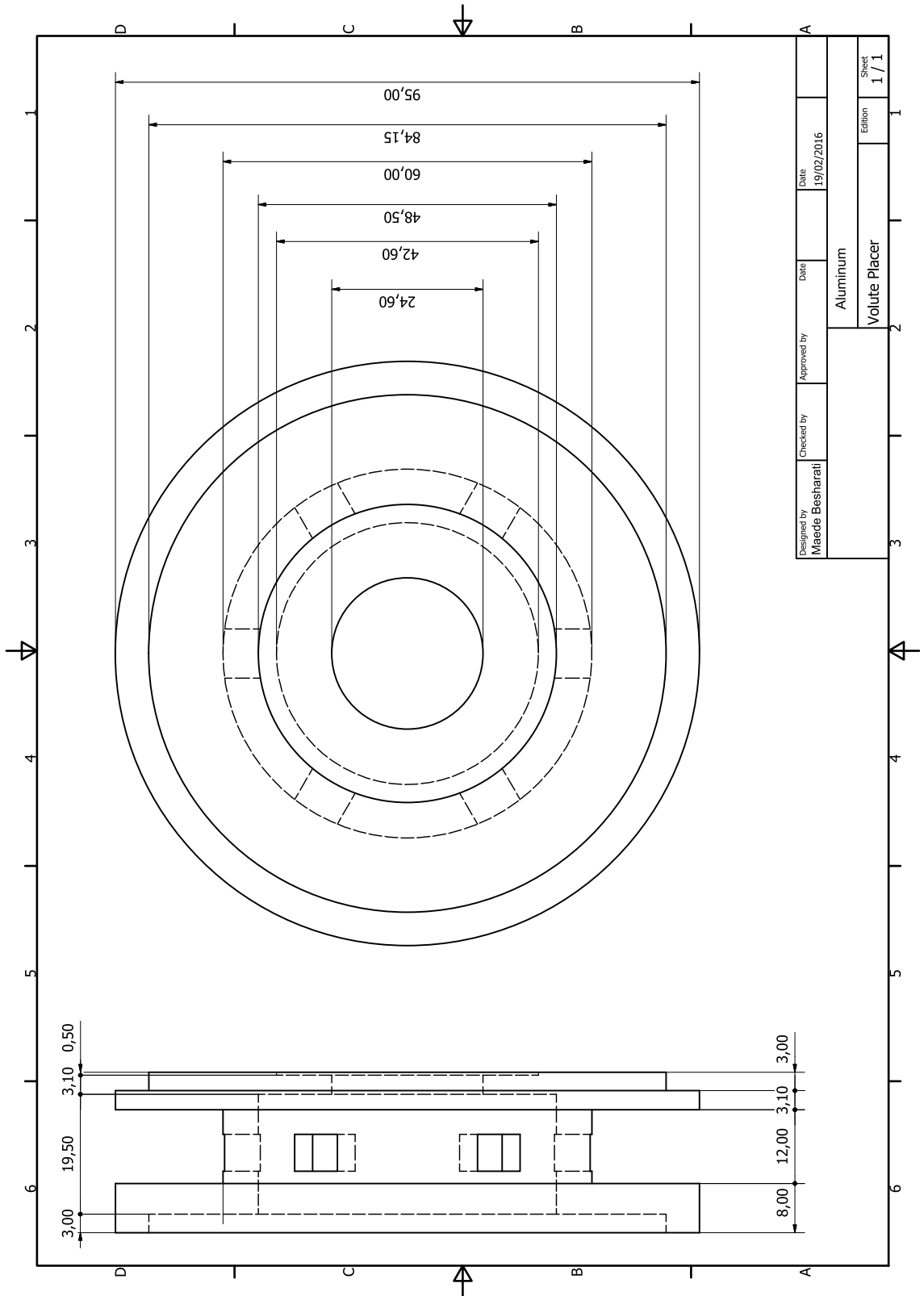


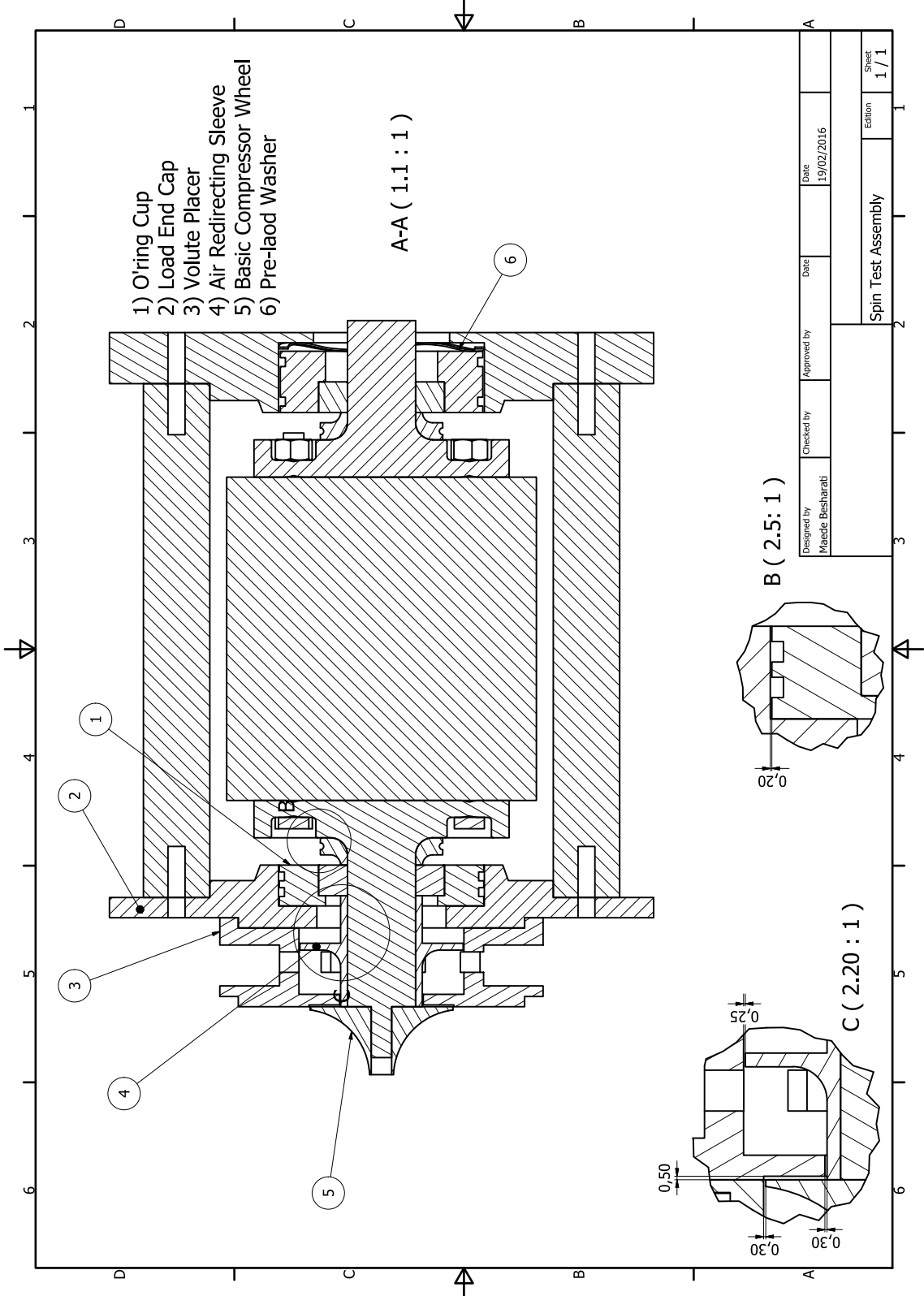


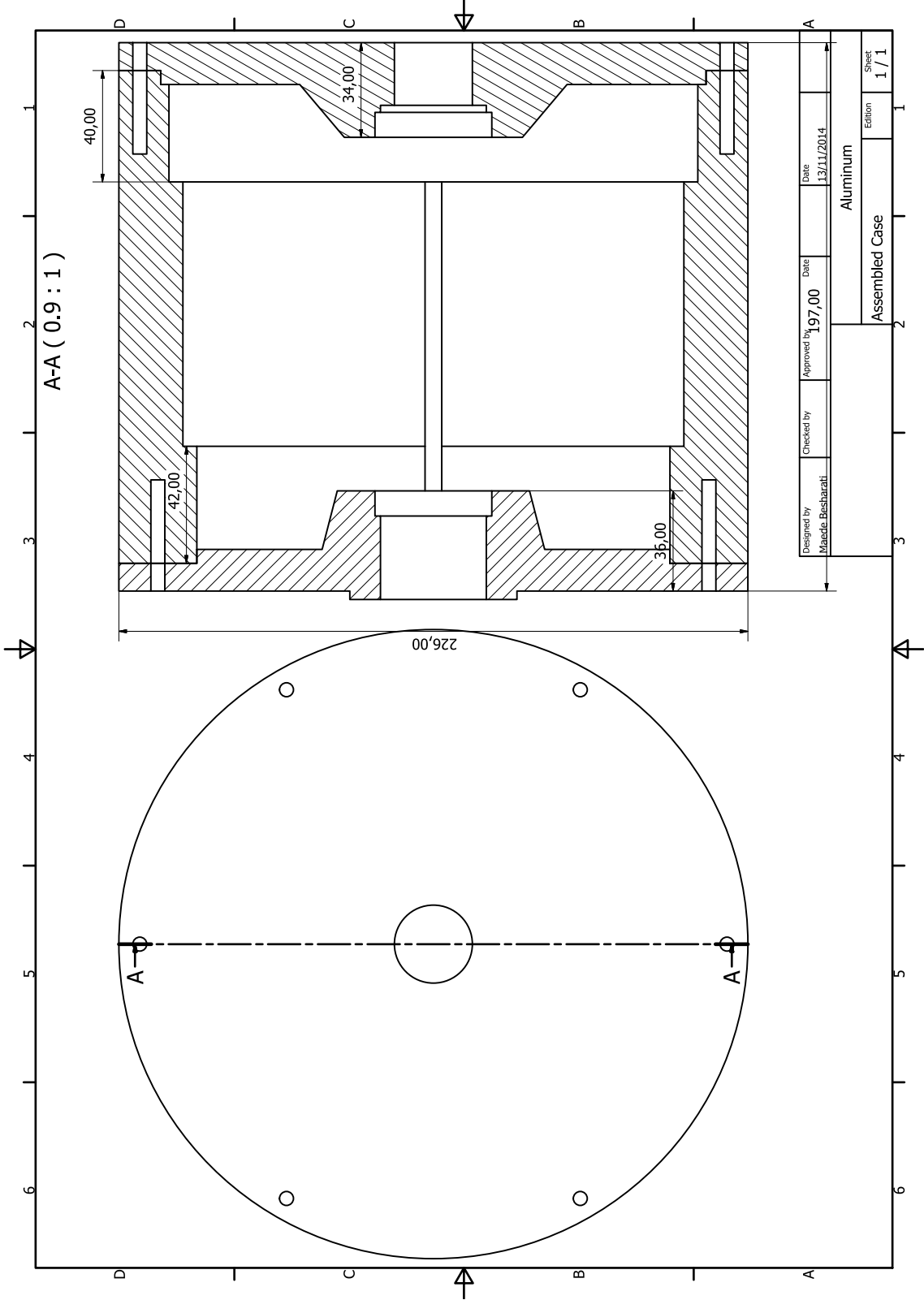
Designed by Maede Besharati	Checked by	Approved by	Date	Date	
				18/02/2016	
			Steel		
			O Ring Cup Load side	Edition	Sheet
					1 / 1

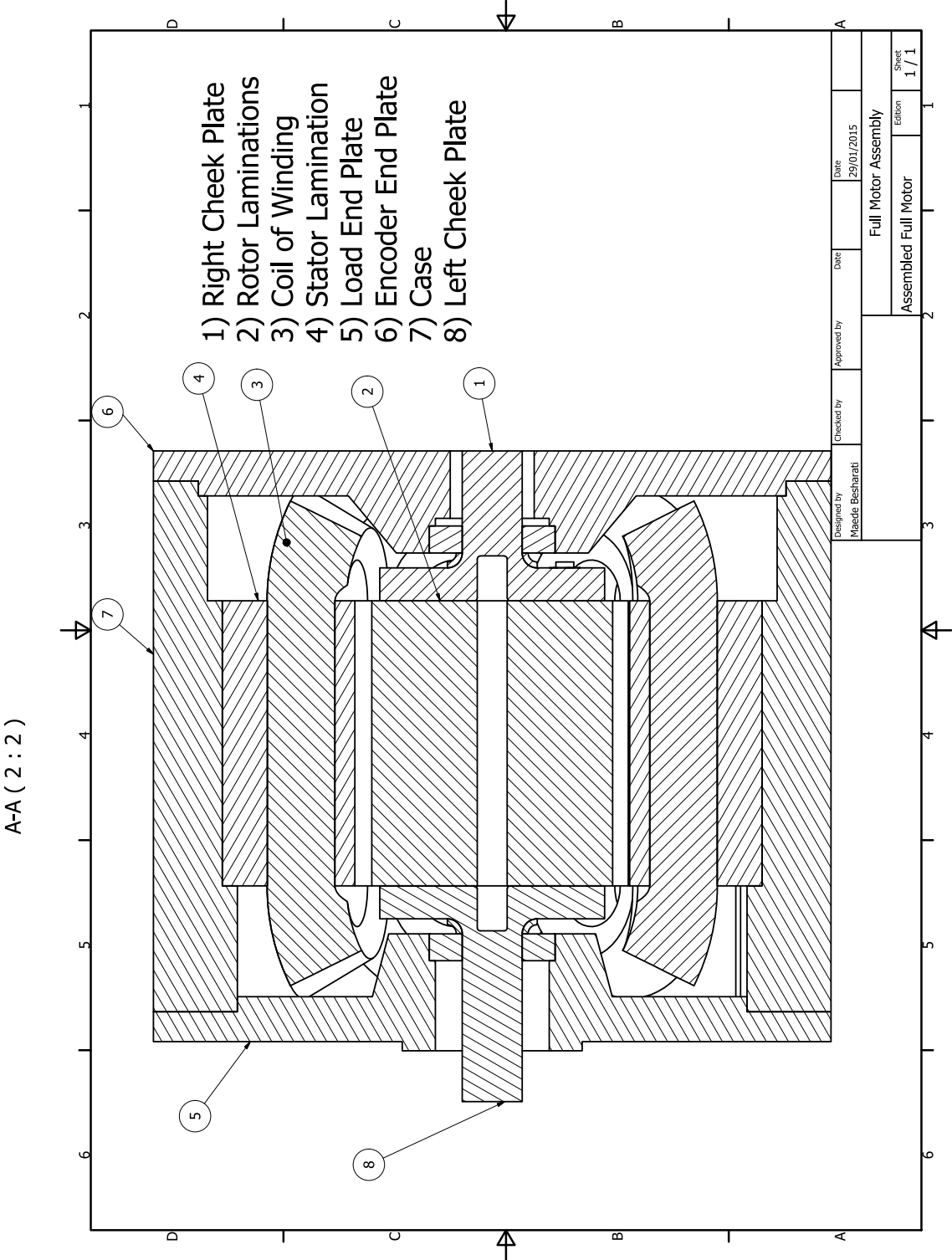


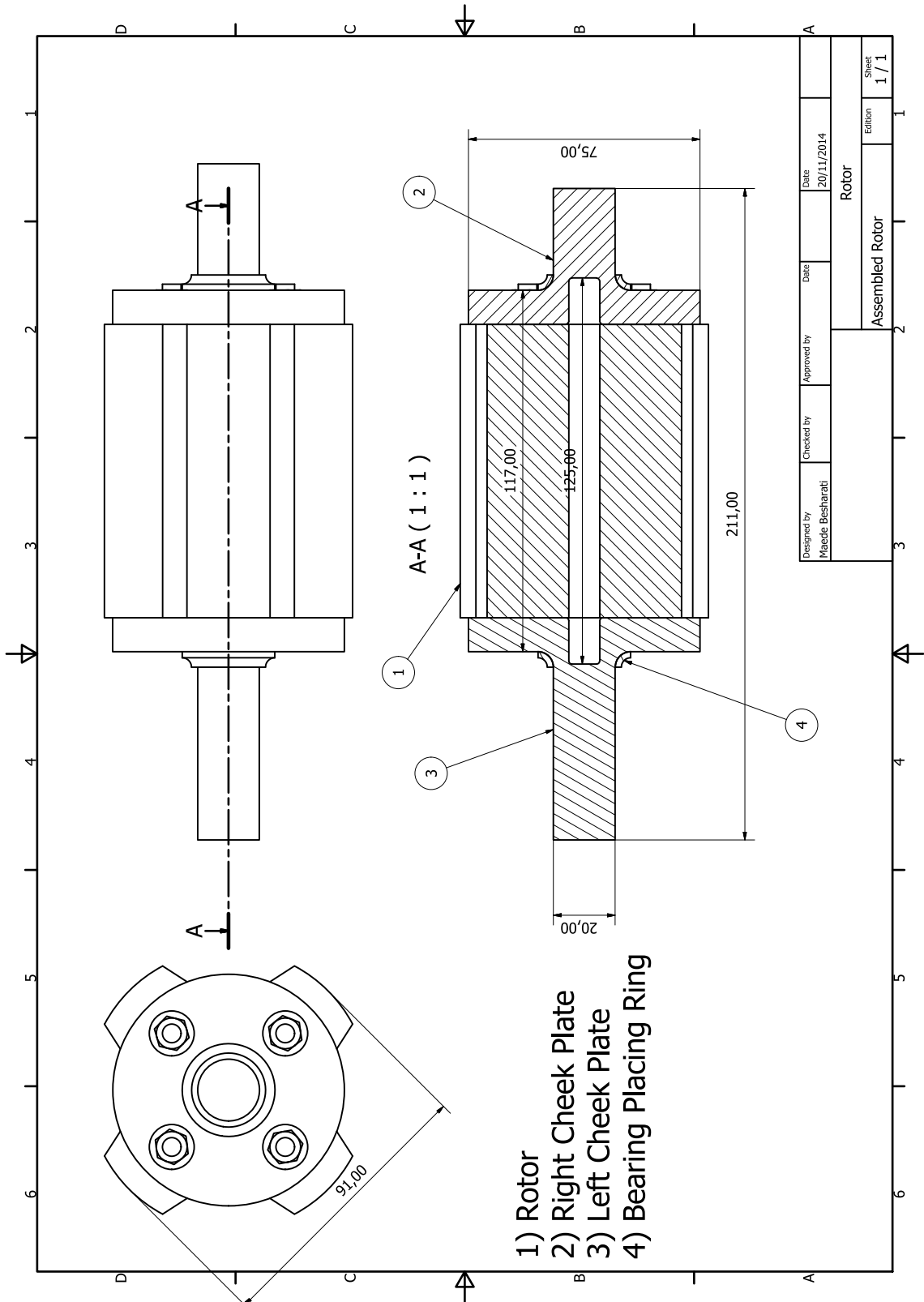


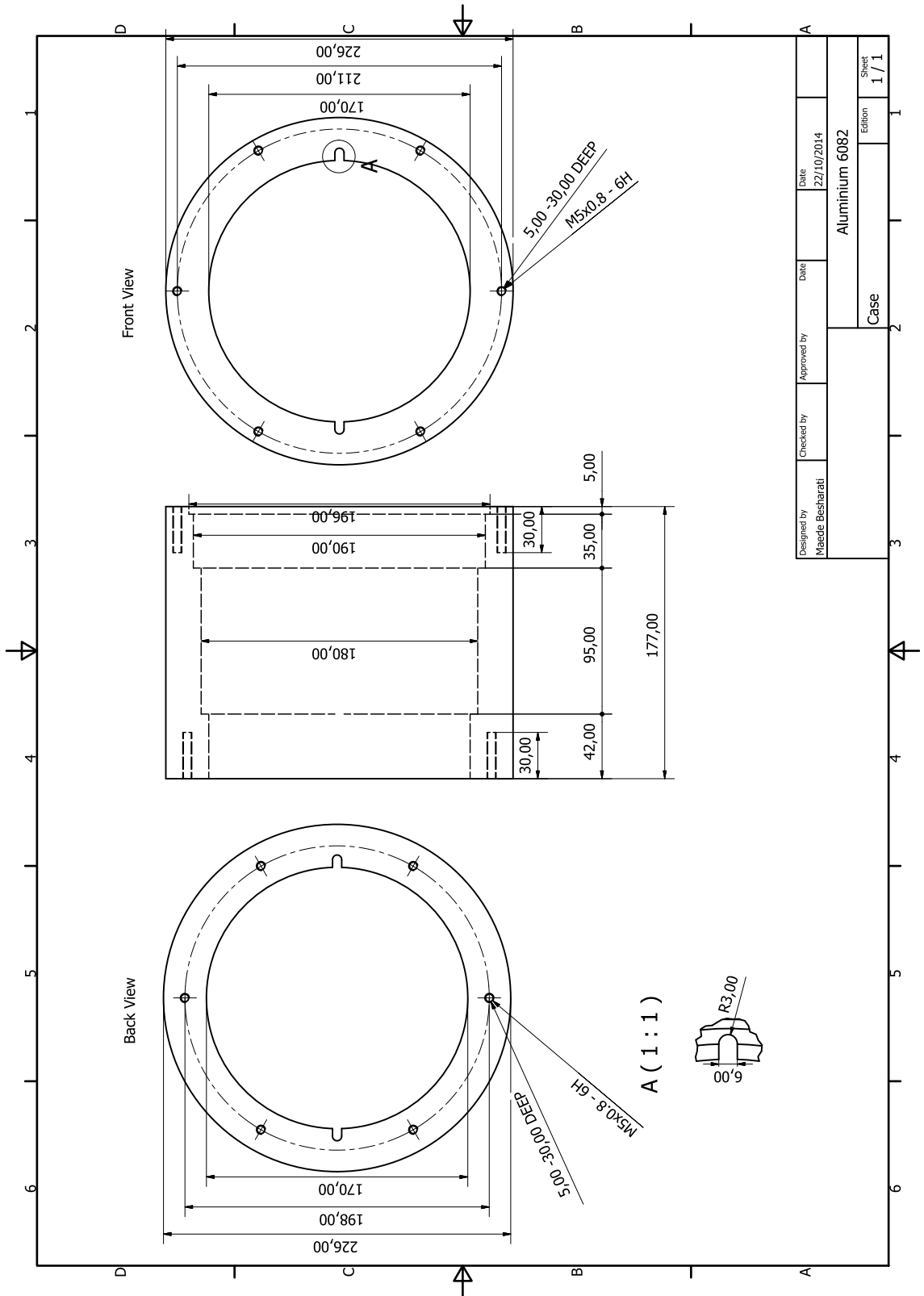




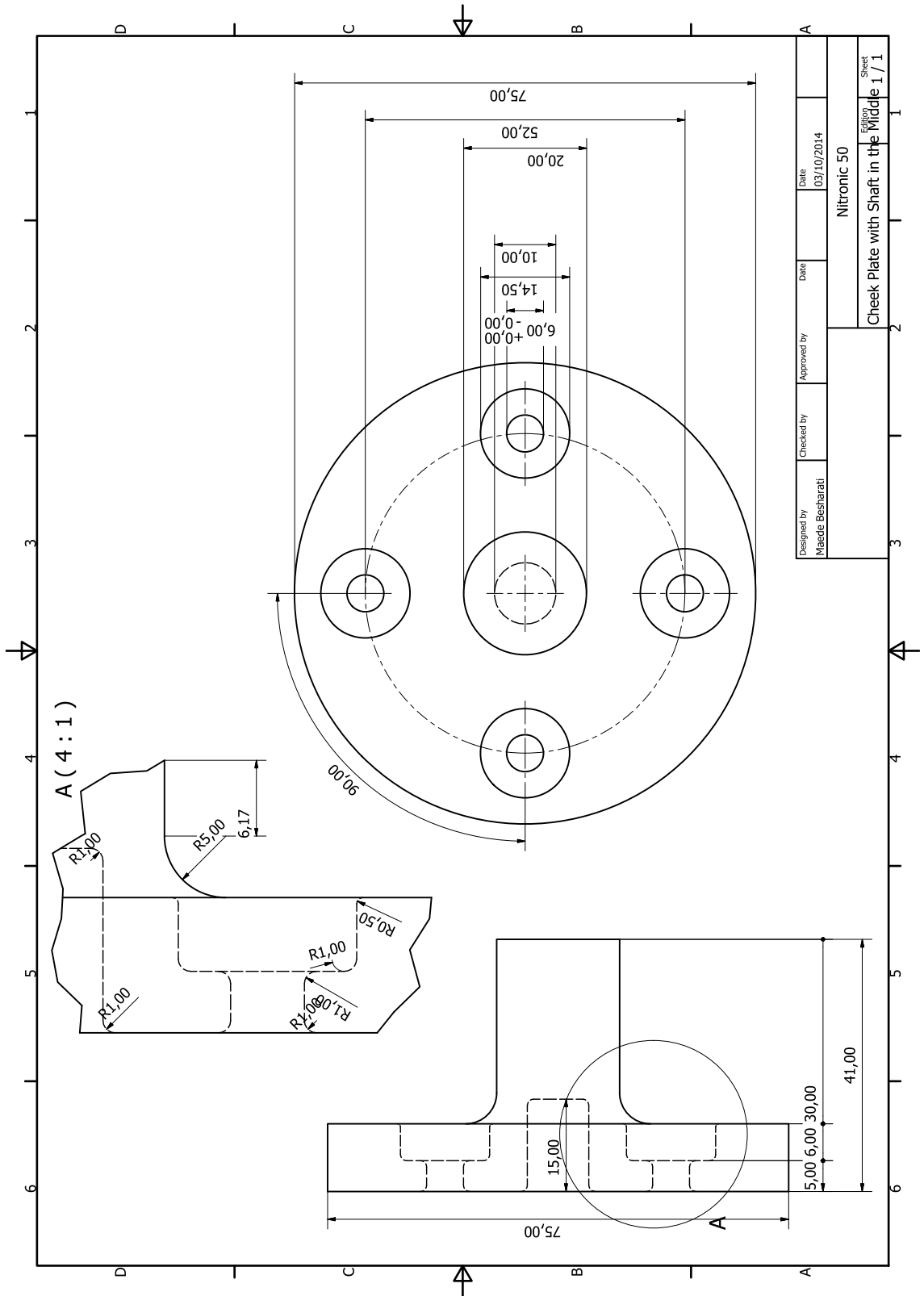


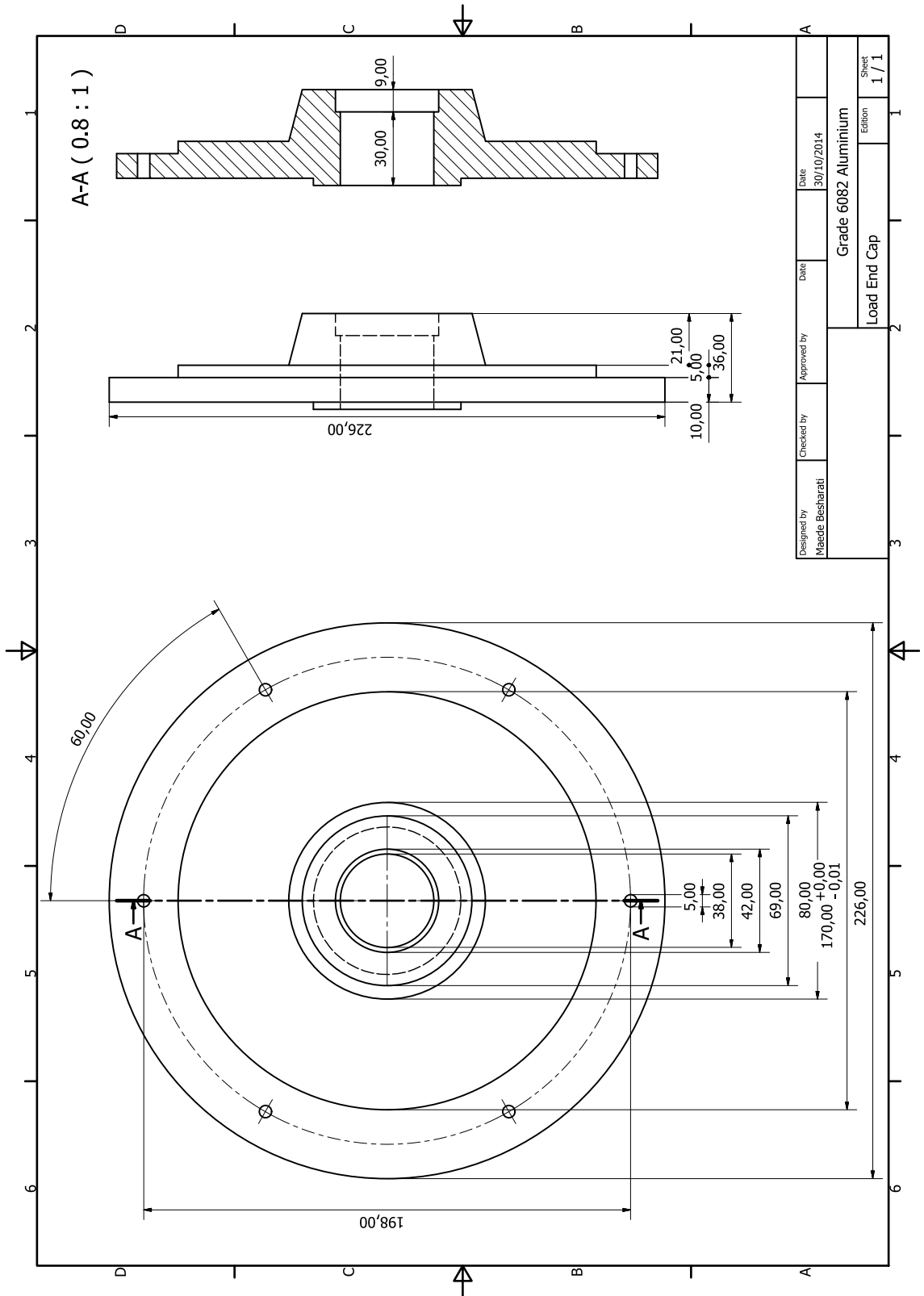


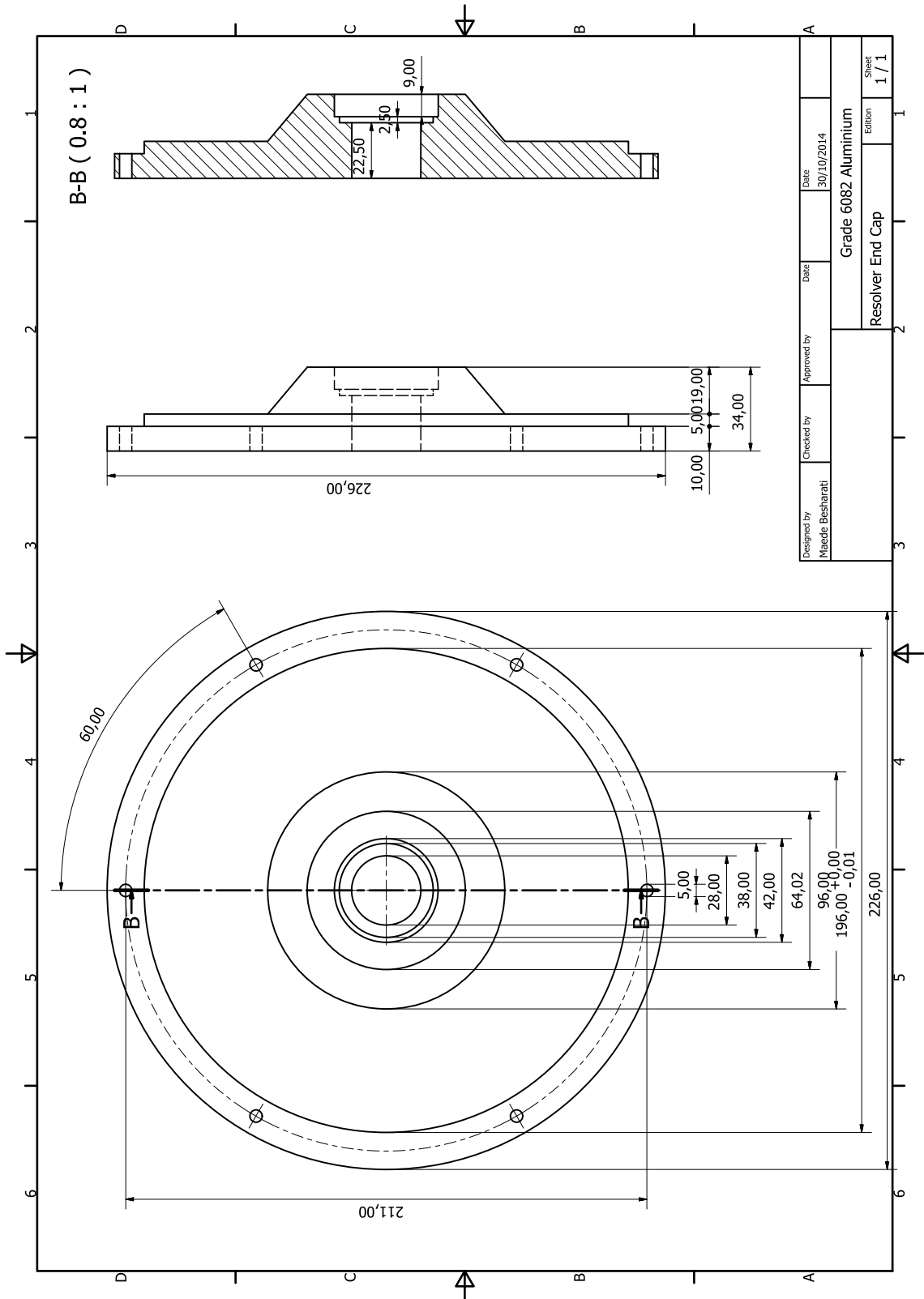




Designed by Maeda Besharati	Checked by	Approved by	Date 22/10/2014	Sheet 1 / 1
Case			Edition	
Aluminium 6082			1 / 1	







References

- [1] R. Yang, N. Schofield, and A. Emadi, “Comparative study between interior and surface permanent magnet traction machine designs,” in *2016 IEEE Transportation Electrification Conference and Expo (ITEC)*, June 2016, pp. 1–6. [Cited on p. 6].
- [2] “Rare metal price,” <http://www.bbc.co.uk/news/magazine-26687605>, accessed: 12-01-2017. [Cited on pp. 6, 7].
- [3] “Rare metal price,” <http://www.magnetsource.com/Solutions-Pages/NEOproperties>, accessed: 12-01-2017. [Cited on pp. 6, 7].
- [4] “World motor vehicle annual production,” https://en.wikipedia.org/wiki/Automotive_industry, accessed: 12-01-2017. [Cited on pp. 6, 8].
- [5] H. Kuss, T. Wichert, and B. Szymanski, “Design of a high speed switched reluctance motor for spindle drive,” in *Compatibility in Power Electronics, 2007. CPE '07*, May 2007, pp. 1–5. [Cited on p. 9].
- [6] J. West, “DC, induction, reluctance and PM motors for electric vehicles,” in *Motors and Drives for Battery Powered Propulsion, IEE Colloquium on*, Apr 1993, pp. 1/1–111. [Cited on p. 9].
- [7] V. Petrus, A. C. Pop, C. S. Martis, J. Gyselinck, and V. Iancu, “Design and comparison of different switched reluctance machine topologies for electric vehicle propulsion,” in *Electrical Machines (ICEM), 2010 XIX International Conference on*, Sept 2010, pp. 1–6. [Cited on p. 9].
- [8] “Toyota prius electric motor,” <http://magneticsmagazine.com/main/articles/simulating-the-toyota-prius-electric-motor/>, accessed: 07-04-2017. [Cited on p. 9].
- [9] P. Lawrenson, J. Stephenson, P. Blenkinsop, J. Corda, and N. Futon, “Variable-speed switched reluctance motors,” *Electric Power Applications, IEE Proceedings B*, vol. 127, no. 4, pp. 253–265, July 1980. [Cited on pp. 9, 10, 11].

-
- [10] M. Feyzi, S. Aghdam, and Y. Ebrahimi, "A comprehensive review on the performance improvement in switched reluctance motor design," in *Electrical and Computer Engineering (CCECE), 2011 24th Canadian Conference on*, May 2011, pp. 000 348–000 353. [Cited on p. 10].
- [11] K. Vijayakumar, R. Karthikeyan, S. Paramasivam, R. Arumugam, and K. Srinivas, "Switched reluctance motor modeling, design, simulation, and analysis: A comprehensive review," *Magnetics, IEEE Transactions on*, vol. 44, no. 12, pp. 4605–4617, Dec 2008. [Cited on p. 10].
- [12] R. Wallace and D. Taylor, "Low-torque-ripple switched reluctance motors for direct-drive robotics," *Robotics and Automation, IEEE Transactions on*, vol. 7, no. 6, pp. 733–742, Dec 1991. [Cited on p. 10].
- [13] J. Finch, J. Faiz, and H. Metwally, "Design study of switched reluctance motor performance," in *Industry Applications Society Annual Meeting, 1992., Conference Record of the 1992 IEEE*, Oct 1992, pp. 242–248 vol.1. [Cited on p. 10].
- [14] I. Chabu, S. Nabeta, and J. Cardoso, "Design aspects of 4:2 pole-2 phase switched reluctance motors," in *Electric Machines and Drives, 1999. International Conference IEMD '99*, May 1999, pp. 63–65. [Cited on p. 10].
- [15] N. Sheth and K. Rajagopal, "Torque profiles of a switched reluctance motor having special pole face shapes and asymmetric stator poles," *Magnetics, IEEE Transactions on*, vol. 40, no. 4, pp. 2035–2037, July 2004. [Cited on p. 10].
- [16] E. Hall M, S. Ramamurthy, and J. Balda, "An enhanced simple method for designing switched reluctance motors under multi-phase excitation," in *Electric Machines and Drives Conference, 2001. IEMDC 2001. IEEE International*, 2001, pp. 715–720. [Cited on p. 10].
- [17] M. Anwar, I. Hussain, and A. Radun, "A comprehensive design methodology for switched reluctance machines," in *Industry Applications Conference, 2000. Conference Record of the 2000 IEEE*, vol. 1, 2000, pp. 63–70 vol.1. [Cited on p. 10].
- [18] M. Moallem, C.-M. Ong, and L. Unnewehr, "Effect of rotor profiles on the torque of a switched-reluctance motor," *Industry Applications, IEEE Transactions on*, vol. 28, no. 2, pp. 364–369, Mar 1992. [Cited on p. 10].
- [19] R. Arumugam, J. Lindsay, and R. Krishnan, "Sensitivity of pole arc/pole pitch ratio on switched reluctance motor performance," in *Industry Applications*
-

-
- Society Annual Meeting, 1988., Conference Record of the 1988 IEEE*, Oct 1988, pp. 50–54 vol.1. [Cited on p. 10].
- [20] R. Krishnan, R. Arumugan, and J. Lindsay, “Design procedure for switched-reluctance motors,” *Industry Applications, IEEE Transactions on*, vol. 24, no. 3, pp. 456–461, May 1988. [Cited on pp. 10, 62].
- [21] M. Ravichandran, V. Achari, C. Joseph, and R. Devasahayam, “A simplified design methodology for switched reluctance motor using analytical and finite element method,” in *Power Electronics, Drives and Energy Systems, 2006. PEDES '06. International Conference on*, Dec 2006, pp. 1–4. [Cited on p. 10].
- [22] J. Finch, “Design method for torque estimation in stepping and switched reluctance motors,” in *Stepper Motors and Their Control, IEE Colloquium on*, Jan 1994, pp. 3/1–3/3. [Cited on p. 10].
- [23] A. Radun, “Design considerations for the switched reluctance motor,” *Industry Applications, IEEE Transactions on*, vol. 31, no. 5, pp. 1079–1087, Sep 1995. [Cited on p. 10].
- [24] A. Miles, “Design of a 5 mw, 9000 v switched reluctance motor,” *Energy Conversion, IEEE Transactions on*, vol. 6, no. 3, pp. 484–491, Sep 1991. [Cited on p. 10].
- [25] B. Fahimi, G. Suresh, and M. Ehsani, “Large switched reluctance machines: a 1 mw case study,” in *Electric Machines and Drives, 1999. International Conference IEMD '99*, May 1999, pp. 84–86. [Cited on pp. 10, 85].
- [26] A. Jack, J. Finch, and J. Wright, “Adaptive mesh generation applied to switched reluctance motor design,” in *Industry Applications Society Annual Meeting, 1990., Conference Record of the 1990 IEEE*, Oct 1990, pp. 230–233 vol.1. [Cited on p. 10].
- [27] I. Chabu, S. Nabeta, and J. Cardoso, “Design aspects of 4:2 pole-2 phase switched reluctance motors,” in *Electric Machines and Drives, 1999. International Conference IEMD '99*, May 1999, pp. 63–65. [Cited on p. 10].
- [28] Y. Tang, “Characterization, numerical analysis, and design of switched reluctance motors,” *Industry Applications, IEEE Transactions on*, vol. 33, no. 6, pp. 1544–1552, Nov 1997. [Cited on p. 10].
- [29] J. Faiz and J. Finch, “Aspects of design optimisation for switched reluctance motors,” *Energy Conversion, IEEE Transactions on*, vol. 8, no. 4, pp. 704–713, Dec 1993. [Cited on p. 11].
-

-
- [30] K. Koibuchi, T. Ohno, and K. Sawa, “A basic study for optimal design of switched reluctance motor by finite element method,” *Magnetics, IEEE Transactions on*, vol. 33, no. 2, pp. 2077–2080, Mar 1997. [Cited on p. 11].
- [31] J. L. Beniwal and R. K. Tripathi, “Speed control of srm drives using a new power converter configuration in electric vehicles,” in *2014 Australasian Universities Power Engineering Conference (AUPEC)*, Sept 2014, pp. 1–6. [Cited on p. 11].
- [32] M. Moallem, C. M. Ong, and L. E. Unnewehr, “Effect of rotor profiles on the torque of a switched-reluctance motor,” *IEEE Transactions on Industry Applications*, vol. 28, no. 2, pp. 364–369, Mar 1992. [Cited on p. 11].
- [33] T. Miller, *Switched Reluctance Motors and Their Control*. OUP Oxford, 1993. [Cited on pp. 12, 57, 61].
- [34] R. Krishnan, *Switched Reluctance motor Drives*. CRC, 2001. [Cited on pp. 14, 57, 59, 61].
- [35] T. Genda and H. Dohmeki, “Characteristics of 4/2 switched reluctance motor for a high speed drive by the excitation angle,” in *Electrical Machines and Systems, 2009. ICEMS 2009. International Conference on*, Nov 2009, pp. 1–6. [Cited on p. 15].
- [36] T. Green, M. Khater, B. Williams, E. El-Shanawany, and A. Hassanein, “A five-phase switched reluctance motor: design and performance,” in *Stepper Motors and Their Control, IEE Colloquium on*, Jan 1994, pp. 7/1–7/4. [Cited on p. 15].
- [37] Y. Kido, N. Hoshi, A. Chiba, S. Ogasawara, and M. Takemoto, “Novel switched reluctance motor drive circuit with voltage boost function without additional reactor,” in *Power Electronics and Applications (EPE 2011), Proceedings of the 2011-14th European Conference on*, Aug 2011, pp. 1–10. [Cited on pp. 15, 16].
- [38] N. Schofield, S. Long, D. Howe, and M. McClelland, “Design of a switched reluctance machine for extended speed operation,” *Industry Applications, IEEE Transactions on*, vol. 45, no. 1, pp. 116–122, Jan 2009. [Cited on p. 17].
- [39] B. Bilgin, A. Emadi, and M. Krishnamurthy, “Comparative evaluation of 6/8 and 6/10 switched reluctance machines for traction application in plug-in hybrid electric vehicles,” in *2011 IEEE International Electric Machines Drives Conference (IEMDC)*, May 2011, pp. 1300–1305. [Cited on p. 18].

-
- [40] Z. Zhu, Z. Azar, and G. Ombach, "Influence of additional air gaps between stator segments on cogging torque of permanent-magnet machines having modular stators," *Magnetics, IEEE Transactions on*, vol. 48, no. 6, pp. 2049–2055, June 2012. [Cited on p. 18].
- [41] S.-H. Mao and M.-C. Tsai, "A novel switched reluctance motor with c-core stators," *IEEE Transactions on Magnetics*, vol. 41, no. 12, pp. 4413–4420, Dec 2005. [Cited on p. 19].
- [42] E. S. Afjei and H. A. Toliyat, "A novel multilayer switched reluctance motor," *IEEE Transactions on Energy Conversion*, vol. 17, no. 2, pp. 217–221, Jun 2002. [Cited on p. 19].
- [43] Y. Hu and W. Ding, "Torque ripple minimization of a novel modular stator switched reluctance motor based on direct instantaneous torque control," in *2016 Eleventh International Conference on Ecological Vehicles and Renewable Energies (EVER)*, April 2016, pp. 1–7. [Cited on p. 19].
- [44] A. Labak and N. C. Kar, "Designing and prototyping a novel five-phase pancake-shaped axial-flux srm for electric vehicle application through dynamic fea incorporating flux-tube modeling," *IEEE Transactions on Industry Applications*, vol. 49, no. 3, pp. 1276–1288, May 2013. [Cited on p. 20].
- [45] K. Nakamura, K. Murota, and O. Ichinokura, "Characteristics of a novel switched reluctance motor having permanent magnets between the stator pole-tips," in *Power Electronics and Applications, 2007 European Conference on*, Sept 2007, pp. 1–5. [Cited on pp. 20, 21].
- [46] M. Ehsani, K. M. Rahman, and H. A. Toliyat, "Propulsion system design of electric and hybrid vehicles," *IEEE Transactions on Industrial Electronics*, vol. 44, no. 1, pp. 19–27, Feb 1997. [Cited on p. 21].
- [47] M. Ruba and D. Fodorean, "Design, analysis and torque control of low voltage high current srm for small automotive applications," in *EUROCON, 2013 IEEE*, July 2013, pp. 1498–1503. [Cited on p. 21].
- [48] J. Miller, A. Gale, P. McCleer, F. Leonardi, and J. H. Lang, "Starter-alternator for hybrid electric vehicle: comparison of induction and variable reluctance machines and drives," in *Industry Applications Conference, 1998. Thirty-Third IAS Annual Meeting. The 1998 IEEE*, vol. 1, Oct 1998, pp. 513–523 vol.1. [Cited on p. 22].
- [49] K. Rahman, B. Fahimi, G. Suresh, A. Rajarathnam, and M. Ehsani, "Advantages of switched reluctance motor applications to ev and hev: design

- and control issues,” *Industry Applications, IEEE Transactions on*, vol. 36, no. 1, pp. 111–121, Jan 2000. [Cited on p. 22].
- [50] S. Kachapornkul, P. Jitkreeyarn, P. Somsiri, K. Tungpimolrut, A. Chiba, and T. Fukao, “A design of 15 kw switched reluctance motor for electric vehicle applications,” in *Electrical Machines and Systems, 2007. ICEMS. International Conference on*, Oct 2007, pp. 1690–1693. [Cited on p. 22].
- [51] H. Hayashi, K. Nakamura, A. Chiba, T. Fukao, K. Tungpimolrut, and D. G. Dorrell, “Efficiency improvements of switched reluctance motors with high-quality iron steel and enhanced conductor slot fill,” *IEEE Transactions on Energy Conversion*, vol. 24, no. 4, pp. 819–825, Dec 2009. [Cited on pp. 22, 23].
- [52] M. Takeno, Y. Takano, A. Chiba, N. Hoshi, M. Takemoto, and S. Ogasawara, “A test result of a 50kw switched reluctance motor designed for a hybrid electric vehicle,” in *2011 IEEE Power and Energy Society General Meeting*, July 2011, pp. 1–2. [Cited on pp. 22, 23].
- [53] T. A. .Burrell, S. L. Campbell, C. L. Coomer, C. W. Ayers, A. A. Wereszczak, J. P. Cunningham, L. E. Seiber, and H. T. Lin, *EVALUATION OF THE 2010 TOYOTA PRIUS HYBRID SYNERGY DRIVE SYSTEM*, March 2011. [Cited on p. 23].
- [54] Y. Takano, M. Takeno, N. Hoshi, A. Chiba, M. Takemoto, S. Ogasawara, and M. A. Rahman, “Design and analysis of a switched reluctance motor for next generation hybrid vehicle without pm materials,” in *Power Electronics Conference (IPEC), 2010 International*, June 2010, pp. 1801–1806. [Cited on p. 23].
- [55] T. Imakawa, K. Chimata, N. Hoshi, A. Chiba, M. Takemoto, and S. Ogasawara, “Characteristic measurements of switched reluctance motor on prototype electric vehicle,” in *Electric Vehicle Conference (IEVC), 2012 IEEE International*, March 2012, pp. 1–8. [Cited on p. 23].
- [56] M. Tanujaya, D. H. Lee, Y. J. An, and J. W. Ahn, “Design and analysis of a novel 4/5 two-phase switched reluctance motor,” in *Electrical Machines and Systems (ICEMS), 2011 International Conference on*, Aug 2011, pp. 1–6. [Cited on pp. 23, 24].
- [57] A. Chiba, Y. Takano, M. Takeno, T. Imakawa, N. Hoshi, M. Takemoto, and S. Ogasawara, “Torque density and efficiency improvements of a switched reluctance motor without rare-earth material for hybrid vehicles,” *IEEE Transactions on Industry Applications*, vol. 47, no. 3, pp. 1240–1246, May 2011. [Cited on p. 24].

-
- [58] M. Takeno, S. Ogasawara, A. Chiba, M. Takemoto, and N. Hoshi, "Power and efficiency measurements and design improvement of a 50kw switched reluctance motor for hybrid electric vehicles," in *2011 IEEE Energy Conversion Congress and Exposition*, Sept 2011, pp. 1495–1501. [Cited on p. 24].
- [59] Y. Takano, T. Maeda, M. Takeno, A. Chiba, N. Hoshi, M. Takemoto, S. Ogasawara, and T. Fukao, "Operating area of a switched reluctance motor with continuous current operation," in *IEEE PES General Meeting*, July 2010, pp. 1–4. [Cited on p. 24].
- [60] M. Takeno, A. Chiba, N. Hoshi, S. Ogasawara, M. Takemoto, and M. A. Rahman, "Test results and torque improvement of the 50-kw switched reluctance motor designed for hybrid electric vehicles," *IEEE Transactions on Industry Applications*, vol. 48, no. 4, pp. 1327–1334, July 2012. [Cited on p. 24].
- [61] K. Kiyota and A. Chiba, "Design of switched reluctance motor competitive to 60-kw ipmsm in third-generation hybrid electric vehicle," *IEEE Transactions on Industry Applications*, vol. 48, no. 6, pp. 2303–2309, Nov 2012. [Cited on pp. 24, 25].
- [62] A. Chiba, M. Takeno, N. Hoshi, M. Takemoto, S. Ogasawara, and M. A. Rahman, "Consideration of number of series turns in switched-reluctance traction motor competitive to hev ipmsm," *IEEE Transactions on Industry Applications*, vol. 48, no. 6, pp. 2333–2340, Nov 2012. [Cited on pp. 25, 26].
- [63] R. D. van Millingen and J. D. van Millingen, "Phase shift torquemeters for gas turbine development and monitoring," *IEEE Transactions on Industrial Electronics*, vol. 5, no. 6, pp. 2946–2959, 1991. [Online]. Available: <http://dx.doi.org/10.1115/91-GT-189> [Cited on pp. 27, 28].
- [64] D. J. B. Smith, "High speed high power electrical machines," Ph.D. dissertation, Newcastle University, 2014. [Cited on pp. 27, 43, 46, 66].
- [65] D. Gerada, A. Mebarki, N. L. Brown, C. Gerada, A. Cavagnino, and A. Boglietti, "High-speed electrical machines: Technologies, trends, and developments," *IEEE Transactions on Industrial Electronics*, vol. 61, no. 6, pp. 2946–2959, June 2014. [Cited on p. 28].
- [66] A. Maeda and H. Tommita, "Power and speed limitation in high speed electrical machines," in *International Power electronics Conference, Yokohama, Japan,*, Apr 1995, pp. 1321–1326. [Cited on pp. 28, 30].
-

-
- [67] M. Rahman, A. Chiba, and T. Fukao, "Super high speed electrical machines - summary," in *Power Engineering Society General Meeting, 2004. IEEE*, June 2004, pp. 1272–1275 Vol.2. [Cited on pp. 28, 30].
- [68] A. Binder and T. Schneider, "High-speed inverter-fed ac drives," in *Electrical Machines and Power Electronics, 2007. ACEMP '07. International Aegean Conference on*, Sept 2007, pp. 9–16. [Cited on p. 29].
- [69] R. R. Moghaddam, "High speed operation of electrical machines, a review on technology, benefits and challenges," in *2014 IEEE Energy Conversion Congress and Exposition (ECCE)*, Sept 2014, pp. 5539–5546. [Cited on pp. 29, 31].
- [70] A. Boglietti, A. Cavagnino, A. Tenconi, and S. Vaschetto, "Key design aspects of electrical machines for high-speed spindle applications," in *IECON 2010 - 36th Annual Conference on IEEE Industrial Electronics Society*, Nov 2010, pp. 1735–1740. [Cited on pp. 29, 31].
- [71] H. C. Lahne, O. Moros, and D. Gerling, "Design considerations when developing a 50000 rpm high-speed high-power machine," in *2015 17th European Conference on Power Electronics and Applications (EPE'15 ECCE-Europe)*, Sept 2015, pp. 1–10. [Cited on p. 31].
- [72] S. Kozuka, N. Tanabe, J. Asama, and A. Chiba, "Basic characteristics of 150,000r/min switched reluctance motor drive," in *Power and Energy Society General Meeting - Conversion and Delivery of Electrical Energy in the 21st Century, 2008 IEEE*, July 2008, pp. 1–4. [Cited on p. 31].
- [73] A. Boglietti, A. Cavagnino, A. Tenconi, and S. Vaschetto, "Key design aspects of electrical machines for high-speed spindle applications," in *IECON 2010 - 36th Annual Conference on IEEE Industrial Electronics Society*, Nov 2010, pp. 1735–1740. [Cited on pp. 31, 45].
- [74] A. V. Radun, "High power density switched reluctance motor drive for aerospace applications," in *Conference Record of the IEEE Industry Applications Society Annual Meeting*, Oct 1989, pp. 568–573 vol.1. [Cited on p. 31].
- [75] E. Richter and C. Ferreira, "Performance evaluation of a 250 kw switched reluctance starter generator," in *Industry Applications Conference, 1995. Thirtieth IAS Annual Meeting, IAS '95., Conference Record of the 1995 IEEE*, vol. 1, Oct 1995, pp. 434–440 vol.1. [Cited on p. 32].
-

-
- [76] E. Richter, J. Lyons, C. Ferreira, A. V. Radun, and E. Ruckstadter, “Initial testing of a 250 kw starter/generator for aircraft applications,” in *SAE Technical Paper*. SAE International, 04 1994. [Online]. Available: <http://dx.doi.org/10.4271/941160> [Cited on p. 32].
- [77] H. Cho and S. Jang, “A design approach to reduce rotor losses in high-speed permanent magnet machine for turbo-compressor,” in *INTERMAG 2006 - IEEE International Magnetism Conference*, May 2006, pp. 209–209. [Cited on pp. 32, 33].
- [78] S. D. Calverley, G. W. Jewell, and R. J. Saunders, “Aerodynamic losses in switched reluctance machines,” *IEE Proceedings - Electric Power Applications*, vol. 147, no. 6, pp. 443–448, Nov 2000. [Cited on p. 32].
- [79] J. Kunz, S. Cheng, Y. Duan, J. Mayor, R. Harley, and T. Habetler, “Design of a 750,000 rpm switched reluctance motor for micro machining,” in *Energy Conversion Congress and Exposition (ECCE), 2010 IEEE*, Sept 2010, pp. 3986–3992. [Cited on pp. 32, 53, 63, 64, 66].
- [80] A. Binder, T. Schneider, and M. Klohr, “Fixation of buried and surface-mounted magnets in high-speed permanent-magnet synchronous machines,” *IEEE Transactions on Industry Applications*, vol. 42, no. 4, pp. 1031–1037, July 2006. [Cited on p. 32].
- [81] N. Bianchi, S. Bolognani, and F. Luise, “Analysis and design of a pm brushless motor for high-speed operations,” *IEEE Transactions on Energy Conversion*, vol. 20, no. 3, pp. 629–637, Sept 2005. [Cited on pp. 32, 34].
- [82] ———, “Potentials and limits of high-speed pm motors,” *IEEE Transactions on Industry Applications*, vol. 40, no. 6, pp. 1570–1578, Nov 2004. [Cited on p. 32].
- [83] J. Dang, S. Haghbin, Y. Du, C. Bednar, H. Liles, J. Restrepo, J. Mayor, R. Harley, and T. Habetler, “Electromagnetic design considerations for a 50,000 rpm 1kw switched reluctance machine using a flux bridge,” in *Electric Machines Drives Conference (IEMDC), 2013 IEEE International*, May 2013, pp. 325–331. [Cited on pp. 32, 66].
- [84] J. Dang, J. R. Mayor, S. A. Semidey, R. G. Harley, T. G. Habetler, and J. A. Restrepo, “Practical considerations for the design and construction of a high-speed srm with a flux-bridge rotor,” *IEEE Transactions on Industry Applications*, vol. 51, no. 6, pp. 4515–4520, Nov 2015. [Cited on p. 32].
-

-
- [85] K. Kiyota, T. Kakishima, A. Chiba, and M. A. Rahman, “Cylindrical rotor design for acoustic noise and windage loss reduction in switched reluctance motor for hev applications,” *IEEE Transactions on Industry Applications*, vol. 52, no. 1, pp. 154–162, Jan 2016. [Cited on p. 33].
- [86] M. Lafoz, P. Moreno-Torres, J. Torres, M. Blanco, and G. Navarro, “Design methodology of a high speed switched reluctance generator drive for aircrafts,” in *2016 18th European Conference on Power Electronics and Applications (EPE'16 ECCE Europe)*, Sept 2016, pp. 1–9. [Cited on p. 34].
- [87] S. M. Jang, H. W. Cho, and S. K. Choi, “Design and analysis of a high-speed brushless dc motor for centrifugal compressor,” *IEEE Transactions on Magnetics*, vol. 43, no. 6, pp. 2573–2575, June 2007. [Cited on p. 34].
- [88] J.-W. Ahn, H. K. M. Khoi, and D.-H. Lee, “Design and analysis of high speed 4/2 srms for an air-blower,” in *2010 IEEE International Symposium on Industrial Electronics*, July 2010, pp. 1242–1246. [Cited on p. 34].
- [89] S. Lin, T. X. Wu, L. Zhou, F. Moslehy, J. Kapat, and L. Chow, “Modeling and design of super high speed permanent magnet synchronous motor (pmsm),” in *2008 IEEE National Aerospace and Electronics Conference*, July 2008, pp. 41–44. [Cited on p. 35].
- [90] C. Zwyssig and J. W. Kolar, “Design considerations and experimental results of a 100 w, 500?000 rpm electrical generator,” *Journal of Micromechanics and Microengineering*, vol. 16, no. 9, p. S297, 2006. [Online]. Available: <http://stacks.iop.org/0960-1317/16/i=9/a=S18> [Cited on p. 35].
- [91] S. A. Long, Z. Q. Zhu, and D. Howe, “Vibration behaviour of stators of switched reluctance motors,” *IEE Proceedings - Electric Power Applications*, vol. 148, no. 3, pp. 257–264, May 2001. [Cited on p. 35].
- [92] Z. Q. Zhu, S. Long, D. Howe, M. C. Tsai, M. F. Hsieh, and T. C. Chen, “Significance of vibration modes in noise and vibration generation of switched reluctance motors,” in *Electrical Machines and Systems, 2003. ICEMS 2003. Sixth International Conference on*, vol. 2, Nov 2003, pp. 672–675 vol.2. [Cited on p. 35].
- [93] K. N. Srinivas and R. Arumugam, “Analysis and characterization of switched reluctance motors: Part ii. flow, thermal, and vibration analyses,” *IEEE Transactions on Magnetics*, vol. 41, no. 4, pp. 1321–1332, April 2005. [Cited on p. 35].
-

-
- [94] C. Y. Wu and C. Pollock, "Analysis and reduction of vibration and acoustic noise in the switched reluctance drive," *IEEE Transactions on Industry Applications*, vol. 31, no. 1, pp. 91–98, January 1995. [Cited on p. 35].
- [95] M. N. Anwar, I. Husain, and A. V. Radun, "A comprehensive design methodology for switched reluctance machines," *IEEE Transactions on Industry Applications*, vol. 37, no. 6, pp. 1684–1692, Nov 2001. [Cited on p. 39].
- [96] W. C. Young, R. G. Budynas, and R. J. Roark, *Roark's formulas for stress and strain*. London : McGraw-Hill, 2000. [Cited on p. 40].
- [97] A. Borisavljevic, H. Polinder, and J. A. Ferreira, "On the speed limits of permanent-magnet machines," *IEEE Transactions on Industrial Electronics*, vol. 57, no. 1, pp. 220–227, Jan 2010. [Cited on pp. 42, 98].
- [98] Z. Huang and J. Fang, "Multiphysics design and optimization of high-speed permanent-magnet electrical machines for air blower applications," *IEEE Transactions on Industrial Electronics*, vol. 63, no. 5, pp. 2766–2774, May 2016. [Cited on p. 44].
- [99] J. D. Ede, Z. Q. Zhu, and D. Howe, "Rotor resonances of high-speed permanent-magnet brushless machines," *IEEE Transactions on Industry Applications*, vol. 38, no. 6, pp. 1542–1548, Nov 2002. [Cited on p. 44].
- [100] C. Zwyssig, S. D. Round, and J. W. Kolar, "An ultrahigh-speed, low power electrical drive system," *IEEE Transactions on Industrial Electronics*, vol. 55, no. 2, pp. 577–585, Feb 2008. [Cited on p. 47].
- [101] G. Genta, *Dynamics of Rotating Systems*. London : Springer, 2005. [Cited on p. 49].
- [102] A. Arkkio, T. Jokinen, and E. Lantto, "Induction and permanent-magnet synchronous machines for high-speed applications," in *2005 International Conference on Electrical Machines and Systems*, vol. 2, Sept 2005, pp. 871–876 Vol. 2. [Cited on p. 52].
- [103] C. Bailey, D. M. Saban, and P. Guedes-Pinto, "Design of high-speed direct-connected permanent-magnet motors and generators for the petrochemical industry," *IEEE Transactions on Industry Applications*, vol. 45, no. 3, pp. 1159–1165, May 2009. [Cited on p. 52].
- [104] C. Zwyssig, S. D. Round, and J. W. Kolar, "Analytical and experimental investigation of a low torque, ultra-high speed drive system," in *Conference Record of the 2006 IEEE Industry Applications Conference Forty-First IAS Annual Meeting*, vol. 3, Oct 2006, pp. 1507–1513. [Cited on p. 53].
-

-
- [105] T. J. E. Miller, *Switched Reluctance Motors and their Control*. Magna Physics Publishing, 2011. [Cited on p. 58].
- [106] N. Fulton and P. Webster, “The development and application of 2-phase switched reluctance drives,” in *Electrical Machines and Drives, 1997 Eighth International Conference on (Conf. Publ. No. 444)*, Sept 1997, pp. 366–370. [Cited on p. 60].
- [107] T. J. E. M. J. R. Hendeshot Jr, *Design of Brushless Permanent Magnet Motors*. Magna Physics Publishing and Clarendon Press, 2011. [Cited on p. 62].
- [108] “M250 35hs data sheet,” <https://www.cogent-power.com/cms-data/downloads>, accessed: 10-11-2016. [Cited on p. 68].
- [109] K. Pullen, “Flywheel assembly,” Jul. 24 2014, wO Patent App. PCT/EP2012/068,340. [Online]. Available: <https://www.google.com/patents/WO2013038027A3?cl=zh> [Cited on p. 70].
- [110] “Spring master wave spring washer data sheet,” <https://www.springmasters.com/sp/wave-spring-washers-3.html>, accessed: 04-10-2016. [Cited on p. 80].
- [111] D. J. B. Atkinson, “High power fault tolerant motors for aerospace applications,” Ph.D. dissertation, Newcastle University, 2007. [Cited on p. 96].
- [112] M. Popescu and D. G. Dorrell, “Proximity losses in the windings of high speed brushless permanent magnet ac motors with single tooth windings and parallel paths,” *IEEE Transactions on Magnetics*, vol. 49, no. 7, pp. 3913–3916, July 2013. [Cited on p. 98].
- [113] P. A. Hargreaves, B. C. Mecrow, and R. Hall, “Calculation of iron loss in electrical generators using finite-element analysis,” *IEEE Transactions on Industry Applications*, vol. 48, no. 5, pp. 1460–1466, Sept 2012. [Cited on p. 100].
- [114] S. H. Won, J. Choi, and J. Lee, “Windage loss reduction of high-speed srm using rotor magnetic saturation,” *Magnetics, IEEE Transactions on*, vol. 44, no. 11, pp. 4147–4150, Nov 2008. [Cited on p. 102].
- [115] K. Kiyota, T. Kakishima, and A. Chiba, “Estimation and comparison of the windage loss of a 60 kw switched reluctance motor for hybrid electric vehicles,” in *Power Electronics Conference (IPEC-Hiroshima 2014 - ECCE-ASIA), 2014 International*, May 2014, pp. 3513–3518. [Cited on pp. 102, 103].
-

- [116] M. F. Momen and I. Husain, "Design and performance analysis of a switched reluctance motor for low duty cycle operation," *IEEE Transactions on Industry Applications*, vol. 41, no. 6, pp. 1612–1618, Nov 2005. [Cited on p. 137].
- [117] C. M. Spargo, B. C. Mecrow, J. D. Widmer, C. Morton, and N. J. Baker, "Design and validation of a synchronous reluctance motor with single tooth windings," *IEEE Transactions on Energy Conversion*, vol. 30, no. 2, pp. 795–805, June 2015. [Cited on p. 150].
- [118] J. D. Widmer and B. C. Mecrow, "Optimized segmental rotor switched reluctance machines with a greater number of rotor segments than stator slots," *IEEE Transactions on Industry Applications*, vol. 49, no. 4, pp. 1491–1498, July 2013. [Cited on p. 151].
- [119] J. D. Widmer, R. Martin, and B. C. Mecrow, "Optimisation of an 80kw segmental rotor switched reluctance machine for automotive traction," in *Electric Machines Drives Conference (IEMDC), 2013 IEEE International*, May 2013, pp. 427–433. [Cited on p. 151].